

*CHARACTERISATION OF SELF-
ASSEMBLED ENGINEERED PROTEINS ON
GOLD NANOPARTICLES AND THEIR
APPLICATION TO BIOSENSING*



Thesis submitted by

Timothy Robson

for the degree of Doctor of Philosophy

Institute for Cell and Molecular Biosciences

Newcastle University

February 2018

ABSTRACT

The use of gold nanoparticles (AuNP) has a long and varied history, thought to cover several thousand years. More recently the unique properties of nanoscale materials have stimulated extensive work on nanoparticles and other nanomaterials leading to their use in novel technologies. AuNPs have been of particular interest for bioscience applications due to their biocompatibility and the ease with which biological molecules can be conjugated to their surface. In this study the assembly of engineered proteins, specifically the transmembrane domain of *Escherichia coli* outer membrane protein A (OmpA_{TM}), onto the surface of AuNPs was investigated both in solution and with the particles attached to a SiO₂ substrate. AuNPs were adhered to SiO₂ surfaces using a novel silane treatment developed by the industrial sponsor and were characterised using spectroscopy, electron and atomic force microscopy. The addition of a single cysteine residue to the OmpA_{TM} structure was shown, by UV-Vis and fluorescence spectroscopy, to increase protein binding at equilibrium and form higher stability protein-AuNP complexes in solution. Following this, engineered OmpA_{TM} proteins containing tandem antibody-binding domains from Streptococcal protein G were assembled on the AuNP surface and their structure interrogated using neutron and light scattering. This revealed an oriented protein layer where the functional domains extend away from the AuNP surface and are available to bind antibodies. OmpA_{TM}-AuNP conjugates were used to develop biosensing assays using both well-established methods, such as lateral flow assays, and novel spectroscopic methods, which use the unique optical properties of AuNPs. Detection of influenza A nucleoprotein, an antigen used to clinically diagnose influenza, was achieved using a bespoke anti-nucleoprotein single-chain antibody domain fused to OmpA_{TM} and assembled on 20 nm diameter AuNPs. The results demonstrate that engineered OmpA_{TM} proteins conjugated to AuNPs can be used to develop novel diagnostics using a range of read out technologies.

ACKNOWLEDGEMENTS

I'd like to thank my supervisor Professor Jeremy Lakey for his kind support and almost unlimited patience, especially when having to listen to my naïve rants about the state of the current geopolitical climate. I am extremely grateful for all the opportunities and encouragement of the last 4 years, without which this work would not have been possible.

I'd also like to thank Deepan and Sion down at Orla for teaching me the mystical arts of membrane protein production, providing me with endless supplies of proteins and detergents, and the many hours of help and advice you've given me.

A Lakey Lab acknowledgements page would not be complete without thanking Helen for being the best lab manager in the universe, making the lab a smooth running and enjoyable place to work and putting up with my whinging and whining when my experiments didn't work (most weeks).

There's a long list of lab members, past and present, I should thank especially Dan for his invaluable help proofreading this Thesis and our many scientific (or not so scientific) discussions, also Nico for helping me with neutron experiments at 2 am and showing how the heck to do the data analysis. I'd like to thank both of you for all the beer, pool, BBQs, meals, films and amusing youtube videos we've shared. It has been a pleasure working with you.

Unquestionably I would not have made it to this point without the care and support of my parents who have continually encouraged me to push myself and believed in me. Adam and Laura, thank you for all of your help and support since I moved up to Newcastle and I'm sorry I moved into a flat just around the corner from your house! I feel very lucky to have such a close family around me who are there when I need them.

Saving the best till last, thank you Beth for continually being my partner in crime. The last four years would not have been the same without you and I certainly wouldn't have made it all the way to end without you, especially when things didn't go as planned. I can't wait to see where our next crazy adventure leads us.

(Hey Dan I've added an oxford comma on this page just for you)

CONTENTS

1 INTRODUCTION.....	1
1.1 GOLD NANOPARTICLE-PROTEIN CONJUGATES	2
1.2 PROTEIN SCAFFOLDS	9
1.3 BACTERIAL OUTER MEMBRANE PROTEINS (OMPs).....	10
1.3.1 <i>Outer Membrane Protein A</i>	14
1.4 NANOSCALE GOLD SURFACE STRUCTURES	19
1.5 SILANE MONOLAYERS.....	21
1.6 CHARACTERISING PROTEIN AND GOLD NANOPARTICLE ARRAYS	24
1.6.1 <i>Surface Analysis</i>	25
1.6.2 <i>Solution Analysis</i>	33
1.7 AIMS	42
2 MATERIALS AND METHODS	43
2.1 MATERIALS	43
2.2 GOLD FUNCTIONALISED SURFACE PREPARATION	43
2.2.1 <i>Piranha Cleaning</i>	43
2.2.2 <i>Silanisation</i>	43
2.2.3 <i>Gold Nanoparticle Deposition</i>	44
2.3 X-RAY PHOTOELECTRON SPECTROSCOPY	45
2.4 NANOPARTICLE SYNTHESIS.....	45
2.4.1 <i>UV-Visible Spectroscopy</i>	45
2.5 TRANSMISSION ELECTRON MICROSCOPY	46
2.6 COLORIMETRIC AMINE DENSITY ASSAY	46
2.7 ATOMIC FORCE MICROSCOPY	47
2.8 SCANNING ELECTRON MICROSCOPY	48
2.9 NEUTRON REFLECTOMETRY	49
2.10 PROTEIN EXPRESSION AND PURIFICATION.....	51
2.11 PHOTOMETRIC PROTEIN CONCENTRATION DETERMINATION	53
2.12 PROTEIN BINDING ANALYSIS	54
2.12.1 <i>Kinetic Experiments</i>	54
2.12.2 <i>Equilibrium Titration</i>	55
2.12.3 <i>NaBH₄ Competition Assay</i>	56
2.12.4 <i>Salt Stability of Protein Conjugated AuNPs</i>	56
2.13 AGAROSE GEL ELECTROPHORESIS OF AUNP	56

2.14 DYNAMIC LIGHT SCATTERING (DLS)	57
2.14.1 IgG Binding to Protein-AuNP Conjugates.....	57
2.14.2 NaBH ₄ Competition.....	58
2.15 NANODROP SPECTROMETER	58
2.16 SMALL ANGLE NEUTRON SCATTERING OF AUNPs	58
2.17 ANALYTICAL ULTRACENTRIFUGATION OF AUNP CONJUGATES.....	59
2.18 FLUORESCENCE MICROSCOPY OF AUNP-GLASS SURFACES.....	59
2.19 CAPILLARY FUNCTIONALISATION	61
2.20 LATERAL FLOW ASSAY	62
3 CHARACTERISING GOLD-GLASS SURFACES WITH SELF-ASSEMBLED PROTEIN MONOLAYERS	64
3.1 INTRODUCTION.....	65
3.2 RESULTS.....	67
3.2.1 Nanoparticle Synthesis.....	67
3.2.2 Surface Functionalisation	68
3.2.3 Silane Monolayer Formation	69
3.2.4 Gold Nanoparticle Deposition	71
3.2.5 Neutron Reflectometry	75
3.3 DISCUSSION.....	88
3.3.1 Surface Characterisation	88
3.4 CONCLUSIONS	95
4 SELF-ASSEMBLY OF ENGINEERED PROTEINS ON GOLD NANOPARTICLES IN SOLUTION	97
4.1 INTRODUCTION.....	98
4.2 RESULTS.....	99
4.2.1 <i>cysOmp_{ATM}</i> Assembly.....	99
4.2.2 <i>GGzOmp_{ATM}</i> Assembly	110
4.3 DISCUSSION.....	125
4.4 CONCLUSIONS	133
5 USING PROTEIN-NANOPARTICLE ASSEMBLIES FOR BIOSENSING	134
5.1 INTRODUCTION.....	135
5.2 RESULTS.....	139
5.2.1 Antibody Binding to Engineered OmpA Monolayers.....	139
5.2.2 Antigen Binding to Single Chain Variable Fragment Fusion Proteins	140
5.3 DISCUSSION.....	146

5.4 CONCLUSIONS	148
6 CONCLUSIONS AND FUTURE WORK.....	150
7 APPENDICES	155
8 REFERENCES.....	163

LIST OF TABLES

TABLE 2.1 SILANE MOLECULE STRUCTURES AND MASS.....	44
TABLE 2.2 EXPRESSED PROTEIN CONSTRUCTS.....	51
TABLE 2.3 PROPERTIES OF THE PROTEINS USED IN THIS STUDY.	53
TABLE 3.1 THEORETICAL SLD VALUES USED FOR CALCULATING THE CONTRAST MATCH SOLUTIONS AND AS STARTING POINTS FOR THE DATA FITTING. OBTAINED USING THE NATIONAL INSTITUTE OF STANDARDS AND TECHNOLOGY (USA) SCATTERING CALCULATOR.	76
TABLE 3.2 LAYER PARAMETERS OBTAINED BY FITTING THE SLAB MODEL TO THE REFLECTIVITY DATA BEFORE AND AFTER PROTEIN ASSEMBLY.....	83
TABLE 3.3 LAYER PARAMETERS OBTAINED BY FITTING THE SPHERE MODEL TO THE REFLECTIVITY DATA.....	86
TABLE 4.1 PSEUDO-SECOND ORDER RATE CONSTANTS AND INITIAL RATES OF CYSOMPA _{TM} AND WTOMPA _{TM} BOTH WITH AND WITHOUT TCEP ADDITION.	104
TABLE 4.2 SUMMARY OF THE PARTICLE SIZE PARAMETERS CALCULATED FROM THE SANS DATA.	122
TABLE 4.3 COMPARISON OF PROTEIN LAYER THICKNESSES FOR GGZOMPA ON PLANAR AND NANOPARTICLE SURFACES.	132
TABLE 7.1 MODEL PARAMETERS FITTED FOR THE AUNP SURFACE USING THE SLAB MODEL.	159
TABLE 7.2 MODEL PARAMETERS FITTED FOR THE GGZOMPA _{TM} COATED SURFACE USING THE SLAB MODEL.....	160
TABLE 7.3 MODEL PARAMETERS FITTED FOR THE AUNP AND GGZOMPA _{TM} COATED SURFACES USING THE SPHERE MODEL.....	161

LIST OF FIGURES

FIGURE 1.1 ELECTRON CLOUD OSCILLATIONS OF GOLD NANOPARTICLES INDUCED BY AN ELECTROMAGNETIC WAVE. ADAPTED FROM (WILLETS AND DUYN, 2007).....	4
FIGURE 1.2 PROTEIN ATTACHMENT STRATEGIES TO GOLD NANOPARTICLES.	5
FIGURE 1.3 THREE STAGE BINDING MODEL OF PROTEINS ON GOLD NANOPARTICLES.....	9
FIGURE 1.4 B-BARREL OUTER MEMBRANE PROTEIN STRUCTURES REPRESENTATIVE OF THE STRUCTURAL VARIETY, BOTH IN SIZE AND OLIGOMERIC STATE.	11
FIGURE 1.5 SCHEMATIC OF OUTER MEMBRANE PROTEIN BIOGENESIS.....	12
FIGURE 1.6 STRUCTURE OF THE BAM COMPLEX, SHOWING THE “TOP HAT” ARRANGEMENT OF THE BAMA BARREL AND ITS FOUR LIPOPROTEIN UNITS.	13
FIGURE 1.7 THE CONFORMATIONAL CHANGES OF THE BAMA BARREL IMPLICATED IN OMP FOLDING AND INSERTION.....	14
FIGURE 1.8 A. CRYSTAL STRUCTURE OF THE OMPA N-TERMINAL DOMAIN BETA-BARREL (PDB ID:1BXW) B. SOLUTION NMR STRUCTURE OF OMPA C-TERMINAL DOMAIN (PDB ID:2MQE) C. POSSIBLE FULL LENGTH STRUCTURE CREATED BY DOCKING THE TWO STRUCTURES IN PYMOL.	15
FIGURE 1.9 POSSIBLE MODELS FOR OMPA LARGE PORE FORMATION.	17
FIGURE 1.10 SCHEMATIC DIAGRAM OF AN ENGINEERED OMPA _{TM} ARRAY SELF-ASSEMBLING ON A PLANAR GOLD SURFACE.....	18
FIGURE 1.11 SCHEMATIC REPRESENTATIONS OF TOP DOWN (A) AND BOTTOM UP (B) FABRICATION TECHNIQUES.....	19
FIGURE 1.12 GENERAL ORGANOSILANE MOLECULE COMPOSITION.....	22
FIGURE 1.13 SCHEMATIC OF APTES MOLECULES ON A SURFACE.	23
FIGURE 1.14 PROPOSED AAPTMS MONOLAYER STRUCTURE ADAPTED FROM (CHEN ET AL., 2006).	24
FIGURE 1.15 SCHEMATIC OF A TYPICAL ATOMIC FORCE MICROSCOPY SET UP.	26
FIGURE 1.16 REFLECTION FROM THE SURFACE OF A MULTI-LAYERED MATERIAL WITH REFRACTIVE INDICES, N_1 AND N_2	29

FIGURE 1.17 SCHEMATIC DIAGRAM OF CONTRAST MATCHING EXPERIMENTS WITH A TWO COMPONENT SYSTEM.....	30
FIGURE 1.18 VISUAL REPRESENTATION OF THE MOMENTUM TRANSFER, Q , OF A REFLECTED NEUTRON BEAM.....	32
FIGURE 1.19 KRETSCHMANN CONFIGURATION SPR SENSOR SUCH AS THOSE USED IN BIACORE INSTRUMENTS.	34
FIGURE 1.20 SCHEMATIC OF A DYNAMIC LIGHT SCATTERING EXPERIMENT.....	35
FIGURE 1.21 VISUAL REPRESENTATION OF THE DIFFERENCES IN THE SCATTERING FLUCTUATIONS OF SMALL AND LARGE PARTICLES IN A SOLUTION.....	36
FIGURE 1.22 TYPICAL SANS INSTRUMENT SET-UP.	37
FIGURE 1.23 THE SCATTERING INTENSITY, $I(Q)$, IS A COMBINATION OF THE FORM FACTOR, $F(Q)$, AND THE STRUCTURE FACTOR, $S(Q)$	38
FIGURE 2.1 SCHEMATIC OF AFM DATA COLLECTION.....	48
FIGURE 3.1 GOLD NANOPARTICLE ASSEMBLY ON AMINE FUNCTIONALISED GLASS SURFACES.....	66
FIGURE 3.2 STRUCTURES OF (3-AMINOPROPYL)TRIMETHOXYSILANE (A) AND (AMINOETHYLAMINOMETHYL)PHENETHYLTRIMETHOXYSILANE (B).	67
FIGURE 3.3. UV-VIS SPECTRA (A) AND REPRESENTATIVE MICROGRAPHS OF SYNTHESISED (B) AND 10 NM COMMERCIAL (C) NANOPARTICLES (BBI SOLUTIONS).....	68
FIGURE 3.4. XPS SURVEY SPECTRA OF BOROSILICATE GLASS COVERSLIPS AFTER SILANISATION AND SUBSEQUENT GOLD DEPOSITION.....	69
FIGURE 3.5. COMPARISON OF THE PRIMARY AMINE DENSITY OF APS AND AAPTMS FILMS ON SILICON WAFERS WITH INCREASING INCUBATION TIME.	70
FIGURE 3.6 REPRESENTATIVE AFM IMAGES OF SILICON BLANK (A), AAPTMS (B) AND APS (C) FUNCTIONALISED SURFACES.	71
FIGURE 3.7. AMINE AVAILABILITY OF AAPTMS MONOLAYER AFTER MULTIPLE GOLD NANOPARTICLE DEPOSITIONS.	72
FIGURE 3.8. REPRESENTATIVE MICROGRAPHS OF AuNP FUNCTIONALISED SURFACES.	73
FIGURE 3.9. GOLD NANOPARTICLE COVERAGE OF AAPTMS FUNCTIONALISED SILICON WAFER CHIPS.....	74

FIGURE 3.10 EFFECT OF THIOL ASSEMBLY ON GOLD NANOPARTICLE COVERAGE AND MORPHOLOGY.	75
FIGURE 3.11 NEUTRON REFLECTOMETRY SET UP.	77
FIGURE 3.12 STRUCTURE OF GGzOMPA _{TM} ARRAYS ON PLANAR GOLD SURFACES ADAPTED FROM (BRUN ET AL., 2015).	78
FIGURE 3.13 NEUTRON REFLECTIVITY PROFILES COMPARING AAPTMS VS AuNP SURFACES (1) AND AuNP VS AuNP + GGzOMPA _{TM} SURFACES (2).	80
FIGURE 3.14 SCHEMATIC REPRESENTATION OF THE SLAB MODEL.	81
FIGURE 3.15 DATA FITTING AND CORRESPONDING SLD PROFILES GENERATED USING THE SLAB MODEL FOR THE AuNP COATED SURFACE.	82
FIGURE 3.16 DATA FITTING AND CORRESPONDING SLD PROFILES GENERATED USING THE SLAB MODEL FOR THE AuNP COATED SURFACE AFTER GGzOMPA _{TM} ASSEMBLY. ..	84
FIGURE 3.17 SCHEMATIC REPRESENTATION OF THE SPHERE MODEL.	85
FIGURE 3.18 DATA FITTING AND CORRESPONDING SLD PROFILES GENERATED USING THE SPHERE MODEL FOR THE AuNP AND AuNP + GGzOMPA _{TM} SURFACES.	87
FIGURE 3.19 FULLY CROSSLINKED AAPTMS MONOLAYER STRUCTURE.	89
FIGURE 3.20 POSSIBLE HYDROGEN BONDING INTERACTIONS OF BME COATED PARTICLES AND A PRIMARY AMINE COATED SURFACE.	91
FIGURE 3.21 SCHEMATIC REPRESENTATION OF THE GGzOMPA _{TM} COATED AuNP SURFACE USING THE SPHERE MODEL.	95
FIGURE 4.1. OVERNIGHT BINDING KINETICS OF CYSOMPA _{TM} , WITH AND WITHOUT FILLER ADDITION.	100
FIGURE 4.2 INITIAL BINDING KINETICS OF WILD TYPE AND CYSOMPA _{TM}	102
FIGURE 4.3 INITIAL PROTEIN BINDING KINETICS AFTER TCEP ADDITION (A+B) AND THE EFFECT OF TCEP ON AuNP ELECTROPHORETIC MOBILITY (C).	103
FIGURE 4.4 PROTEIN FOOTPRINTS USED FOR THEORETICAL BINDING CAPACITY CALCULATIONS.	105
FIGURE 4.5 UV-VIS SPECTROSCOPY (A AND B) AND PROTEIN:AuNP STOICHIOMETRY (C AND D) DATA FOR 1 OD _{525NM} 20 NM AuNPs TITRATED WITH INCREASING PROTEIN CONCENTRATION, AFTER OVERNIGHT INCUBATION.	106

FIGURE 4.6. AGAROSE GEL ELECTROPHORESIS (A), UV-VIS SPECTROSCOPY (B) AND DLS (C) RESULTS FOR 20 NM AuNPs CONJUGATED WITH WTOMPA _{TM} AND CYSOMPA _{TM}	107
FIGURE 4.7. PROTEIN-AuNP STABILITY WHEN CHALLENGED WITH INCREASING NABH ₄ CONCENTRATIONS.	108
FIGURE 4.8 MEASURING PROTEIN BINDING USING A NANODROP TM ND-1000 SPECTROPHOTOMETER AND COMPARISON WITH THE CARY 4E SYSTEM.....	109
FIGURE 4.9. GOLD NANOPARTICLE SAMPLES AFTER OVERNIGHT INCUBATION WITH INCREASING GGZOMPA _{TM} CONCENTRATION.	110
FIGURE 4.10 OVERNIGHT BINDING OF GGZOMPA _{TM} WITH AND WITHOUT PROTEIN INDUCED PARTICLE AGGREGATION.....	111
FIGURE 4.11. ASSEMBLY OF GGZOMPA _{TM} PROTEINS ON AuNPs AND BINDING TO A MAb.	112
FIGURE 4.12. INCREASE IN THE D _{HYD} OF PROTEIN CONJUGATED AuNPs AFTER INCUBATION WITH IgG.	113
FIGURE 4.13. AGAROSE GEL ELECTROPHORESIS (A), UV-VIS SPECTROSCOPY (B) AND DLS (C) RESULTS FOR GGZ AND CYSOMPA _{TM} CONJUGATED PARTICLES.....	114
FIGURE 4.14 TRANSMISSION ELECTRON MICROSCOPY OF GGZOMPA _{TM} CONJUGATED NANOPARTICLES.....	115
FIGURE 4.15. STABILITY DATA FOR GGZOMPA _{TM} CONJUGATED AuNPs WITH AND WITHOUT FILLER.	116
FIGURE 4.16 PARTICLE SIZE DISTRIBUTIONS, BY DLS, OF THE NANOPARTICLE SAMPLES USED FOR SANS AFTER 48 HOURS DIALYSIS IN D ₂ O.	117
FIGURE 4.17 RAW SANS SCATTERING DATA FOR THE 20 NM AuNPs AND GGZOMPA _{TM} COATED PARTICLES.	118
FIGURE 4.18 FITTING OF THE 20 NM AuNP SANS SCATTERING PROFILE BY THE BAYESAPP PROGRAM IS SHOWN BEFORE (A) AND AFTER (C) TRUNCATION OF THE DATA AT LOW Q. THE PAIR DISTANCE DISTRIBUTION FUNCTIONS GENERATED BY THE PROGRAM ARE SHOWN ON THE RIGHT OF THE CORRESPONDING DATA SET (B AND D).	120

FIGURE 4.19 SCHEMATIC DIAGRAM OF AN AUNP WITH A SINGLE GGzOMPATM PROTEIN STANDING ON THE SURFACE.	121
FIGURE 4.20 (A) PROTEIN COATED AUNP NEUTRON SCATTERING DATA WITH THE BAYESAPP FITS REPRESENTED BY THE SOLID LINES. (B) THE P(R) PLOTS GENERATED FROM THE INDIRECT FOURIER TRANSFORM OF THE DATA.	123
FIGURE 4.21 SEDIMENTATION COEFFICIENT DISTRIBUTIONS OF GGzOMPATM CONJUGATED PARTICLES.	125
FIGURE 4.22 EXAMINATION OF THE SOLVENT ACCESSIBLE SURFACE CHARGE AND NET CHARGE OF THE OMPATM TRANSMEMBRANE DOMAIN.	127
FIGURE 4.23 THE THREE PROPOSED BINDING REGIMES OF WTOMPATM AND CYSOMPATM ON GOLD NANOPARTICLES.	131
FIGURE 5.1 SCHEMATIC OF A LATERAL FLOW ASSAY.	136
FIGURE 5.2 GOLD NANOPARTICLE AGGREGATION INDUCED BY CROSSLINKING WITH A MULTIVALENT ANALYTE.	137
FIGURE 5.3 B1 DOMAIN FROM GROUP G STREPTOCOCCI WITH THE HELIX AND BETA STRAND INVOLVED IN ANTIBODY BINDING INDICATED IN BLUE.	138
FIGURE 5.4 SCHEMATIC OF LSPR BIOSENSOR ASSAY FOR FLUA NP DETECTION.	139
FIGURE 5.5. FLUORESCENCE INTENSITY OF CYSOMPATM AND GGzOMPATM SURFACES AFTER INCUBATION WITH ALEXAFLUOR 488 CONJUGATED RABBIT IGG.	140
FIGURE 5.6. INFLUENZA A NUCLEOPROTEIN BINDING TO SCFvOMPATM AND IGAPOMPATM CONJUGATED AUNPS.	141
FIGURE 5.7 BULK REFRACTIVE INDEX SENSITIVITY OF AUNP FUNCTIONALISED BOROSILICATE GLASS CAPILLARIES.	142
FIGURE 5.8. THE SHIFT IN Λ_M AFTER ASSEMBLY OF CYSOMPATM AND SCFvOMPATM ON AUNP FUNCTIONALISED GLASS CAPILLARIES AND SUBSEQUENT INCUBATION WITH FLUA NP.	143
FIGURE 5.9 SCHEMATIC DIAGRAM OF THE INFLUENZA A NUCLEOPROTEIN LATERAL FLOW ASSAY.	144
FIGURE 5.10 LATERAL FLOW STRIPS SHOWING INFLUENZA NUCLEOPROTEIN BINDING TO SCFvOMPATM CONJUGATED PARTICLES AND BINDING SPECIFICITY.	145

FIGURE 6.1 OMPA _{TM} SURFACE CHARGE BEFORE (A) AND AFTER (B) MUTATION OF THE CHARGED RESIDUES.	154
FIGURE 7.1 GRAPHICAL REPRESENTATION OF THE BOOTSTRAP ERROR ANALYSIS FOR THE AuNP SURFACE USING THE SLAB MODEL.	156
FIGURE 7.2 GRAPHICAL REPRESENTATION OF THE BOOTSTRAP ERROR ANALYSIS FOR THE AuNP + GGzOMPA _{TM} SURFACE USING THE SLAB MODEL.	157
FIGURE 7.3 GRAPHICAL REPRESENTATION OF THE BOOTSTRAP ERROR ANALYSIS FOR THE AuNP AND AuNP + GGzOMPA _{TM} SURFACES USING THE SPHERE MODEL.	158
FIGURE 7.4 FITTING OF THE GGzOMPA _{TM} SURFACE USING THE SLAB MODEL OF A BARE AuNP SURFACE.	162

LIST OF ABBREVIATIONS AND ACRONYMS

AAPTMS – (Aminoethylaminomethyl)phenethyltrimethoxysilane

Ail – Adhesion and invasion locus

AFM – Atomic force microscopy

APTES – Aminopropyltriethoxysilane

APBS – Adaptive Poisson-Boltzmann solver

APS – Aminopropyltrimethoxysilane

AUC – Analytical ultracentrifugation

AuMW – Gold matched water (73% D₂O, 27% H₂O)

AuNP – Gold nanoparticle

BAM – Beta-barrel assembly machinery

BSA – Bovine serum albumin

βME – Beta-mercaptoethanol

CCD – Charge coupled device

CMC – Critical micelle concentration

cysOmpA_{TM} – Cysteine modified transmembrane domain of OmpA

DDM – n-Dodecyl β-D-maltoside

DLS – Dynamic light scattering

DNA – Deoxyribonucleic acid

E. coli – Escherichia coli

EM – Electromagnetic

EtOH – Ethanol

Fc – Fragment crystallisable region of an antibody

FhuA – Ferrichrome-iron receptor

GB3 – third IgG-binding domain of Protein G

GGzOmpA_{TM} – Tandem B domains from protein G and z domain linker from protein A fused to the C terminus of a circularly permuted OmpA_{TM}

HEPES – 4-(2-hydroxyethyl)-1-piperazineethanesulphonic acid

HR-TEM – High resolution transmission electron microscopy

IgAPOmpA_{TM} – Alpha helical IgA protease domain fused to the C terminus of a circularly permuted OmpA_{TM}

IgG – Immunoglobulin G

ILL – Institut Laue-Langevin, Grenoble France

IM-MS – Ion mobility mass spectroscopy

IPTG – Isopropyl β-D-1-thiogalactopyranoside

ITC – Isothermal titration calorimetry

ISIS – ISIS neutron and muon source, Oxford UK

LamB – Maltoporin

LB – Lysogeny broth

LFA – Lateral flow assay

LPS – Lipopolysaccharide

LSPR – Local surface plasmon resonance

MBS – 2-Mercapto-5-benzimidazole sulfonic acid

MRI – Magnetic resonance imaging

MWCO – Molecular weight cut off

NaBH₄ – Sodium borohydride

NaCl – Sodium chloride

Ni-NTA – Nickel-nitrilotriacetic acid

NMR – Nuclear magnetic resonance

NR – Neutron reflectometry

OD – Optical density

OmpA – Outer membrane protein A

OmpA_{TM} – Transmembrane domain of outer membrane protein A

OmpC – Outer membrane protein C

OmpF – Outer membrane protein F

OmpT – Outer membrane protein T

OmpX – Outer membrane protein X

PDB – Protein Database

RPM – Revolutions per minute

SAM – Self-assembled monolayer

SANS – Small angle neutron scattering

SAXS – Small angle X-ray scattering

scFv - Single chain variable fragment

scFvOmpA_{TM} – Single chain variable fragment and alpha helical linker from IgA protease fused to the C terminus of a circularly permuted OmpA_{TM}

SDS-PAGE – Sodium dodecyl sulphate – polyacrylamide gel electrophoresis

SEM – Scanning electron microscopy

SERS – Surface enhanced raman spectroscopy

SH-C11-OEG6 – (11-Mercaptoundecyl)hexa(ethylene glycol)

Skp – Seventeen kilodalton protein

SLD – Scattering length density

SMW – Silicon matched water (38% D₂O, 62% H₂O)

SPR – Surface plasmon resonance

ssDNA – Single stranded DNA

SurA – Survival protein A

TBS – Tris buffered saline

TCEP – Tris(2-carboxyethyl)phosphine hydrochloride

TEM – Transmission electron microscopy

thioAlkylPEG – (11-Mercaptoundecyl)hexa(ethylene glycol)

TIF – Tagged image file

TM-Domain – Transmembrane-domain

TNF – Tumour necrosis factor

wtOmpA_{TM} – wild type transmembrane domain of OmpA

XPS – X-ray photoelectron spectroscopy

LIST OF APPENDICES

APPENDIX 1: NEUTRON REFLECTOMETRY DATA ANALYSIS	156
---	-----

1 INTRODUCTION

1.1 Gold Nanoparticle-Protein Conjugates

The use of gold nanoparticles has a long history, thought to date back more than 2000 years, with evidence of scientists from China and India having access to colloidal gold solutions as far back as the 4th and 5th centuries B.C. Despite this long history, the facile synthesis of well-defined gold nanoparticles was not achieved until the 20th century with the development of the citrate reduction method by Turkevich in 1951 (Turkevich et al., 1951). Further work by Frens (Frens, 1973) and alternative syntheses by Brust (Brust et al., 1994) have improved the ability to control particle size and enabled the introduction of new chemistries to the particle surface during synthesis.

The syntheses mentioned above generate gold nanoparticle suspensions by the reduction of a solution of chloroauric acid (HAuCl_4), where gold has an oxidation state of +3, to metallic gold, which has an oxidation state of 0. Chloroauric acid is formed by dissolving metallic gold in a mixture of nitric and hydrochloric acid, known as aqua regia. The formation of a stable gold nanoparticle solution also requires a stabilising surface ligand to be introduced to the nanoparticle surface. In the Turkevich method (the most widely used synthesis) trisodium citrate is used as both the reducing agent and stabilising surface ligand (Turkevich et al., 1951). Reduction of Au(III) to Au(0) by citrate leads to the formation of acetone dicarboxylate and carbon dioxide. The exact mechanism of gold nanoparticle synthesis by the Turkevich method is not fully understood. It is thought that the reduction of AuCl_4^- leads to the formation of small seed particles, which then grow to form the larger gold nanoparticles (Wuithschick et al., 2015). Free citrate molecules can then coordinate to the gold nanoparticle surface through their carboxylate groups, stabilising the particle from further growth (Park and Shumaker-Parry, 2014). Several parameters can be adjusted to tune the size of the gold nanoparticles, including the citrate/ AuCl_4^- ratio, reaction pH and chloride ion concentration (Ji et al., 2007; Zhao et al., 2012).

It was already known in the 1950s that adsorbed proteins and other hydrophilic molecules could stabilise gold colloid suspensions against aggregation by electrolytes (Slabaugh, 1962; Williams and Chang, 1951). Faulk and Taylor (Faulk and Taylor, 1971) took this idea further by conjugating antibodies to particles for use as markers for transmission electron microscopy (TEM) studies of *Salmonella* surface antigens. Immunogold particles have continued to be the most widely used labels for electron microscopy of biological samples. The electron dense nature of gold provides excellent

contrast, while their small size and the highly specific binding of antibodies make them ideal probes for precisely labelling cellular components and surface antigens (Cloeckert et al., 1990; Rash et al., 1998). Gold nanoparticles have become an attractive platform for biomedical applications due to their biocompatibility and the wealth of available attachment strategies for biological molecules such as proteins, DNA and peptides (Bartczak and Kanaras, 2011; Falabella et al., 2010; Robinson et al., 2010). Applications in photothermal therapies, drug delivery, imaging and diagnostics have also been explored.

Many applications in imaging and diagnostics take advantage of the unique optical properties of gold nanoparticles. These properties are caused by the coherent oscillation of conduction band electrons induced by the electromagnetic field of incident light photons (Figure 1.1). The collective oscillations of the particle's electrons are known as the local surface plasmon, with its resonance frequency observable by an absorption maximum in the visible electromagnetic spectrum (Huang and El-Sayed, 2010; Willets and Duyne, 2007). The local surface plasmon resonance (LSPR) peak is dependent on several factors, including the size and shape of the particle and the dielectric constant of any bound molecules and the surrounding medium. Changes in the LSPR of gold nanoparticles have been utilised for observing biomolecule binding both in solution and on surfaces (Liang et al., 2011; Nath and Chilkoti, 2004; Tsai et al., 2005; Willets and Duyne, 2007; Zhao et al., 2008). The interaction of light with gold nanoparticles is extremely strong, for example the scattering cross-section of an 80 nm nanoparticle is 10^6 times greater than the fluorescence cross-section of a fluorescein molecule, which allows them to be observed even using low resolution imaging techniques such as dark field microscopy.

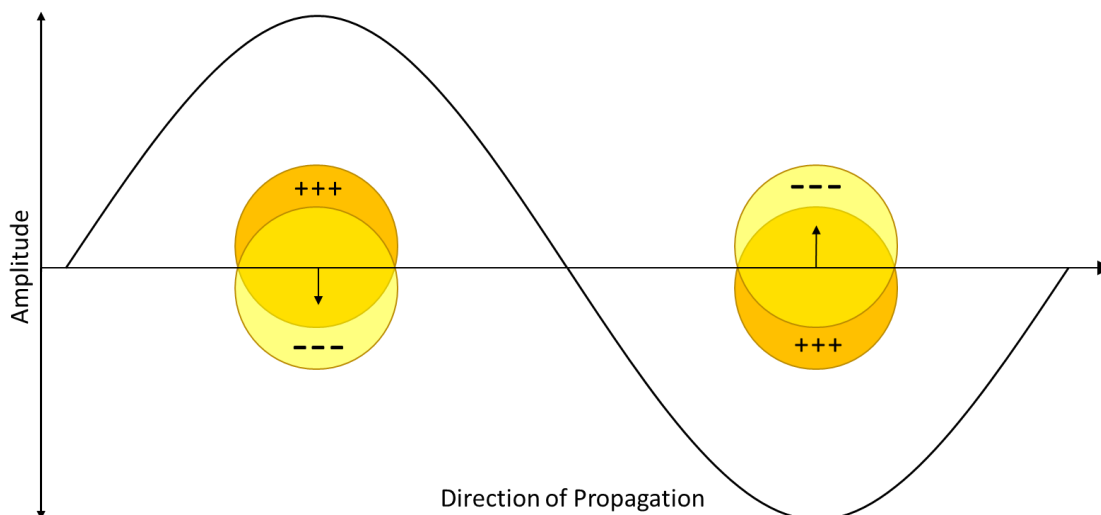


Figure 1.1 Electron cloud oscillations of gold nanoparticles induced by an electromagnetic wave. Adapted from (Willets and Duyne, 2007)

A secondary effect of photon absorption by AuNPs is non-radiative heat generation (Huang and El-Sayed, 2010). This has been utilised in photothermal cancer treatments, when the nanoparticles are excited, usually with near infrared radiation, they cause localised hyperthermia in tumour cells leading to cell death. Antibody conjugation to AuNPs can be used to target specific tumours and the development of such hybrid nanoparticles has enabled real time imaging by MRI and ultrasound during photothermal therapy (Ke et al., 2011; Larson et al., 2007).

Other therapeutic strategies have been explored, particularly using AuNPs as drug delivery vehicles (Dreaden et al., 2012; Dykman and Khlebtsov, 2012; Niemeyer, 2001). One of the first examples of this approach delivered tumour necrosis factor (TNF), an anticancer, protein biologic, to colon carcinoma tumour cells in an *in vivo* mouse model. Recombinant TNF was directly conjugated to AuNPs and administered intravenously with accumulation in the tumour observed by a bright red colour change (Paciotti et al., 2004).

Specific Attachment of Proteins to AuNPs

While many proteins are conjugated to AuNPs through non-specific adsorption, it can be beneficial for binding to be mediated through higher specificity interactions. There are three main strategies for specifically conjugating proteins to gold nanoparticles, covalent or electrostatic binding to a surface ligand, direct binding to the surface and secondary interactions with a bound protein (Figure 1.2). The chosen protein and the application of the nanoparticle conjugate will dictate which strategy is best suited.

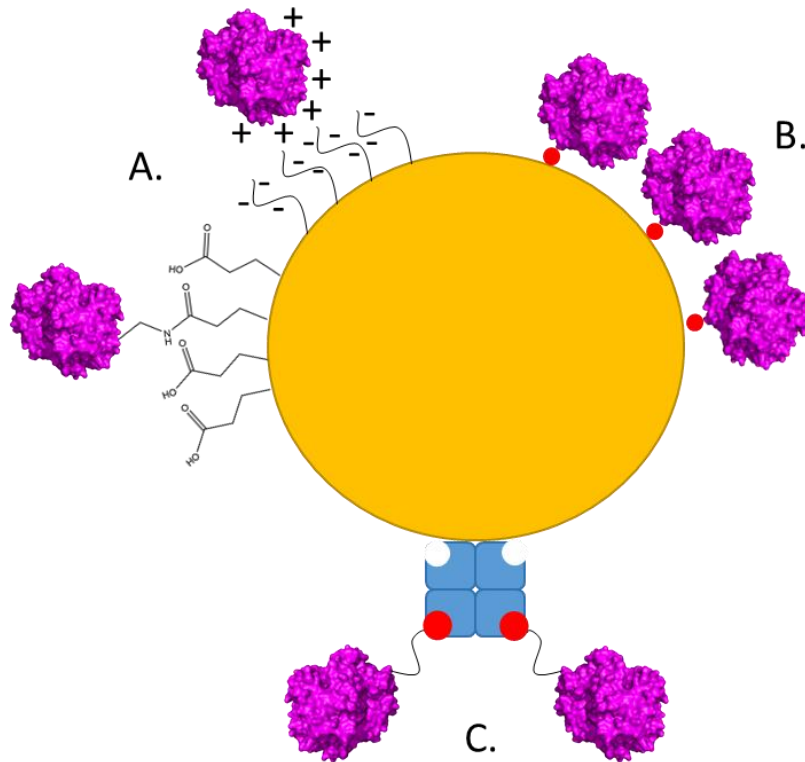


Figure 1.2 Protein attachment strategies to gold nanoparticles. A. Electrostatic or covalent coupling to surface capping ligands, such as negatively charged ligands or EDC/NHS coupling of primary amines to surface carboxyl groups. B. Direct attachment to the nanoparticle surface through free cysteine residues. C. Indirect attachment through a surface bound protein such as streptavidin binding to biotinylated proteins.

During nanoparticle synthesis a stabilising capping ligand is introduced on to the nanoparticle surface with the most commonly used ligand being sodium citrate (Park and Shumaker-Parry, 2014). The charged capping ligands help stabilise the particles through mutual electrostatic repulsion. Electrostatic attraction between these ligands and proteins is commonly exploited for binding. This can take place via general charge interactions, such as antibodies with citrate ligands, or more specific interactions, such as a Ni^{2+} -NTA ligand with a polyhistidine tagged protein (Ma et al., 2015). Binding via these interactions can be transient and suffer from exchange effects; this is especially problematic if the desired application has a complex sample environment containing multiple proteins (Green et al., 1999; Wang et al., 2016).

More permanent covalent attachment of proteins to capping ligands has been intensely studied. New chemistries can be effectively introduced via assembly of alkylthiol compounds on the nanoparticle surface which form good quality monolayers on gold surfaces through stable sulphur-gold bonds (Bain et al., 1989; Love et al., 2005).

The most commonly used chemistry for biomolecule attachment is 1-ethyl-3-(3-dimethylaminopropyl)carbodiimide/N-hydroxysuccinimide (EDC/NHS) coupling which forms an amide bond between the terminal carboxyl group of the capping ligand with free primary amines of the protein (Bartczak and Kanaras, 2011; Sehgal and Vijay, 1994). For larger proteins with several reactive amines this method results in multiple orientations which can be detrimental to sensitivity in sensing applications (Puertas et al., 2010). More specific chemistries can be used, such as maleimide coupling to cysteine residues (Kuhn et al., 2007) and hydrazide coupling to polysaccharides in the Fc region of antibodies (Kumar et al., 2008).

Direct attachment of proteins on the AuNP surface can be achieved through endogenous or engineered cysteine residues in the protein structure (Lee et al., 2007; Liu et al., 2009; Terrettaz et al., 2002). The resulting gold-thiol bonds provide stable binding, directed orientation and a simplified functionalisation process (X. Wang et al., 2017).

Secondary interactions can also be used to mediate binding to the nanoparticle surface. The two most common examples are avidin-biotin binding and protein A/G binding to antibodies. The Avidin-biotin complex is the strongest known non-covalent interaction ($K_d \sim 10^{-14}$ M), which provides an extremely stable link, while a range of commercially available biotin derivatives can be used to functionalise the protein of choice (Sapsford et al., 2013). Protein A and G are antibody binding proteins from *S. aureus* and group G *Streptococci* respectively. Both have been used to bind immunoglobulins to nanoparticles for surface display, mediated through the Fc region of the antibody (Brun et al., 2015; Gronenborn and Clore, 1993; van der Heide and Russell, 2016).

It has been proposed by Medintz (Medintz, 2006) that the reliable generation of functional protein surfaces on nanoparticles requires 5 key criteria:

- Homogeneous binding
- Control over the final protein orientation
- Control over the distance from the surface
- Control over the protein density on the surface
- Control over the affinity of the protein to the surface

Although some of these requirements can be met using the attachment strategies described above, there are currently none that would satisfy all five. Much of the work on functional protein surfaces has been focussed on antibodies and their derivatives. It

remains to be seen if a general attachment method that facilitates controlled assembly of any protein can be developed.

Direct Protein-Nanoparticle Binding (Protein Adsorption)

General protein adsorption to nanoparticles is usually termed as non-specific. This is more a reflection of the variety of interactions that are possible between proteins and the nanoparticle surface. Several binding modes have been described for proteins to gold nanoparticle surfaces; electrostatic interactions, hydrophobic interactions and covalent bonds can all play a role in this process. The degree to which each of these interactions contributes to binding will vary depending on the structure of the protein, the charges of both protein and nanoparticle and, in the case of gold, the availability of free cysteine residues for covalent bond formation. Other possible considerations include, the retention of secondary structure upon binding, i.e. whether proteins denature and “spread” on the surface, interactions between neighbouring proteins and whether multi-layered protein coronas are formed. Protein binding to particles and surfaces is extremely important for many processes including, bioprocessing, biosensing and drug delivery and although extensively studied, the complex, multi-faceted nature of protein binding makes detailed mechanistic information difficult to elucidate.

The binding mechanisms of several model proteins, such as bovine serum albumin and ubiquitin, to gold nanoparticles has been intensively studied. These studies have shown that electrostatic interactions significantly affect binding. For example, the adsorption capacity of citrate coated AuNPs increases with lower pH for small globular proteins (Wang et al., 2016) and the orientation of α -Synuclein binding is dependent on the particle surface charge (Lin et al., 2015). Larger, more complex proteins, such as BSA, undergo significant structural transitions, with changes in the pH further affecting binding affinity and the structure of the protein layer (Li et al., 2008; Tsai et al., 2011). Electrostatic contributions are generally intuitive, with opposing charges causing attraction between the protein and nanoparticle, however, similar net charges are not enough to completely abolish binding (Wang et al., 2016). More detailed studies of the binding surfaces of ubiquitin and GB3 have identified critical lysine residues involved in particle binding (Ceccon et al., 2016; Wang et al., 2016; Zanzoni et al., 2016). This exemplifies how both global parameters, such as net charge, and protein specific features, such as individual residues or conformational transitions, can have significant effects on protein binding.

Several techniques have been used to extract thermodynamic, stoichiometric and structural information. Scattering techniques, such as dynamic light scattering (DLS) and small angle neutron scattering (SANS), have been used to probe the structures of protein layers (Jans et al., 2009; Kumar et al., 2011; Li et al., 2008; Tsai et al., 2011). Stoichiometric information has been acquired using; nuclear magnetic resonance (NMR), agarose gel electrophoresis, isothermal titration calorimetry (ITC) and fluorescence spectroscopy (Goy-López et al., 2012; Ma et al., 2015; Wang et al., 2014; Wangoo et al., 2008). In addition to stoichiometry, thermodynamic information can be obtained from NMR, ITC and fluorescence spectroscopy. Most of these techniques have their limitations, whether that is during data collection, for example the inner filter effect complicating fluorescence spectroscopy (Ameer et al., 2012), or the modelling required for data analysis. As discussed above, binding events are often complex, with several interacting components. Many groups have previously used overly simplistic thermodynamic models to describe their systems, leading to wide variation in the results from different studies (Latour, 2015). More complex models have been developed but their usage is not always trivial and must be optimised for each protein-nanoparticle system (Rabe et al., 2011).

A general three-stage binding model has been proposed by Wang et al (Wang et al., 2014) where initial association is dynamic and reversible, driven by electrostatic interactions (Wang et al., 2016). The bound proteins are then able to reorganise on the particle surface maximising the space available for further protein binding. Finally, “hardening” of the protein layer occurs with proteins becoming irreversibly bound, a process that is accelerated by available cysteine residues that can form stable sulphur-gold bonds. The proposed model assumes that there are no significant structural changes to the protein on binding to the nanoparticle surface.

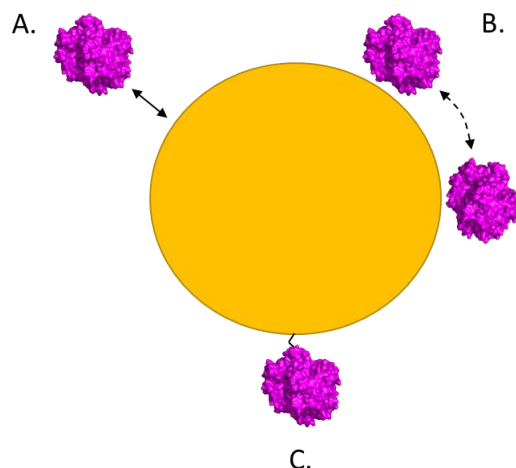


Figure 1.3 Three stage binding model of proteins on gold nanoparticles. A. Dynamic, reversible binding to the surface. B. Protein reorganisation. C. “Hardening” of the protein layer, which is accelerated by the formation of gold-thiol bonds. Adapted from (Wang et al., 2014).

1.2 Protein Scaffolds

The generation of protein-nanoparticle conjugates that maintain the biological function of the attached proteins can be challenging, especially if structural changes occur during binding. The functional domains of other proteins may not be stable when isolated or produced recombinantly. It is possible to overcome these problems using protein engineering methods, for example, improving protein stability through rational design or inserting functional motifs into more stable protein scaffolds (Nuttall and Walsh, 2008; Yang et al., 2015). The advances in DNA technology developed in the 1970s, allowing gene modification, led to a revolution in protein engineering (Leatherbarrow and Fersht, 1986). Site directed mutagenesis (Carter, 1986) is now a routine technique used in biochemistry laboratories around the world. More recent developments in synthesis techniques have significantly reduced the cost of whole gene synthesis, making more complex engineered constructs possible (Hughes et al., 2011). Due to the complexities of *de novo* protein design (Huang et al., 2016) most protein engineering requires the use of a protein scaffold which is modified to bestow novel properties or change its functional activity. Desirable features of a scaffold include, high stability, easy expression and, of course, regions that are insensitive to sequence variation.

Affinity binding molecules are an area that has seen particular development in this regard with a wide number of different scaffolds available. These can be based on antibody fragments, bacterial protein domains and also human protein domains (Johnson et al., 2012; Löfblom et al., 2011; Nuttall and Walsh, 2008). Most of the

development in this area has been on loop display scaffolds where the variable region is a surface exposed loop (Nuttall and Walsh, 2008). Large libraries of loop variations can be made and then screened for activity against the target using phage display technologies (Li et al., 2015).

Protein scaffolds have also been explored for regenerative medicine and tissue engineering applications with bacterial and silk protein polymers adapted to encourage cell growth (Roque et al., 2014; Schacht et al., 2016). The design of tissue scaffolds is more involved, with the mechanical properties of the material important for supporting cell growth. Materials implanted in the host must also be biodegradable which adds further design considerations that need to be met (Mano et al., 2007).

Bacterial outer membrane proteins, β -barrel proteins in particular, have been subject to intense research as protein scaffolds. Two main engineering approaches have been pursued, modifying the central pore of the barrel structure for use in sensing technologies (Ayub and Bayley, 2016) and modifying the extracellular region of the protein for use as peptide and protein display scaffolds (Fleetwood et al., 2014; Rice et al., 2006). The self-assembling nature of beta barrel proteins has also been exploited for their use as surface display platforms. The addition of a cysteine residue into a basement loop of the barrel drives assembly on to gold surfaces, leading to oriented protein arrays that can display peptide motifs or functional domains that have been engineered into the outer loops (Brun et al., 2008, 2015; Cisneros et al., 2006; Shah et al., 2007). This could be a promising approach for displaying functional domains or motifs on the surface of gold nanoparticles.

1.3 Bacterial Outer Membrane Proteins (OMPs)

The cell envelope of Gram-negative bacteria is comprised of an inner and outer membrane that sandwich a crosslinked peptidoglycan layer. The inner membrane is a classical phospholipid bilayer, whereas the outer membrane consists of a uniquely asymmetric bilayer with a lipopolysaccharide (LPS) outer leaflet and phospholipid inner leaflet. The profound asymmetry of the bilayer and cation crosslinking of the outer LPS leaflet forms an extremely tight and impermeable barrier (Clifton et al., 2015). Selective uptake of nutrients into the cell is facilitated by the large number of integral membrane proteins present in the outer membrane (Nikaido, 2003). Unlike the inner membrane where proteins consist of hydrophobic alpha-helices, outer membrane proteins are

usually β -barrels, with arrays of antiparallel beta sheets that form a barrel like structure. The hydrophobic core region of the barrel sits in the membrane while the hydrophilic ends extend into the periplasmic and extracellular spaces. The β -barrel proteins of the outer membrane carry out a wide array of biological functions, with a correspondingly wide structural variety (Figure 1.4). Examples of these proteins and their functions include: non-specific porins, OmpF and OmpC, selective transporters, LamB and FhuA, bacterial adhesion factors, OmpX and Ail, and membrane bound proteases, OmpT (Fairman et al., 2011).

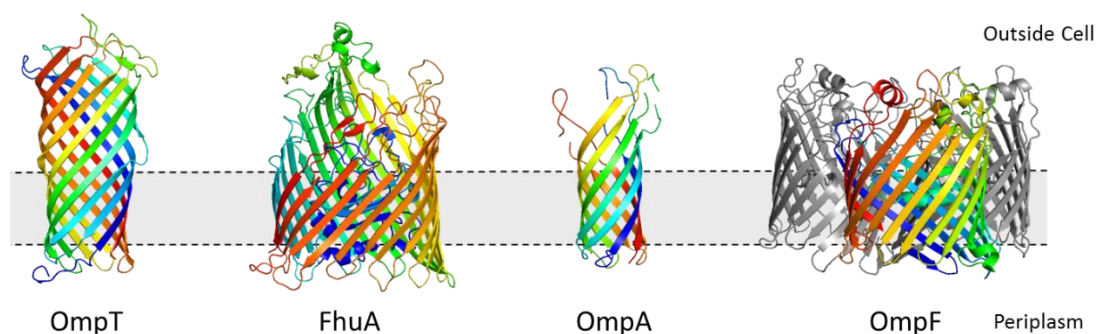


Figure 1.4 β -barrel outer membrane protein structures representative of the structural variety, both in size and oligomeric state. From the left the 10-stranded OmpT (PDB ID:1I78), 22-stranded FhuA which contains an N-terminal plug domain in the barrel lumen (PDB ID:1BY3), 8-stranded transmembrane domain of OmpA without its associated periplasmic C-terminal domain (PDB ID:1BXW) and trimeric 16-stranded OmpF (PDB ID:2J1N). The hydrophobic core of the outer membrane is represented by the shaded region.

The biogenesis of outer membrane proteins is still a relatively poorly understood process. After synthesis in the cytoplasm an N-terminal signal sequence targets the unfolded polypeptide chain to the SecYEG translocon, facilitating transport across the inner membrane into the periplasm (Tamm et al., 2004; Tsirigotaki et al., 2017). Once in the periplasm the signal sequence is cleaved by the signal peptidase and the unfolded protein is bound by the chaperones, Skp and SurA, which are required for transport across the periplasm and stabilise the unfolded intermediate, preventing aggregation (Lyu and Zhao, 2015; McMorran et al., 2014). Folding and insertion of the mature protein is then carried out by the beta-barrel assembly machinery, known as the BAM complex (Figure 1.5).

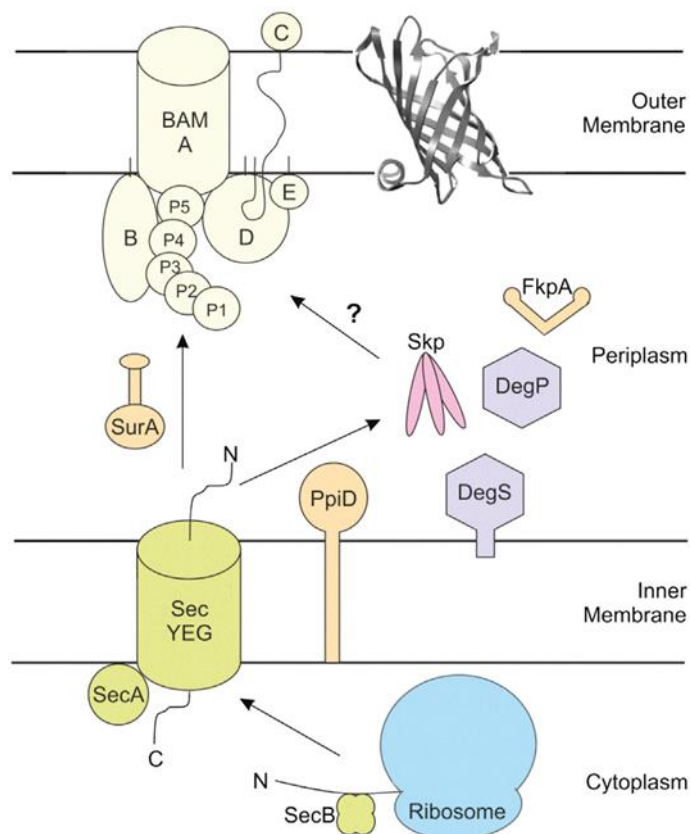


Figure 1.5 Schematic of outer membrane protein biogenesis. The nascent polypeptide chain is synthesised by a cytoplasmic ribosome and targeted to the SecYEG translocon machinery via an N-terminal signal sequence. After translocation into the periplasm the unfolded protein is transported to the outer membrane by the chaperones, SurA and Skp, and inserted by the BAM complex. Reproduced with permission from (McMorran et al., 2014).

Recently, the mechanisms of periplasmic transport, folding and insertion into the outer membrane have been the subject of intense research. The complex interplay between the periplasmic chaperones and their respective pathways are not well understood, with some evidence that they act as a dynamic reservoir to shuttle the unfolded protein to the outer membrane (Costello et al., 2016). Biophysical studies of the trimeric Skp chaperone have shown that the unfolded OMP is held inside a hydrophobic cage, with the size of the cavity dependent on the bound protein. If expansion of the cavity is not enough to encapsulate the protein, a second Skp trimer can be recruited (Schiffrin et al., 2016). Further biophysical experiments using single-molecule force spectroscopy have shown that SurA and Skp stabilise unfolded OMPs and help direct folding of the polypeptide chain into a lipid bilayer (Thoma et al., 2015).

In vitro, β -barrel proteins can spontaneously fold into detergent micelles and lipid bilayers, however, in the cell the BAM complex is necessary for efficient folding into the outer membrane. The complex comprises of five units, the main unit, BamA, is an outer membrane β -barrel with five polypeptide transport associated (POTRA) domains that interact with the four lipoprotein subunits BamB, C, D and E. The structure of the full complex has only recently been reported, and shows the lipoproteins forming a ring beneath BamA in a “top hat” arrangement (Gu et al., 2016; Han et al., 2016) (Figure 1.6).

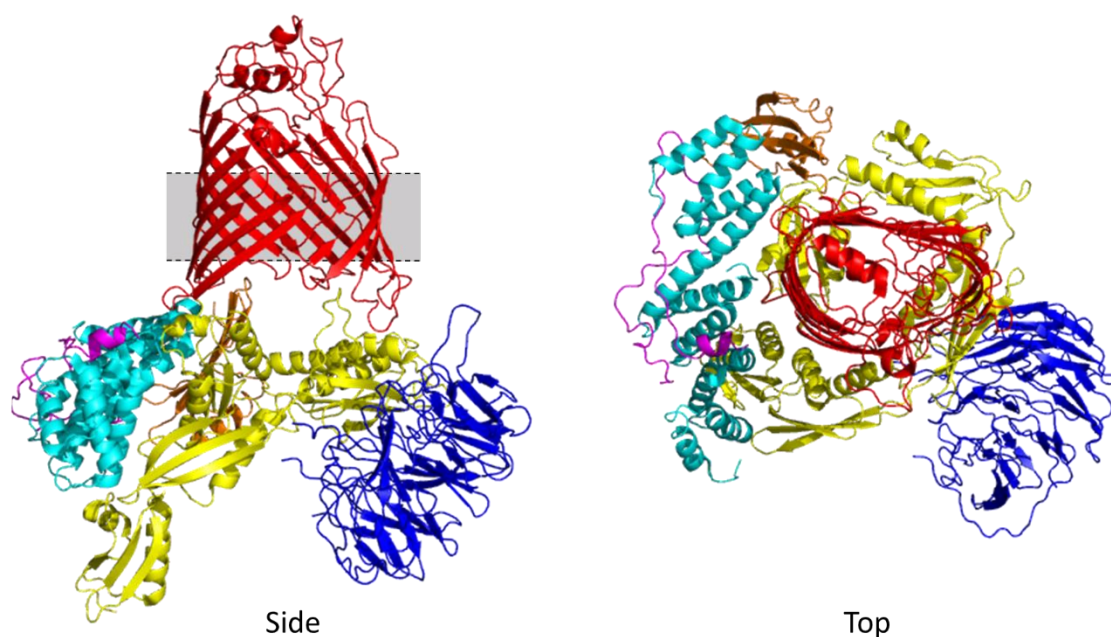


Figure 1.6 Structure of the BAM complex, showing the “top hat” arrangement of the BamA barrel and its four lipoprotein units. The transmembrane β -barrel of BamA is highlighted to separate it from the five periplasmic POTRA domains and the four lipoproteins BamB, BamC, BamD and BamE. The membrane core is indicated by the shaded region. PDB ID: 5D00

Structural and biochemical studies are beginning to elucidate the mechanism of protein insertion through the BAM complex, which appears to be driven by a rotation of the lipoprotein complex, possibly initiated by substrate binding (Gu et al., 2016). The changes in the lipoprotein complex are associated with conformation switching of the BamA barrel, from an inward open (lateral closed) state, to a lateral open state. In the lateral closed state the barrel is open to the periplasm and presumably able to accept the substrate OMP. Switching to the lateral open states separates the $\beta 1$ and $\beta 16$ strands as a result of barrel distortion (Gu et al., 2016; Iadanza et al., 2016) (Figure 1.7). Lateral

gating of the BamA barrel is required for its function, suggesting that the new OMP is inserted into the membrane through this opening while mediating β -strand formation (Iadanza et al., 2016; Noinaj et al., 2014).

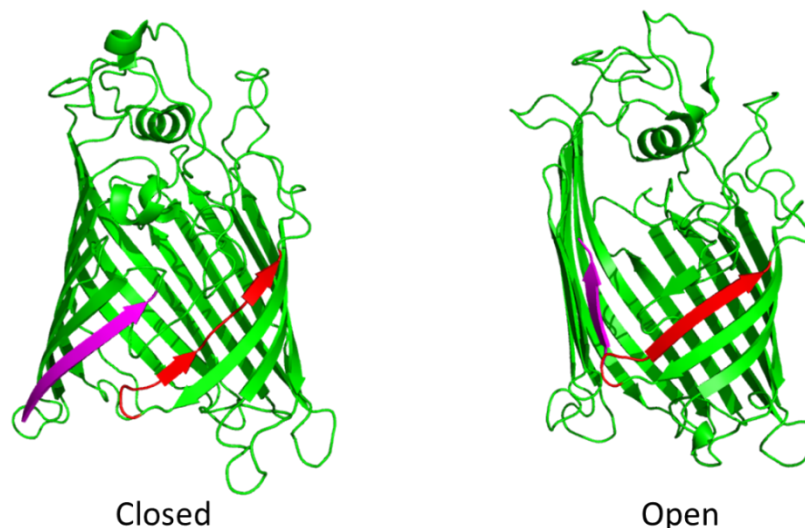


Figure 1.7 The conformational changes of the BamA barrel implicated in OMP folding and insertion. The $\beta 1$ and $\beta 16$ strands are highlighted and can be seen to pull apart in the open state as a result of barrel distortion. (PDB IDs: 5D0O and 5EKQ)

1.3.1 Outer Membrane Protein A

Outer membrane protein A is a 325 amino acid integral membrane protein from the Gram-negative bacterium *E. coli*. The protein comprises of two separate domains, the 171 amino acid N-terminal domain forms an 8-stranded transmembrane beta-barrel (Pautsch and Schulz, 2000) while the remaining 154 residues form a C-terminal periplasmic domain connected by a flexible linker region, thought to play a role in peptidoglycan binding (Figure 1.8) (Ishida et al., 2014). Although structures of both domains are now available crystallisation of the full length protein remains elusive.

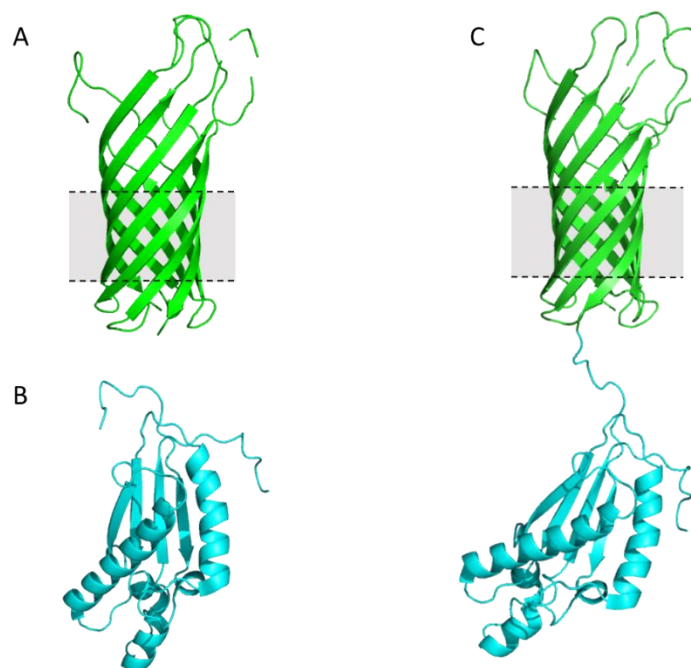


Figure 1.8 A. Crystal structure of the OmpA N-terminal domain beta-barrel (PDB ID:1BXW) B. Solution NMR structure of OmpA C-terminal domain (PDB ID:2MQE) C. Possible full length structure created by docking the two structures in PyMol. The membrane core is indicated by the shaded region.

There is still a level of controversy surrounding the *in vivo* structure and function of full length OmpA. Early vesicle reconstitution experiments showed that OmpA exists in closed and open channel forms when subjected to a sucrose gradient (Sugawara and Nikaido, 1994). Further evidence for two OmpA forms was provided by single channel measurements with large and small conductance states observed (Arora et al., 2000). This was in contradiction to the available crystal structures of the transmembrane domain, which did not show a continuous pore. Subsequently, the existence of the small channel conductance was rationalised by transient hydrogen bond switching using molecular dynamics simulations (Bond et al., 2002) and later proven through mutagenesis experiments (Hong et al., 2006). Formation of the large pore conformation was only observed with the full length protein which led to a structural model being proposed where a 16-stranded transmembrane barrel forms by insertion of the C-terminal domain into the transmembrane domain (A Figure 1.9) (Nikaido, 2003; Stathopoulos, 1996; Zakharian and Reusch, 2005). However, this model was not supported by secondary structure measurements by CD spectroscopy (Danoff and Fleming, 2011; Sugawara et al., 1996).

More recent work has shown that the C-terminal domain does indeed bind the peptidoglycan layer (Ishida et al., 2014) and both *in vitro* and *in vivo* crosslinking studies have identified a C-terminal dimer interface that occurs between the isolated domain and full length protein (Ishida et al., 2014; Marcoux et al., 2014; Zheng et al., 2011). Low resolution structural models of full length OmpA dimers have been generated from ion mobility-mass spectroscopy (IM-MS) (Marcoux et al., 2014) and small angle x-ray scattering (SAXS) (Døvling Kaspersen et al., 2014) which proposed that dimerisation is initiated through the C-terminal domain, bringing the two N-terminal β -barrels together. Physical separation of the N and C-terminal domains was also confirmed by NMR experiments of proteins reconstituted in a membrane mimetic environment (Ishida et al., 2014).

If one considers that the most likely role of the C-terminal domain is to facilitate binding to the peptidoglycan layer and also that it has the ability to dimerise with a second OmpA monomer, then the possibility of the large pore conformer being the result of C-terminal domain insertion into the membrane becomes much less likely. Protein insertion into the outer membrane is generally blocked by a kinetic barrier, which is lowered by the BAM complex to allow outer membrane protein folding. This barrier coupled with the peptidoglycan and dimer interactions of C-terminal domain would lead to an energetically unfavourable transition.

A second model for the large pore formation was proposed by Zheng *et al* (Zheng et al., 2011) where the C-terminal domain initiates dimersation of OmpA, bringing the N-terminal domains together to form a 16-stranded β -barrel (B Figure 1.9). Although there is no structural data showing a 16-stranded barrel in full length OmpA there is some evidence to support this model. Nikaido (Nikaido, 2003) reported that the open channel conformers are observed in an oligomeric form and *in vitro* studies have shown that the transmembrane domain forms folded and unfolded oligomeric species, suggesting that OmpA_{TM} is able to form higher order structures through domain swapping (H. Wang et al., 2013).

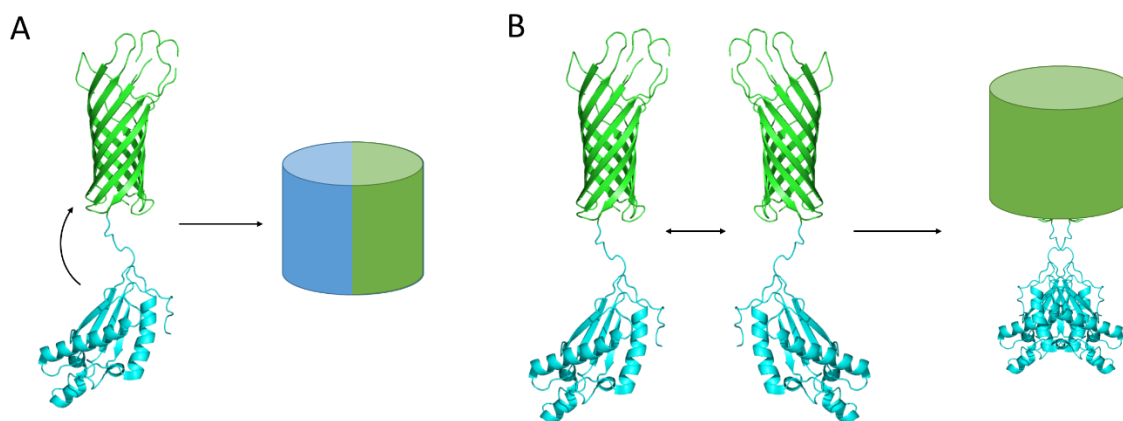


Figure 1.9 Possible models for OmpA large pore formation. (A) The C-terminal model, where the C-terminal domain inserts itself into the N-terminal domain to form a 16 stranded β -barrel. (B) The N-terminal model, where OmpA dimerises through the C-terminal domain, followed by the two N-terminal domains forming a 16 stranded β -barrel through domain swapping.

Transmembrane Domain

As discussed above the OmpA transmembrane domain is an 8 stranded β -barrel that, in its small pore form, is a non-specific porin allowing slow diffusion of small solutes through the membrane (Sugawara and Nikaido, 1992). β -barrel proteins are highly thermostable, with OmpA_{TM} in particular having an unfolding temperature greater than 80°C (Burgess et al., 2008; Smith et al., 2007). AFM unfolding studies of the OmpA homologue from *Klebsiella pneumoniae* revealed the particularly high mechanical strength of 8-stranded beta-barrels when compared to larger porins, possibly linked to their role as a membrane anchors (Bosshart et al., 2012). As well as high thermal and mechanical stability, OmpA_{TM} shows remarkable sequence flexibility with circular permutations and even multiple concatenated TM-domains shown to fold correctly into detergent micelles (Andersen et al., 2016; Koebnik, 1996).

Beta-Barrel Assembly on Gold Surfaces

The addition of a single cysteine residue into a short turn of a β -barrel was first shown to enable self-assembly on a gold surface with the 16-stranded homotrimeric protein OmpF. After assembly, a stabilising thiolipid layer was deposited on the surface to mimic the outer membrane environment. Retention of the beta structure was confirmed by Fourier transform infrared spectroscopy and binding functionality was shown by surface plasmon resonance and impedance spectroscopy (Terrettaz et al., 2002). Further work with atomic force microscopy was able to visualise the characteristic

homotrimeric structure of OmpF on flat gold surfaces in high resolution (Cisneros et al., 2006).

This approach was then successfully applied to OmpATM assembly on gold surfaces (Shah et al., 2007). The high stability, monomeric nature and sequence flexibility of OmpATM make it an excellent candidate for use as a protein scaffold. Previous studies have already explored inserting peptide motifs into the extracellular loops and more extensive changes such as the addition of multiple concatenated domains (Brun et al., 2015; Shah et al., 2007). The structure of surface assembled OmpATM proteins, engineered with tandem antibody binding domains from protein A has been shown using neutron reflectometry (Brun et al., 2008; Le Brun et al., 2011). The proteins form oriented arrays embedded in a thioAlkylPEG monolayer, with the functional domains displayed away from the surface where they are free to bind antibodies that are in solution (Figure 1.10). The thioAlkylPEG molecule helps stabilise the protein monolayer, with its length of approximately 30 Å matching the height of the hydrophobic core of OmpA. This type of system has been proposed as a platform for label free biosensing of antigens such as viral nucleoproteins (Brun et al., 2015).

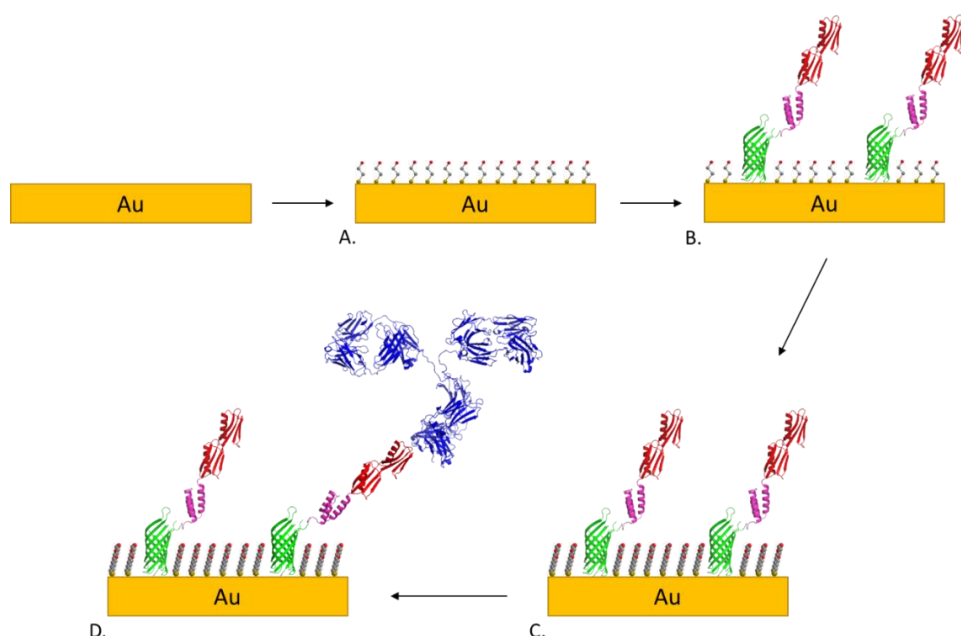


Figure 1.10 Schematic diagram of an engineered OmpATM array self-assembling on a planar gold surface. (A) The gold surface is passivated with β -mercaptoethanol (not to scale). (B) OmpATM engineered with tandem antibody binding domains and a linker domain is deposited on the surface. (C) The surface is backfilled with a stabilising thioAlkylPEG monolayer. (D) The antibody binding domains are free to bind IgG. Adapted from (Brun et al., 2015).

1.4 Nanoscale Gold Surface Structures

The control of materials on the micro and nano scale has become a defining feature of the silicon age; semiconductor devices for computer systems are now routinely fabricated with nanometer precision (Thompson and Parthasarathy, 2006). There are two opposing approaches to the generation of nanoscale features or patterns. The first, known as the top down or directed approach, uses templates to selectively pattern a substrate either by protecting certain areas or guiding the formation of new material (A Figure 1.11). This is the basis of the common lithographic techniques that are used in semiconductor production among other applications. The second approach, termed bottom up, takes small molecular building blocks and creates nanoscale structures via self-assembly (B Figure 1.11). This is also known as the biological approach (Seeman and Belcher, 2002).

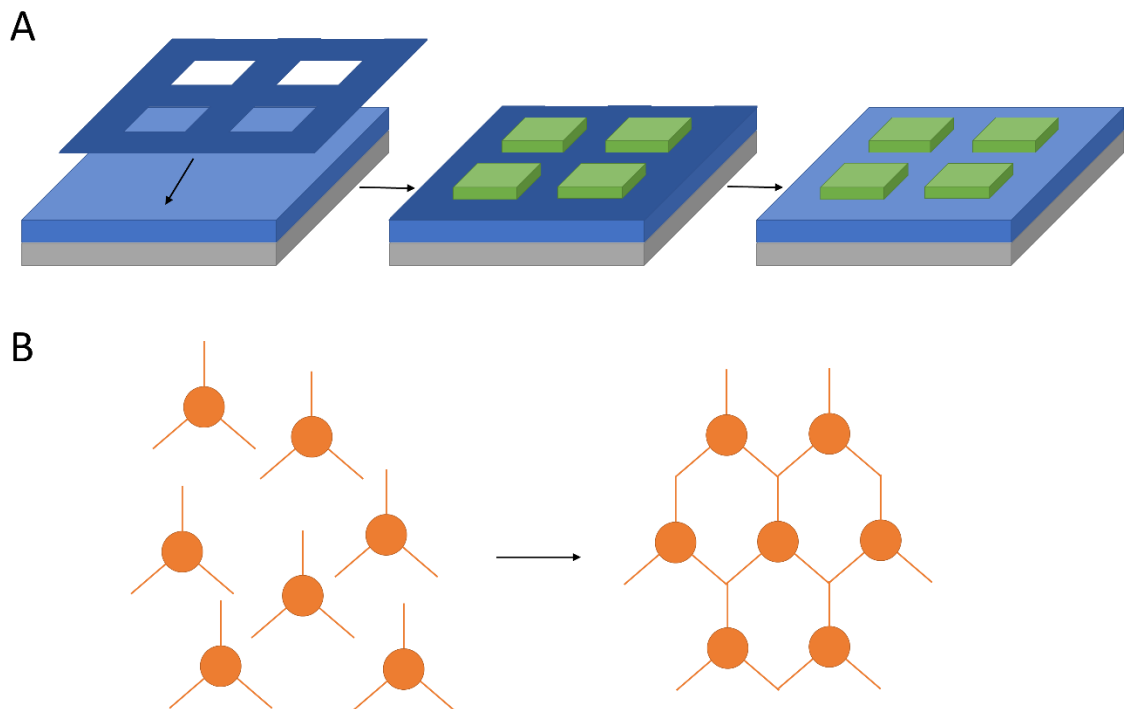


Figure 1.11 Schematic representations of top down (A) and bottom up (B) fabrication techniques. (A) A mask is placed on the substrate, which selectively protects areas from the growth of new material or removal of a layer of the substrate. The mask is then removed to reveal the constructed pattern. (B) Small building blocks are added together that can self-assemble through inter-block interactions to generate a patterned material.

Top Down

A variety of lithographic techniques have been used to generate nanoscale gold patterns on surfaces. Many of these studies have been motivated by the unusual behaviour of

light interacting with periodic metallic structures in the nanoscale regime (Gao et al., 2006). One of the most widely used patterns are nanohole arrays which can be made using a variety of techniques including electron beam lithography (Sharpe et al., 2008; Yu and Golden, 2007) and nanoimprint lithography (Chen et al., 2009; Martinez-Perdiguero et al., 2013). Nanoimprint lithography utilises a mould that has nanostructures patterned on the surface, a polymer based resist is then imprinted with the desired pattern by pressing with the mould while heating (Chou et al., 1996). A gold layer can then be added by evaporation techniques (Martinez-Perdiguero et al., 2012) or alternatively is revealed by etching (Chen et al., 2009). The main advantage of using the nanoimprint approach is the ability to scale up for mass manufacture, which is not possible using electron beam lithography. Gold nanohole arrays have been reported as possible sensor devices using either surface enhanced raman spectroscopy (SERS) (Armas et al., 2016; Yu and Golden, 2007) or surface plasmon resonance (SPR) to detect changes at the gold surface (Chen et al., 2009; Kwak et al., 2005; Martinez-Perdiguero et al., 2013; Sharpe et al., 2008).

Bottom Up

The generation of nanostructured gold nanoparticle arrays via bottom up methodologies can be approached in two ways; self-assembly of a template with defined binding sites or by direct self-assembly of gold nanoparticles on to a surface. Synthetic polymers, DNA and proteins can all be used to mediate self-assembly of gold nanoparticle into nanostructures (Ofir et al., 2008). Diblock copolymer films that phase separate into discrete microarchitectures have been used to direct gold nanoparticle assembly. Selective binding to one half of the diblock polymer generates patterned gold nanoparticle substrates (Shenhar et al., 2005; Zehner et al., 1998). Biological molecules such as DNA and proteins offer an almost infinite number of complex assembly architectures, from the helical structures provided by DNA origami (Liu et al., 2014) to self-assembled cage structures made from viral proteins (Liljeström et al., 2014). DNA templates can be utilised in two ways; nanoparticles labelled with a single piece of ssDNA can be assembled together by Watson-Crick base pairing to form networks (Tan et al., 2011) or alternatively cationically functionalised nanoparticles can be assembled on anionic DNA molecules through charge-charge interactions (Ganguli et al., 2004). Protein templates can be used in a similar fashion; protein surfaces arranged as 2D crystals with engineered binding sites have been used to direct nanoparticle assembly

(McMillan et al., 2002) and a novel protein helix has been used to create intricate gold nanoparticle patterns (Chen et al., 2008).

Direct surface assembly of gold nanoparticles is by far the easiest method of generating arrays. Nanoparticles are kept in solution by repulsive surface charges, therefore, these forces must be overcome to initiate binding to the surface. This can be done by applying an external force, such as in electrophoresis or solvent evaporation, modification of the particle surface with ligands such as alkanes or modification of the substrate surface with a linker molecule which is usually amine terminated. Electrophoresis has been used to deposit gold nanoparticle thin films on to transparent indium tin oxide electrodes, the films were poorly ordered but retained their optical properties (Bailey et al., 2000; Chandrasekharan and Kamat, 2001; Zhu et al., 2012). Sub-monolayer coverages of gold nanoparticles can be more easily attained by simply depositing negatively charged nanoparticles from solution on to a surface functionalised with an amine-terminated organosilane monolayer. Charge interactions facilitate binding to the surface while repulsion between particles prohibits the formation of close packed arrays, with the bound nanoparticles retaining their unique SPR and SERS properties. This method has been used on glass to generate inexpensive substrates for possible bio-sensor applications (Grabar et al., 1995, 1996a, 1997; Kaminska et al., 2008; Kumari and Moirangthem, 2016; Nath and Chilkoti, 2004; Seitz et al., 2003). To form more highly ordered 2D arrays of gold nanoparticles alkanethiol molecules can be assembled on the nanoparticle surface where the favourable interactions between the alkyl chains allow close packing arrangements of the particles (Kim et al., 2001; Ochiai et al., 2014). Further to alkanethiol modification, 2D arrays can be encouraged to form by solvent evaporation on the surface where the receding droplet forces a close packed arrangement on the surface. Variations of this technique have been applied with particles already bound to a surface (Liu et al., 2002) and with particles self-assembled at the air water interface (Santhanam et al., 2003).

1.5 Silane Monolayers

Organosilane molecules (Figure 1.12) have been used for modifying surfaces since the mid-twentieth century and have a wide range of industrial uses in composite production, paint adhesion, polymer reinforcement and water repellent coatings (Materne et al., n.d.).

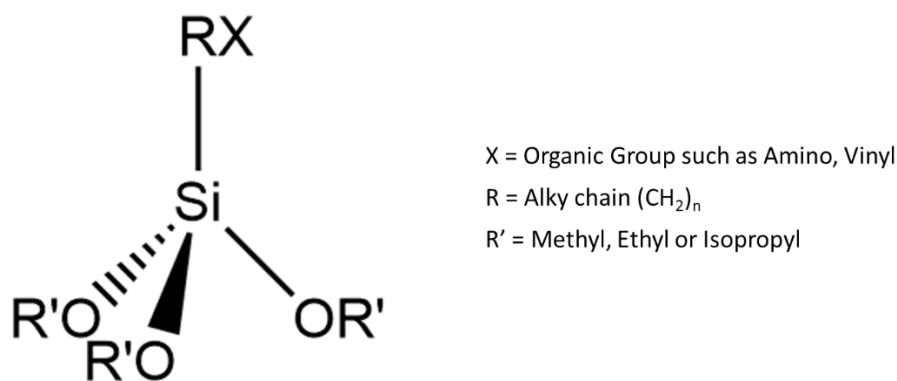


Figure 1.12 General organosilane molecule composition

It is the ability of these molecules to form a bridge between inorganic substrates and organic compounds such as polymers that makes them so useful. Self-assembled monolayers form on hydroxylated surfaces after hydrolysis of the three alkoxy groups at the base of the molecule. The binding mechanisms and structures of organosilane films have been topics of intense study by both academic and industrial researchers. One group of organosilane molecules, those that are terminated in amino groups, have been widely studied and are of particular interest to this study as they are used for biomolecule and gold nanoparticle attachment (Grabar et al., 1995; Jang and Liu, 2009; Thakurta and Subramanian, 2012). The most commonly used aminosilanes, aminopropyltriethoxysilane (APTES) and its methoxy derivative aminopropyltrimethoxy-silane (APS), are the most rigorously studied. Both molecules display very similar chemistries and are used to generate self-assembled monolayers on surfaces (Argekar et al., 2013; Cui et al., 2011).

The morphology of APTES films is highly dependent on the deposition conditions that are used. A great deal of work has been carried out to understand the effects of the solvent system, reaction temperatures and incubation times on the structure of APTES films. As mentioned, water is necessary to initiate hydrolysis of the alkoxy groups for binding to the SiO₂ surface, however an aqueous solvent is not always needed, with the surface water on the substrate enough to mediate the reaction (Engelhardt and Orth, 1987). Many protocols use anhydrous solvents to try and prevent multilayer formation from reactive intermediates (Argekar et al., 2013; Vandenberg et al., 1991). Multilayer formation does occur in anhydrous solvents when samples are incubated for several hours (Argekar et al., 2013). Deposition at room temperature leads to monolayers that are mostly bound through electrostatic interactions (Chiang et al., 1982). APTES

multilayers are complex arrangements of molecules with multiple orientations that are mainly connected through hydrogen bonding and electrostatic interactions (Argekar et al., 2013)(Figure 1.13). Electrostatically bound layers are not very stable and can be removed by solvent washes (Argekar et al., 2013; Vandenberg et al., 1991). Stable, covalently bound monolayers can be formed by first removing the poorly bound multilayers followed by a high temperature curing step ($\sim 120^{\circ}\text{C}$) (Argekar et al., 2013).

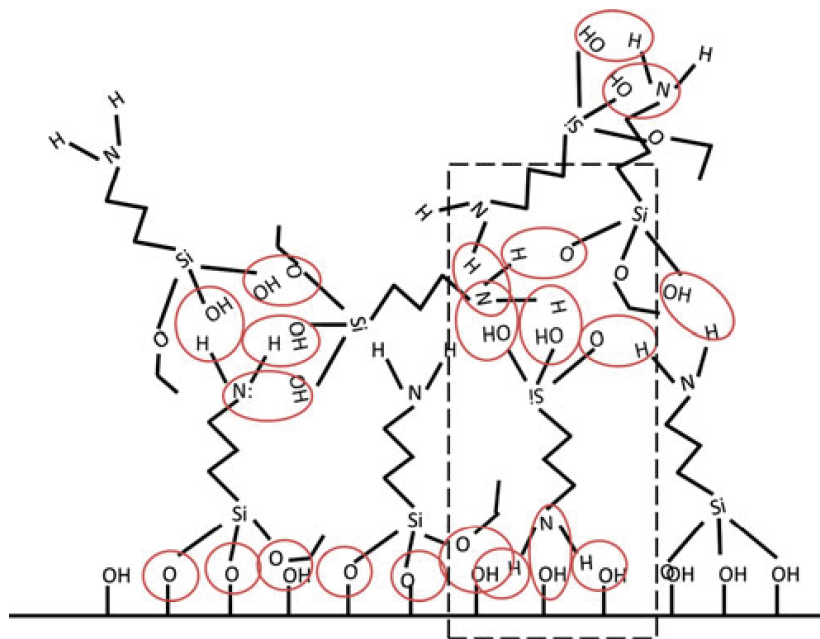


Figure 1.13 Schematic of APTES molecules on a surface. A large number of covalent and hydrogen bonding interactions are possible (highlighted in red), both between molecules and the surface. These interactions lead to multilayer formation. Reprinted with permission from Argekar *et al.* Copyright Materials Research Society

Aryl containing silanes, such as AAPTMS (Table 2.1) used in this study, are much less prevalent in the literature. Arylsilane molecules have been reported as good candidates for UV lithography applications (Brandow et al., 2008; Dressick et al., 1996). The aryl moiety is a photolabile chromophore that absorbs at 193 nm. Irradiation of arylsilane films stimulates cleavage of Si-C or C-N bonds, releasing some or all of the organic portion of the silane molecule (Dressick et al., 1996). Lithographic techniques can be used to generate patterned surfaces with different chemical compositions using self-assembled monolayers of these molecules. The structure of AAPTMS monolayers has not been rigorously investigated, however Chen *et al.* (Chen et al., 2006) have proposed a model for cured AAPTMS monolayers where the structure is reinforced by hydrogen bonding between the terminal amine groups and hydrophobic interactions between the aryl groups, such as π -stacking and van der Waals forces (Figure 1.14). This is

1.6.1 Surface Analysis

X-Ray Photoelectron Spectroscopy (XPS)

X-ray photoelectron spectroscopy is a widely used surface analysis technique that provides information on the elemental composition and electronic environment of a substrate. XPS relies upon the principle of the photoelectric effect, whereby electron emission from a surface is stimulated by X-ray irradiation. Photoelectron emission is not limited to X-ray excitation sources, with electron emission induced by light irradiation providing early proof of photon quantisation (Einstein, 1905).

An XPS spectrometer measures the kinetic energy of the emitted electrons ($E_{kinetic}$) and since the energy of the incident X-ray photons (E_{photon}) is known, the binding energy ($E_{binding}$) of the electron can be calculated simply, by conservation of energy:

$$E_{binding} = E_{photon} - (E_{kinetic} + \phi) \quad [1.1]$$

Where ϕ , the work function, is an adjustable instrumental correction factor relating to the detector efficiency. The binding energy of the electron is related to the element it originates from and the orbital it occupies. Detecting the characteristic energies of the emitted electrons allows the oxidation state, electronic structure and elemental composition of the surface to be deduced. As the electrons need to escape from the surface to reach the detector, only the top atomic layers of the surface are analysed, this makes XPS an excellent technique for probing thin layers of material (Chusuei and Goodman, 2003).

Atomic Force Microscopy (AFM)

AFM generates images by following the movement of a probe as it is scanned across the surface in a raster pattern. The surface topology is determined by observing the deflections of the cantilever. This is usually detected using an optical system where a laser is reflected from the back of the cantilever into a photodetector. Interactions with the surface causes the light path to change, moving the position of the beam around the quadrants of the photodetector. This allows both positional and force information to be recorded (Rugar and Hansma, 2008). AFMs provide excellent height resolution but can suffer from relatively poor lateral resolution due to tip convolution. This is particularly problematic if the width of the surface features of interest are significantly smaller than the tip of the probe.

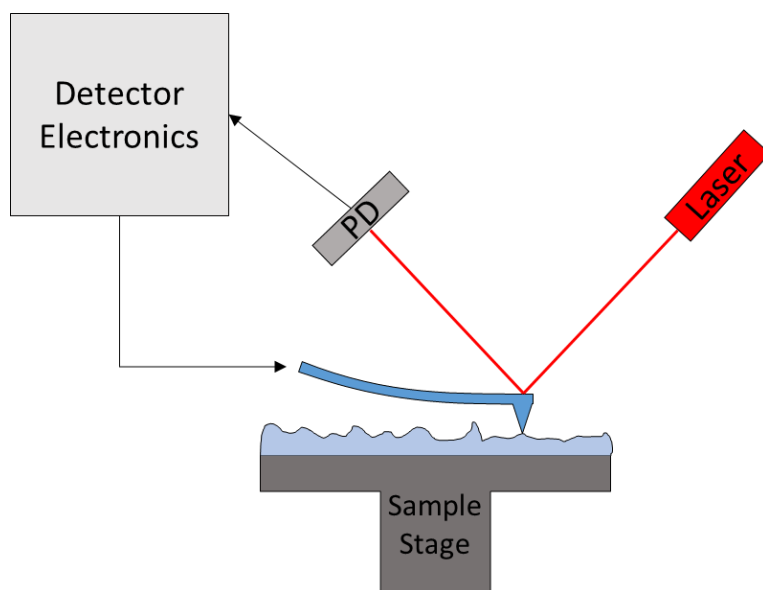


Figure 1.15 Schematic of a typical atomic force microscopy set up. A piezoelectric stage moves the sample with respect to the cantilever and probe tip. Deflection of the probe by features on the sample surface causes the reflected laser beam to move on the photodetector (PD).

AFM is routinely used to image the nanoscale topology of surfaces such as nanoparticle assemblies (Grabar et al., 1996a; Nath and Chilkoti, 2004). The development of the AFM fluid cell (Drake et al., 1989) has facilitated imaging of biomolecule samples in aqueous buffers. Membrane systems have been quite well studied using this technique as it provides images of membrane proteins and other cellular machines in their native environment (Muller, 2008; Schabert et al., 1995). It has also been used to confirm that the membrane protein OmpF maintains its native conformation when tethered to a solid surface (Cisneros et al., 2006). Single molecule force spectroscopy experiments, usually where a surface bound protein is tethered to the AFM tip before applying a pulling force, have attracted great interest for investigating the mechanical properties of proteins (Casuso et al., 2011). This method was first used to look at unfolding of the muscle protein Titin which contains multiple repeats of immunoglobulin type domains (Rief et al., 1997) and has since been used to characterise the physical properties of numerous proteins (Puchner and Gaub, 2009) including α -helical membrane proteins and the 8-stranded beta-barrel protein OmpA from *K. pneumoniae* (Bosshart et al., 2012).

Electron Microscopy

Electron microscopy encompasses several imaging techniques that use beams of electrons to illuminate a sample. The wavelength of accelerated electron beams are up to 100,000 times shorter than light, allowing much greater magnification to be achieved. The two most common electron microscope configurations are transmission and scanning.

In a transmission electron microscope (TEM) the detector is situated below the sample, which is loaded on to thin carbon grids. Images are formed by observing the number of electrons that are transmitted through the sample stage to the detector. This is where the major limitation of TEM presents itself. Samples must be sufficiently thin so that electrons can pass through, which may require difficult sample preparation. However, the resolution of modern TEMs is excellent with High-Resolution TEMs (HRTEM) able to resolve individual atoms (Williams and Carter, 2009).

Nanoparticle characterisation is routinely carried out by TEM; the electron dense core of metal nanoparticles gives good contrast on electron microscopy grids and is used for assessing the quality of synthesised particles (Brust et al., 1994; Pyrz and Buttrey, 2008). Negative staining can be used to visualise molecules containing lighter elements, such as proteins (Roque et al., 2014). The stain consists of a heavy metal salt, commonly uranyl acetate, which is added to the grid after depositing the sample. Areas that contain the protein are visible as they are lighter than the surrounding stain. This method has also been used to visualise protein assemblies on nanoparticle surfaces (Ma et al., 2015).

In contrast to TEM, a scanning electron microscope (SEM) uses a finely focused beam of electrons that are raster scanned across the sample and back scattered electrons or secondary electron emissions are detected to form the image. As it is not required for the electrons to pass through the sample, much larger samples can be analysed and the accelerating voltages are much lower. SEMs are excellent for imaging the nanoscale topology of a material and many have integrated energy dispersive X-ray analysers for combined elemental analysis (Goldstein et al., 2012).

Nanoparticle assemblies on surfaces such as silicon and glass are routinely imaged by SEM (Kumari and Moirangthem, 2016; Ochiai et al., 2014). It is not possible to image the nanoscale topology of biological samples by SEM as a conductive surface is required to combat charging effects from the electron beam. This is usually done by

coating with a thin layer of gold or carbon, which will mask the nanoscale features of a biological sample.

Neutron Reflectometry

Neutron reflectometry is an established technique for analysing the nanoscale structure of surfaces and interfaces (Penfold and Thomas, 1990). Neutrons are subatomic particles with no net electric charge and a slightly higher mass than a proton. According to wave-particle duality a beam of fast moving neutrons will also act as a wave. The wavelength, λ , of the neutron beam can be calculated from its momentum, p , using the de Broglie equation:

$$\lambda = \frac{h}{p} \quad [1.2]$$

Where h is the Planck constant 6.26×10^{-34} Joule seconds

So called “cold neutrons”, such as those produced by neutron sources, exhibit a range of optical phenomena that are analogous to those seen in classical optics (Klein and Werner, 1983). Specular reflection of neutrons from the interfaces of multi-layered materials can be used to gain information about their thickness and composition.

When an incident beam of radiation passes through a multi-layered material, with different refractive indices, the differential reflection and refraction from their interfaces generates a pattern of constructive and destructive interference (Figure 1.16). The corresponding peaks and troughs in the reflectivity profile can be used to calculate the thickness and refractive index of the constituent layers. A common example of this phenomenon is the multi-coloured iridescence observed when light is reflected off thin layers of oil on the surface of water.

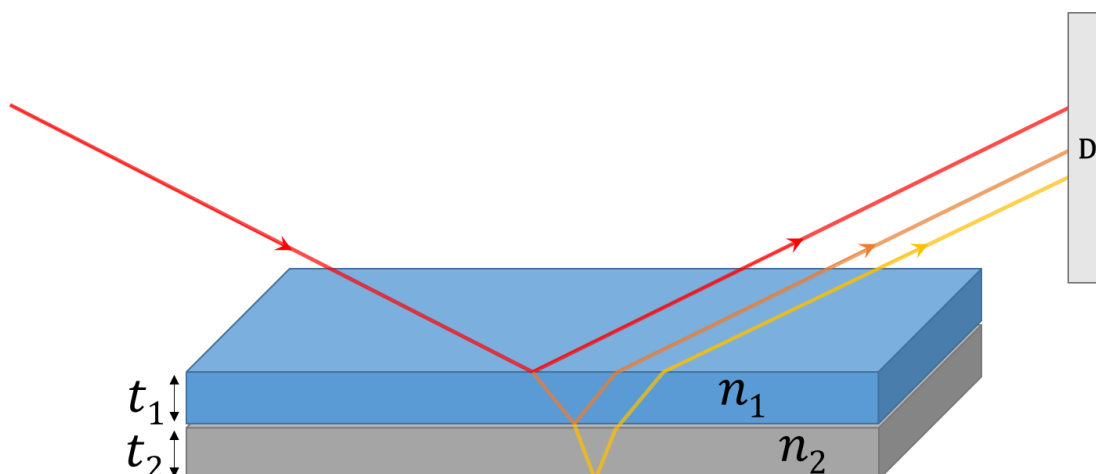


Figure 1.16 Reflection from the surface of a multi-layered material with refractive indices, n_1 and n_2 . When a beam of radiation, light for example, meets the interface of two layers with different refractive indices some of the light will be reflected while the rest is refracted and continues through the next layer until it meets another interface. The change in the distance travelled by the ray, which depends on the layer thickness, t_1 and t_2 , shifts the phase of the waves with respect to one another. The resulting interference pattern at the detector, D, can be used to determine the layer thicknesses.

Neutrons are an extremely powerful probe of nanoscale systems, this is due to their small wavelength ($\sim \text{\AA}$), highly penetrating nature and isotope sensitivity. Unlike X-rays which interact with the electron cloud surrounding an atom, neutrons are nuclear scatters. This property provides the two main advantages of neutron experiments. Scattering values vary quite widely across the periodic table, unlike X-rays that correlate with atomic number, with many metals exhibiting very low scattering. This allows complex experimental equipment to be used *in situ* on the beamline, such as flow cells and pressure chambers, when collecting data. The isotopic sensitivity of neutrons, typified by the difference in hydrogen and deuterium scattering (-3.74×10^{-5} and $6.67 \times 10^{-5} \text{\AA}$ respectively), can be used to highlight or mask components of complicated systems through isotope labelling and contrast matching (Figure 1.17). It is the sensitivity of neutron experiments to hydrogen and deuterium that attracts researchers of biological systems to this technique (Lakey, 2009).

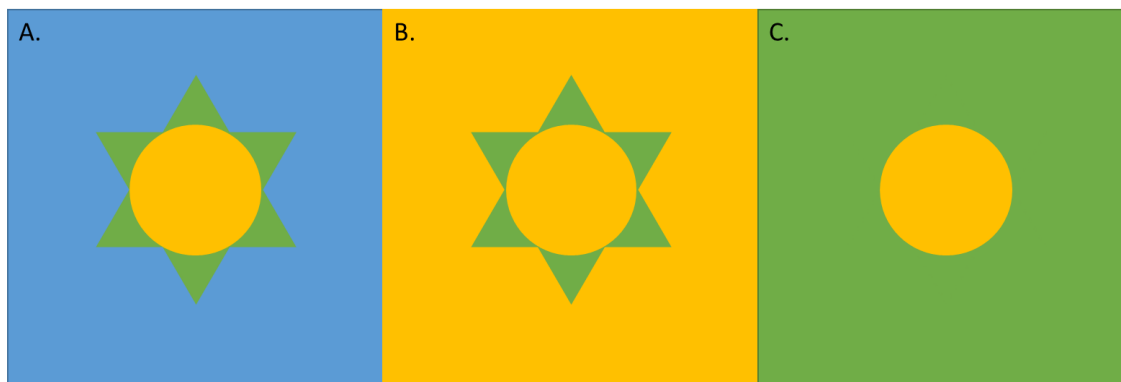


Figure 1.17 Schematic diagram of contrast matching experiments with a two component system. In the first experiment (A) the scattering of both components is observed and cannot be deconvoluted from one another. If two further experiments are carried out, (B) and (C), where the scattering of the media is equal to the **sphere** and **triangles** respectively, then their individual contributions can be calculated and used to model the system as a whole.

There are two types of neutron sources; spallation sources, such as the ISIS neutron and muon source in the UK, and reactor sources, such as the Institut Laue-Langevin (ILL) in France. The ISIS spallation source generates neutrons by directing a packet of protons towards a target made of solid tungsten. The protons are accelerated to 84% the speed of light using a synchrotron before being sent towards the target. Bombardment of the tungsten atoms with the high-energy protons drives neutrons from the nucleus in a process known as spallation. A methane filled moderator cools the neutrons by inelastic scattering so that their wavelength is in the correct range before directing towards the material that is being interrogated. Spallation sources produce a “white” beam of neutrons, which means they have a broad distribution of wavelengths. For meaningful data to be collected the wavelength distribution of each neutron pulse must be measured. ISIS is a time of flight (ToF) source, which means that a clock is started when the target is struck with the proton packet and the time that the neutrons take to reach the detector is recorded for each pulse. From this information, the wavelength of the neutrons can be calculated.

A reactor source generates neutrons through nuclear fission using Uranium 235;



Where n are neutrons and X and Y are fission fragments. Research reactors, in comparison to power reactors, have compact cores that are optimised to produce as many neutrons as possible. Similarly to a spallation source, a moderator, which is

usually the reactor coolant, is used to cool the “fast” neutrons. The slower “thermal” neutrons that are used in neutron experiments, are also needed to maintain the fission chain reaction. The wavelength distribution of the neutrons produced by the reactor can be tuned by changing the moderator used.

When a neutron is scattered by matter it will undergo a change in momentum, termed momentum transfer or Q , which can be calculated from the vectors of the incident, k_i , and reflected beam, k_r , from the following equation (see also Figure 1.18):

$$Q = k_i - k_r \quad [1.4]$$

The value of Q is dependent on the wavelength of the neutrons (λ) and the angle (θ) at which it strikes the interface and can be calculated using the following equation;

$$Q = \frac{4\pi \sin\theta}{\lambda} \quad [1.5]$$

The scattering intensity is strongly affected by the difference in the refractive indices at the boundary of the two components. For neutrons, the refractive index is known as the scattering length density, ρ , and can be calculated from the sum of the scattering contributions of each species in the material:

$$\rho = \sum_j b_j n_j \quad [1.6]$$

Where b is the coherent scattering and n is the number density of the species j .

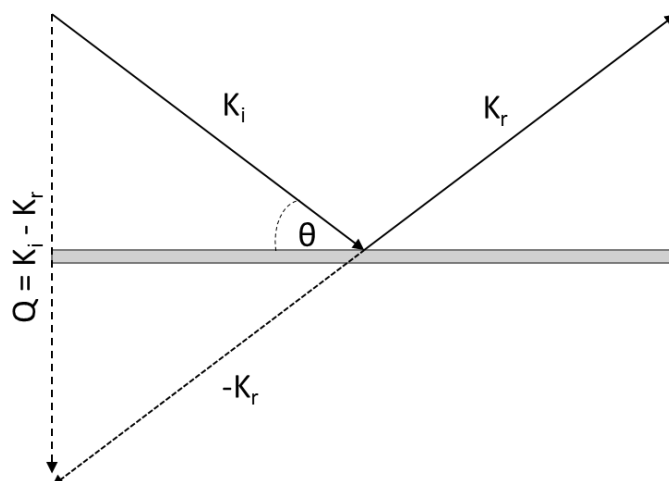


Figure 1.18 Visual representation of the momentum transfer, Q , of a reflected neutron beam. The sum of the incident, K_i , and negative reflected, $-K_r$, wave vectors clearly describes a vector, Q , that is perpendicular to the reflection surface. Information about the material composition at different depths can be obtained by collecting reflection data over a range of Q values.

In a reflectivity experiment the scattering intensity is measured over a range of momentum transfers to give a reflectivity profile depending on the length scale needed. For a pulsed source, such as ISIS, where a white beam of neutrons is used, samples are measured at several angles to achieve the required Q range. When collecting reflectometry data only the amplitudes of the reflections are measured. The lack of phase information results in many possible solutions to the Fourier transform of the data, therefore, for a single data set is not possible to find a unique solution. This is known as the phase problem, and is overcome by taking several measurements using different solvent contrasts. Simultaneously fitting of the multiple contrasts significantly reduces the range of possible solutions (Hughes et al., 2008). A reference layer is also used, which is usually the substrate that the unknown system is assembled on. This is analogous to heavy metal replacement in X-ray crystallography experiments.

Neutron reflectivity experiments have been used to interrogate protein layer structures at solid and liquid interfaces with extremely high depth resolution (\AA). It is the ability of neutron experiments to differentiate between components of complex biological systems through selective masking or highlighting that provides an unmatched level of detail (Lakey, 2009). This has allowed the orientation of assembled protein surfaces to be deduced (Brun et al., 2008, 2015; Holt et al., 2009) and protein binding to membrane systems and protein surfaces to be observed (Clifton et al., 2011; Krueger et al., 2001;

Mazzer et al., 2017). A further advantage of neutron beams, for biological samples in particular, is their non-destructive nature which allows long data acquisition times, unlike X-rays which cause significant sample damage.

1.6.2 Solution Analysis

Surface Plasmon Resonance (SPR)

Surface plasmon resonance has become a standard technique for measuring the kinetics and affinities of biomolecular interactions, particularly in receptor-ligand binding studies. SPR is analogous to the LSPR of nanoparticles and is observed when light interacts with the conduction band electrons of very thin gold films (usually ~50 nm), i.e. below the wavelength of light. There are several commercial instruments available with varying detection methods (“SPR Instruments,” n.d.; Wijaya et al., 2011). The most common is the BIAcore system which uses the Kretschmann configuration (Jönsson et al., 1991). Briefly this consists of a gold-coated glass sensor chip that interfaces with a prism on the glass side and with a microfluidics system on the gold side (Figure 1.19). A protein or ligand is immobilised on the gold surface and possible binding partners injected over chip via the microfluidics system. Detection is carried out by exploiting the angular dependence of the surface plasmon resonance condition (Willets and Duyne, 2007). Light absorption at the metal surface depends on the SPR frequency and the incident angle. Biomolecule binding at the gold surface causes a shift in the SPR frequency, which is detected by a corresponding shift in the angle at which light is absorbed.

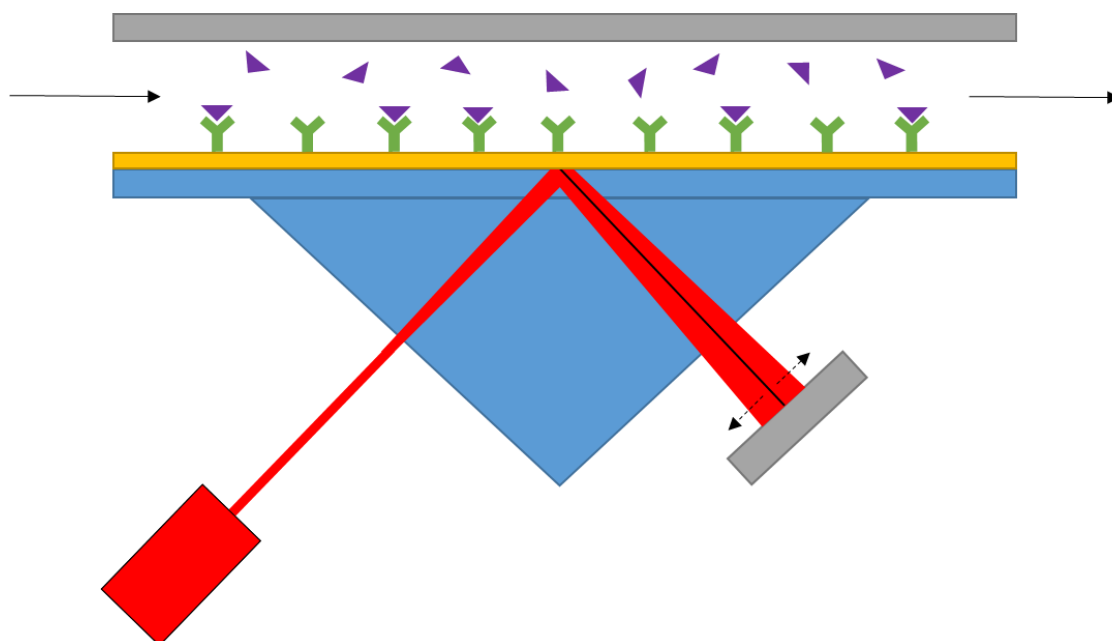


Figure 1.19 Kretschmann configuration SPR sensor such as those used in BIAcore instruments. Monochromatic laser light is reflected from the interface of the gold-glass layer, first passing through a prism to introduce multiple angles of incidence. Changes in the refractive index at the gold surface causes a shift in the surface plasmon resonance angle, which is observed as a dark region at the detector.

Changes in the LSPR of gold nanoparticles can also be used for the detection of biomolecule binding (Anker et al., 2008). As discussed above changes in the dielectric constant on the surface of gold nanoparticles can be detected by a corresponding change in the LSPR peak. The change in the LSPR wavelength can be calculated as a function of the change in the refractive index using the following equation;

$$\Delta\lambda_{max} = m\Delta n \left[1 - \exp\left(-2d/l_d\right) \right] \quad [1.7]$$

Where m is the refractive index response of the particles, Δn is the change in the refractive index due to the bound species, d is the layer thickness and l_d is the characteristic EM-field-decay length (Whitney et al., 2005; Willets and Duyne, 2007).

When investigating binding of biological molecules on the surface of an AuNP the change in the refractive index, Δn , is dependent on two factors, the inherent refractive index of the molecule and its density on the surface. Therefore, when comparing proteins of similar size and refractive indices, the relative densities of the protein layers at the nanoparticle interface can be estimated from the change in the LSPR wavelength. This is observed by UV-Vis spectroscopy as both a peak shift in the extinction spectrum

and an increase in the extinction maximum. The extinction spectrum is a combination of both the absorption and scattering of the particles. Further to changes in the refractive index, peak maxima can be affected by resonance coupling with bound molecules, increased scattering due to the change in size and inter-particle coupling effects (Dahlin et al., 2006; Haes et al., 2004). Both the peak wavelength and peak maxima have been successfully used to follow biomolecular binding events with LSPR sensors (Dahlin et al., 2006; Nath and Chilkoti, 2004).

Dynamic Light Scattering (DLS)

Dynamic light scattering (DLS) is a widely used technique for assessing the size of particles in solution. In a dynamic light scattering experiment a beam of monochromatic laser light is directed at a scattering solution in a cuvette with a detector placed at an angle, θ , to the sample (Figure 1.20).

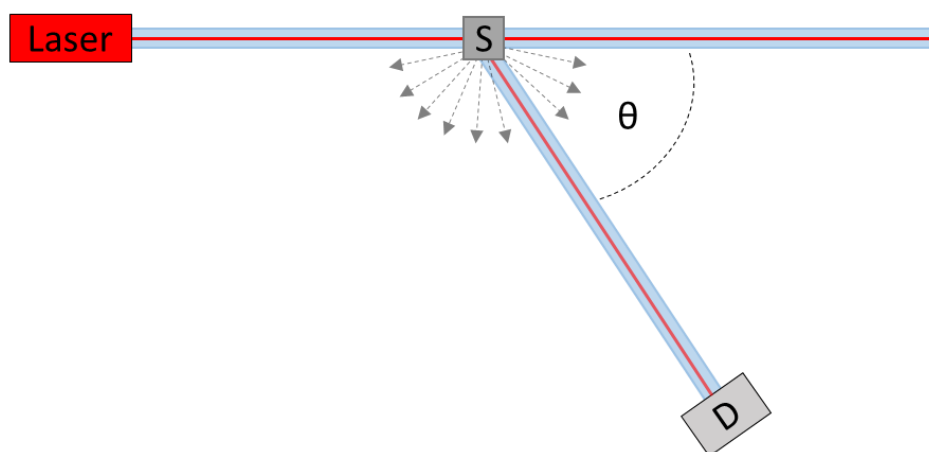


Figure 1.20 Schematic of a dynamic light scattering experiment. Monochromatic laser light is directed at a sample, S, in a cuvette and is scattered in all directions. Some of the scattered light reaches the detector, D, which is placed at an angle to the sample, θ .

Light hitting the particles in the solution is scattered in all directions with some reaching the detector. The resulting scattering pattern is constantly changing due to the dynamic nature of the particles in the solution. By measuring the fluctuations in the scattering intensity over time an autocorrelation function can be plotted, this is a measure of the similarity between the scattering pattern at a time, t , and the initial scattering at $t = 0$ (Berne and Pecora, 2000). The diffusion constant (D) of the particles can be determined by analysing the correlation function over time. From the diffusion constant, it is possible to calculate the hydrodynamic radius (R_{hyd}) of the scattering particles;

$$R_{hyd} = \frac{kT}{6\pi\eta D} \quad [1.8]$$

Where k is the Boltzmann constant, T is the temperature and η is the viscosity of the liquid. More simply, if you consider the movement of particles in a solution, those that are small will move rapidly due to thermal motion. This will manifest itself as fast, erratic fluctuations in the scattering and a rapid decay in the correlation function over time. Larger particles will move more slowly, therefore, exhibiting slower scattering fluctuations and a corresponding change in the correlation function (Figure 1.21).

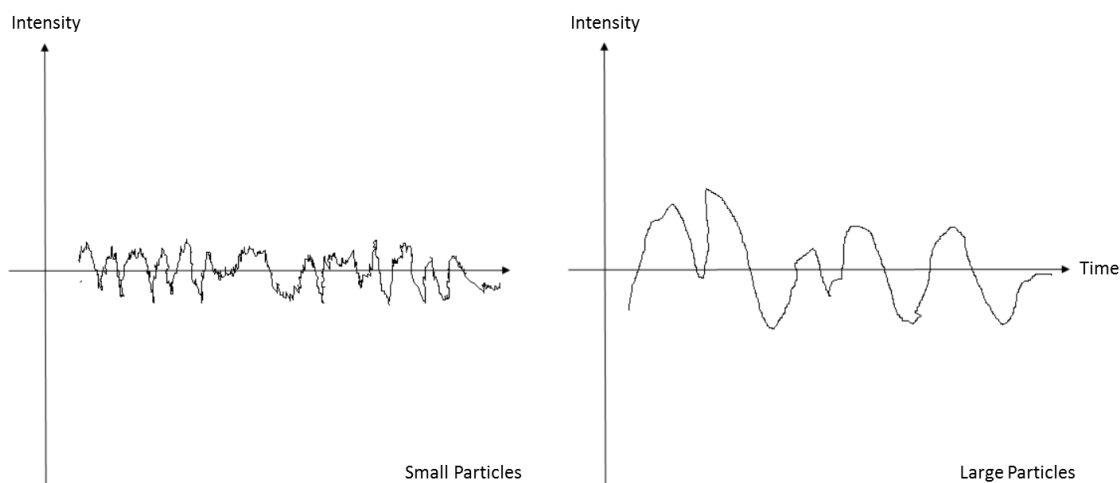


Figure 1.21 Visual representation of the differences in the scattering fluctuations of small and large particles in a solution.

DLS has been extensively used for nanoparticle characterisation, with the high scattering cross section of noble metal nanoparticles well suited to such experiments. However, care must be taken when both selecting and preparing samples for DLS analysis. Irregular shapes and multi-component mixtures are not well described by the autocorrelation function. Strongly scattering non-spherical gold nanoparticles have been shown to exhibit false peaks in the particle size distribution, while smaller (< 20 nm diameter) more weakly scattering samples can suffer from secondary peaks at larger sizes due to the scattering contribution of larger contaminants or aggregates. This is caused by the power law relationship between the scattering intensity and the diameter of the particles (D). The scattering intensity increases at a rate of D^6 , therefore a particle of twice the size would exhibit 64 times greater scattering (Khlebtsov and Khlebtsov, 2011). The main advantage of DLS over other methods of particle size determination, such as TEM, is the ability to easily collect *in situ* data of a large ensemble of particles.

DLS has become an invaluable tool for investigating biomolecule assembly helping several groups characterise protein-nanoparticle assemblies, usually in conjunction with spectroscopic techniques and electron microscopy (Casals et al., 2010; Goy-López et al., 2012; Jans et al., 2009; Lacerda et al., 2010; Ma et al., 2015). The sensitivity of light scattering experiments to aggregation has also led to its use as a detection method for protein binding assays with conjugated nanoparticles (Liu and Huo, 2009; Liu et al., 2009).

Small Angle Neutron Scattering (SANS)

Just as in a light scattering experiment, such as DLS above, SANS is carried out by illuminating a sample with a beam of radiation. In the case of small angle scattering a detector is placed directly behind the sample and collects the scattering pattern resulting from low angle elastic scattering. A beam stop is placed in the centre of the detector to block the direct beam. As discussed with neutron reflectometry the size range that is observed in a neutron experiment is determined by the Q range, which is dependent on the incident angle and neutron wavelength. For a SANS experiment the Q range is selected by varying the sample-detector distance instead of the angle of incidence (Figure 1.22).

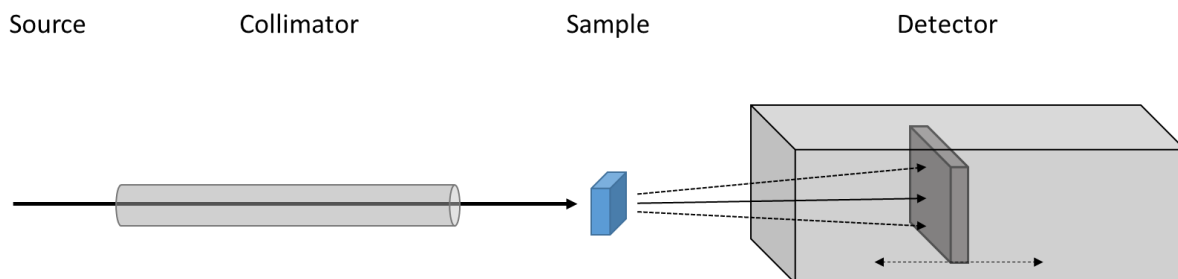


Figure 1.22 Typical SANS instrument set-up. The neutrons supplied by the source are collimated with a set of neutron guides before striking the sample. The detector, that is inside an evacuated chamber, can be moved depending on the Q range that is of interest.

A two-dimensional radial scattering pattern is observed at the detector, which is converted to a one-dimensional scattering profile by taking a radial average. The features of the scattering profile contain information about the shape of the individual particles and their interactions with one another, known as the form factor and the structure factor respectively (Figure 1.23). For a dilute solution of uniform particles with no long range order it can be assumed there are no correlations between the separated particles, i.e. $S(Q) = 1$, resulting in a uniform circular scattering pattern. For

isotropic samples a simple analysis of small angle scattering data can be carried out to obtain the radius of gyration of the individual particles. This method was first proposed by André Guinier (Guinier, 1939) and is carried out on very low angle scattering data. At low concentrations and low Q the scattering intensity can be written as:

$$I(Q) = I(0) \exp\left(\frac{-R_g^2 Q^2}{3}\right) \quad [1.9]$$

Where $I(Q)$ is the scattering intensity, $I(0)$ is the intensity at $Q = 0$, R_g is the radius of gyration and Q is the momentum transfer. Therefore, the R_g can be obtained by plotting the log of the intensity against the Q^2 . The radius of gyration is the average distance of the scattering atoms from the centre of the object and as such is not very good at describing complex anisotropic shapes.



Figure 1.23 The scattering intensity, $I(Q)$, is a combination of the form factor, $F(Q)$, and the structure factor, $S(Q)$.

For samples with multiple components whose SLDs vary, it is possible to carry out more complex fitting of scattering data to obtain detailed information about their structure. However, small angle scattering data suffers from the phase problem, just like reflectivity experiments, therefore it is necessary to collect data from multiple solvent contrasts in order to confidently fit a complex model.

As in reflectometry experiments, neutron scattering benefits from its sensitivity to lighter elements in the periodic table such as hydrogen. This has led to their extensive use in studying polymeric and protein systems. SANS studies of polymeric colloids and nanoparticles are quite common (Ballauff, 2001; Förster et al., 1999). Low resolution

structures of protein complexes are also commonly obtained by SANS (Clifton et al., 2012; Guo et al., 1990; Yong et al., 2002), with some experiments combining X-ray and neutron scattering data to aid data analysis (Arunmanee et al., 2016; Svergun et al., 1998). In comparison, very few studies have been carried out on protein-nanoparticle systems with only lysozyme-silica nanoparticle and human serum albumin-gold nanoparticle interactions investigated with this technique (Kumar et al., 2011; Spinozzi et al., 2017).

Analytical Ultracentrifugation (AUC)

AUC exploits the fundamental physical properties of particles in a solution to provide information on their size and shape. When a gravitational field is applied to a sample the mass will redistribute so that gravitational and chemical potential energies match. In an AUC experiment the gravitational field is applied by a centrifuge, which will cause the particles to sediment in the sample cell. Detection of the sedimenting components can be carried out by three optical methods, absorbance, interference and fluorescence. Two experiments are possible; the rate that the samples move due to the gravitational force can be measured (sedimentation velocity experiment) or the concentration distribution of the sample can be measured at equilibrium (equilibrium sedimentation experiment).

If one considers the sedimentation of a particle in a centrifuge, the force exerted on the particle can be expressed as:

$$F = M_p \omega^2 r \quad [1.10]$$

Where M_p is the mass of the particle, ω is the rotor speed in radians per second and r is the distance from the centre of the rotor. As the particle is in a solvent there will be a counterforce equal to the mass of the displaced solvent, therefore the buoyant mass of a particle, M_b , can be calculated as:

$$M_b = M_p(1 - \bar{v}\rho) \quad [1.11]$$

Where \bar{v} is the partial specific volume of the particle and ρ is the density of the solvent. There will also be a frictional force that is dependent on the velocity and frictional coefficient. Balancing these forces results in an expression for the sedimentation coefficient, s :

$$s = \frac{M_b}{f} \quad [1.12]$$

Therefore, the sedimentation coefficient is proportional to the buoyant mass of the particle, M_b , and inversely proportional to the frictional coefficient, f . In a sedimentation velocity experiment it is the shape and motion of a boundary moving through the cell that is measured, which will spread over time due to diffusion. Hence by measuring the concentration distribution over time it is possible to calculate both the diffusional coefficient and sedimentation coefficient of a sample by using the Lamm equation (Behlke and Ristau, 1997; Cole et al., 2008).

AUC has become an invaluable tool for investigating protein aggregation in the biopharmaceutical industry (Berkowitz, 2006) and for protein-protein binding (Howlett et al., 2006). One of the key advantages of the technique is the ability to carry out measurements under physiologically relevant conditions in a non-destructive manner. More recently, nanoparticle-biomolecule interactions have been investigated with studies carried out on gold nanoparticle-DNA conjugates using a combination of light scattering, AUC and agglomeration of AuNPs when in contact with protein solutions (Falabella et al., 2010; Zook et al., 2011). The polydispersity of both the metallic cores and surface coating ligands of gold nanoparticles makes simultaneous characterisation of the two parameters difficult. This is a possible area where AUC could become more widely used with a method of nanoparticle analysis reported by Carney *et al* which can obtain accurate size, density and weight distributions of nanoparticles using a single experiment (Carney et al., 2011).

Electrophoresis

The electrophoretic separation of biomolecules has become a universal and vital technique used around the world. Electrophoresis techniques work on the principle that a charged particle in a solution will be subjected to a directional force when an electric field is applied. The electrophoretic velocity (U) is described by Smoluchowski's formula:

$$U = \left(\frac{\varepsilon \zeta}{\eta} \right) E \quad [1.13]$$

Where ε is the dielectric constant of the liquid, η is the viscosity, ζ is the zeta potential of the particle and E is the applied field. The electrophoretic mobility is the ratio of the velocity and applied field (U/E). This presents a problem for separation, as particles with the same composition will have equal mobility regardless of their size or shape. To overcome this, several techniques using capillaries and gels have been developed which

introduce additional forces to allow separation. Capillary electrophoresis exploits electro-osmotic effects with charged species at the capillary wall (Grossman and Colburn, 2012) while gel electrophoresis separates by restricting mobility through a porous gel membrane.

For biomolecule separation, the two most popular gel systems are agarose and polyacrylamide. Polyacrylamide gels form the bases of SDS-PAGE and are made from a crosslinked network of polymerised acrylamide, the pore size can be varied by changing the acrylamide concentration and the ratio of a bifunctional crosslinker. This system is extremely popular for separating proteins, with several methods that can separate proteins between 1 and 100 kDa in size (Hames, 1998; Laemmli, 1970; Schagger, 2006).

Agarose is a polymer extracted from seaweed that forms a gel when dissolved in water, facilitated by a 3D hydrogen bonding network. Agarose has larger average pore sizes compared to polyacrylamide, making agarose gels ideal for the separation of large proteins (>200 kDa) and DNA fragments (Smith, 1996). The pore sizes of agarose gels are also ideal for the separation of nanoparticle species. Hanauer *et al* successfully separated polymer coated gold and silver nanoparticles according to their geometric shape (Hanauer et al., 2007). Additionally, discrete protein-nanoparticle and DNA-nanoparticle assemblies have been identified (Claridge et al., 2008; Ma et al., 2015; Zanchet et al., 2002). Finally, the conformation of oligonucleotides on the surface of gold nanoparticles has also been investigated by examining their mobility (Parak et al., 2003).

1.7 Aims

Gold nanoparticle-protein assemblies are an area of great interest and intense research. The motivation for this research is the increasing use of these assemblies as therapeutic and biomedical agents and their continued use in biosensing technologies. Although much of the literature has investigated the formation of protein layers or coronas, very few detailed structural studies are available. The complex nature of protein-surface interactions and the huge variety of proteins studied have also made definitive mechanistic information on protein binding and organisation difficult to obtain. In this study, a self-assembling protein system, previously characterised on planar gold surfaces, was applied to nanoparticles with the project focussed on three main questions:

1. What is the structure of gold nanoparticle assemblies on AAPTMS functionalised silicon dioxide surfaces?
2. Do engineered OmpA_{TM} proteins assemble in an oriented fashion on to gold nanoparticles?
3. Can engineered OmpA_{TM}:AuNP conjugates be used for sensing biological molecules?

In order to understand both components of the protein-nanoparticle system a combinatorial approach was required. Gold nanoparticle assemblies on silane modified silicon dioxide surfaces were directly interrogated by X-ray spectroscopy, force and electron microscopy and neutron reflection. The structure and assembly of proteins on the nanoparticle surface was investigated by spectroscopic, scattering and electrophoretic techniques. Finally the use of novel protein-AuNP conjugates for biomolecule sensing was explored using lateral flow and spectroscopic assays.

2 MATERIALS AND METHODS

2.1 Materials

All chemicals were purchased from Sigma-Aldrich (Poole, Dorset, UK) unless otherwise stated. Gold nanoparticles were purchased from BBI Solutions (Cardiff, UK). (Aminoethylaminomethyl)phenethyltrimethoxysilane was purchased from Fluorochem Ltd (Hadfield, UK).

2.2 Gold Functionalised Surface Preparation

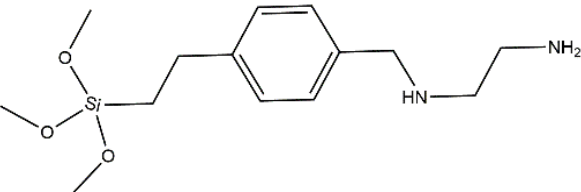
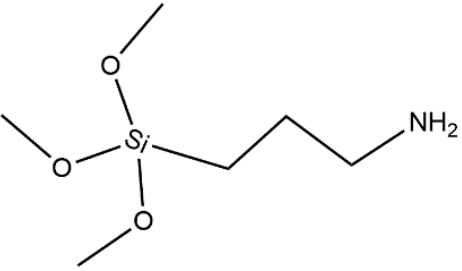
2.2.1 Piranha Cleaning

Borosilicate glass coverslips (VWR, UK) and silicon wafer chips (Agar Scientific, UK) were cleaned with piranha solution to remove any organic contaminants on the surface prior to functionalisation. Piranha solution was made by mixing concentrated sulphuric acid with a 30% hydrogen peroxide solution in a 3:1 ratio. Just enough piranha solution was added to fully cover the surface of each sample and incubated for 30 minutes. The piranha solution was carefully removed and added to the piranha waste bottle before washing the samples three times with copious amounts of distilled water. All steps were carried out in clean dry glassware in a fume cupboard.

2.2.2 Silanisation

Two different silane molecules were used for surface functionalisation during this study, shown below in Table 2.1.

Table 2.1 Silane molecule structures and mass.

<i>Silane</i>	<i>Structure</i>	<i>Molecular mass/ gmol⁻¹</i>
(Aminoethylaminomethyl) phenethyltrimethoxysilane (AAPTMS)		298.45
(3-Aminopropyl)trimethoxysilane (APS)		179.29

To activate the silane for surface functionalisation 1 ml of silane solution was added to 95 ml of ethanol and 5 ml of distilled water in a glass staining dish and stirred for 10 minutes with a magnetic flea. The activated solution was then diluted to 200 ml with ethanol to give a 0.5% v/v silane solution. Piranha cleaned samples were suspended in the solution using a coverslip rack or mesh basket and incubated for 30 minutes with stirring. After silanation the samples were washed with ethanol and sonicated in ethanol three times using a XB2 ultrasonic bath (Grant Instruments, UK) for 1 minute. Finally, the samples were washed with nanopure water (Thermo Scientific, UK) and dried using an air-line.

2.2.3 Gold Nanoparticle Deposition

Silanised samples were separated into individual wells in a 12 well polystyrene plate. Approximately 200 μ l of commercial or synthesised nanoparticle solution at 1 OD_{525nm} concentration in nanopure water was added to each well to cover the surface of the sample and incubated for between 10 and 60 minutes on a 3D rocking platform (Stuart Scientific, UK). The samples were washed with nanopure water before sonicating in nanopure water three times using a XB2 ultrasonic bath (Grant Instruments, UK) for 1 minute and drying with an air-line. Dry samples were then stored in a clean 6 well polystyrene plate and sealed with parafilm before use.

2.3 X-Ray Photoelectron Spectroscopy

Borosilicate glass coverslips (VWR, UK) at each stage of the gold deposition process were analysed by Dr Jose Portoles of the National EPSRC XPS User Service (NEXUS) at Newcastle University using a Kratos Axis NOVA Spectrometer with a micro-focussed monochromated Al K α X-ray source. Survey spectra were collected using a wide analysis area of 300 x 700 μ m, pass energy of 160 eV and step size of 1.00 eV. Three measurements were carried out in non-overlapping areas for each sample. Spectra were analysed using the CASA XPS software (Casa Software Ltd, UK).

2.4 Nanoparticle Synthesis

To begin 0.072 g of Gold(III) Chloride was added to a 20 ml glass vial, 7.2 ml of nanopure water added by pipette and stirred for 1 minute until fully dissolved. A 7 ml aliquot of the resulting yellow solution was diluted into 90 ml of nanopure water in a 100 ml glass vial. The diluted solution was stirred for 1 minute with a Teflon coated magnetic flea before cooling in the fridge with a separate 50 ml aliquot of nanopure water for at least 1.5 hours. Next 0.316 g of 2-Mercapto-5-benzimidazole sulfonic acid (MBS) and 0.095 g of sodium borohydride (NaBH₄) were added to separate 2 ml glass vials. The refrigerated nanopure water was taken from the fridge and 10 ml added to the MBS and dissolved by sonication. A further 5 ml aliquot of the refrigerated nanopure water was taken and added to the NaBH₄ which was dissolved by stirring. Both solutions were then cooled in the freezer for 15 minutes before use. The gold(III) chloride solution was taken from the freezer and incubated on ice with stirring. A 1.4 ml aliquot of the MBS solution was added to the gold(III) chloride and stirred for 20 seconds before 1.75 ml of the cold NaBH₄ solution was rapidly added and incubated for a further 5 minutes with stirring. Finally, approx. 12 g of prewashed Amberlite MB-150 mixed exchange resin was added to the gold nanoparticle solution and incubated on ice for 5 minutes. The Amberlite resin was removed from the resulting nanoparticle solution by gravity filtration with a grade 1 Whatman filter paper into a fresh 100 ml glass vial. The concentration of the resulting nanoparticle solution was analysed by UV-vis spectroscopy with optical densities of between 1 and 2 at 525 nm routinely obtained.

2.4.1 UV-Visible Spectroscopy

Nanoparticle spectra were acquired in a 10 mm pathlength quartz cuvette (Hellma GmbH) using a Shimadzu UV1800 spectrometer between 400-800 nm.

2.5 Transmission Electron Microscopy

Gold Nanoparticle Analysis

A 10 μ l droplet of gold nanoparticle solution was added to a 200 mesh carbon coated grid and incubated at room temperature for 5 minutes, excess liquid was removed by touching with a Whatman filter paper and dried under a heat lamp before use. Samples were visualised using a Philips CM100 TEM with a compustage. Magnifications between 30000x and 180000x were routinely used. The resulting high resolution images were saved in a tagged image format (TIF) and analysed using Image J (NIH, USA).

Gold Nanoparticle-Protein Conjugate Analysis

A 200 mesh, carbon coated, glow discharged grid was prepared using the single droplet method (Harris, 1997). The grid was touched to a 10 μ l droplet of AuNP-Protein conjugate for 30 seconds before excess liquid was removed by Whatman filter paper. The grid was washed, to remove excess buffer components, by touching to 2 x 20 μ l water droplets which were removed by Whatman filter paper. Finally, the grid was stained by touching a 20 μ l droplet of 2% uranyl acetate solution, excess liquid removed by filter paper and air dried before visualising with a Philips CM100 TEM. The resulting high resolution images were saved as TIFs and analysed using Image J (NIH, USA).

2.6 Colorimetric Amine Density Assay

Buffers used:

Coomassie Blue Staining Buffer:

- 0.5 mg/ml Coomassie Brilliant Blue G250
- 10% v/v Methanol
- 5% v/v Glacial Acetic Acid
- 85% Nanopure Water

Washing Buffer:

- 10% v/v Methanol
- 5% v/v Glacial Acetic Acid
- 85% v/v Nanopure Water

Destain Buffer:

- 50% v/v Methanol
- 50% v/v 0.25 M Na₂CO₃

A modified method from Coussot et al (Argekar et al., 2013; Coussot et al., 2010) was used. Silanised silicon wafer chips were transferred to a 24 well plate and 150 μ l of staining buffer carefully added on to the polished surface and incubated for 5 minutes at room temperature on the laboratory rocker. The staining buffer was then removed and each chip washed 5 times with 300 μ l of washing buffer to remove any unbound Coomassie. The chips were then removed to a clean well before adding 150 μ l of destain buffer and incubated for 1 minute to extract the bound Coomassie dye. All 150 μ l of the destain was removed and added to an Eppendorf type tube containing 3 μ l of 6.85 M HCl to acidify the dye and maximise absorbance. Absorbance at 610 nm was measured in triplicate using the NanoDropTM ND1000 spectrometer and the Coomassie concentration calculated using the extinction coefficient of 83,100 cm⁻¹ M⁻¹. The number of Coomassie molecules was calculated from the concentration using Avogadro's constant, 6.02×10^{23} mol⁻¹. Coomassie binds to protonated amines with a 1:1 stoichiometry so the amine density was calculated by dividing the area by the number of extracted Coomassie molecules in solution.

Amine availability after gold deposition

The amine density assay was carried out on triplicate AAPTMS functionalised silicon wafer chips as described above. The functionalised wafer chips were then incubated with 250 μ l of commercial 10 nm gold nanoparticle solution at 0.3 OD_{525nm} for 10 minutes before repeating the amine assay. This was carried out for 2 more nanoparticle depositions.

2.7 Atomic Force Microscopy

All images were acquired using a NanoWizard III Bio AFM (JPK Systems, Germany) on a Halcyonics Micro 40 anti-vibration table with silicon nitride 0.6 μ m cantilevers (Bruker model DNP-10). Silicon wafer chip samples were mounted on a glass slide with superglue before use. The resonant frequency of each probe was measured using the built-in software before imaging. Images were collected in tapping mode, where the tip is oscillated close to its resonance frequency and scanned across the surface using a raster pattern (Figure 2.1). Images were analysed using the built-in JPK software.

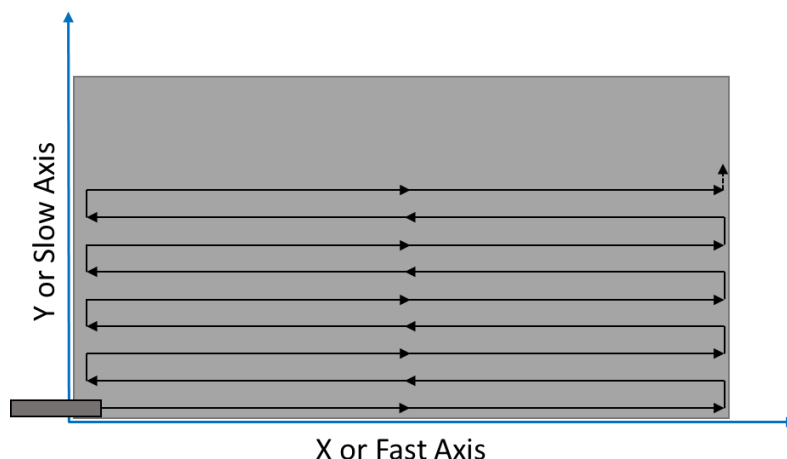


Figure 2.1 Schematic of AFM data collection. The probe is scanned across the sample in a raster pattern which gives rise to a “fast” and “slow” axis, relating to the direction of travel of the probe.

2.8 Scanning Electron Microscopy

Silicon wafer chips of approximately 1 cm x 1 cm in size were functionalised with either commercial or synthesised gold nanoparticles before mounting on aluminium specimen stubs with carbon adhesive discs. Microscopy was carried out by Leon Bowen at the Electron and FIB Microscopy Unit, Durham University. Samples were visualised using an FEI Helios Nanolab 600 microscope equipped with an Elstar UHR immersion lens. Images were acquired using working distances between 3.0 and 4.5 mm and an accelerating voltage of 5 kV. Magnifications between 30000x and 180000x were routinely used. The resulting high resolution images were saved as TIFs before analysis using Image J.

ImageJ Analysis

Images were converted to 8-bit grey scale and cropped to remove the lower information bar. Conversion of the image to an 8-bit scale assigns each pixel of the image with a value between 0 and 255 depending on its grey shade. The threshold tool was then used to select the region of the grey scale that only included the gold nanoparticles. After selecting the particles, the measure tool used to calculate the % area of the image occupied by the nanoparticles. Average surface coverages were calculated using three separate images of each sample.

2.9 Neutron Reflectometry

Buffers used:

ROG 8 Buffer:

- 1% w/v n-octyl- β -D-glucopyranoside (Anatrace, USA)
- 50 mM tris(hydroxymethyl)aminomethane pH 8

HEPES Buffer:

- 20 mM 4-(2-hydroxyethyl)-1-piperazineethanesulfonic acid pH 7.4
- 150 mM Sodium Chloride

Sample Preparation

A single-crystal silicon block, 80 mm x 50 mm x 20 mm, with a single polished face was first piranha cleaned before two 30 rounds of cleaning using a UV ozone cleaner (Ossila Ltd, UK). The polished face was silanised by immersing in a glass Petri dish containing a 0.5% v/v AAPTMS (Fluorochem, UK) solution in aqueous ethanol (95% EtOH and 5% H₂O) and incubating for 30 minutes on a laboratory rocker. The surface was washed with ethanol and sonicated 3 times for 1 minute in an ethanol bath before washing with nanopure water and drying with a nitrogen line. 15 ml of 20 nm gold nanoparticles at 1 OD₅₂₅ supplemented with 1 mM sodium chloride was added to the silanised face and incubated for 30 minutes. The solution was agitated every 10 minutes with a pipette. After 30 minutes the nanoparticle solution was removed and the block sonicated 3 times for 1 minute in a water bath. This process was repeated 3 times. The functionalised block was mounted in a custom solid-liquid flow cell before protein assembly (see Section 3.2.5).

Protein assembly was carried out using the syringe port on the solid-liquid cell. 20 ml of ultrapure water was injected to wash the surface before adding 20 ml of 1% v/v 2-mercaptoethanol solution. The cell was washed with 20 ml of nanopure water before adding 15 ml of 1.14 μ M GGzOmpA_{TM} in ROG 8 buffer and incubating for 10 minutes. The cell was washed with 15 ml of HEPES buffer followed by 15 ml of 1% w/v sodium dodecylsulphate solution. The washes were repeated before a second incubation with GGzOmpA_{TM} solution. The cell was washed with 15 ml of HEPES buffer followed by 15 ml of 1% w/v sodium dodecylsulphate solution before adding 15 ml of 100 μ M (11-mercaptoundecyl)hexa(ethylene glycol) (SH-C11-OEG6) in ROG 8 buffer and incubating for 10 minutes. The wash steps were repeated again before a second

incubation with SH-C11-OEG6 solution. The wash steps were carried out for a final time before measuring on the beamline. Both the GGzOmpA_{TM} and SH-C11-OEG6 solutions were incubated with 25 mM tris(2-carboxyethyl)phosphine (TCEP) for 30 minutes before use.

Data Acquisition

The solid-liquid flow cells were mounted on the sample stage of the INTER beamline at the ISIS spallation neutron source, Oxford UK. A full alignment was carried out so that measurements of the specular scattering from the functionalised surface could be taken. The inlet of the flow cell was attached to a Hitachi HPLC pump for automatic changing of the contrast buffers. Samples were measured using neutrons with a wavelength range of 2-14 Å and at two incident angles, 0.7 and 2.3°, to give a Q range of 0.01-0.35 Å⁻¹. A transmission measurement was carried out for the silicon block and subtracted from the sample data to remove any scattering contributions from the block.

Data Reduction

The raw reflectivity data was processed so that it is in a usable format for analysis. This is known as data reduction and was carried out using the MantidPlot program (Arnold et al., 2014). The ISIS Reflectometry plugin was used which carries out three processes on the data. Firstly the transmission measurement was subtracted and secondly the data sets from the two incident angles were stitched together to form a single reflectivity profile. The final process is known as binning, the data acquired by the detector is analogue, therefore, it must be quantized into discrete values so that it can be analysed. To do this the Q range is divided into small intervals, or “bins”, with the intensity data in each “bin” averaged. Each individual data point generated by the binning process has an associated intensity value, the mean intensity, and error, from the standard error of the mean.

Data Fitting

Data fitting was carried out using the RasCAL reflectivity fitting program in Matlab build R2015a (Clifton et al., 2011). The “Bootstrap” error analysis tool was used in RasCal. This tool estimates the error by re-sampling the data and carrying out data fitting from random parameter starting values. Error estimates were calculated from 100 fitting runs.

2.10 Protein Expression and Purification

All of the plasmids for the protein constructs were supplied by Orla Protein Technologies Ltd (Newcastle Upon Tyne, UK). The expression plasmid used was a modified pET8c vector with a 6x His tag at the N-terminus (Politou et al., 1994). None of the proteins contained a signal sequence so formed cytoplasmic inclusion bodies when over expressed in *E. coli*. After expression and cell lysis the inclusion bodies were purified using immobilised metal affinity chromatography (IMAC) and refolded by rapid dilution into detergent buffer (Shah et al., 2007).

Table 2.2 Expressed Protein Constructs

<i>Protein</i>	<i>Molecular Mass / Da</i>	<i>Number of Amino Acids</i>
<i>wtOmpA_{TM}</i>	21385.4	197
<i>cysOmpA_{TM}</i>	21399.7	197
<i>GGzOmpA_{TM}</i>	44019.4	401
<i>scFvOmpA_{TM}</i>	58557.6	544

Buffers used:

Lysing Buffer:

- Bugbuster™ Solution
- 10 µg / ml lysozyme
- 2.5 µg / ml nuclease

Urea Binding Buffer:

- 8 M Urea
- 20 mM Sodium Phosphate pH 7.2
- 100 mM Sodium Chloride
- 20 mM Imidazole

Urea Elution Buffer:

- 8 M Urea
- 20 mM Sodium Phosphate pH 7.2
- 100 mM Sodium Chloride
- 500 mM Imidazole

Refolding Buffer

- 34 mM Octyl β -D-Glucopyranoside (Melford) (CMC of ~18 mM)
- 50 mM Ethanolamine pH 10
- 1 mM TCEP

Expression

Competent BL21(DE3) *E. coli*, made using a modified rubidium chloride method (Maniatis et al., 1982), were transformed with a chosen plasmid, spread on an LB agar plate, supplemented with 100 ug/ml ampicillin, and incubated at 37°C overnight. 250 ml of LB (lysogeny broth) medium supplemented with 100 μ g/ml ampicillin was inoculated with a single colony and incubated overnight at 37°C with 150 rpm stirring. A further 750 ml of LB medium, supplemented with 100 μ g/ml ampicillin, was added to the starter culture and incubated for 1 hour at 37°C with 150 rpm stirring before induction by the addition of isopropyl β -D-1-thiogalactopyranoside (IPTG) to a final concentration of 1 mM. The culture was grown for a further 5 hours and the cells extracted by centrifugation at 4,500 x g for 10 minutes. The supernatant was removed and the cell pellet resuspended in 25 ml of lysing buffer and incubated for 15 minutes at room temperature before freezing overnight. The lysate was thawed before centrifugation at 17,000 x g for 25 minutes, the supernatant was removed and the pellet resuspended in 25 ml of 1/10 Bugbuster™ solution followed by a second centrifugation at 17,000 x g for 15 minutes. The supernatant was removed and the pellet resuspended in 25 ml of 1/10 Bugbuster™ solution before a final centrifugation at 17,000 x g for 25 minutes to produce the final inclusion body pellet.

Purification

The inclusion body pellet was dissolved by agitation in a minimum of urea binding buffer and the solution clarified by centrifugation at 20,000 x g benchtop Picofuge (Biorad, USA) for 10 minutes before loading on to a 5 ml HisTrap HP column (GE Healthcare, USA). The column was washed with 5 column volumes of urea binding buffer before the protein was eluted with a 50:50 mix of urea elution buffer and urea binding buffer. The fractions corresponding to the adsorption peak at 280 nm were collected, pooled and concentrated to 1 mg/ml using a 30K molecular weight cut off (MWCO) Vivaspin centrifugal concentrator (Sartorius Stedim, France).

Refolding

Refolding was carried out by 1 in 20 rapid dilution of the purified inclusion bodies into refolding buffer while maintaining a final protein concentration < 0.5 mg/ml, followed by 48 hour incubation at 37°C. GGzOmpA_{TM} refolding buffer was supplemented with 300 mM arginine, scFvOmpA_{TM} refolding buffer contained both 300 mM NaCl and 300 mM arginine. Refolding was confirmed by the observation of a heat modifiable band shift on a 12% Tris-Glycine SDS-PAGE gel. β -barrel proteins are resistant to SDS unfolding, therefore, protein folding can be determined by running SDS-PAGE samples with and without boiling. A characteristic shift in the observed molecular weight will occur on heating if the protein is folded. Refolded protein stocks were stored at 4°C.

2.11 Photometric Protein Concentration Determination

Protein concentration was routinely determined using the NanodropTM ND-1000 spectrometer. The absorbance at 280 nm was measured and the concentration calculated using the Beer-Lambert law:

$$A = \epsilon cl \quad [2.1]$$

Where ϵ is the molar extinction coefficient ($M^{-1} cm^{-1}$), c is the concentration (M) and l is the pathlength (cm). All samples were measured in triplicate with the average used to calculate the concentration. The molar extinction coefficients of the proteins were calculated by summing the extinction coefficients of the tryptophan and tyrosine residues in the amino acid sequence (5690 and 1280 $M^{-1}cm^{-1}$ respectively).

Table 2.3 Properties of the proteins used in this study.

<i>Protein</i>	<i>Molar Extinction Coefficient / $M^{-1} cm^{-1}$</i>	<i>Molecular Mass / Da</i>	<i>pI</i>	<i>Number of Amino Acids</i>
<i>wtOmpA</i>	45090	21385.4	6.17	197
<i>cysOmpA</i>	45090	21399.7	6.17	197
<i>GGzOmpA</i>	68300	44019.4	4.94	401
<i>IgAPOmpA</i>	43890	31993.3	5.94	286
<i>scFvOmpA</i>	88155	58557.6	5.72	544
<i>FluA NP</i>	54235	56875.2	9.27	567

2.12 Protein Binding Analysis

Buffers used:

DDM Buffer:

- 0.5% w/v n-Dodecyl β -D-maltoside (Melford Ltd, UK)
- 10 mM Tris HCl pH 8

For protein-nanoparticle binding studies the protein stocks were first buffer exchanged from the refolding buffer into DDM buffer using a PD10 desalting column (GE Healthcare, USA), this buffer was chosen because of the low CMC of DDM (0.008% w/v). For experiments using the SH-C11-OEG6 filler solution, this was prepared from a 53 mM stock in ethanol by first diluting 1 in 66 in ethanol followed by 1 in 10 in DDM buffer containing 5 mM TCEP. Dilution into the TCEP buffer was followed by a 30 minute incubation and a final dilution of 1 in 10 in DDM buffer before use, resulting in a final filler concentration of 8 μ M.

All protein binding experiments were carried out at a final nanoparticle concentration of 1 OD_{525nm}. The commercial 20 nm AuNP stock (10 OD_{525nm}) was first diluted in nanopure water before addition of the protein solution.

2.12.1 Kinetic Experiments

Kinetic experiments following binding of the wtOmpA_{TM}, cysOmpA_{TM} and GGzOmpA_{TM} proteins to commercial 20 nm gold nanoparticles were carried out using a Cary 4E UV-vis spectrometer. Spectra were acquired between 400-800 nm with a 1 cm pathlength black quartz cuvette with a 100 μ l capacity (Type 105.201-QS Hellma GmbH, Germany). Baseline correction was carried out using the cuvette filled with nanopure water. Experiments were initiated by mixing 180 μ l of nanoparticle solution, in nanopure water, with 20 μ l of protein solution, in DDM buffer, using a P200 pipette and quickly adding to the cuvette in the sample environment of the spectrometer. Final protein concentrations of 0.8 and 1.6 μ M were used, equating to protein:AuNP molar ratios of 638:1 and 1276:1 respectively.

Overnight Kinetics

Overnight kinetics spectra were acquired on the Cary 4E spectrometer between 400-800 nm every 10 minutes for 940 minutes (94 acquisitions) with a scan rate of 600 nm/min and data interval of 1 nm.

Initial Kinetics

Initial kinetics spectra were acquired on the Cary 4E spectrometer between 400-800 nm every 33 seconds for 1221 seconds (37 acquisitions) with a scan rate of 1000 nm/min and data interval of 1.11 nm. Three separate samples were measured for each protein.

Samples containing TCEP were incubated in 10 mM TCEP for 30 minutes then diluted to 8 μ M in DDM before a final dilution of 1 in 10 into the gold nanoparticle solution, to give final protein and TCEP concentrations of 0.8 μ M and 0.22 mM respectively.

2.12.2 Equilibrium Titration

wtOmpA_{TM} and cysOmpA_{TM} binding to 20 nm gold nanoparticles with increasing protein concentration was measured using the Cary 4E spectrometer. Aliquots of commercial AuNP solution, 180 μ l in nanopure water, were added to 20 μ l of protein solution, in DDM buffer, to give a final AuNP concentration of 1 OD_{525nm} and a range of protein concentrations between 0.016 and 0.8 μ M. Triplicate samples were made at each concentration and incubated overnight before acquiring UV-vis spectra between 400-800 nm.

Fluorescence Spectroscopy

Fluorescence spectroscopy experiments were carried out to measure the residual protein concentration after binding to gold nanoparticles. Cary Eclipse fluorescence spectrometer was used, with excitation set at 280 nm and emission scanned between 300 and 450 nm using a 120 nm/min scanning speed, 0.5 seconds averaging and 1 nm data interval. The band width was set at 10 nm for both excitation and emission to give a high sensitivity and a 5 mm square cuvette (Type 101-016-40-QS Helma GmbH, Germany) used for all samples with a 250 μ l sample volume. For each protein, standards were made by serial dilution of a stock solution into water, care was taken to maintain the same level of DDM detergent in the standards as would be in the unknown samples. Standards of 1, 0.5, 0.25, 0.125, 0.0625 and 0.0125 μ M were made and measured in duplicate at room temperature. The peak integral of each standard was taken between 300 and 400 nm, averaged and a calibration curve plotted.

Samples were made in triplicate as per the UV-Vis spectroscopy experiments. After overnight incubation 300 μ l of sample was added to a 1.5 ml Eppendorf tube and centrifuged at 20,000 x g for 10 minutes in an Eppendorf 4518 R centrifuge at 20°C. The supernatant was carefully removed so as not to disturb the nanoparticle pellet and

the protein concentration measured using the Cary Eclipse. The peak integrals were averaged for each triplicate set of samples and the protein concentration calculated from the linear regression equation of the standard curve.

2.12.3 NaBH₄ Competition Assay

The stability of wtOmpA_{TM} and cysOmpA_{TM} conjugated 20 nm gold nanoparticles was assessed using a NaBH₄ competition assay. Commercial AuNPs at 1 OD_{525nm} concentration were incubated overnight with their respective protein at a final concentration of 0.8 μM. A series of NaBH₄ solutions were made by serial dilution of a 125 mM stock, in nanopure water, to give 1.5, 1, 0.5, 0.25 and 0.05 mM final NaBH₄ concentrations when 20 μl was added to 180 μl of the protein-AuNP conjugate stock. The protein-AuNP samples were then incubated for 3 hours at room temperature before acquiring the UV-Vis spectrum between 400-800 nm using the Cary 4E spectrometer.

2.12.4 Salt Stability of Protein Conjugated AuNPs

The stability of 20 nm gold nanoparticles conjugated with the GGzOmpA_{TM} when challenged with increasing NaCl concentration was assessed using the Cary 4E spectrometer. Protein-AuNP conjugates were made using commercial nanoparticles, in nanopure water, at 1 OD_{525nm} concentration that were incubated with protein, in DDM buffer, at a final concentration of 0.8 μM for 15 minutes before adding Filler, in DDM buffer, to a final concentration of 0.8 μM and incubating for a further 15 minutes. 100 μl of the AuNP-Protein conjugate was then diluted 1 in 2 in a range of NaCl solutions, in nanopure water, to give final NaCl concentrations of 50, 100, 200, 300, 400, 500 and 1000 mM. The samples were incubated for 30 minutes before acquiring the UV-Vis spectrum between 400-800 nm.

2.13 Agarose Gel Electrophoresis of AuNP

Buffers used:

TB Buffer pH 8:

- 90 mM Tris HCl
- 90 mM Boric Acid

Running Buffer:

- 90 mM Tris HCl
- 90 mM Boric Acid
- 0.025% w/v Tween 20

Loading Buffer:

- 90 mM Tris HCl
- 90 mM Boric Acid
- 30% w/v Glycerol
- 0.05% w/v Tween 20

Protein-AuNP conjugates were made by overnight incubation of commercial 20 nm gold nanoparticles, in nanopure water, and protein, in DDM buffer, at final concentrations of 10 OD_{525nm} and 8 µM respectively. Electrophoresis experiments were carried out using 20 µl of sample mixed with 5 µl of loading buffer before adding to the well of a 1% agarose gel prepared with TB buffer. Gels were run for 70 minutes at 100 V.

2.14 Dynamic Light Scattering (DLS)

A Malvern Zetasizer Nano S instrument was used to analyse samples by DLS. A 45 µl quartz cuvette (Type 105.251-QS Hellma GmbH, Germany) was used for data acquisition. Measurements were carried out on automatic mode in duplicate with three replicate samples. Particle size analysis was carried out using the Malvern Zetasizer software version 7.11.

Before carrying out DLS measurements any remaining protein or detergent was removed from 200 µl aliquots of the protein-AuNP samples by centrifugation at 20,000 x g in an Eppendorf 4518 R centrifuge at 20°C for 4 minutes. The supernatant was removed carefully so that the pellet was not disturbed and resuspended in 200 µl nanopure water.

2.14.1 IgG Binding to Protein-AuNP Conjugates

AuNP-Protein conjugates were incubated with a monoclonal α -vinculin antibody at a final concentration of 1 µM in nanopure water (Sigma Aldrich V1931, used due to availability) for 10 minutes before centrifugation at 20,000 x g in an Eppendorf 4518 R

centrifuge at 20°C for 4 minutes. The supernatant was removed and the pellet resuspended in nanopure water and analysed by the Zetasizer Nano S.

2.14.2 NaBH₄ Competition

AuNP-Protein conjugates were made by incubating 20 nm gold nanoparticles, at 1 OD_{525nm}, overnight at room temperature with protein at 0.8 µM final concentration, samples containing filler were incubated for 30 minutes with protein before filler addition at 0.8 µM final concentration. AuNP conjugates were centrifuged at 20,000 x g in an Eppendorf 4518 R centrifuge at 20°C for 4 minutes and the AuNP pellet resuspended in filtered nanopure water. 50 µl aliquots were incubated with NaBH₄ for 30 minutes at final concentrations of 1, 5 and 20 mM before analysis by the Zetaizer Nano S.

2.15 Nanodrop Spectrometer

2 µl AuNP-protein conjugate samples were analysed in the UV-Vis mode of a ND-1000 spectrometer (Thermofisher Scientific, UK). Nanopure water was used for baseline correction and spectra were acquired between 300-700 nm. The data was exported as an ASCII file and analysed using Microsoft Excel.

2.16 Small Angle Neutron Scattering of AuNPs

Sample Preparation

AuNP conjugates were prepared at 1 OD_{525nm} by overnight incubation with 0.8 µM GGzOmpA_{TM} and 0.8 µM filler, using the same method as section 2.12. All samples were centrifuged at 20,000 x g in an Eppendorf 4518 R centrifuge at 20°C for 5 minutes and the pellet was resuspended in 1/10th the volume with D₂O. The cap from a 1.5 ml Eppendorf tube was removed and 200 µl of AuNP conjugate added by pipette. The open end of the cap was then sealed using 40K MWCO dialysis membrane and the AuNP conjugate dialysed for 72 hours in 50 ml of D₂O with 2 buffer changes. After measuring the SANS of the GGzOmpA_{TM} and filler conjugated AuNP sample an alkaline phosphatase conjugated IgG (EMD Millipore, UK), that had been dialysed in D₂O, was added to a final concentration of 1 µM and incubated for 1 hour before a second SANS measurement was carried out.

Data Collection

Data was collected on the Sans2D beamline at the ISIS spallation neutron source (Oxford, UK) with a 4 m sample to detector distance and wavelength range of 2-14 Å, covering a Q range of 0.005 to 0.3 Å⁻¹. Measurements were carried out in 1 mm path length quartz cuvettes (Hellma GmbH, Germany) with approximately 300 µl of sample at 20°C. A buffer blank was collected in a quartz cuvette for the same acquisition time as the AuNP samples. The scattering data was reduced to a one-dimensional scattering profile and the scattering of the buffer subtracted using the SANS2D plugin within the MantidPlot program (Arnold et al., 2014).

Data Analysis

The scattering data was analysed using the BayesApp online web server (Hansen, 2012). This program carries out an indirect Fourier transform of the data to generate a pair distance distribution function or p(r) plot. From the p(r), the radius of gyration, R_g, was calculated and the maximum distance, D_{max}, obtained.

2.17 Analytical Ultracentrifugation of AuNP Conjugates

AuNP conjugate samples were analysed by Dr A Solovyova at the Newcastle University Protein and Proteome Analysis (NUPPA) facility. Sedimentation velocity experiments were carried out using a Beckman Coulter ProteomLab XL-I analytical ultracentrifuge, with both absorbance (530 nm) and interference detection. Data was analysed using SEDFIT (NIH, USA).

2.18 Fluorescence Microscopy of AuNP-Glass Surfaces

Buffers used:

DDM Buffer:

- 10 mM Tris HCl pH 8
- 0.5% w/v n-Dodecyl β-D-maltoside

TBS Buffer:

- 50 mM Tris HCl pH 8
- 150 mM Sodium Chloride

TBS-Tween:

- 50 mM Tris HCl pH 8

- 150 mM Sodium Chloride
- 0.05% Tween 20

Coverslip Preparation

22 x 22 mm borosilicate glass coverslips were silanized with 0.5% AAPTMS, using the same method as section 2.2.2, before incubating with 20 nm AuNP at 1 OD_{525nm} concentration for 30 minutes. After AuNP functionalisation the coverslip was moved into a 4-well ChamSlide CMS chamber (Live Cell Instrument, South Korea), this device provides 4 individually sealed chambers.

Protein Preparation

Protein stocks in DDM buffer were diluted to 0.1 mg/ml and incubated in 25 mM TCEP for 30 minutes before use, the 53 μ M SH-C11-OEG6 filler stock in ethanol was diluted 1 in 1000 in 10 mM Tris and incubated with 25 mM TCEP for 30 minutes before use. Alexa Fluor 488 conjugated rabbit anti-mouse IgG antibody at 1 mg/ml (Life Technologies, USA) was diluted 1 in 20 in TBS buffer before use.

Protein Assembly

Each well of the ChamSlide chamber was washed with 2 x 200 μ l of 1% w/v SDS followed by 2 x 200 μ l of TBS buffer. 200 μ l 1% v/v β -mercaptoethanol was added and incubated for 5 minutes before removal and washing with 2 x 400 μ l of TBS buffer. 200 μ l of protein solution was then added and incubated for 10 minutes before removal and washing with 2 x 400 μ l TBS buffer. Wells were then washed with 2 x 200 μ l 1% w/v SDS followed by 2 x 400 μ l of TBS buffer. Protein addition and washes were repeated before 200 μ l of filler solution, in 10 mM Tris buffer, was added and incubated for 10 minutes. The filler was removed and washed with 2 x 400 μ l TBS before followed by 2 x 200 μ l 1% w/v SDS and final wash of 2 x 400 μ l TBS buffer. 200 μ l of the diluted Alexa Fluor 488 conjugated antibody was added and incubated for 10 minutes before removal and washing with 3 x 400 μ l TBS-tween buffer.

Fluorescence Microscopy

Microscopy was carried out with a Nikon T1 microscope using a 488 nm filter, 6 random fields of view were taken for each well and saved as 16 bit grey scale tagged image files. The resulting TIF images were analysed using the ImageJ program, due to the large size of the camera sensor in relation to the column of light from the illuminator the images suffered from a dark area around their edges, known as a vignette effect. To

counteract this the centre of each image was cropped using the same size square. The mean pixel intensity of each image was then calculated using the measurement tool within ImageJ.

2.19 Capillary Functionalisation

Borosilicate glass capillaries (Hirschmann Laborgeräte GmbH, Germany) were washed several times with ethanol before use. A 0.5% AAPTMS solution was prepared as in Section 2.2.2, 100 μ l was drawn into the capillary and incubated for 30 minutes. The capillary was rinsed with ethanol and immersed in a beaker of ethanol before sonicating twice with an XB2 ultrasonic bath (Grant Instruments, UK) for 1 minute. The capillary was then rinsed with nanopure water before drawing up 100 μ l of 5 OD_{525nm} 20 nm gold nanoparticle solution and incubating for 30 minutes. The AuNP solution was removed and the capillary sonicated twice for 1 minute in a beaker of nanopure water.

Protein Assembly

Protein and filler solutions were prepared as in 2.18. Protein assembly was carried out *in situ* in the Cary 4E using a syringe connected to the capillary by a section of rubber hose. 1 ml of 1% v/v β -mercaptoethanol was injected and incubated for 5 minutes before washing with 2 ml of TBS buffer. 1 ml of protein solution was then injected and incubated for 15 minutes before washing with 2 ml of TBS buffer. 1 ml of filler solution was then injected through the capillary and incubated for 15 minutes followed by washing with 2 ml of TBS buffer followed by 1 ml of 1% w/v SDS and finally rinsed with 2 ml of nanopure water.

Protein Binding

The 6 mg/ml recombinant influenza A nucleoprotein (Orla Protein Technologies, UK) stock was diluted 1 in 100 in water, 1 ml was injected in to the capillary and incubated for 5 minutes before taking a measurement.

Data Collection

Spectra were acquired by the Cary 4E spectrophotometer, the sample stage was modified to allow a single capillary to stand in the beam. A baseline correction was carried out with a glass capillary filled with nanopure water. Each sample measurement was carried out 4 times and averaged to give the final spectrum.

2.20 Lateral Flow Assay

Buffers used:

Antibody binding buffer:

- 10 mM sodium carbonate pH 9.5

PBS:

- 50 mM sodium phosphate pH 7.4
- 150 mM Sodium chloride

Blocking Buffer:

- 50 mM sodium phosphate pH 7.4
- 150 mM sodium chloride
- 2% w/v bovine serum albumen

TBS-Tween:

- 50 mM Tris HCl pH 7.8
- 150 mM sodium chloride
- 0.05% Tween 20

Flow Strip Preparation

Nitrocellulose membrane was cut into a 4 cm x 30 cm strip before use. Antibody was diluted to 0.5 mg/ml in antibody binding buffer and 70 μ l loaded in a P200 tip, this was then inserted in a P2 tip to form a “fountain pen”, which restricts the fluid flow to give a thin antibody line. The pipette was removed and the pen tapped until the solution reached the bottom of the tip. An antibody line was then drawn across the membrane using a ruler and the areas with a tight single line were marked. A second line was then added using the same technique approximately 10 mm below the first. The membrane was blocked overnight in blocking buffer at 4°C. After overnight blocking the membrane was washed with PBS and dried before cutting into 4 cm x 0.5 cm strips.

Running Samples

7.5 μ l of AuNP-protein conjugate at 10 OD_{525nm} concentration was mixed with 7.5 μ l of FluA NP solution and incubated for 5 minutes before adding to the end of a nitrocellulose strip. A piece of paper towel was held on the other end to act as a sink

pad, once the AuNP solution had migrated to the end, the strip was washed 5 times with 20 μ l aliquots of TBS-tween.

3 CHARACTERISING GOLD-GLASS SURFACES WITH SELF-ASSEMBLED PROTEIN MONOLAYERS

3.1 Introduction

Gold has seen widespread use for biomolecule attachment to surfaces. This is due, in part, to the large number of chemical linkers available (Jonkheijm et al., 2008) and the ease in which new chemistries, for example N-Hydroxysuccinimide or primary amine groups, can be introduced on the surface via self-assembly of thiol molecules (Bain et al., 1989; Love et al., 2005). Protein assembly on gold can also be achieved by direct binding to the surface through the addition of cysteine residues in to the protein structure (Brun et al., 2008; Cisneros et al., 2006; Shah et al., 2007).

Traditionally the manufacture of well-defined thin planar gold coatings for such applications requires the use of sputtering equipment (Kelly and Arnell, 2000), which can be expensive and requires specialist training. More recently gold nanoparticles have been used to coat glass surfaces for biomolecule attachment with possible applications in biosensing (Kumari and Moirangthem, 2016; Nath and Chilkoti, 2004). To generate these surfaces, first the glass is functionalised with a silane linker molecule, usually terminated in a primary amine, before deposition of the gold nanoparticles from solution (Figure 3.1). Particle attachment is primarily mediated by charge interactions between the positively charged, protonated amine and the negatively charged anions on the nanoparticle surface. Mixed monolayers of primary amine and sulphhydryl groups have been used for AuNP deposition which can also facilitate covalent bonds between the sulphur and gold (Haddada et al., 2016). Manufacture is relatively straightforward and can be done on the bench. Although the topology of nanoparticle assemblies on glass and other surfaces has been studied (George et al., 2008; Grabar et al., 1997; Kumari and Moirangthem, 2016; Nath and Chilkoti, 2002; Seitz et al., 2003) the structure of associated protein layers on the nanoparticle is poorly understood. Understanding and controlling the structure and orientation of assembled protein layers can be of high importance, particularly for biosensing applications (Kausaite-Minkstimiene et al., 2010; Puertas et al., 2010).

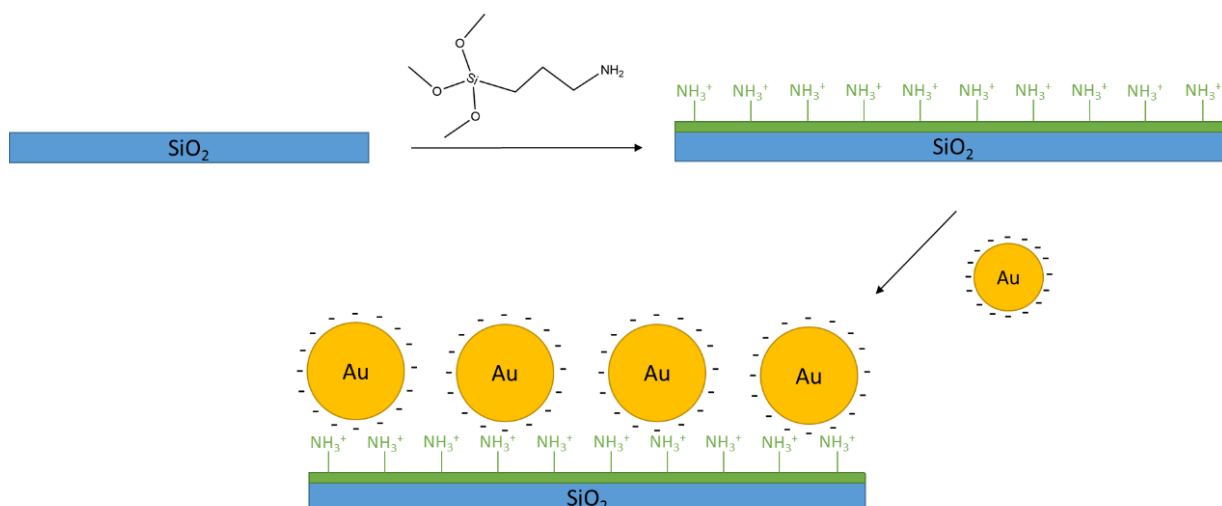


Figure 3.1 Gold nanoparticle assembly on amine functionalised glass surfaces. First the glass surface is functionalised with an amine terminated silane molecule, via a condensation reaction. The AuNPs are then deposited from solution with binding mediated by charge-charge interactions between the positively charged surface and negatively charged AuNPs

The industrial CASE (collaborative award in science and engineering) partner of this project, Orla Protein Technologies, in conjunction with Nippon Sheet Glass have developed an improved method for depositing gold nanoparticles on borosilicate glass and assembling functional protein layers on the nanoparticle surface. Usually silane surfaces are deposited in anhydrous toluene followed by a high temperature curing step (Argekar et al., 2013; Seitz et al., 2003; Vandenberg et al., 1991), with some studies also carrying out high temperature annealing of the nanoparticle surface (Kumari and Moirangthem, 2016). In comparison, all steps in our method use simple equipment, in aqueous solvents at room temperature. This study was concerned with understanding the nanoscale structure of the nanoparticle surfaces and the assembled protein arrays.

To create a detailed picture of the surface layers each component was characterised and its effect on the nanoscale topology investigated using several techniques. Initially the effect of the silane layer on nanoparticle assembly was investigated. The silane molecule used in the Orla-Nippon method, (Aminoethylaminomethyl) phenethyltrimethoxysilane (AAPTMS) (B Figure 3.2), is an unusual linker, therefore, comparisons were made with a more conventional silane molecule, (3-Aminopropyl)trimethoxysilane (APS) (A Figure 3.2). Further to the comparison of the silane molecule, the effect of nanoparticle size and concentration were investigated in

relation to surface coverage. Finally, neutron reflectometry was employed to elucidate the structure of assembled protein arrays on deposited nanoparticles.

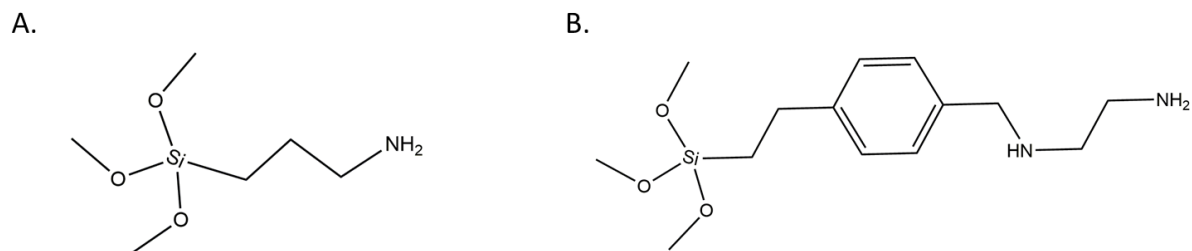


Figure 3.2 Structures of (3-Aminopropyl)trimethoxysilane (A) and (Aminoethylaminomethyl)phenethyltrimethoxysilane (B).

3.2 Results

3.2.1 Nanoparticle Synthesis

Gold nanoparticles were synthesised using a modified Brust-Schiffrin method (Brust et al., 1994). This method uses sodium borohydride to reduce chloroaurate ions (AuCl_4^-) in the presence of a thiol capping ligand and has been shown to generate small (<10 nm) well-defined nanoparticles. The polydispersity and size of the nanoparticles are acutely dependent on the temperature of the reaction mixture during synthesis. Both the synthesised and commercially purchased nanoparticles were assessed by UV-Vis spectroscopy and TEM. The synthesised particles were found to have high polydispersity and be non-uniform in shape, whereas the commercially purchased particles had a low polydispersity and more uniform shape (Figure 3.3 b). It was therefore decided to continue the project with the commercially purchased nanoparticles.

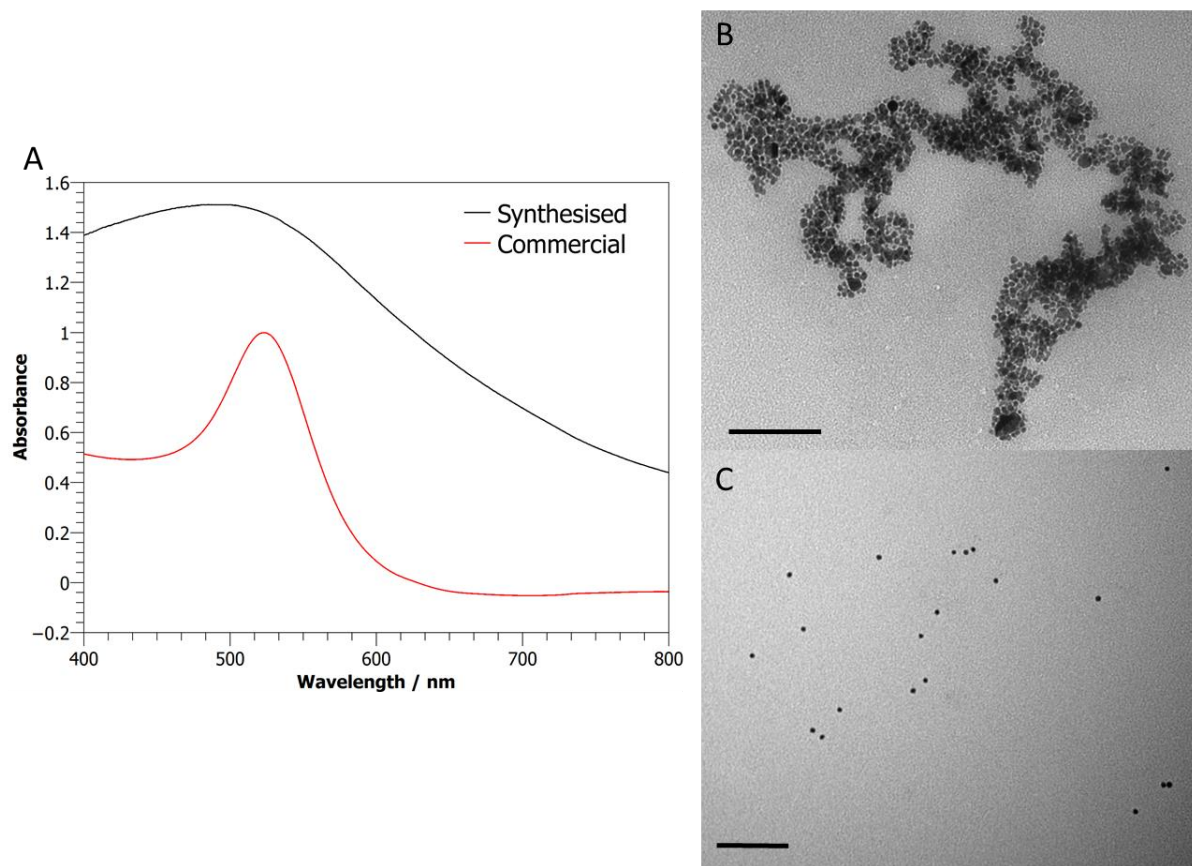


Figure 3.3. UV-Vis spectra (A) and representative micrographs of synthesised (B) and 10 nm commercial (C) nanoparticles (BBI Solutions). 100 nm scale bars.

3.2.2 Surface Functionalisation

X-Ray Photoelectron Spectroscopy (XPS)

XPS was used to analyse the elemental composition of borosilicate glass coverslip surfaces at each step of the functionalisation process (Figure 3.1). The different components are detected by interrogating the surface with a beam of X-rays. The energy of the electrons emitted from the surface can be used to identify the constituent elements and their electronic environment (see Section 1.6.1 for a more detailed discussion). Characteristic peaks corresponding to the nitrogen from the organosilane primary amine and the metallic gold of the nanoparticles were observed in the survey spectra after each deposition, thus confirming the addition of each component of the system on the surface (Figure 3.4).

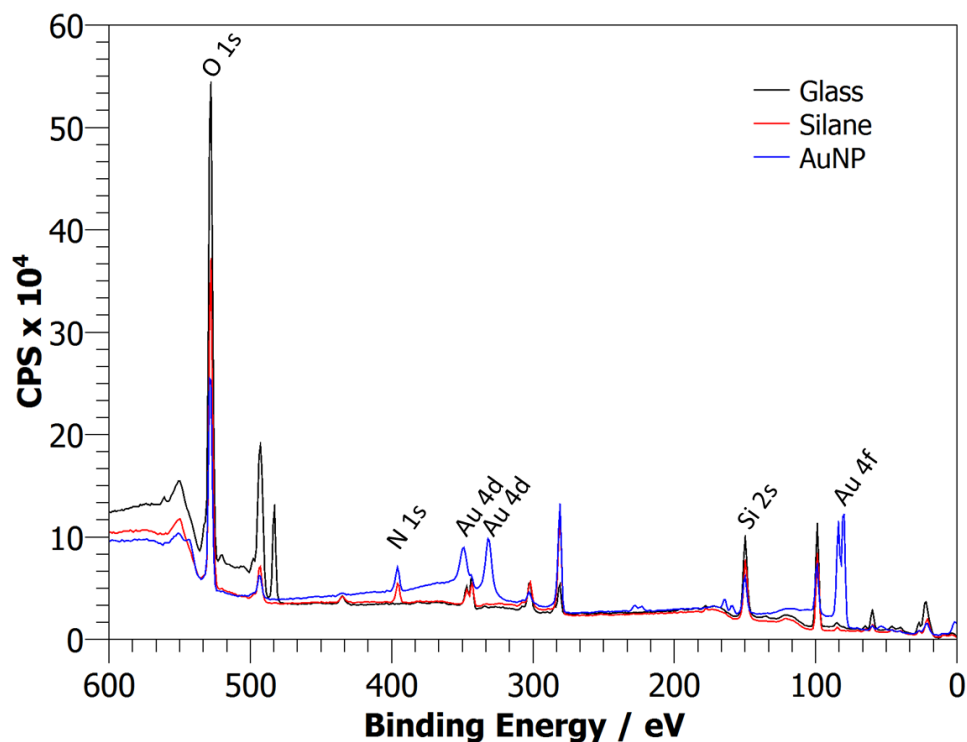


Figure 3.4. XPS Survey spectra of borosilicate glass coverslips after silanisation and subsequent gold deposition. The samples were surveyed over a large surface area, 300 x 700 μm . The binding energies of the detected electrons were calculated and assigned to their respective elements and molecular orbitals. The relative abundance of each element is correlated to the height of the peak (in electron counts per second). A clear peak corresponding to nitrogen 1s electrons appears after the silanisation process (red line) followed by multiple gold 4d and 4f peaks after gold deposition (blue line).

3.2.3 Silane Monolayer Formation

The quality of silane monolayers when using two different silane molecules (Table 2.1) was assessed. APS is a commonly used molecule to add primary amine groups to glass surfaces for biomolecule and nanoparticle assembly (Grabar et al., 1995; Thakurta and Subramanian, 2012). AAPTMS on the other hand is a much less commonly used, with very few studies in the literature, but was patented for generating biomolecule retaining materials by Corning Glass Inc (Lewis, 2006).

Amine Density of APS and AAPTMS Monolayers

A colorimetric Coomassie assay, modified from Coussot (Coussot et al., 2010), was used to estimate the amine density of APS and AAPTMS films deposited on polished silicon wafer chips with increasing incubation time. The silane molecule binds to the native oxide layer that forms on silicon substrates after exposure to air (Raider et al.,

1975). Coomassie dye binds in a 1:1 ratio with primary amines, therefore the average amine density was calculated by measuring the bound dye concentration. AAPTMS appeared to assemble faster reaching a higher amine density at 10 minutes, however, at the 30 and 60 minute time points the difference between the two aminosilanes became much less pronounced (Figure 3.5).

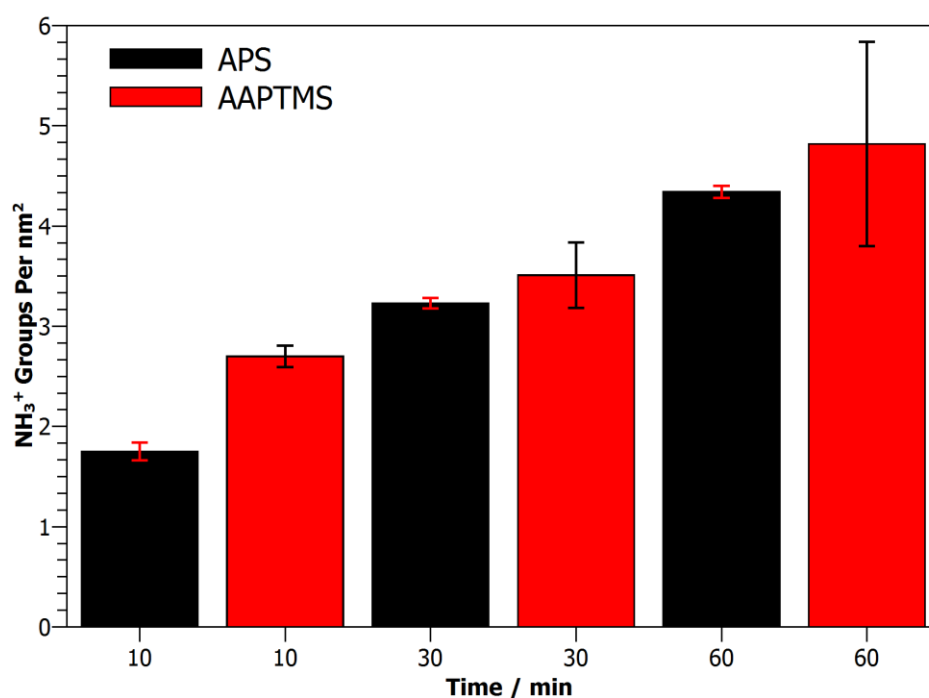


Figure 3.5. Comparison of the primary amine density of APS and AAPTMS films on silicon wafers with increasing incubation time. Primary amine density calculated using the colorimetric Coomassie assay by dividing the number of bound Coomassie molecules by the surface area of the functionalised silicon wafer chip. Error bars represent the standard error of the mean based upon 3 samples.

APS and AAPTMS Monolayer Roughness

The roughness of APS and AAPTMS monolayers on silicon wafer chips was investigated by atomic force microscopy in comparison to a blank wafer surface. The blank silicon surface was extremely flat and almost completely featureless. The addition of AAPTMS on the surface had very little effect on the surface roughness with only a few features of around 3-4 nm in height. APS deposition led to large island like features, with heights up to 50 nm, indicative of complex multilayer structures being formed (Figure 3.6).

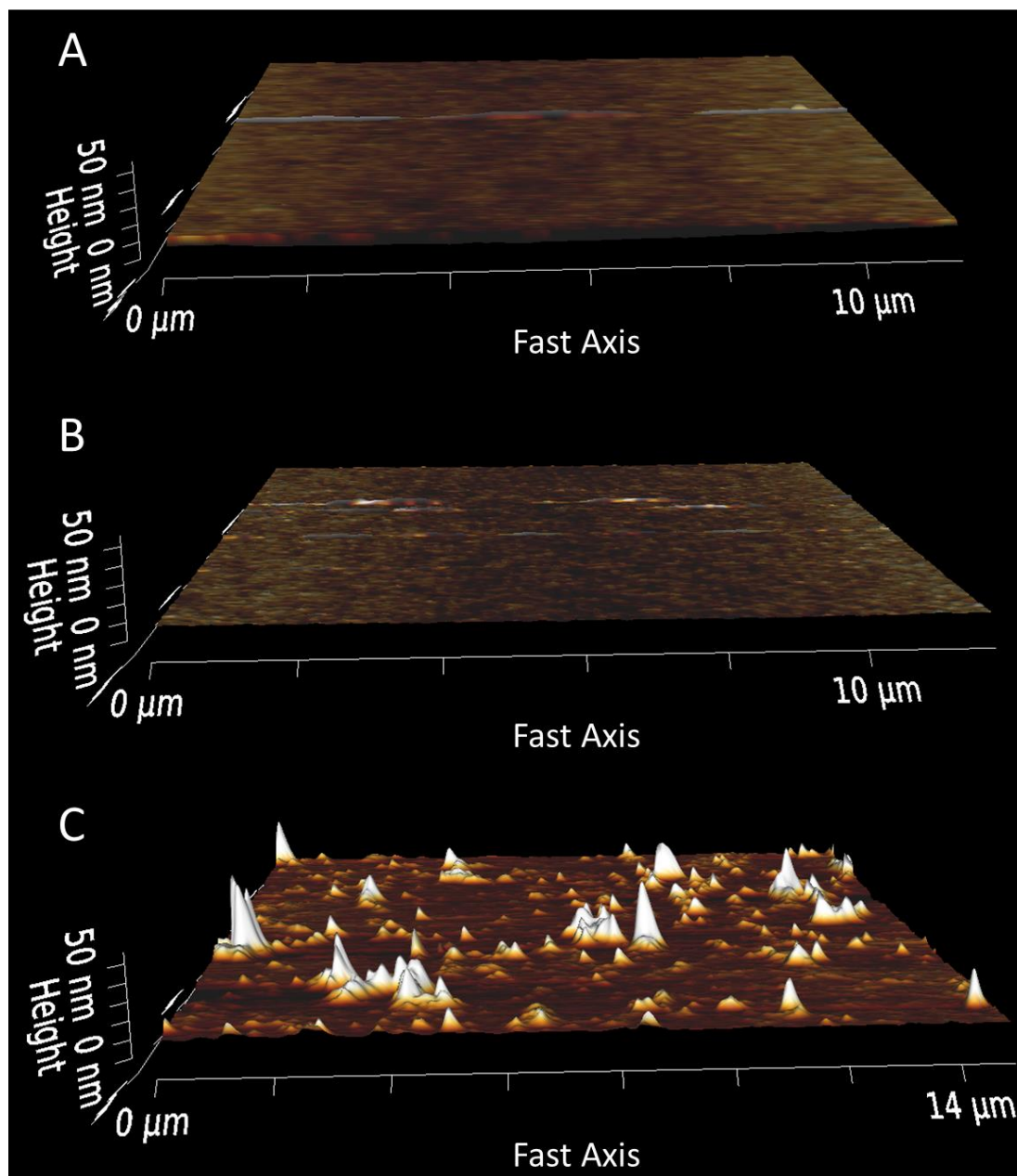


Figure 3.6 Representative AFM images of silicon blank (A), AAPTMS (B) and APS (C) functionalised surfaces. Each of the silane functionalised surfaces were incubated for 60 minutes in a 0.5% v/v silane solution (95:5 EtOH:H₂O) before imaging. Images were acquired in tapping mode with the fast axis indicating the direction of the probe along the surface.

3.2.4 Gold Nanoparticle Deposition

Amine Availability after Gold Deposition

The availability of amine groups on AAPTMS functionalised silicon wafer chips after multiple gold deposition steps was measured using the colorimetric Coomassie assay. A large decrease in the available amine groups was observed after the first nanoparticle deposition, indicating that binding is mediated through the terminal amine of the silane

monolayer. Successive depositions lowered the number of available amine groups further (Figure 3.7). As expected some remain available as the gold nanoparticles are unable to form a packed monolayer due to electrostatic repulsion (Grabar et al., 1997).

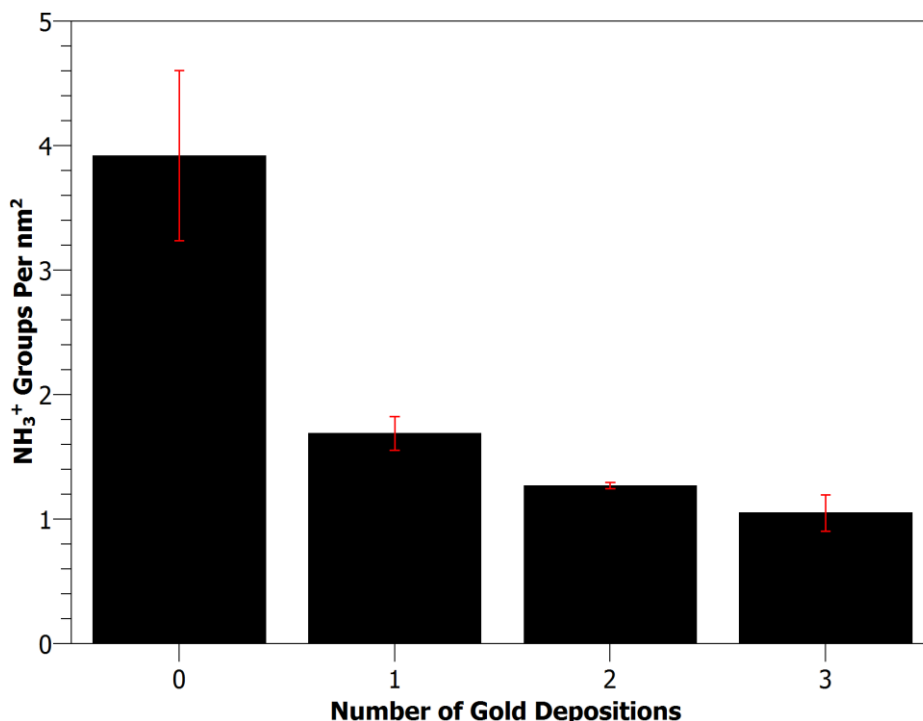


Figure 3.7. Amine availability of AAPTMS monolayer after multiple gold nanoparticle depositions. Determined by colorimetric Coomassie assay on silicon wafer segments. Each gold deposition was carried out for 10 minutes with 10 nm gold nanoparticles at 0.3 OD_{525nm}. Error bars represent the standard error of the mean based upon 3 samples.

Nanoparticle Coverage

Effect of aminosilane layer on coverage

The effect of AAPTMS on the nanoparticle coverage was investigated in comparison to blank silicon wafers and APS functionalised wafer chips using SEM. Gold nanoparticle deposition on AAPTMS functionalised wafers gave uniform sub-monolayer coverage across the sample surface (A Figure 3.8). In comparison, unfunctionalised wafers showed large areas of bare surface (B Figure 3.8). Nanoparticle deposition on APS wafers was concentrated into large island like structures (C Figure 3.8).

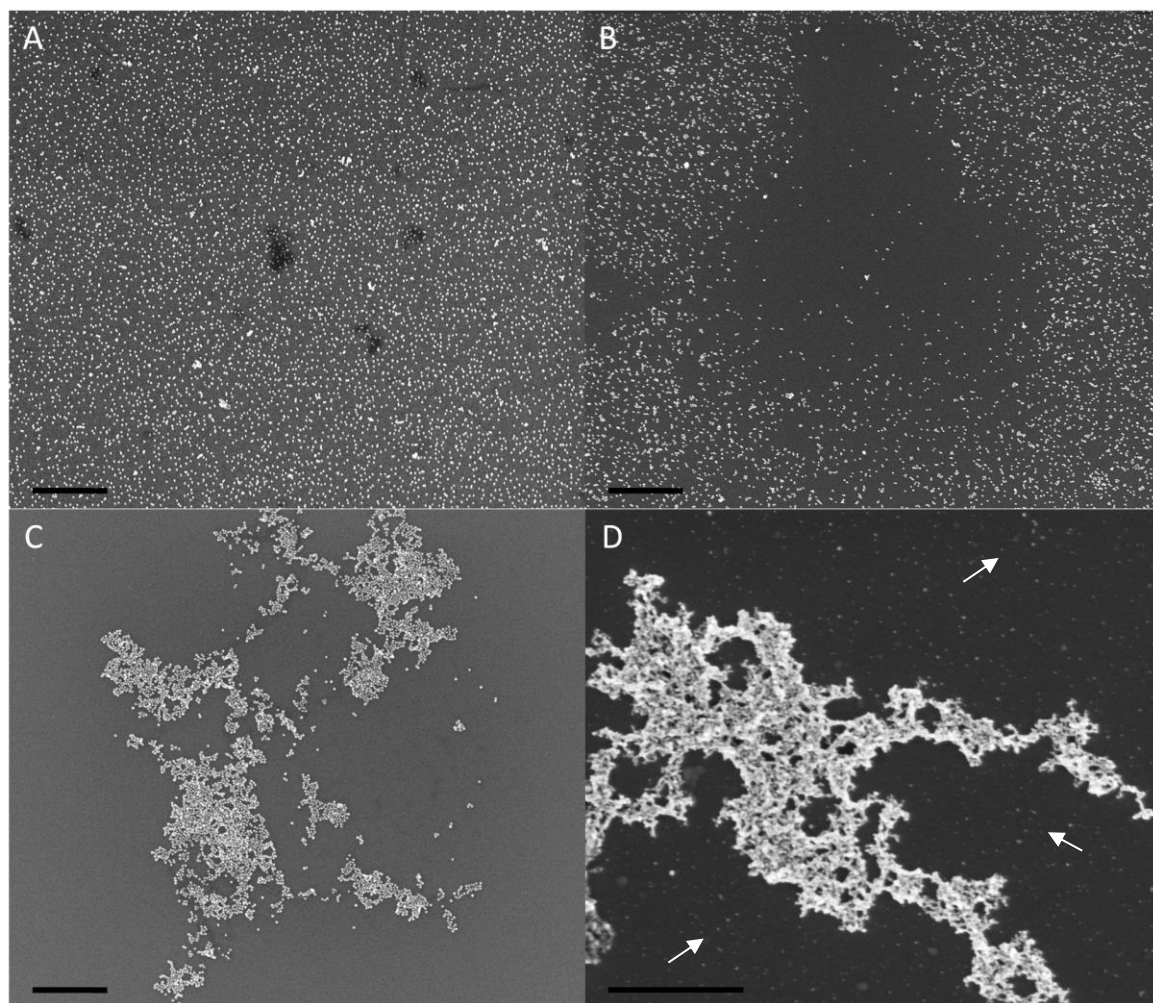


Figure 3.8. Representative micrographs of AuNP functionalised surfaces. From the top left AAPTMS and commercial AuNPs (A), commercial AuNPs (B), APS and commercial AuNPs (C) and AAPTMS with in house synthesised AuNPs (D). The white arrows in the synthesised particle image indicate areas away from the aggregates of more uniform coverage of smaller particles. The contrast of the images has been increased to aid visualisation, 500 nm scale bars.

Synthesised gold nanoparticles

In house synthesised gold nanoparticles were deposited on to AAPTMS functionalised silicon wafer chips and imaged by SEM. Large agglomerate structures, comparable to those seen by TEM (Figure 3.3), were visible with a background of more uniformly spaced smaller particles on the surface (D Figure 3.8).

Nanoparticle size

10 and 20 nm commercial gold particles were deposited on AAPTMS functionalised silicon wafer chips and imaged using SEM. The percentage area coverage on the surface was calculated using ImageJ (Section 2.8) on duplicate samples. The 20 nm particles

showed a significantly higher coverage than the 10 nm particles with values of $36.65 \pm 1.67\%$ and $13.13 \pm 0.76\%$ respectively (A Figure 3.9).

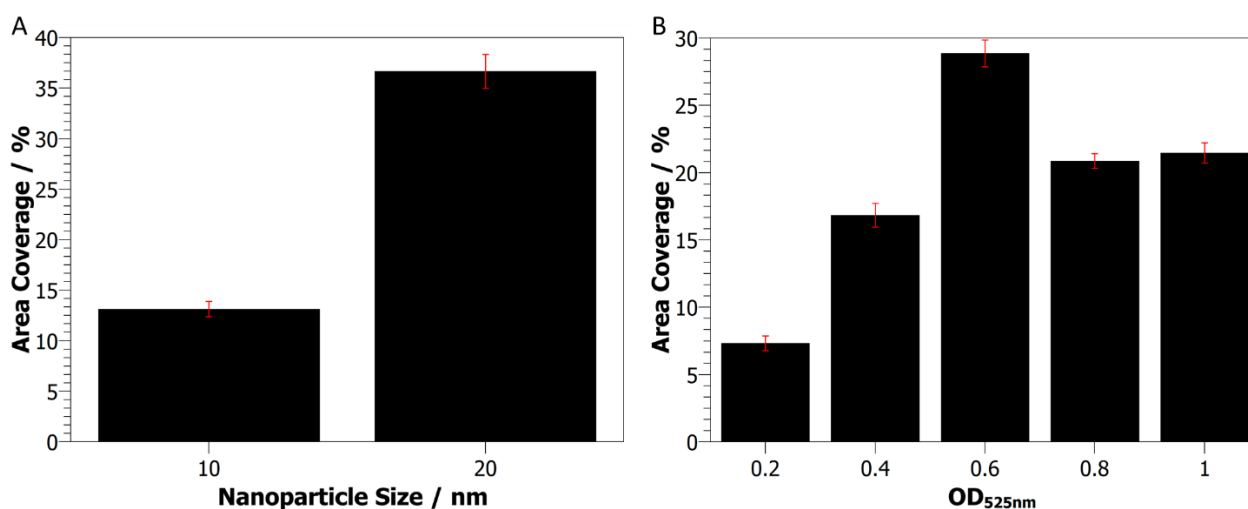


Figure 3.9. Gold nanoparticle coverage of AAPTMS functionalised silicon wafer chips. Comparison of 10 and 20 nm sized commercial particles (A) and increasing OD_{525nm} of 20 nm particles (B). Coverages were calculated from three representative images of between 4 and 8 μm^2 , using ImageJ.

Concentration dependence

20 nm gold nanoparticles were deposited on AAPTMS functionalised silicon wafer chips with optical densities between 0.2 and 1 at 525 nm and imaged using SEM. The percentage area coverage was calculated using ImageJ on triplicate samples. Between 0.2 and 0.6 OD_{525nm} there is a clear trend of increasing coverage, above this concentration the coverage plateaued with a reduction in the area coverage observed between 0.6 and 0.8 (B Figure 3.9).

Thiol Assembly

As the gold nanoparticle surfaces will be incubated with thiol molecules during the assembly of the protein surface (discussed in further detail in section 3.2.5), the effect of self-assembled thiol monolayers on the coverage and morphology of deposited AuNPs was visualised by SEM. 10 nm particles deposited on AAPTMS functionalised silicon wafer chips were incubated with 1% β ME and 100 μM SH-C11-OEG3 (thioAlkylPEG) solutions respectively for 15 minutes before visualisation. ThioAlkylPEG was used as the filler molecule when assembling proteins on the particle surface (Figure 3.12). Deposition of the 10 nm AuNP resulted in even fields of particles across the sample. Morphological changes were observed for the β ME sample with islands of closely

located particles formed. The overall nanoparticle coverage remained the same as the 10 nm particle sample suggesting that few particles detached from the surface. No change in the morphology of the thioAlkyPEG coated particles was observed however there was a 3.6 fold loss in the nanoparticle coverage.

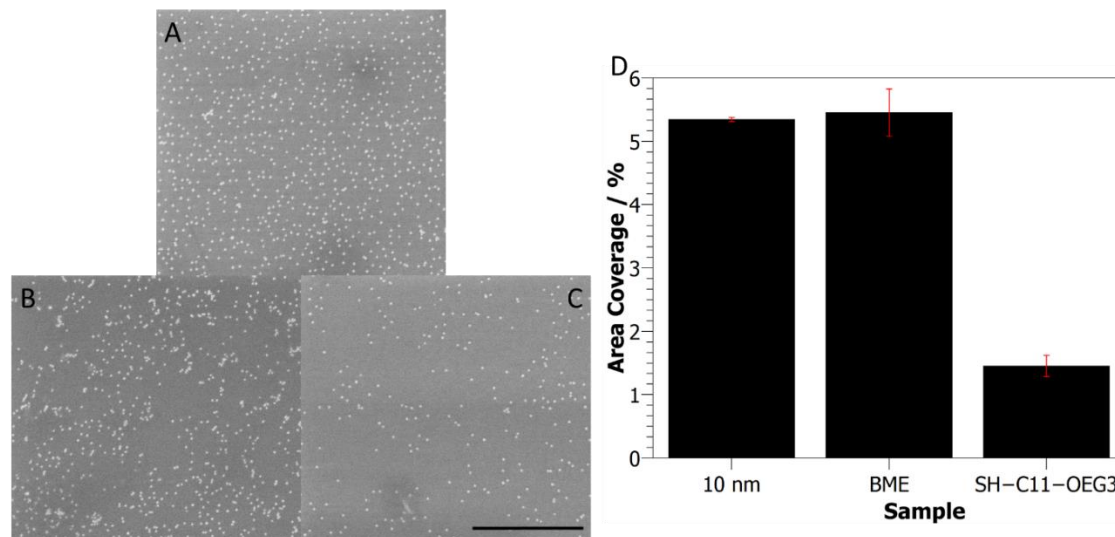


Figure 3.10 Effect of thiol assembly on gold nanoparticle coverage and morphology. Representative SEM images of deposited 10 nm particles before (A) and after incubation with BME (B) and SH-C11-OEG3 (C). Coverages were calculated from three representative images of between 4 and 8 μm^2 , using ImageJ (D). The contrast and brightness of the shown images (A, B, C) was increased to aid visualisation but was not applied during quantitative analysis. 500 nm scale bar. Error bars represent the standard error of the mean based upon 3 fields of view.

3.2.5 Neutron Reflectometry

Gold nanoparticle deposition and subsequent protein assembly was followed by neutron reflectometry (NR). Experiments were carried out on a 50 mm \times 80 mm \times 30 mm single crystal silicon block with a single face polished to ~ 3 Å roughness average (Ra), which was coated with an AAPTMS monolayer, using the method described in Section 2.2.2, before nanoparticle deposition. Three solvent contrasts were used when carrying out NR measurements of the deposited gold nanoparticles, H₂O, silicon matched water (SMW, 38% D₂O, 62% H₂O) and D₂O. A fourth contrast, gold matched water (AuMW, 73% D₂O, 27% H₂O), was also used for measurements of protein coated particles. The ratios of H₂O and D₂O for the contrast solutions were calculated from the scaled sum of the H₂O and D₂O SLDs that matched the theoretical SLD of silicon and gold respectively. A table of the theoretical SLD values used in this study is provided below. Two measurement angles, 0.7 and 2.3 degrees, were used to give a Q range of 0.01 to

0.35 Å⁻¹. The block was mounted in a custom made solid/liquid cell, which provides a small sealed chamber that could be filled with solvent through two liquid ports. The cell was then bolted to a sample stage with the polished surface facing downwards. The neutron beam was directed through the silicon block and reflected from the solid/liquid interface (Figure 3.11). A computer controlled HPLC pump automatically changed the contrast buffer between measurements, which were all carried out on the INTER beamline at the ISIS neutron and muon source (Oxford, UK).

Table 3.1 Theoretical SLD values used for calculating the contrast match solutions and as starting points for the data fitting. Obtained using the National Institute of Standards and Technology (USA) scattering calculator.

<i>Substance</i>	<i>Theoretical SLD</i> / $\times 10^{-6} \text{ \AA}^{-2}$
<i>H2O</i>	-0.56
<i>D2O</i>	6.38
<i>Silicon</i>	2.07
<i>Silicon Dioxide</i>	4.19
<i>AAPTMS</i>	0.97
<i>Gold</i>	4.62
<i>GGzOmpATM</i>	1.99
<i>ThioAlkylPEG</i>	0.93

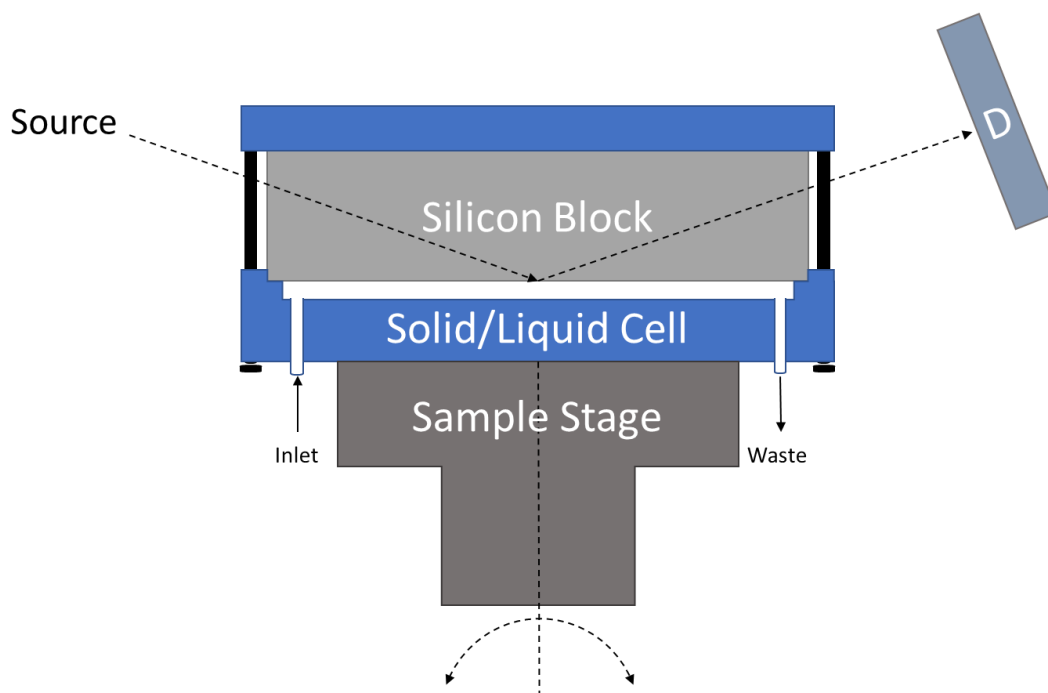


Figure 3.11 Neutron reflectometry set up. The solid/liquid cell was mounted on to a sample stage that tilted with respect to the incoming neutron beam to set the measurement angle. A computer controlled HPLC pump was attached to the liquid cell inlet to change the contrast solvent. The neutrons were directed through the silicon block and reflected towards the detector (D) from the sample surface, at the solid/liquid interface.

Assembly of Engineered OmpA_{TM}

Protein assembly was carried out *in situ* using the same method as previous NR experiments on planar gold surfaces (Brun et al., 2008, 2015; Le Brun et al., 2011). The protein used, GGzOmpA_{TM}, consists of a circularly permuted OmpA_{TM} domain with 3 additional domains, a Z-domain from protein A and tandem B-domains from protein G, fused to the N-terminus (Brun et al., 2015). A thioAlkylPEG filler molecule, (11-mercaptoundecyl)hexa(ethylene glycol), was used to backfill the surface after protein addition. Addition of the filler helps stabilise the protein layer and direct the orientation of the OmpA_{TM} domain. The structure of this protein array has previously been determined on planar gold surfaces by neutron reflectometry (Brun et al., 2015) (Figure 3.12).

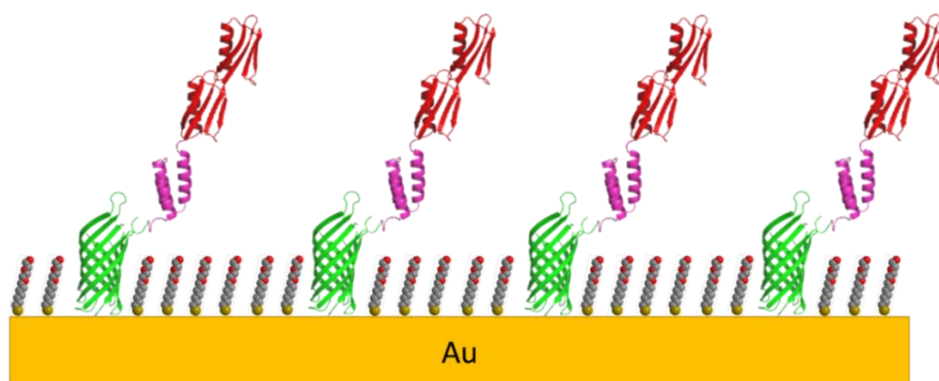


Figure 3.12 Structure of GGzOmpA_{TM} arrays on planar gold surfaces adapted from (Brun et al., 2015). The OmpA_{TM} domain is embedded in a dense thioAlkylPEG layer with the protein A and protein G domains extended away from the surface.

Analysing Neutron Reflectometry Data

Neutron reflectometry data essentially provides information on the neutron refractive index, also known as the scattering length density or SLD, across the z-axis perpendicular to the sample surface. As discussed in Section 1.6.1, the phase information is lost when collecting reflectivity data, therefore, the reflectivity profile cannot be directly converted into a unique SLD profile using a Fourier transform. The most commonly used approach is to construct a plausible model of the matter distribution at the sample surface. The model parameters are then adjusted so that the theoretically calculated reflectivity curve agrees with the measured data. It is important that the initial construction of the model and any fixed parameters are validated by prior characterisation of the system and its components. Analysis of such data requires careful interpretation as many possible solutions will exist that fit the data equally well. To aid data analysis, multiple measurements of the sample are carried out in different solvent contrasts and simultaneously fitted to the same model. Usually, the sample is approximated by dividing into a number of parallel layers (Clifton et al., 2011; Hughes et al., 2008) that are assumed to have uniform density along the z-axis and can have their interfaces broadened by roughness effects, which is known as the Parratt formalism (Parratt, 1954). When analysing a solid/liquid system, such as the one used in this study, the layers are described by four parameters; thickness, SLD, roughness and coverage. The coverage parameter (C_L) allows for defects in the layer which are filled by the solvent. This is accounted for by varying the effective SLD of the layer (SLD_{eff})

using a scaled sum of the layer SLD (SLD_{lay}) and the solvent SLD (SLD_{sol}) (Hughes et al., 2008);

$$SLD_{eff} = \left(\frac{C_l}{100} SLD_{lay}\right) + \left(\left(1 - \frac{C_l}{100}\right) SLD_{sol}\right) \quad [3.1]$$

In this study the reflectivity profiles were analysed by the RasCal program (Clifton et al., 2011) which uses an optical matrix formalism (Born and Wolf, 1970) to fit the layer model to the reflectivity data. Initially the model parameters were populated with approximate starting values and the theoretically calculated reflectivity curve compared against the measured data. The difference between the calculated reflectivity profile and the experimental data was assessed with a Pearson's chi-squared (χ^2) test, where a lower χ^2 value signifies a better fit, and the χ^2 reduced by adjusting the parameters using an iterative least squares minimisation routine. The error in the fitted model parameters was estimated using the "bootstrap" error analysis function within RasCal, which re-samples subsets of the original data and carries out fitting from random starting values. The distribution of parameter values obtained from the fitting of the re-sampled data sets was then used to estimate the fitting errors.

Neutron Reflectometry Data

It is possible to observe the assembly of the gold nanoparticles and protein layer on the substrate by a simple comparison of the reflectivity data after each addition (Figure 3.13). Comparing the reflectivity profiles from each contrast also highlights the need for multiple data sets from different solvent contrasts to build a detailed model. The gold nanoparticles and proteins have quite different SLDs, 4.62×10^{-6} and $1.993 \times 10^{-6} \text{ \AA}^{-2}$ respectively, so are more/less visible in opposing solvents. In H_2O ($-0.56 \times 10^{-6} \text{ \AA}^{-2}$) both the addition of the gold and the protein is visible from changes in the reflectivity, however, the greater difference between the AuNP and H_2O SLDs causes a more drastic change in the reflectivity profile (A1+2 Figure 3.13). In SMW ($2.07 \times 10^{-6} \text{ \AA}^{-2}$) only the addition of the AuNP is visible as the SLD is too close to the protein to provide a significant level of contrast (B1+2 Figure 3.13). In this solvent, the intensity of the reflected neutrons is significantly reduced, with consequently larger error, as the contribution from the silicon block is completely removed. Once again in D_2O ($6.38 \times 10^{-6} \text{ \AA}^{-2}$) addition of the both the AuNPs and protein is visible, with a more visible change in the reflectivity on protein addition as there is a greater difference between the protein and D_2O SLDs (C1+2 Figure 3.13).

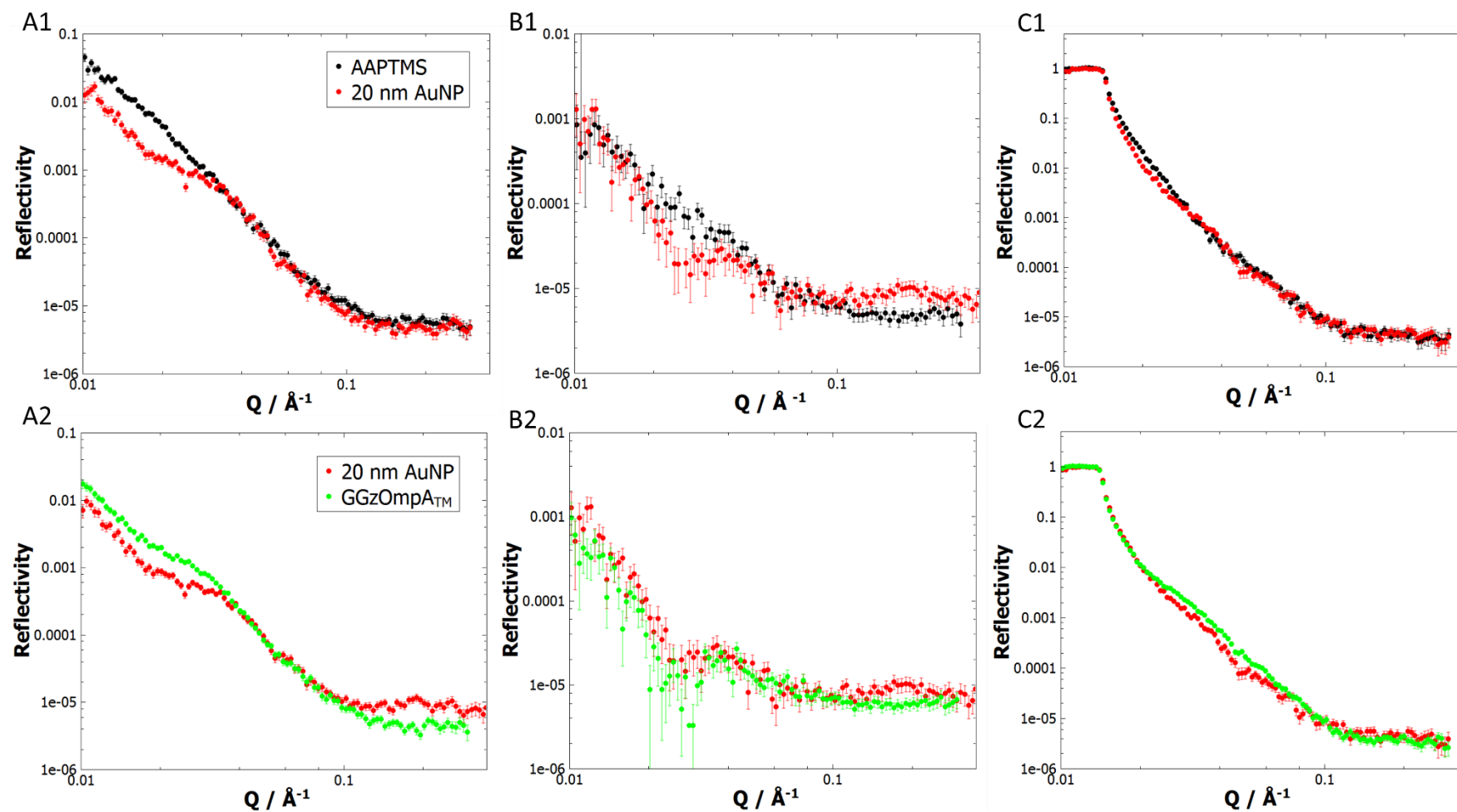


Figure 3.13 Neutron reflectivity profiles comparing AAPTMS vs AuNP surfaces (1) and AuNP vs AuNP + GGzOmpA_{TM} surfaces (2). The letter denotes the solvent contrast with A = H₂O, B = Silicon Matched Water and C = D₂O.

Model Fitting

Qualitative assessment of the reflectivity data allows little analysis on the structure of the surface layers that are formed. Detailed structural analysis requires the data sets to be fit to a model. Two separate models were used to analyse the reflectometry data.

The first was a simple slab model which split the different substrate components into individual layers. The nanoparticles were divided in two with each half comprised of five layers that were mirrored across the midline of the particle (Figure 3.14). The spherical shape was modelled by constraining the gold coverage of the layers so that the coverage of layer $5 \geq 4 \geq 3 \geq 2 \geq 1$. Quite a high level of roughness was allowed between the gold layers to provide a smooth shape. As discussed above roughness is described using the Parratt formalism where the interface between the two layers is able to broaden and become less well defined. This model was made using the minimum number of constraints to give as “real” an interpretation of the data as possible. For the protein assembly a single outside protein layer was added, which was comprised of both the protein and filler molecules, and the SLD of the gold nanoparticle was allowed to vary in proportion to the volume fraction of the protein layer.

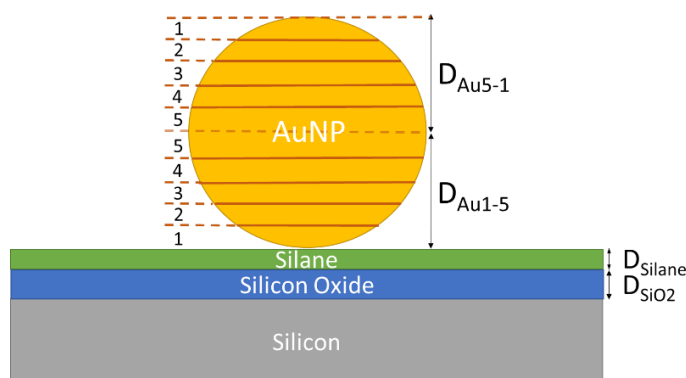


Figure 3.14 Schematic representation of the slab model. The substrate components have individual layers and the nanoparticle is split into two sets of five layers that are mirrored through the centre of the particle.

The simple slab model fitted well to the deposited AuNP surface data, with a χ^2 of 7.89, and the resulting SLD profile clearly described spherical objects on the surface of the substrate (Figure 3.15). This is most visible in the H_2O contrast as a “hump” in the SLD profile between ~ 80 and 260 \AA (B Figure 3.15). The resulting thicknesses of the layers from the model gave reasonable values with a $15.04 \pm 0.12 \text{ \AA}$ SiO_2 layer, $8.57 \pm 2.00 \text{ \AA}$ silane layer and $179.18 \pm 5.66 \text{ \AA}$ gold nanoparticles. The AuNP coverage on the surface, taken from the layer describing the centre of the gold sphere, was $23.01 \pm 6.18\%$.

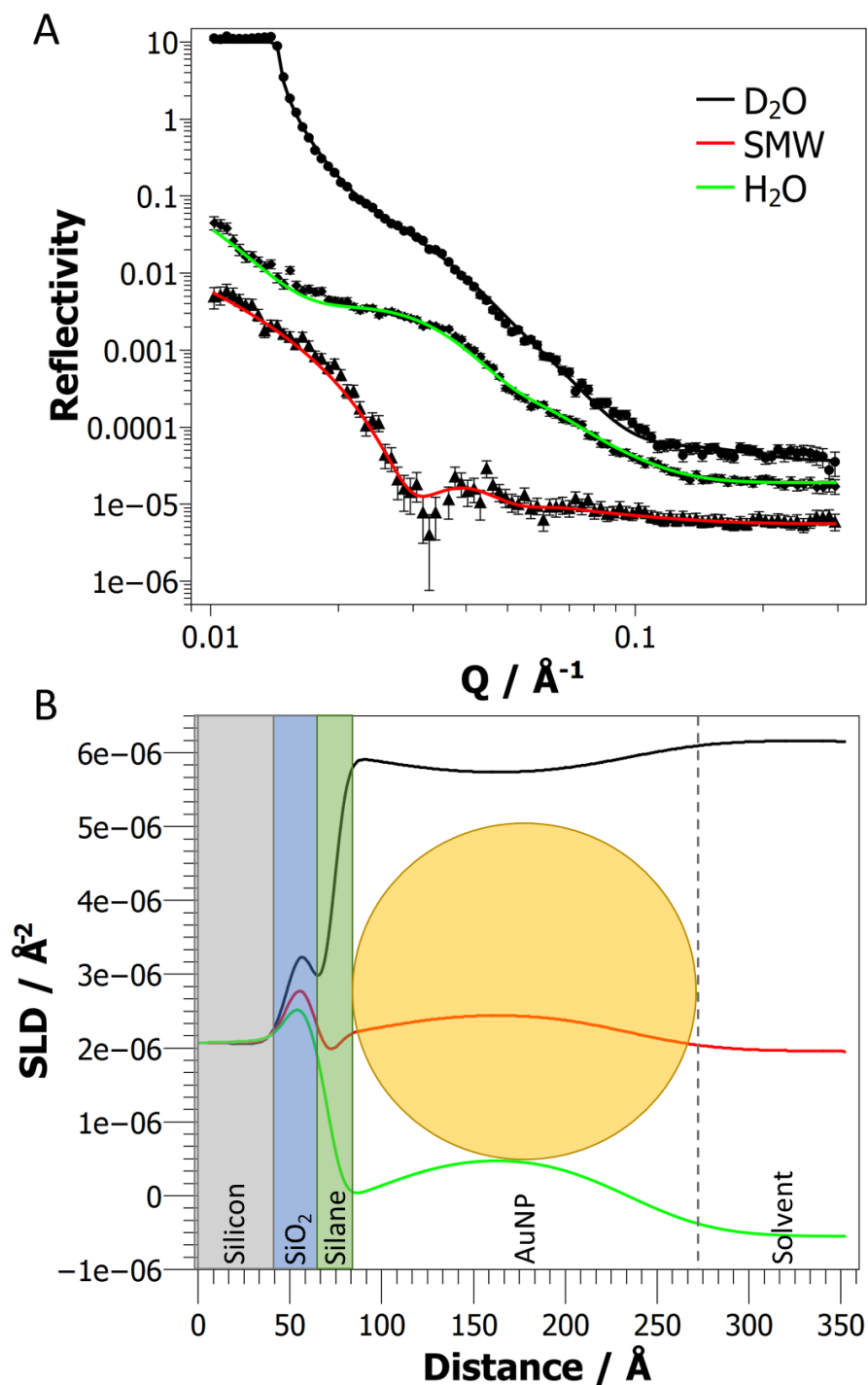


Figure 3.15 Data fitting and corresponding SLD profiles generated using the slab model for the AuNP coated surface. (A) Reflectivity data with the model fits represented as solid lines and the reflectivity profiles offset for clarity. The colours represent the different solvent contrasts, D_2O , SMW and H_2O . (B) The fitted SLD profiles show the change in the SLD as a function of distance away from the substrate surface, in the Z-Axis. A schematic representation of the surface is overlaid on the SLD profiles to highlight the different regions of the sample.

Fitting of the slab model to the AuNP surface data after protein addition was not as good as the bare AuNP surface, with a χ^2 value of 15.31 compared with 7.89 for the AuNP surface. Deviations of the model fit from the reflectivity data can be seen in the D₂O and AuMW contrasts at higher Q (black and blue solid lines in A Figure 3.16). The thickness values obtained for the silicon oxide and silane layers were comparable with the AuNP data at 14.32 ± 1.27 and 11.91 ± 4.73 Å respectively. However, both the nanoparticle and protein layer thicknesses were much lower than expected, 153.69 ± 14.25 and 30.33 ± 9.56 Å respectively. To fit the data the model also significantly increased the gold roughness, from 35.48 to 65.51 Å, which blurs the edges of the particle making it difficult to resolve the outer protein layer. Blurring of the model was also reflected in the higher error values for all the parameters when compared with AuNP surface. The higher error and increased roughness needed to fit the reflectivity data would suggest that the parameters of this model were not appropriate to describe the protein coated AuNP system. The fitted layer parameters obtained, and their respective error, for the data before and after protein assembly are compared in Table 3.2. The parameter starting values were estimated from the theoretical size of the silane molecule and from previous electron microscopy and neutron reflectometry data. To confirm that the poor fitting of the AuNP and protein layers was not due to a lack of protein assembly on the surface, the data was also analysed using the bare AuNP slab model. This model was unable to fit the AuNP + GGzOmpA_{TM} reflectivity data satisfactorily (Appendix Figure 7.4).

Table 3.2 Layer parameters obtained by fitting the slab model to the reflectivity data before and after protein assembly.

<i>Parameter</i>	<i>AuNP Surface</i>	<i>AuNP + GGzOmpA_{TM}</i>	<i>Starting Value</i>
<i>Silicon Oxide Thickness / Å</i>	15.04 ± 0.12	14.32 ± 1.27	10
<i>Silane Thickness / Å</i>	8.57 ± 2.00	11.91 ± 4.73	11
<i>AuNP Thickness / Å</i>	179.18 ± 5.66	153.69 ± 14.25	200
<i>AuNP Roughness / Å</i>	35.48 ± 10.62	65.51 ± 15.76	20
<i>AuNP Coverage / %</i>	23.01 ± 6.18	23.71 ± 11.70	25
<i>GGzOmpA_{TM} Thickness / Å</i>	N/A	30.33 ± 9.56	100

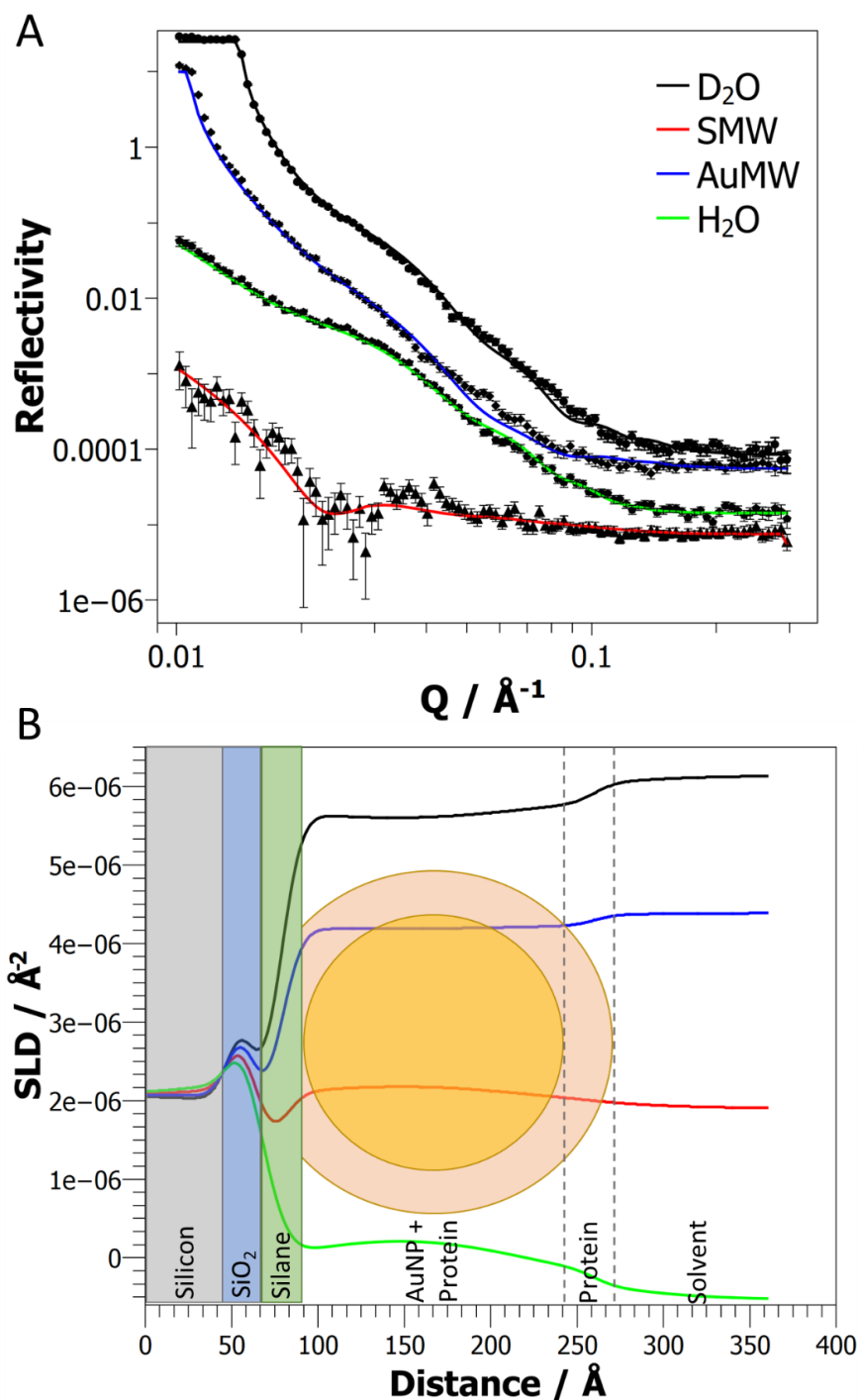


Figure 3.16 Data fitting and corresponding SLD profiles generated using the slab model for the AuNP coated surface after GGzOmpATM assembly. (A) Reflectivity data with the model fits represented as solid lines and reflectivity profiles offset for clarity. The colours represent the different solvent contrasts, D_2O , AuMW, SMW and H_2O . (B) A schematic representation of the surface is overlaid on the fitted SLD profiles to highlight the different regions of the sample. The orange layer around the nanoparticle represents the fitted protein and filler layer.

Sphere Model

The second model, known as the sphere model, separated the surface into a set of packed cubes that sit on the silane layer. Each cube contained an AuNP, comprised of 200 gold layers, and formed a fractional coverage on the surface. The protein coating was split into two layers, the inner layer contained both the thioAlkylPEG filler and protein and the outer layer contained only the protein. This double layer was allowed to form a fractional coverage on the particle surface apart from the interface between the particle and the surface (Figure 3.17). The sphere model was adapted from work done by Rebecca Welbourn in her PhD thesis (Welbourn, 2016). When using this model the data sets for the AuNP surface before and after protein assembly were fitted simultaneously.

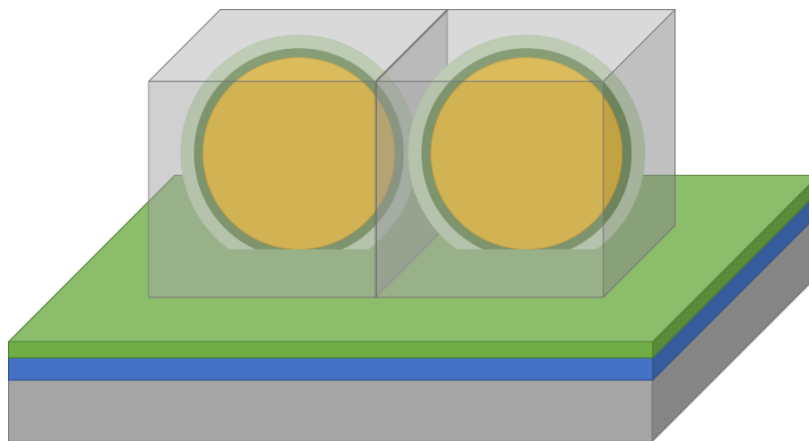


Figure 3.17 Schematic representation of the sphere model. The nanoparticles are modelled inside a set of packed cubes on the surface. The protein coating is split into a double layer that covers the nanoparticle except at the interface with the silane layer.

The fitting of the more complex sphere model to the reflectivity data was not as good as the simple slab model, with deviations from the data most significant in the D2O and AuMW contrasts (black and blue solid lines in A + B Figure 3.18) and a χ^2 value of 65.24 compared with 7.89 and 15.31 for the slab model before and after protein assembly. However, a higher χ^2 would be expected for the sphere model as a greater number of the model parameters were constrained and twice the number of data sets were fitted simultaneously. The layer thicknesses obtained were reasonable and the silicon oxide, silane and AuNP values (15.06 ± 0.15 , 8.01 ± 1.02 and 183.69 ± 4.82 Å respectively) were in good agreement with the slab model of the AuNP surface. Once again, the AuNP shape can be seen clearly in the fitted SLD profile as a “hump” between ~ 95 and 275 Å (solid lines in C Figure 3.18). After protein addition the protein

layer on the nanoparticle can be seen as a pronounced extension of the particle “hump” in the fitted SLD profile (dashed lines in C Figure 3.18). The reduction in the AuNP SLD after protein addition is due to both a loss in the total AuNP coverage, from $38.90 \pm 0.78\%$ to $21.44 \pm 1.76\%$, and also the contribution of the protein and filler on the surface which have lower SLDs than gold (1.993 and $0.216 \times 10^{-6} \text{ \AA}^{-2}$ respectively). The dual protein layer described a densely packed first layer that covered $99.10 \pm 1.59\%$ of the particle surface and a more diffuse second layer that had a coverage of $15.62 \pm 6.24\%$. The thicknesses of the respective layers were 22.94 ± 2.93 and $75.09 \pm 0.18 \text{ \AA}$ which gave a combined protein layer thickness of 98.02 \AA . The layer parameters obtained from the sphere model after fitting are summarised in Table 3.3. Once again the starting parameters were estimated from theoretical length of the silane molecule and previous electron microscopy and neutron reflectometry data.

Table 3.3 Layer parameters obtained by fitting the sphere model to the reflectivity data

<i>Parameter</i>	<i>Fitted Value</i>	<i>Starting Value</i>
<i>Silicon Oxide Thickness / \AA</i>	15.06 ± 0.15	10
<i>Silane Thickness / \AA</i>	8.01 ± 1.02	11
<i>AuNP Thickness / \AA</i>	183.69 ± 4.82	200
<i>AuNP Coverage (without protein) / %</i>	38.90 ± 0.78	25
<i>AuNP Coverage (with protein) / %</i>	21.44 ± 1.76	25
<i>Inner Protein Layer Thickness / \AA</i>	22.94 ± 2.93	30
<i>Inner Protein Layer Coverage / %</i>	99.10 ± 1.59	90
<i>Outer Protein Layer Thickness / \AA</i>	75.09 ± 0.18	100
<i>Outer Protein Layer Coverage / %</i>	15.62 ± 6.24	25

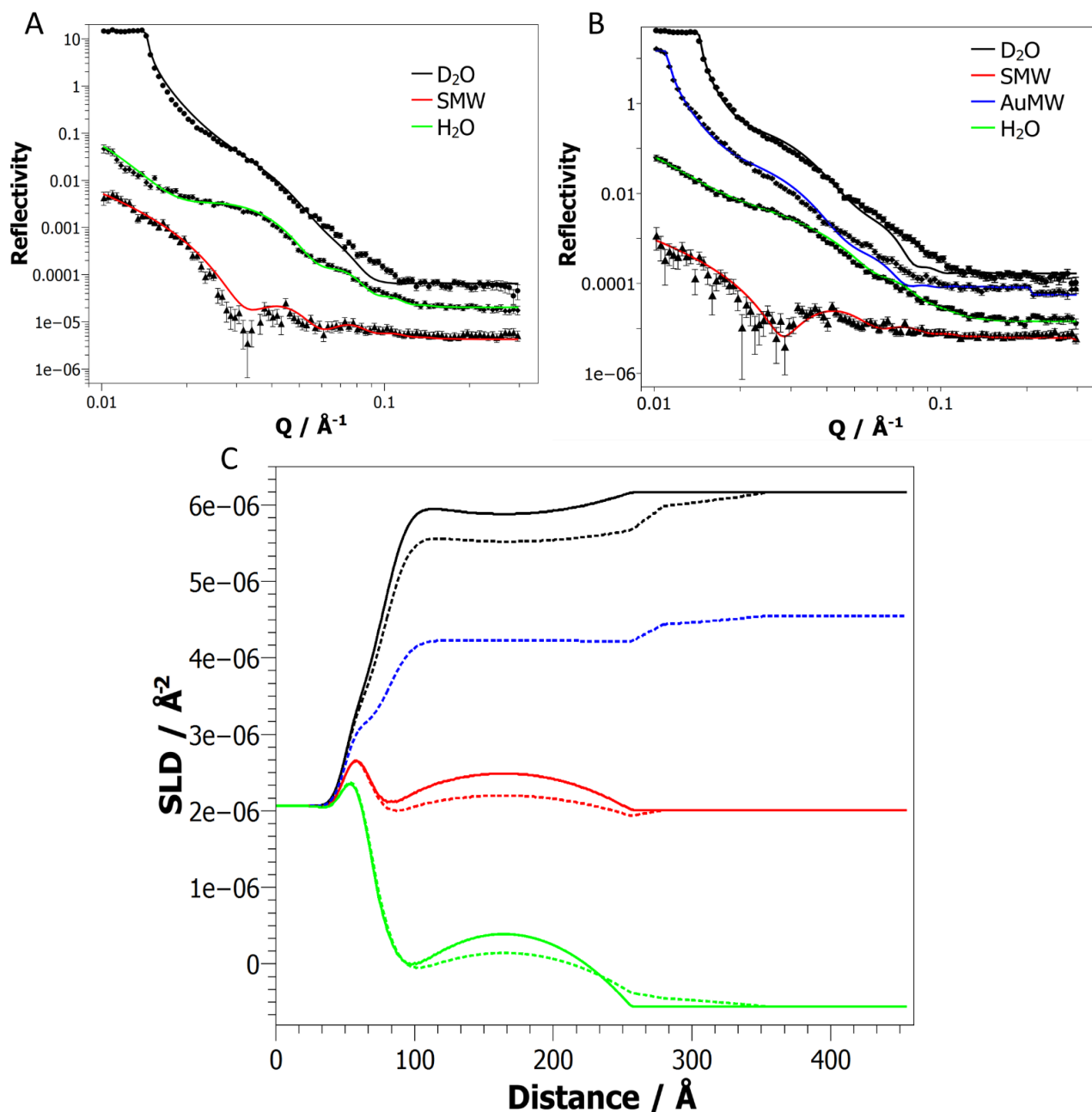


Figure 3.18 Data fitting and corresponding SLD profiles generated using the sphere model for the AuNP and AuNP + GGzOmpA_{TM} surfaces. (A) AuNP and (B) AuNP + GGzOmpA_{TM} reflectivity data are plotted on separate graphs, with the model fits represented by solid lines and the reflectivity profiles offset for clarity. (C) The fitted SLD profiles have been overlaid with the solid and dashed lines representing the AuNP and AuNP + GGzOmpA_{TM} surfaces respectively. The colours represent the different solvent contrasts used D_2O , SMW, AuMW and H_2O .

3.3 Discussion

3.3.1 Surface Characterisation

AAPTMS forms monolayers from aqueous ethanol deposition

AAPTMS surfaces made using the aqueous ethanol method, developed by Nippon Sheet Glass, were shown by AFM to be very smooth, suggesting monolayer formation. Further evidence for a dense monolayer was supplied by the colorimetric amine assay, with ~ 4 molecules/nm² observed. This result gives an area per molecule of ~ 25 Å² which is in good agreement with X-ray reflectivity studies of packed silane monolayers (Geer et al., 1994) and other self-assembled monolayer structures (Buscher et al., 1996). While the APS layers had similar amine surface densities, AFM images showed large island like structures that are similar to aggregates observed in previous studies (Argekar et al., 2013). Argekar *et al* state that amine densities above 2 molecules/nm² result in multilayer formation of APS and it has been shown that deposition from aqueous ethanol leads to multi-layered structures (Vandenberg et al., 1991). AAPTMS can generate well-ordered monolayers (Chen et al., 2006; Dressick et al., 1996) however previous studies have used curing steps to complete covalent binding to the SiO₂ substrate. This work would suggest that even without a curing step organised AAPTMS layers are formed, most likely mediated through hydrophobic interactions between the aryl groups and hydrogen bonding between the amines. Although it is unlikely that a continuously bonded network, like in Figure 3.19, is formed without curing, the AAPTMS layers are more stable and more resistant to multilayer formation than APS.

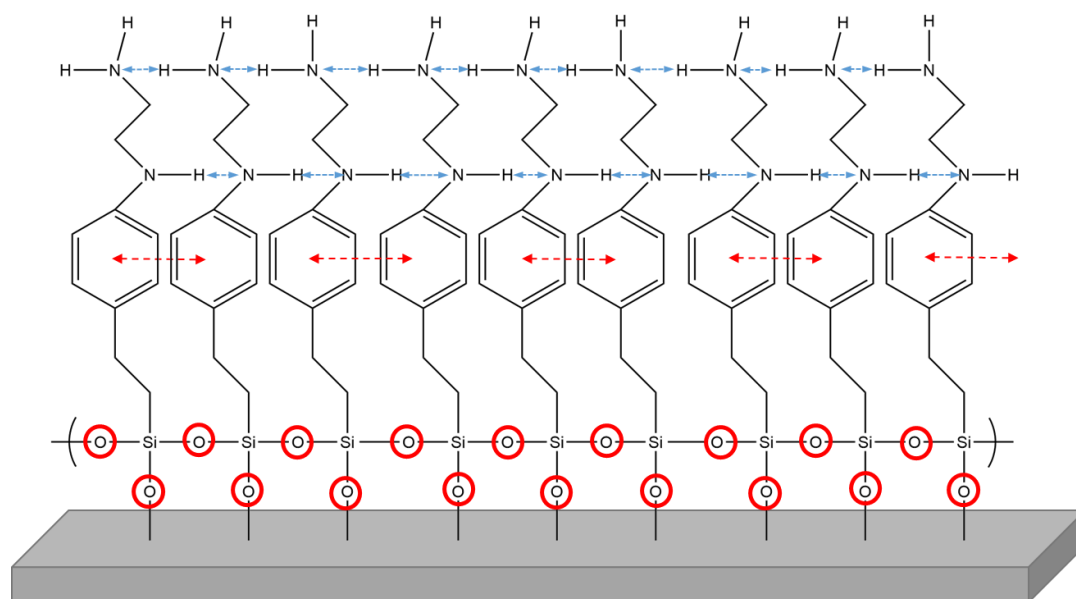


Figure 3.19 Fully crosslinked AAPTMS monolayer structure. It is unlikely that a fully crosslinked silane structure (highlighted in red circles) would be formed without a temperature curing step. However a pi-stacking and hydrogen bonding network (red and blue arrows) could be responsible for the higher stability of the AAPTMS film.

A smooth stable silane monolayer is required for uniform particle coverage

SEM images of gold nanoparticles deposited on APS layers show concentrated islands of particle deposition and large areas without nanoparticle coverage. This uneven coverage could be due to unstable APS layer being washed away after its initial deposition with only areas that contained larger aggregates retaining silane on the surface. Interestingly the silicon surface without silane showed some areas of fairly uniform nanoparticle deposition which were not seen with APS. By far the most uniform coverage was observed for AAPTMS functionalised silicon substrates with both the 10 and 20 nm particles used in this study. Although aggregated structures were seen when depositing the in house synthesised particles, the background contained a more uniform distribution of smaller particles. This observation suggests that the aggregates were formed in solution before binding to surface and not due to areas of multi-layered AAPTMS.

The large difference in coverage between the 10 and 20 nm particles indicates that binding to the surface is biased towards the surface area of the particle rather than the number of particles. In a 1 OD_{525nm} concentration solution there are 8 times as many 10 nm particles than 20 nm, whereas the surface area of the individual 20 nm particles is 4 times larger than the 10 nm. Work here and elsewhere (Grabar et al., 1996b; Nath and Chilkoti, 2004) has shown that nanoparticle coverage is correlated with the particle

concentration, therefore the greater interaction surface of 20 nm particles must outweigh their lower concentration in comparison with 10 nm particles. The area coverage of 20 nm particles on AAPTMS surfaces are comparable to other studies on cured APTES monolayers and PEG surfaces (Grabar et al., 1997; Haddada et al., 2016). The main advantage of the AAPTMS method is the ability to produce uniform, dense sub-monolayer particle coverage of the surface without the need for anhydrous conditions or curing steps.

Thiol assembly causes reorganisation

Different behaviour was observed for gold nanoparticle surfaces incubated with β -ME and thioAlkylPEG solutions after surface assembly. These behaviours are due to modification of interparticle and particle-surface interactions. Interparticle interactions can be described by classical Derjaguin-Landau-Vervey-Overbeek (DLVO) theory. Citrate coated particles are protected by repulsive electric double layer interactions from the negatively charged surface ligands (Biggs et al., 1993). The stability of gold nanoparticles in solution can be tuned by exchanging citrate anions for organic thiol molecules, reducing electrostatic repulsion and increasing van der Waals attraction (Kim et al., 2001). Tuning of interparticle interactions has been used to initiate particle reorganisation on surfaces to generate closely packed nanoparticle arrays. This was achieved by exchanging the citrate layer with thioalkane molecules to introduce favourable hydrophobic and van der Waals interactions between the particles (Brown and Johnson, 1997; Ochiai et al., 2014; Osterloh et al., 2004). Particle-surface interactions are also affected, changing from electrostatic to van der Waals forces, allowing greater particle mobility (Brown and Johnson, 1997; Osterloh et al., 2004). β ME incubation did not result in a loss of surface coverage but did cause an increase in aggregated clusters of particles, which is consistent with the displacement of citrate ions on the surface and a concomitant change in the interparticle and particle-surface interactions. This behaviour would indicate that the electrostatic attraction to the surface and repulsive forces between particles are replaced by hydrogen bonding from the pendant alcohol groups (Figure 3.20). The β ME- β ME interactions appear to be weaker than those observed for long alkyl chains with a number of individually located particles remaining. The stability in the nanoparticle coverage suggests that strong particle-surface interactions remain.

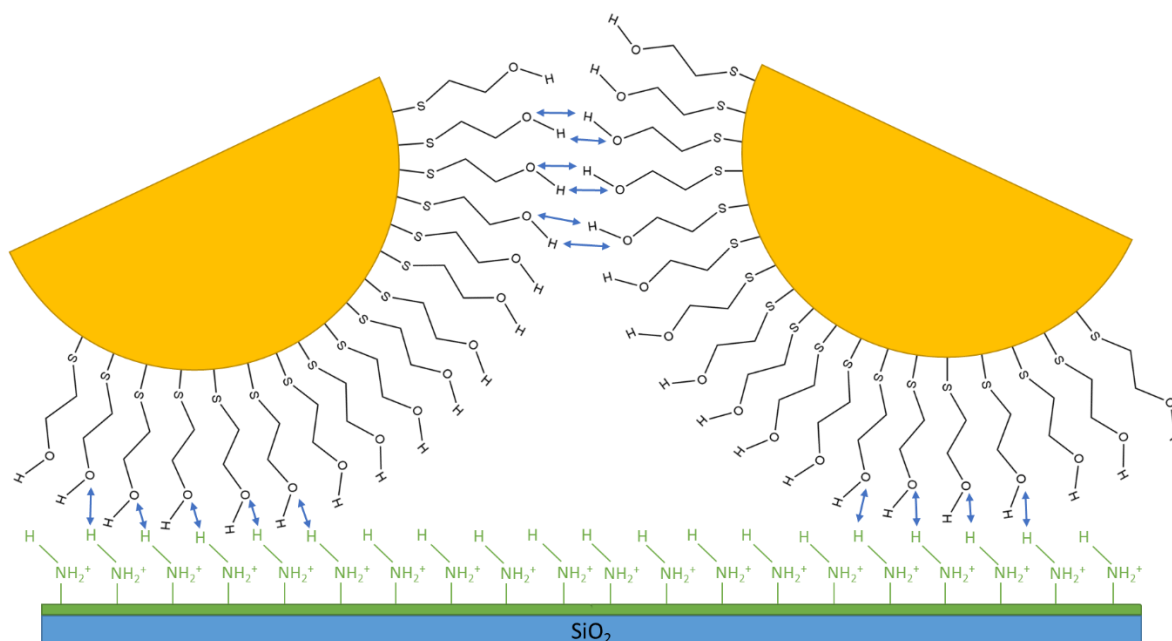


Figure 3.20 Possible hydrogen bonding interactions of β ME coated particles and a primary amine coated surface. Hydrogen bonds are indicated by blue arrows. AuNP and ligand sizes not to scale.

Incubation with the thioAlkylPEG solution resulted in a significant loss of particles from the surface, however no morphological changes were observed for the remaining particles. The particle removal could be due to weaker interactions between the thioAlkylPEG and the amine surface and would be compounded by the detergent in the buffer used. As no significant increase in groups of particle aggregates on the surface were observed it is likely that the terminal ethylene glycol repeats of the ligand do not confer increased interparticle attraction. This finding would be consistent with the use of PEG coatings on gold nanoparticles to improve their stability in solution (Manson et al., 2011).

Neutron Reflectometry

Deposition of gold nanoparticles on to the silane surface could be clearly observed by neutron reflectometry. The thicknesses of the SiO₂, silane and gold nanoparticle layers obtained from the two models fitted to the reflectivity data were in good agreement. These values, ~15, 8 and 180 Å respectively, were reasonable for the expected structure of the system. A protective layer of native SiO₂ is formed on bare silicon surfaces when exposed to air, which is usually in the region of 10-15 Å for a single crystal block (Kuhl et al., 1998; Mazzer et al., 2017). The silane thickness would suggest monolayer formation on the surface, consistent with the AFM images acquired for AAPTMS

modified silicon wafers. AAPTMS has a theoretical length of 10.7 Å, calculated from the bond lengths of the carbon chain, however silane monolayers are usually aligned at an angle to surface (Wang et al., 2005; Yi et al., 2008) which would account for some of the difference between the two values. The slightly lower than expected particle thickness, 20 nm AuNPs were used, is most likely due to polydispersity of the particles and also the sub-monolayer coverage of the surface.

Modelling of the protein layer was more difficult, adding a single protein layer to the slab model, that contained both the filler and protein molecules, did not describe the protein-nanoparticle system very well. The slab models reliance on using roughness to create the smooth shape of the particle would make any surface components more difficult to resolve. Therefore, it is not surprising that the model struggled to fit realistic values for the AuNP and proteins layer thicknesses to the AuNP + GGzOmpA_{TM} data, resulting in 153.69 and 30.33 Å respectively. While the quality of the model fitting to the reflectivity data was still relatively good when using this model ($\chi^2 = 15.31$), the ambiguity of the model could be seen in the higher level of error for all of the fitted parameters.

A more realistic AuNP layer thickness of 183.69 Å was obtained for the GGzOmpA_{TM} coated AuNPs when using the sphere model. This was achieved by simultaneously fitting the SiO₂, silane and AuNP layers to both data sets. It was necessary to allow the AuNP coverages to be fit independently, which reduced from 38.90% to 21.44% after protein assembly. AuNP loss was also observed by SEM when incubating particles with the thioAlkylPEG filler so the reduction in the coverage was not unexpected. The protein surface was modelled as a dual layer with the inner layer containing both the OmpA barrel and filler molecules and the outer layer containing the extended protein domains. The thickness of the inner layer, 22.93 Å, while comparable with a previous study on the GGzOmpA_{TM} system (Brun et al., 2015), was nearly 10 Å shorter than the theoretical length of the thioAlkylPEG filler molecule used (32.6 Å). Once again it is worth noting that the molecules in a self-assembled monolayer can be oriented at an angle to the surface, resulting in a lower monolayer thickness than the length of the molecule. However, a 22.93 Å layer would require the molecules to be at 45° to the surface which is an unrealistically large angle. The outer layer, at 75.09 Å, was much shorter than expected when compared with previous GGzOmpA_{TM} measurements on planar surfaces (Brun et al., 2015). This is most likely due to variation in the protein

layer across the sample, with the possibility of some poorly organised proteins or steric hindrance from closely packed AuNPs. However, the overall thickness fitted for this layer, 98 Å, is still significantly longer than an OmpA_{TM} domain (60 Å) or a protein lying down on the surface. The difficulties in fitting the protein layers highlights both the complicated nature of the system being modelled and also the limitations of NR.

Neutron reflectometry is an averaging technique where a wide beam, of around 50 mm, is reflected from the surface. Therefore, samples with high levels of order, such as a packed SAM, can be easily observed as the signal from the highly repetitive units is reinforced to give sharp, distinct features in the reflectivity profile. When analysing a more disordered system, such as the deposited nanoparticles in this study, the average of all the possible geometric configurations of the nanoparticles is observed. Assembly of the protein layer on the nanoparticle surface adds further possible variation in both the protein coverage and the orientation of the protein, especially if there are steric clashes with closely located particles. The more variable the surface structure, the more ambiguous the data becomes, which can be seen as a smoothing of the features in the reflectivity profile (Le Brun et al., 2011). While variation in the particle and protein coverages was accounted for in the sphere model, an idealised system was still being fitted where all the particles are equivalent and don't interact with one another. Further to this, the model also assumes the interface between the particles and the surface remained unchanged after protein and filler assembly which is not necessarily true. Taking into account the assumptions and caveats of the sphere model, the neutron data still provides strong evidence that the majority of the GGzOmpA_{TM} proteins were assembled in an oriented fashion on the nanoparticle surface with the OmpA_{TM} domain embedded in a filler layer. The difference in the height of the protein when compared with previous studies on planar gold, 98 to 135 Å, is most likely due to the mixed population of particle geometries and protein conformations. Another possible contributing factor was the relatively low protein coverage, $15.62 \pm 6.24\%$, which was approximately half the maximum protein coverage observed previously on planar surfaces (Brun et al., 2015; Le Brun et al., 2011). The proposed structure of the assembled GGzOmpA_{TM} protein on the AuNPs using the sphere model is shown in Figure 3.21.

While the quality of the neutron reflectometry data collected in this study was not ideal, NR experiments are unmatched in their ability to provide both Ångström resolution structural data and differentiate between the protein and nanoparticle layers. This was

achieved by matching the SLDs of the protein and gold components of the sample with the SLD of the outer solvent. The effect of contrast matching could be seen in the fitted SLD profiles. In the AuMW contrast the shape of the gold nanoparticle was lost and the protein layer remained visible (dashed blue line Figure 3.18), whereas, in SMW only the gold nanoparticles were visible in the SLD profile (dashed red line Figure 3.18). As discussed previously in Section 1.5, the combination of both protein and gold nanoparticles on the sample surface presented a significant challenge when collecting high resolution structural information. State of the art electron microscopy techniques, such as SEM, can provide nanometer resolution images of nanoparticle surfaces, as shown in this study and others (Kumari and Moirangthem, 2016; Ochiai et al., 2014), but are insensitive to the lighter elements of organic materials. Generally, techniques more suited to interrogating organic molecules on surfaces are limited in the amount of structural information they can provide. Fourier transform infra-red (FTIR) spectroscopy has been used to confirm the secondary structure of assembled protein layers on gold (Terrettaz et al., 2002) and surface enhanced raman spectroscopy (SERS) could be used to investigate protein layers on deposited nanoparticle surfaces (Armas et al., 2016; Freeman et al., 1995; Kaminska et al., 2008), however, neither of these techniques are able to provide information on the protein layer structure. Surface plasmon resonance (SPR) has been used to monitor the thickness and density of surface grown polymer layers (Emilsson et al., 2017) and the properties of deposited laminin layers have been investigated using a combination of SPR and quartz crystal microbalance with dissipation (QCM-D) (Malmström et al., 2007). How applicable these methods are to the nanoparticle system investigated in this study is unclear. Both approaches have been used with protein layers on planar surfaces, just as previous neutron reflectometry experiments, so would need to be adapted for the more complex surface topology presented by the deposited nanoparticles. For SPR in particular, the addition of the gold nanoparticles, which have their own plasmon field, would cause multipole effects and possibly others problems due to plasmon coupling (Okamoto and Yamaguchi, 2003).

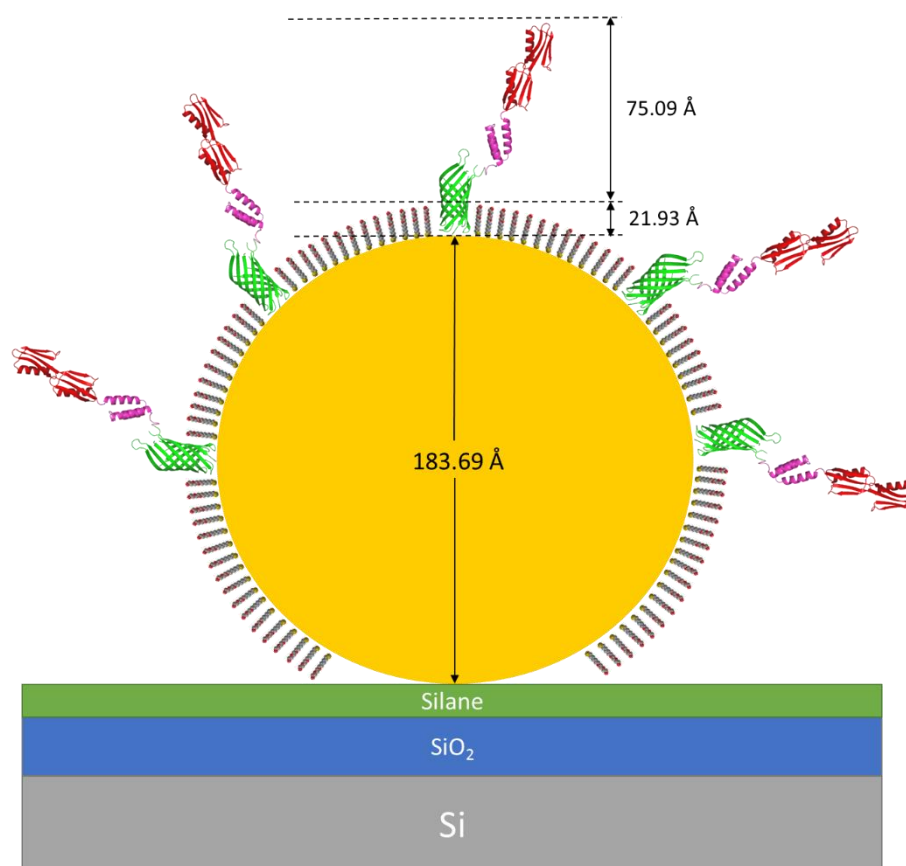


Figure 3.21 Schematic representation of the GGzOmpA_{TM} coated AuNP surface using the sphere model. The GGzOmpA_{TM} protein was embedded in a dense layer of the thioAlkylPEG filler molecule with the antibody binding domains extending away from the particle surface. The layer thicknesses obtained are the average of all the particles on the surface.

3.4 Conclusions

In this chapter it has been shown that the silane, AAPTMS can be used to generate stable monolayers on silicon oxide surfaces when deposited from aqueous ethanol at room temperature. These layers have a high density of available amine moieties, ~ 4 per nm^2 , that can bind to citrate coated gold nanoparticles. Assembly of gold nanoparticles from solution results in sub-monolayer formation with a maximum area coverage of $\sim 35\%$ observed for 20 nm particles. While the density and morphology of the assembled particles are comparable with work published by others on APTES functionalised surfaces (Grabar et al., 1997; Seitz et al., 2003), the AAPTMS method does not require strict anhydrous deposition conditions and high temperature curing of the silane layer to maintain stability.

The structure of an engineered OmpA_{TM} protein, GGzOmpA_{TM}, after assembly on the gold nanoparticle surface with a thioAlkylPEG filler molecule was investigated by

neutron reflectometry. Through this technique, it was shown that the majority of the proteins assemble in an oriented fashion with the OmpA_{TM} barrel embedded in a dense thioAlkylPEG monolayer and the GGz domains extended away from the surface. The particles were completely covered in a GGzOmpA_{TM}-filler monolayer which was comprised of approximately 16% protein. This work represents one of the first studies on the structure of self-assembled protein arrays on deposited nanoparticle surfaces.

4 SELF-ASSEMBLY OF ENGINEERED PROTEINS ON GOLD NANOPARTICLES IN SOLUTION

4.1 Introduction

Gold nanoparticle conjugates have been used in medicine and biology for over 100 years and are currently used in a wide variety of applications including; diagnostics, drug delivery and photothermal therapeutics (Choi et al., 2010; Dreaden et al., 2012; Huang and El-Sayed, 2010). The ability of modern synthesis techniques to produce nanoparticles of defined size and geometries coupled with the number of attachment strategies for biological molecules and their low cytotoxicity make AuNPs an attractive platform for biological applications (Jazayeri et al., 2016; Shukla et al., 2005).

Although widely used, the conjugation of proteins, particularly antibodies, is commonly achieved through simple adsorption processes and not by a specific interaction such as via a chemical linker. This gives little control over the orientation of attached protein layers which could be detrimental in applications where the display of certain domains is crucial for functionality (Kausaite-Minkstimiene et al., 2010).

Considering the maturity of the research field very few detailed studies have been published on the nanoscale structure and orientation of proteins on nanoparticle surfaces. Quantification of the binding affinity and capacity of proteins can be quite variable depending on the techniques used (Boulos et al., 2013; Brewer et al., 2005; Spinozzi et al., 2017; Wang et al., 2014; G. Wang et al., 2017). More recently the binding mechanisms, including the residues responsible, have become better understood for globular proteins (Lin et al., 2015; Siriwardana et al., 2013; Wang et al., 2016) but the complex rearrangement of proteins after initial association with the nanoparticle surface remains difficult to investigate.

It has been shown that outer membrane proteins from *E. coli* can self-assemble on to the surface of gold, with the addition of a cysteine residue to direct binding through a gold-thiol bond (Brun et al., 2008; Cisneros et al., 2006; Shah et al., 2007; Terrettaz et al., 2002). The orientation of engineered OmpA monolayers is guided by the addition of a membrane mimicking filler molecule, usually a poly(ethyleneglycol) terminated alkane thiol, which also reduces non-specific binding to the surface (Figure 1.10) (Le Brun et al., 2011). The self-assembling nature and high stability of the OmpA beta-barrel make it an ideal scaffold protein for the display of functional domains on gold surfaces, with a range of applications including label free biosensing (Brun et al., 2015).

To understand the assembly of the transmembrane domain of OmpA (OmpA_{TM}) on the surface of AuNPs two proteins, wild type (wtOmpA_{TM}) and cysteine modified

(cysOmpA_{TM}), were studied to investigate binding kinetics, quantify equilibrium binding and measure the stability of the resulting AuNP-protein complexes. To confirm the correct orientation of assembled protein layers, the biological activity of a more extensively engineered OmpA_{TM} protein with three IgG-binding domains: two B domains from *Streptococcus spp*, followed by a single Z-domain of *Staphylococcus aureus* Protein A fused to the N-terminus of circularly permuted OmpA_{TM} (GGzOmpA_{TM}) was characterised and specific protein-protein interactions investigated.

The intrinsic local surface plasmon resonance (LSPR) of the AuNPs was used for the detection of protein binding at the nanoparticle surface. As discussed previously LSPR occurs when nanoparticles interact with light photons, creating a plasmon wave that oscillates around the particle (Willets and Duyne, 2007). The oscillation frequency is dependent on multiple factors including the size of the nanoparticle and the refractive index of its environment. Protein binding at the nanoparticle surface can be observed by a shift in the LSPR peak in the absorption spectrum (Fujiwara et al., 2006).

Typically, the peak wavelength, λ_{\max} , is taken using a simple peak picking algorithm. For a more rigorous interrogation of spectral changes the barycentric mean, λ_m , can be used (Chalton and Lakey, 2010). This is calculated using the following equation;

$$\lambda_m = \frac{\sum I(\lambda) \times \lambda}{\sum I(\lambda)} \quad [4.1]$$

Where $I(\lambda)$ is the absorbance at wavelength λ . Analysis by this method enables precise detection of small changes in the spectrum. To complement the spectroscopic data changes in both the hydrodynamic size and charge of the particles were also investigated by scattering and electrophoretic methods.

4.2 Results

4.2.1 cysOmpA_{TM} Assembly

The effects on assembly of inserting a cysteine residue in a periplasmic loop of the transmembrane domain of OmpA_{TM} was investigated in this study using several techniques. Binding kinetics were followed by UV-Vis spectroscopy, equilibrium binding, structure and stoichiometry were analysed by DLS, UV-Vis and fluorescence spectroscopy and protein-nanoparticle stability by UV-Vis spectroscopy and DLS.

Overnight Binding Kinetics

Overnight assembly of cysOmpA_{TM} onto AuNPs was followed by UV-Vis spectroscopy. An 8 μM cysOmpA_{TM} solution, in DDM buffer (0.5% w/v n-Dodecyl β -D-maltoside, 10 mM Tris, pH 8), was added to the nanoparticle solution by a 1/10 dilution immediately before data collection. Initially, cysOmpA_{TM} binds to the nanoparticle surface in a rapid manner, slowing after approximately an hour. The λ_m continued to shift to longer wavelengths indicating that protein binding to the surface continued to occur even after 15 hours. Addition of the SH-C11-OEG6 filler molecule at 30 minutes after protein addition initiated a rapid increase in the λ_m followed by an apparent stabilisation of the particle surface with no further binding observed (Figure 4.1).

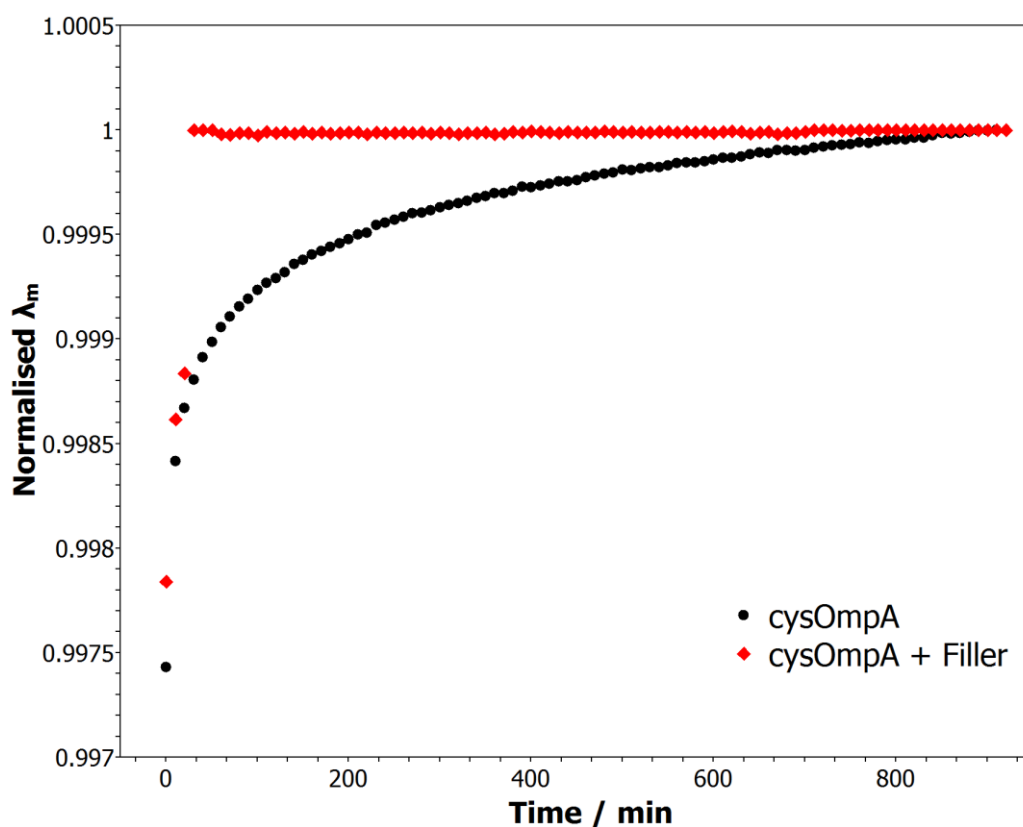


Figure 4.1. Overnight binding kinetics of cysOmpA_{TM}, with and without filler addition.

The protein solution was added to the nanoparticles by a 1/10 dilution immediately before data collection. Spectra were acquired (400-800 nm) every 10 minutes for 920 minutes. The barycentric mean wavelength, λ_m , was calculated for the extinction peak (500-600 nm) for each spectrum and normalised to 1 to aid comparison of the two samples. Filler solution was added by 1/10 dilution after 30 minutes for the filler sample.

Initial Binding Kinetics

The initial binding kinetics of cysOmpA_{TM} and wtOmpA_{TM} were followed by UV-Vis spectroscopy (A Figure 4.2). A modified pseudo-second order kinetic model can be used to describe the binding kinetics, if it is assumed the protein is available in excess (Boulos et al., 2013; G. Wang et al., 2017). The pseudo-second order rate constant (k_2) can be extracted from a linear pseudo-second order kinetic curve using the following equation;

$$\frac{t}{\Delta\lambda_m} = \frac{t}{\Delta\lambda_e} + \frac{1}{k_2(\Delta\lambda_e)^2} \quad [4.2]$$

Where t is the time in seconds, $\Delta\lambda_m$ is the shift in the mean wavelength and $\Delta\lambda_e$ is the mean wavelength shift at equilibrium. Rate constants of 7.58×10^{-3} and $4.89 \times 10^{-3} \text{ s}^{-1} \text{ nm}^{-1}$ were calculated for cysOmpA_{TM} and wtOmpA_{TM} respectively. These results are consistent with timeframes observed for bovine serum albumin (BSA) and human serum albumin (HSA) binding to AuNPs (Boulos et al., 2013; Cedervall et al., 2007). The initial binding rate, h , can be estimated from Equation 4.2, as $t/\Delta\lambda_m$ approaches 0 (Ho, 2006),

$$h = k_2(\Delta\lambda_e)^2 \quad [4.3]$$

This gave initial rates of 6.77×10^{-3} and $4.72 \times 10^{-3} \text{ s}^{-1} \text{ nm}$ for cysOmpA_{TM} and wtOmpA_{TM} respectively.

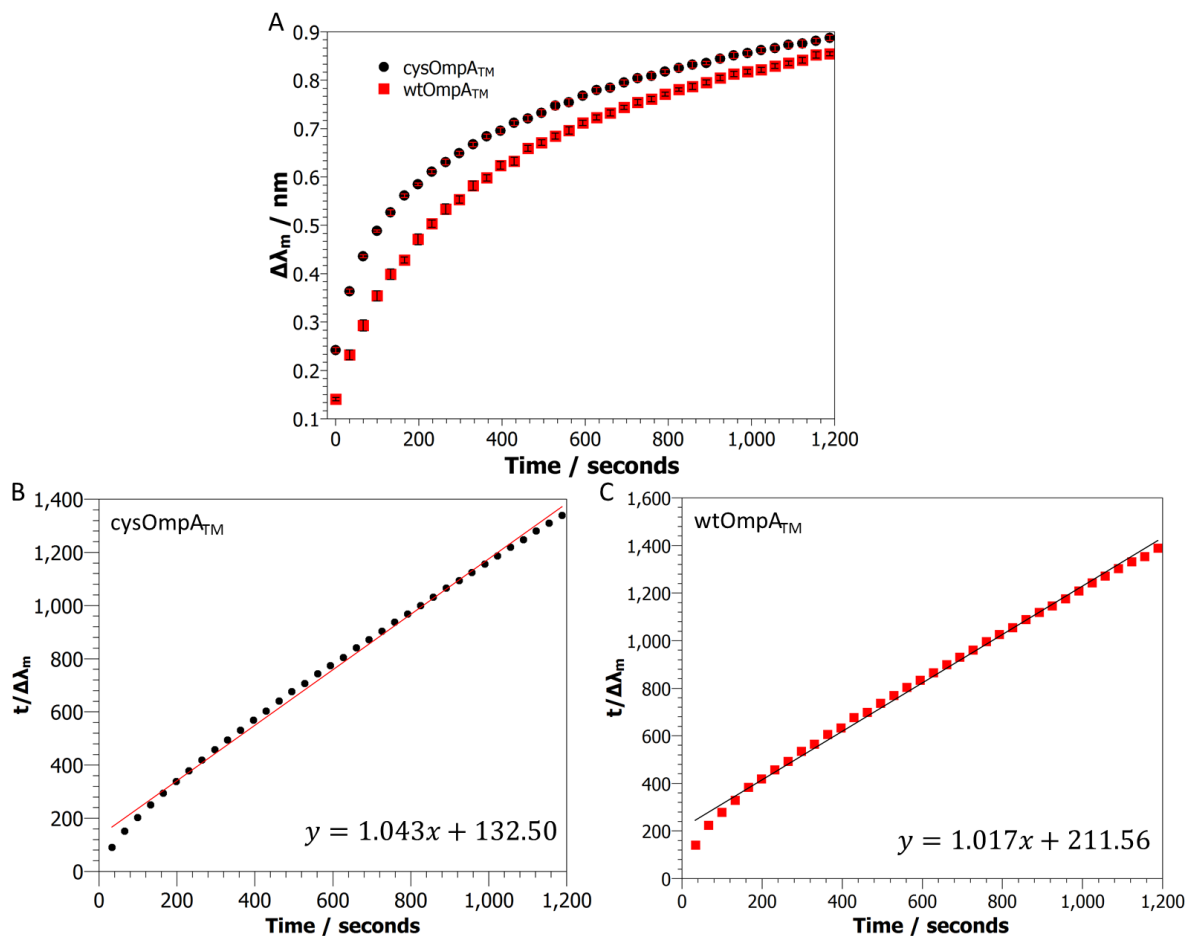


Figure 4.2 Initial binding kinetics of wild type and cysOmpA_{TM}. Binding kinetics were followed by UV-Vis spectroscopy with spectra acquired every 33 seconds between 400-800 nm. The results were plotted as a shift in the λ_m over time (A). Linear pseudo-second order kinetic curves were generated for cysOmpA_{TM} (B) and wild type (C) showing good correlation with R^2 values of 0.995 and 0.994 respectively. Error bars represent the standard error of the mean based upon 3 samples.

Effect of TCEP addition on binding kinetics

Kinetic experiments were carried out with the proteins incubated with 10 mM Tris(2-carboxyethyl)phosphine (TCEP), a reducing agent used to selectively reduce disulphides (Burns et al., 1991), for 30 minutes prior to addition to the AuNP solution. This had a significant effect on the binding curves with an increase in overall protein binding observed. This was the case for both the wild type and cysOmpA_{TM}, however, the effect on the cysOmpA_{TM} variant was much more pronounced than for the wtOmpA_{TM} (A and B Figure 4.3). Subsequently citrate coated AuNPs incubated with TCEP were run on a 1% agarose gel, revealing that the electrophoretic mobility of the particles increased with the TCEP concentration. This suggests that the addition of

TCEP modifies the surface charge of the AuNPs which is discussed in more detail in Section 4.3 (C Figure 4.3).

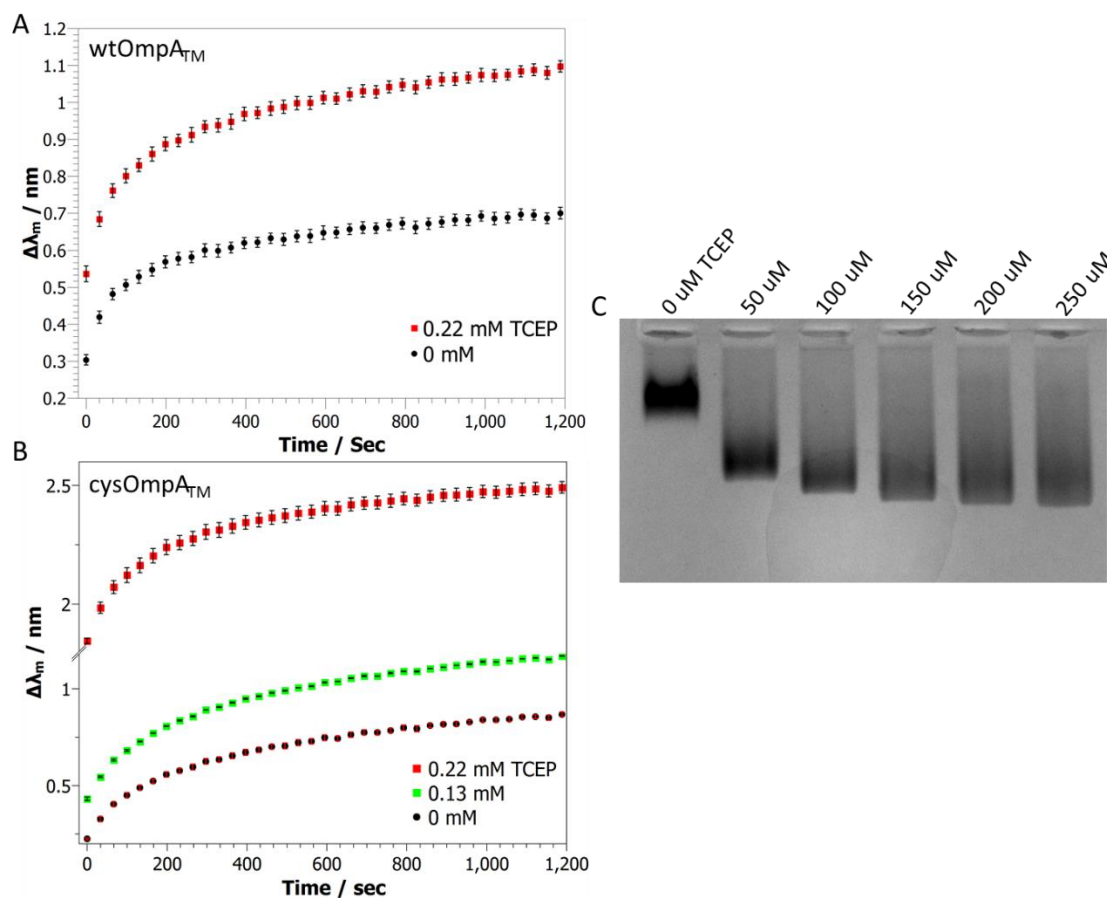


Figure 4.3 Initial protein binding kinetics after TCEP addition (A+B) and the effect of TCEP on AuNP electrophoretic mobility (C). Wild type (A) and cysOmpA_{TM} (B) were incubated with TCEP for 30 minutes prior to mixing with the AuNP solution. Once again binding kinetics were followed by UV-Vis spectroscopy with spectra acquired every 33 seconds $n = 3$. Bare AuNPs were titrated with increasing TCEP concentration and run on a 1% agarose gel (C). Both the mobility of the AuNPs and the distribution of the nanoparticles in the gel band are increased with TCEP concentration.

The pseudo-second order rate constants and initial rates for the TCEP samples were calculated using Equations 4.2 and 4.3 respectively (summarised in Table 4.1). This revealed an increase in the rate constant for both wild type and cysOmpA_{TM} of 3.01 and 1.96 times respectively at 0.22 μM . TCEP had a greater effect on the initial rate, with increases of 4.18 and 14.06 times for wtOmpA_{TM} and cysOmpA_{TM} respectively.

Table 4.1 Pseudo-second order rate constants and initial rates of cysOmpA_{TM} and wtOmpA_{TM} both with and without TCEP addition.

<i>Sample</i>	<i>Pseudo-Second Order Rate Constant (k₂) / × 10⁻³ s⁻¹ nm⁻¹</i>	<i>Initial Rate (h) / × 10⁻³ s⁻¹ nm</i>	<i>Estimated Equilibrium Shift (Δλ_e) / nm</i>
<i>cysOmpA_{TM}</i>	7.58 ± 0.45	6.77 ± 0.40	0.94 ± 0.01
<i>cysOmpA_{TM} + 0.13 μM TCEP</i>	7.39 ± 0.47	11.55 ± 0.74	1.25 ± 0.01
<i>cysOmpA_{TM} + 0.22 μM TCEP</i>	14.86 ± 1.09	95.24 ± 7.01	2.53 ± 0.01
<i>wtOmpA_{TM}</i>	4.89 ± 0.21	4.72 ± 0.20	0.98 ± 0.01
<i>wtOmpA_{TM} + 0.22 μM TCEP</i>	14.76 ± 1.12	19.73 ± 0.15	1.15 ± 0.01

Equilibrium Binding

The theoretical binding capacity of OmpA_{TM} on AuNPs can be calculated using geometric constraints. A simple method for this, from Wang et al (Wang et al., 2014), uses the radius of gyration (R_g) of the protein and the radius of the particle (R_{AuNP}) to predict the adsorption capacity (N_{max});

$$N_{max} = \frac{4R_{AuNP}^2}{R_G^2} \quad [4.4]$$

Giving a capacity of 142 protein molecules for a 20 nm particle, assuming an R_G of 16.76 Å, calculated using PyMOL. However, for non-spherical proteins, R_G is not the best descriptor of the overall size. To account for the possible oriented nature of proteins on the surface a maximum and minimum capacity was calculated by dividing the surface area of the nanoparticle by the footprint of OmpA_{TM} proteins standing or lying on the particle surface. The estimated boundaries for the two protein footprints used are shown in Figure 4.4, giving areas of 718.24 and 1608 Å² for the stood up and lying down proteins respectively. For a 20 nm particle, with a surface area of 125,663 Å², this gave a theoretical binding capacity of between 78-175 proteins per particle.

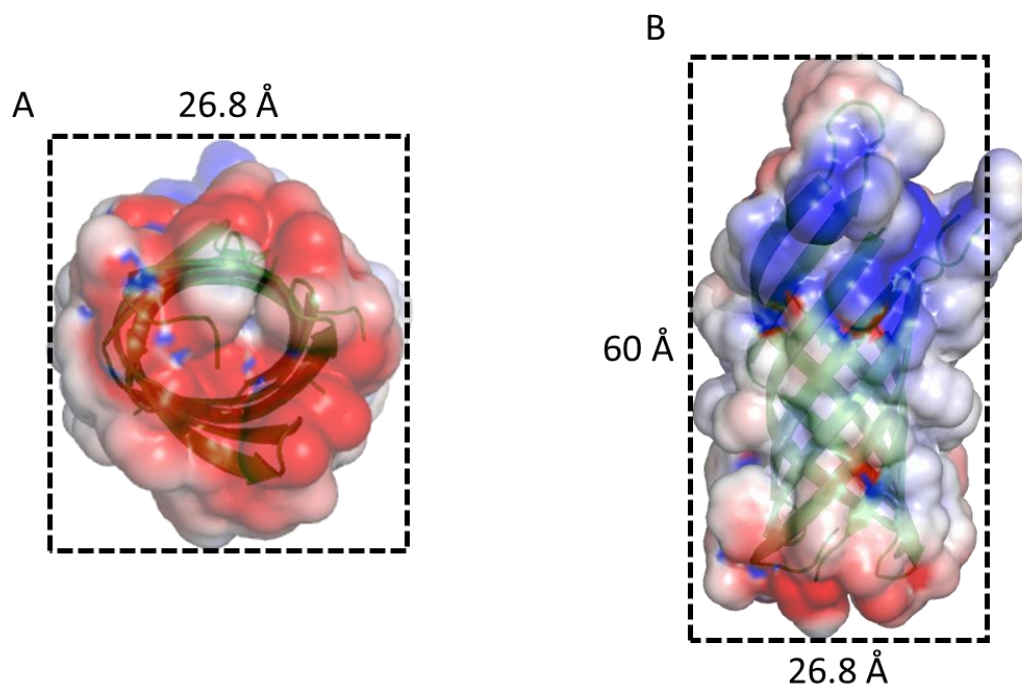


Figure 4.4 Protein footprints used for theoretical binding capacity calculations. The base of the OmpA barrel was used for stood up proteins (A) with the area of the side of the barrel used to approximate the footprint of a protein lying on the surface (B). The solvent accessible surface was generated using APBS with the distance measurements carried out with the measurement wizard in PyMOL.

Equilibrium binding was investigated by titrating an AuNP stock solution with increasing protein concentration. Protein binding was then analysed using UV-Vis and fluorescence spectroscopy. Both *cysOmpA_{TM}* and *wtOmpA_{TM}* show greater binding with increasing protein concentration. Below 0.16 μM only minor differences between the two proteins are observed, above this concentration *cysOmpA_{TM}* exhibits higher equilibrium binding. This becomes particularly evident with protein reduced by TCEP before addition to the AuNP. The increased shift in the λ_m indicates higher protein binding for both the wild type and cysteine proteins after TCEP incubation, in agreement with kinetic experiments (A and B Figure 4.5). Once again, the difference in apparent protein binding is greater for the cysteine containing *OmpA_{TM}* than with the wild type when reduced with TCEP.

The maximum average protein binding observed by fluorescence spectroscopy, 173.5 ± 30.6 proteins per particle, for *cysOmpA_{TM}* equates to a surface coverage of $99.10\% \pm 17.50\%$ when using the geometrically calculated maximum capacity of 175. This is much higher than the maximum coverage observed for planar surfaces (Brun et al.,

2008). The lower average binding of wtOmpA_{TM}, 80.0 ± 15.8 proteins per particle, is suggestive of a less ordered protein layer but could also be due to a less favourable binding enthalpy from the lack of a gold-thiol bond.

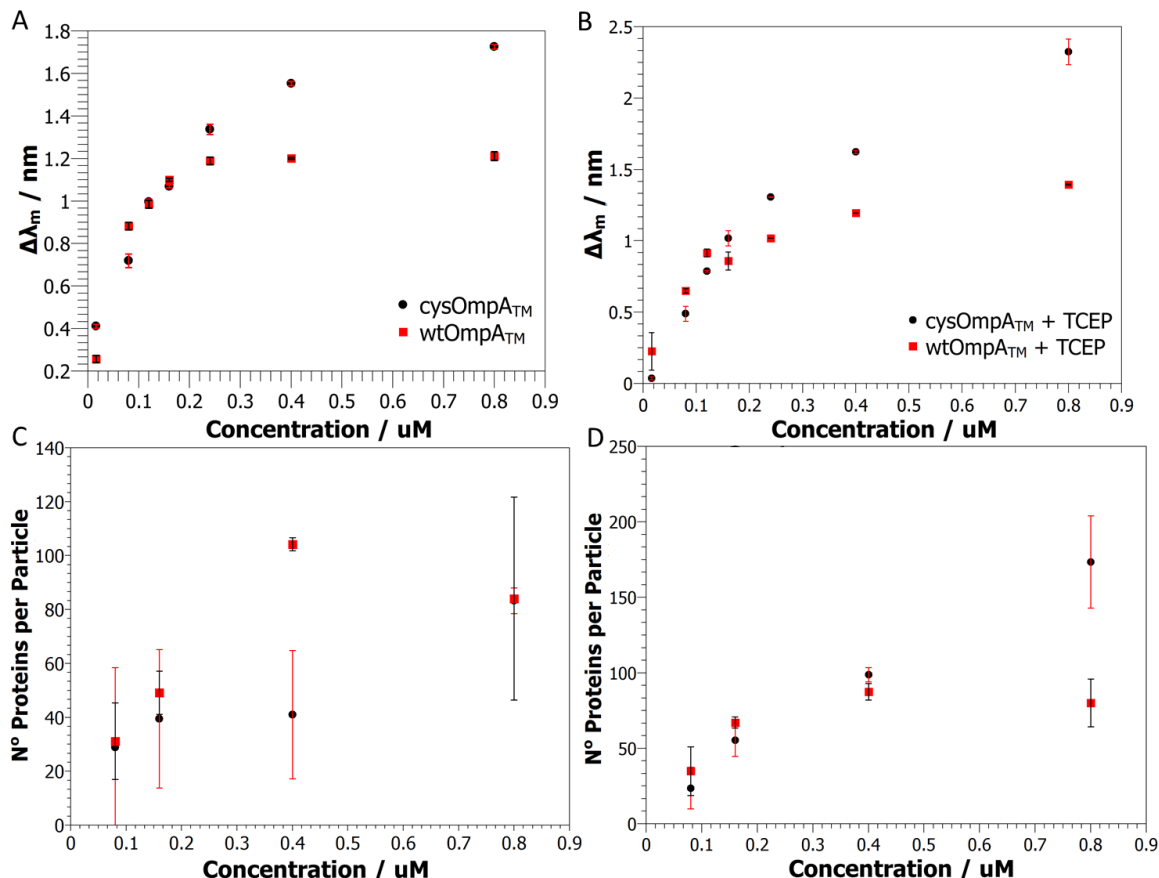


Figure 4.5 UV-Vis spectroscopy (A and B) and Protein:AuNP stoichiometry (C and D) data for 1 OD_{525nm} 20 nm AuNPs titrated with increasing protein concentration, after overnight incubation. A and C were carried out without prior TCEP incubation of the protein, B and D were incubated with 10 mM TCEP for 30 minutes before mixing with the AuNP solution. The UV-Vis data is presented as a shift in the λ_m as function of protein concentration. The Protein:AuNP stoichiometry was calculated using fluorescence spectroscopy (see Section 2.12.2). Error bars represent the standard error of the mean based upon 3 samples.

Equilibrium binding and the protein-nanoparticle structure was further explored by examining the electrophoretic mobility of the protein-nanoparticle conjugates in conjunction with DLS and UV-Vis measurements. cysOmpA_{TM} conjugated particles migrated faster, suggesting that these were either smaller in size or had increased protein binding (A Figure 4.6). This was corroborated by DLS and UV-Vis spectroscopy measurements showing that these particles were both slightly smaller and had a larger shift in the λ_m than wtOmpA_{TM} (B and C Figure 4.6). The addition of a

thioAlkylPEG filler molecule, which is used to stabilise the protein monolayer (Figure 3.12), to both the wtOmpA_{TM} and cysOmpA_{TM} conjugated particles showed an increase in the hydrodynamic diameter (D_{hyd}) and corresponding retardation in the electrophoretic mobility. Protein and filler coated particles migrated in a tighter band, suggestive of a more homogeneous sample when compared to those with just protein.

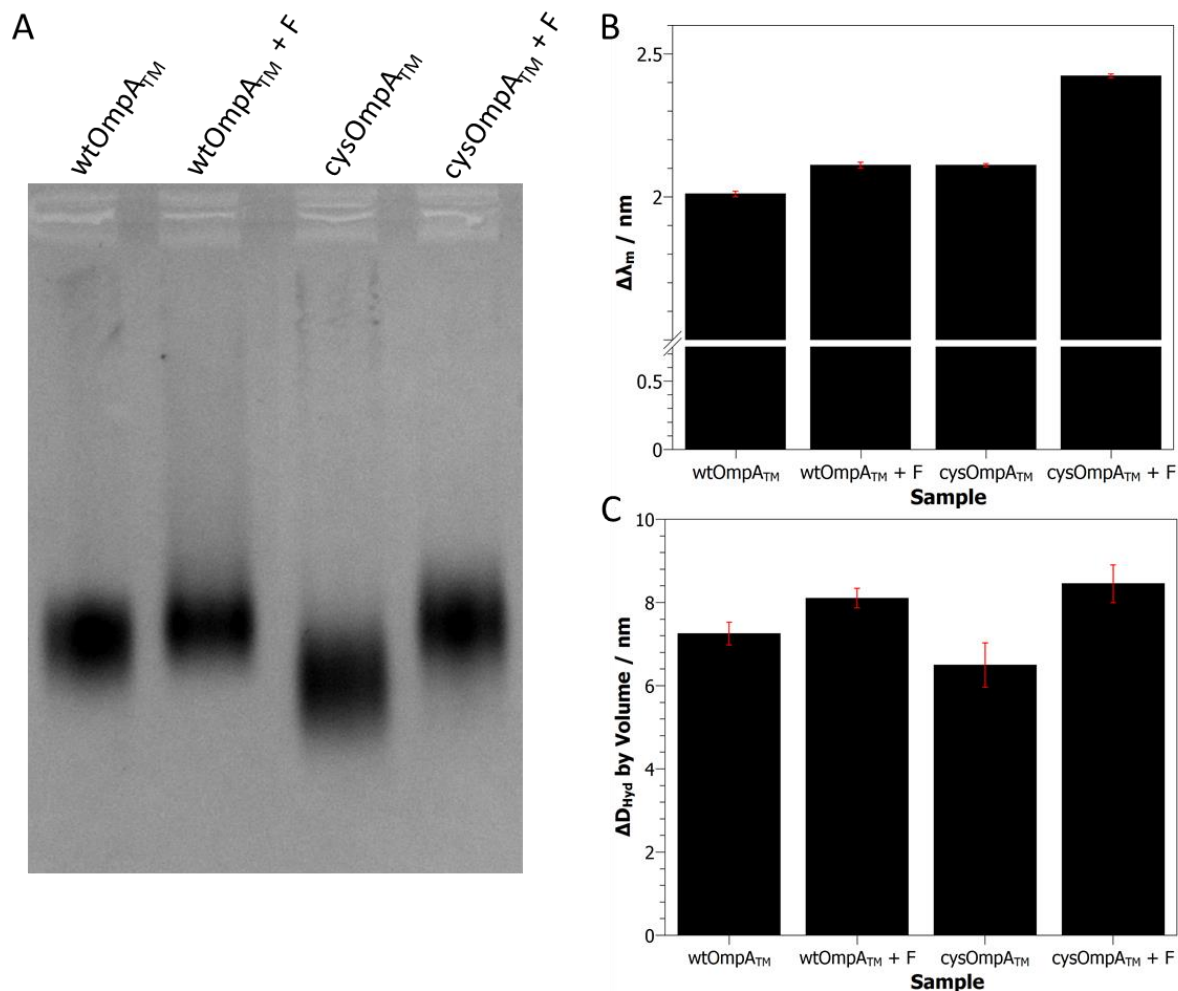


Figure 4.6. Agarose gel electrophoresis (A), UV-Vis spectroscopy (B) and DLS (C) results for 20 nm AuNPs conjugated with wtOmpA_{TM} and cysOmpA_{TM}. 20 nm AuNP at 10 OD_{525nm} were incubated with 8 μ M protein overnight before separating on a 1% agarose gel. F designates 8 μ M filler addition after 30 minutes of protein incubation. UV-Vis spectroscopy and DLS samples were split into three aliquots, centrifuged and resuspended at 1 OD_{525nm} to remove any residual protein or filler before measuring. Error bars represent the standard error of the mean based upon duplicate measurements.

Stability

Sodium borohydride (NaBH₄) competition was used to investigate the stability of the protein-nanoparticle complexes. Instead of utilising the reductive power of NaBH₄ this

assay took advantage of the high affinity of the borohydride ion (BH_4^-) for the gold nanoparticle surface and has previously been used to remove organothiol compounds from both planar gold films and nanoparticles (Ansar et al., 2013; Yuan et al., 2008). Changes in the bound protein layer were analysed by UV-Vis spectroscopy and dynamic light scattering (DLS) with cysteine modified OmpA_{TM} showing greater stability when challenged with NaBH_4 than the wild type (Figure 4.7 below). An increase in the D_{hyd} at 1 mM NaBH_4 was observed for both cysOmpA and wtOmpA even though a reduction in the λ_m was seen by spectroscopy at that concentration. This effect was much more pronounced for cysOmpA_{TM} than the wild type. The addition of the SH-C11-OEG6 filler molecule increased the stability of both cys and wtOmpA_{TM} conjugated particles, remaining stable up to 20 mM NaBH_4 . There was, however, still a reduction in the D_{hyd} of wtOmpA_{TM} particles after filler addition which was not seen with the cysOmpA_{TM} (C Figure 4.7).

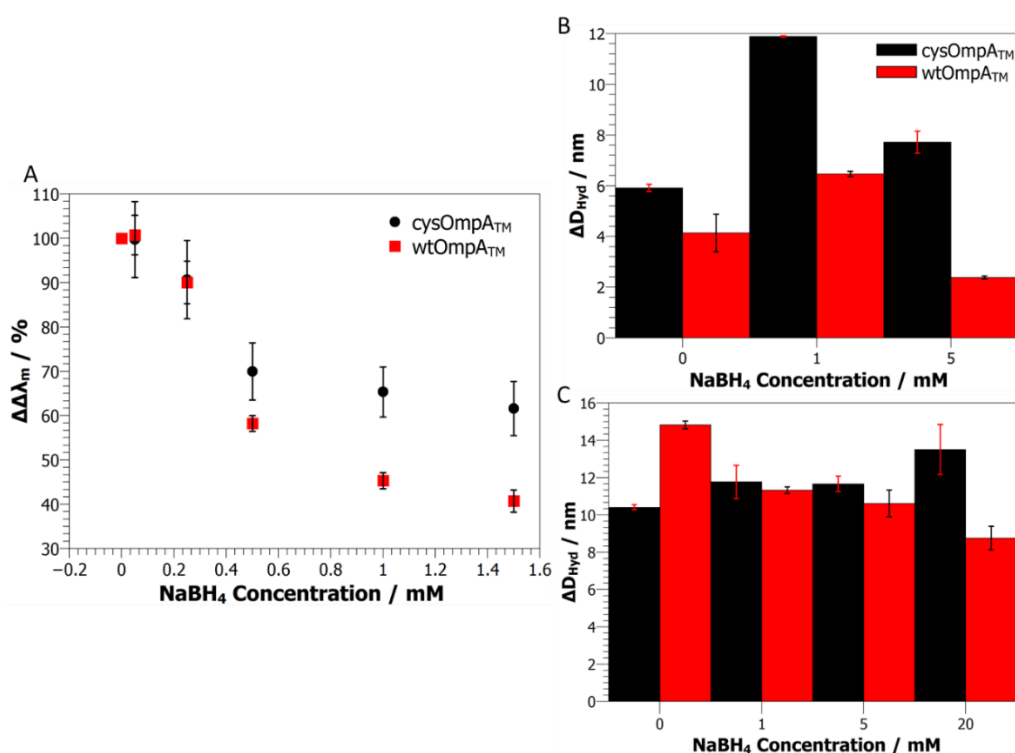


Figure 4.7. Protein-AuNP stability when challenged with increasing NaBH_4 concentrations. Wild type and cysOmpA_{TM} conjugated 20 nm AuNPs were incubated with increasing NaBH_4 concentrations for 3 hours before measuring protein loss by UV-Vis spectroscopy and DLS. (A) Spectroscopy results are presented as the percentage shift in the $\Delta\lambda_m$ ($\Delta\Delta\lambda_m$) when compared with conjugated particles before NaBH_4 addition. DLS results show the change in the D_{hyd} , after blank AuNP subtraction, for conjugated particles both with (C) and

without (B) filler addition. Error bars represent the standard error of the mean based upon 3 samples.

Cary 4E vs NanoDrop Spectrometer

The robustness of calculating the mean wavelength using the barycentre was tested by measuring samples with both the Cary 4E and NanoDropTM spectrophotometers. The NanoDropTM is a microvolume spectrometer that forms a liquid column with a path length of approximately 1 mm instead of using a traditional cuvette (“NanoDrop,” n.d.). By using this method samples of 2 μl in volume can be measured, however, the absorbance of the sample is 10 times lower than a spectrum acquired with a 10 mm cuvette leading to increased noise levels (A Figure 4.8). Analysis of the LSPR peak of AuNPs titrated with cysOmpA_{TM} measured by each spectrometer showed remarkable consistency (B Figure 4.8) for both the calculated $\Delta\lambda_m$ and the standard error. Statistical analysis of the $\Delta\lambda_m$ using a paired T-test gave p-values of above 0.05 for all concentrations with the majority above 0.1 indicating that there is no significant difference between the two data sets. These results show that the $\Delta\lambda_m$ is a robust measure of protein binding even when using low absorbance data with higher levels of background noise.

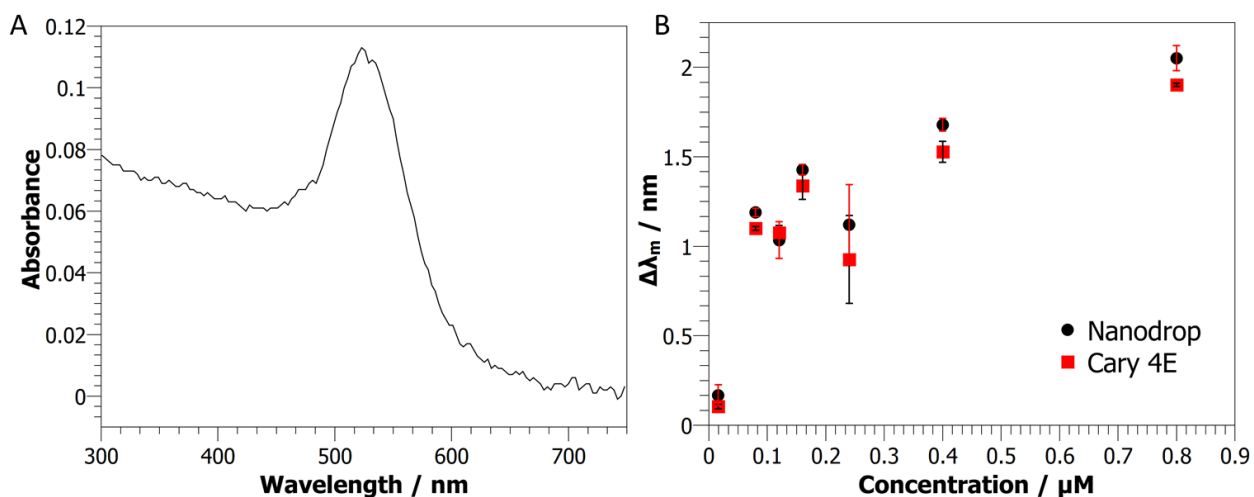


Figure 4.8 Measuring protein binding using a NanoDropTM ND-1000 spectrophotometer and comparison with the Cary 4E system. A representative gold nanoparticle spectrum is shown from the ND-1000 (A), the low absorbance is due to the NanoDrop using a 1 mm pathlength column of sample to measure the absorbance. (B) Shifts in the λ_m are comparable between the two systems for AuNPs titrated with cysOmpA_{TM}. Triplicates of each concentration were measured on both spectrometers.

4.2.2 GGzOmpA_{TM} Assembly

The same analytical techniques were applied to the assembly of the fusion protein GGzOmpA_{TM}. This construct contains two IgG-binding B domains from Protein G and one Z domain from protein A fused to the N-terminus of a circularly permuted OmpA_{TM} scaffold.

Optimisation of GGzOmpA_{TM} Conjugation

20 nm AuNPs at 1 OD_{525nm} were incubated with 0.16, 0.4, 0.8, 1.28 and 1.6 μ M GGzOmpA_{TM} overnight. These concentrations equate to molar ratios of between 127.6:1 and 1276:1, protein:nanoparticles. Visual inspection of the samples revealed that aggregation of the nanoparticles was present above 0.8 μ M (Figure 4.9). The buffer volume was kept constant across the samples to remove any possible detergent effects.

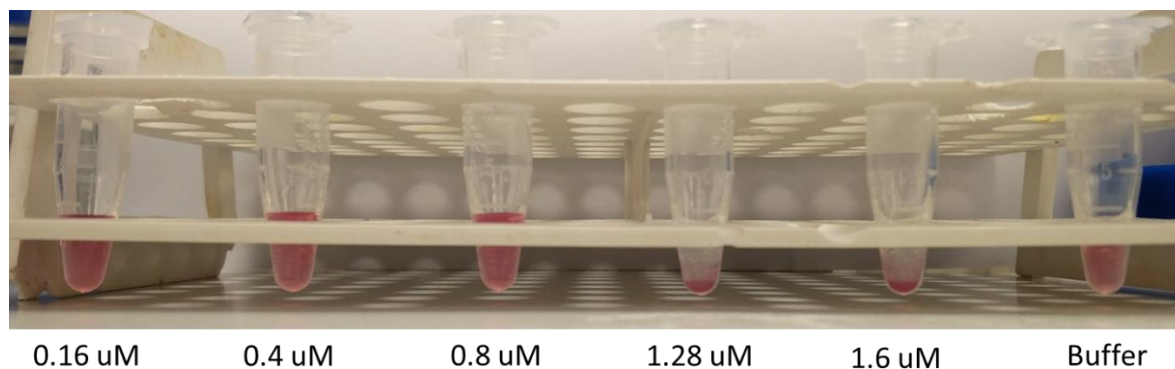


Figure 4.9. Gold nanoparticle samples after overnight incubation with increasing GGzOmpA_{TM} concentration. All samples were made with 20nm AuNPs at 1 OD_{525nm} with the final protein concentrations indicated above. The buffer sample only contained 0.5% DDM buffer.

Binding Kinetics

GGzOmpA_{TM} binding was followed by UV-Vis spectroscopy acquiring spectra every 10 minutes for 440 minutes. A similar binding curve to cysOmpA_{TM} was observed at 0.8 μ M with the maximum absorbance of the sample remaining stable over the entire time period (A Figure 4.10). Conversely, when incubated with 1.6 μ M protein the change in the λ_m becomes more complex, complemented by an exponential decay in the maximum absorbance as most of the nanoparticles crashed out of solution (B Figure 4.10).

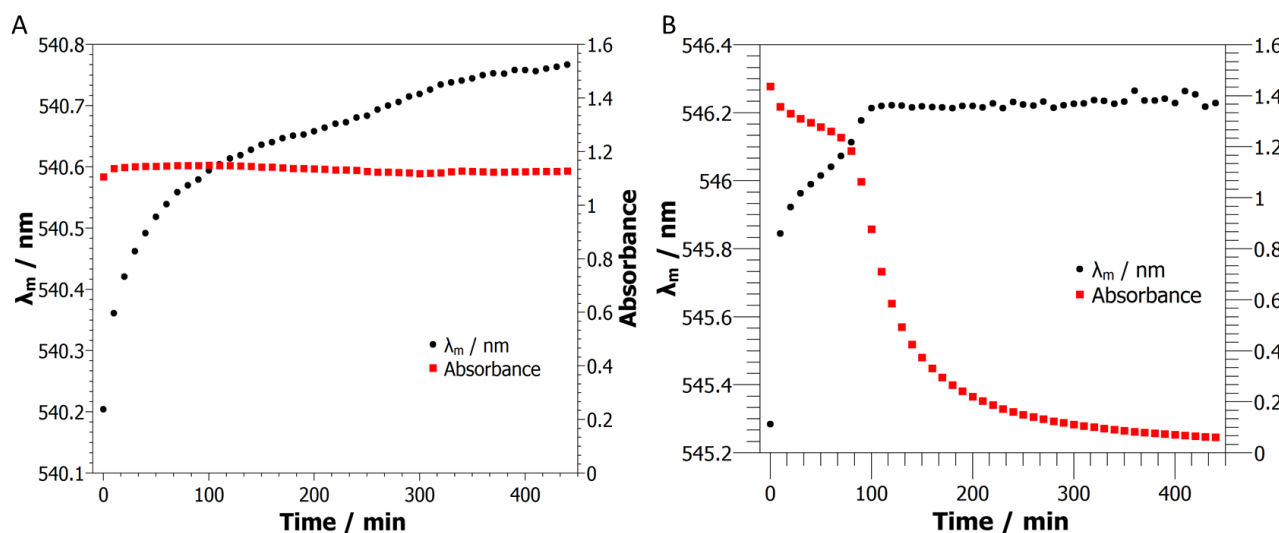


Figure 4.10 Overnight binding of GGzOmpA_{TM} with and without protein induced particle aggregation. UV-Vis data showing the change in the λ_m and max absorbance over time of 1 OD₅₂₅ AuNP samples incubated with 0.8 μM (A) and 1.6 μM (B) GGzOmpA_{TM}. The absorbance was taken from the maximum of the LSPR peak.

Dynamic Light Scattering

Assembly of GGzOmpA_{TM}, with filler and the subsequent binding of a monoclonal antibody was followed by DLS. The step wise building of the protein layers on the surface can be clearly seen (Figure 4.11). The protein layer thicknesses of 12.13 nm \pm 0.68 and 19.26 nm \pm 2.04, for GGzOmpA_{TM} with filler and after mAb binding respectively, are in good agreement with the published lengths of GGzOmpA_{TM} arrays (13.5 nm) and GGzOmpA_{TM}-IgG complexes (17.5 nm) on planar surfaces (Brun et al., 2015).

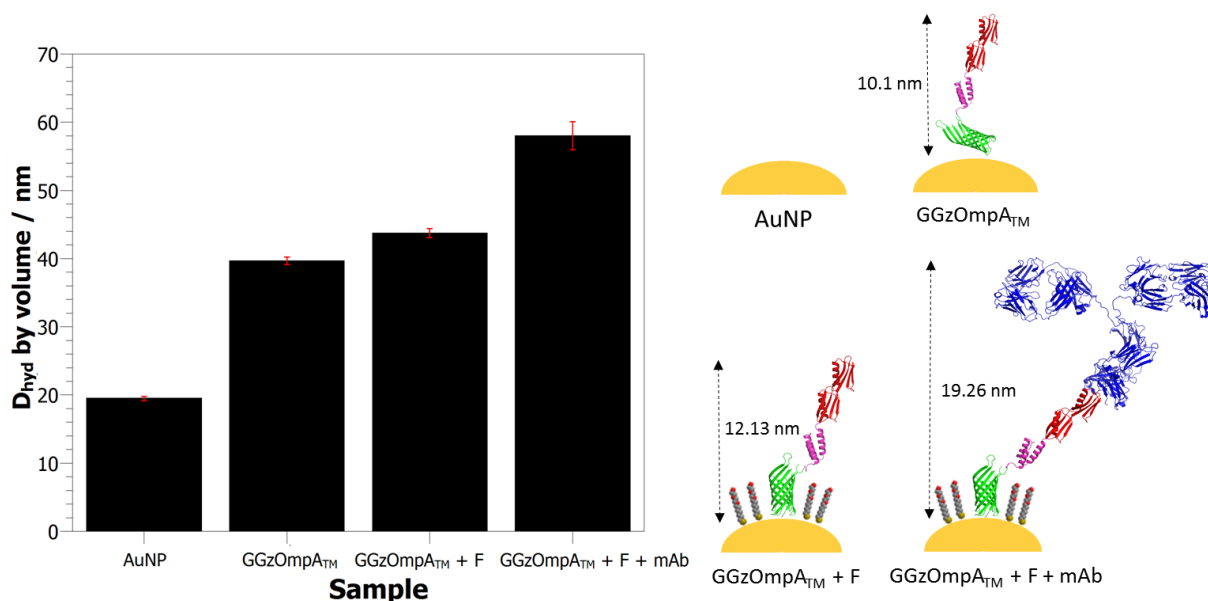


Figure 4.11. Assembly of GGzOmpA_{TM} proteins on AuNPs and binding to a mAb. A stepwise increase in the mean D_{hyd} of AuNPs after GGzOmpA_{TM} assembly and binding to a monoclonal antibody can be seen by DLS (left). On the right is a schematic representation of the protein assembly and mAb binding on the nanoparticle surface with the average protein layer thickness calculated from the increase in the D_{hyd} . Error bars represent the standard error of the mean based upon 3 samples.

Binding specificity

To test the specificity of the monoclonal antibody binding, AuNPs conjugated with wtOmpA_{TM}, cysOmpA_{TM} and GGzOmpA_{TM} were incubated with approximately 1 μ M of a monoclonal IgG before analysing by DLS. The GGzOmpA_{TM} particles exhibited a much greater size increase than the wtOmpA_{TM} and cysOmpA_{TM} indicating that a specific interaction occurred between the antibody binding domains and the IgG protein (Figure 4.12).

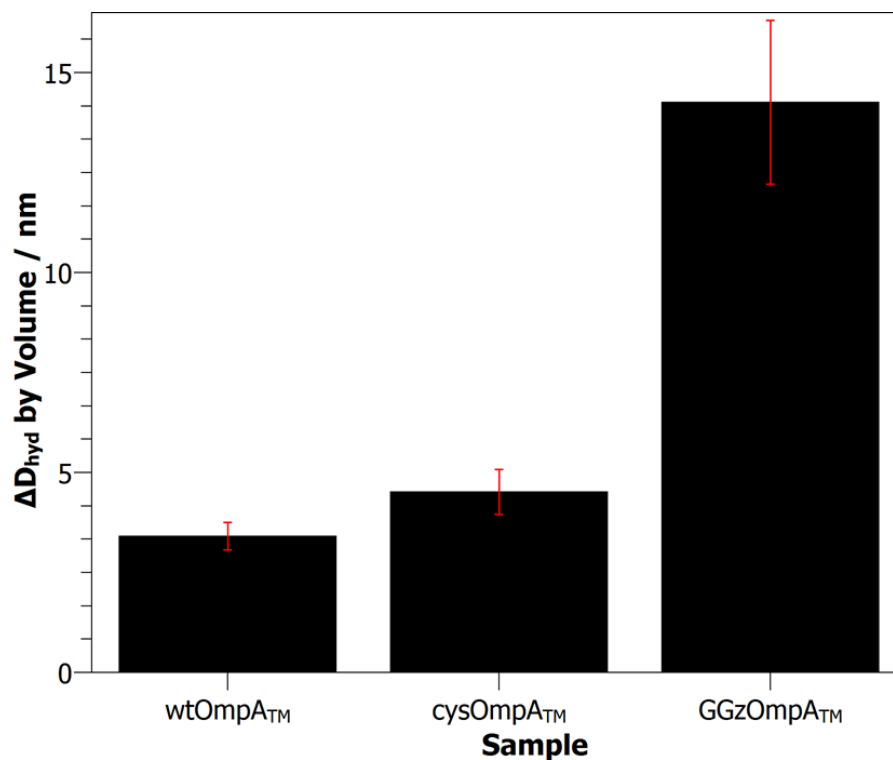


Figure 4.12. Increase in the D_{hyd} of protein conjugated AuNPs after incubation with IgG. 1 OD_{525nm} protein conjugated particles, with filler, were incubated with 1 μM of a monoclonal IgG for 10 minutes. Excess antibody was removed by centrifugation before measurement of the particle size by DLS. Error bars represent the standard error of the mean based upon 3 samples.

Agarose Gel Electrophoresis

GGzOmpA_{TM} conjugated particles migrate slower than cysOmpA_{TM} particles when run on a 1% agarose gel (A Figure 4.13). This is consistent with the much larger size of the particles seen by DLS (C Figure 4.13). The shift in the λ_m of the GGzOmpA_{TM} particles is much greater than for cysOmpA_{TM} but the apparent binding of filler is similar for both samples (B Figure 4.13). Although the electrophoresis band appears tighter for GGzOmpA_{TM} there is also more of a “tail” which is suggestive of aggregates in the sample.

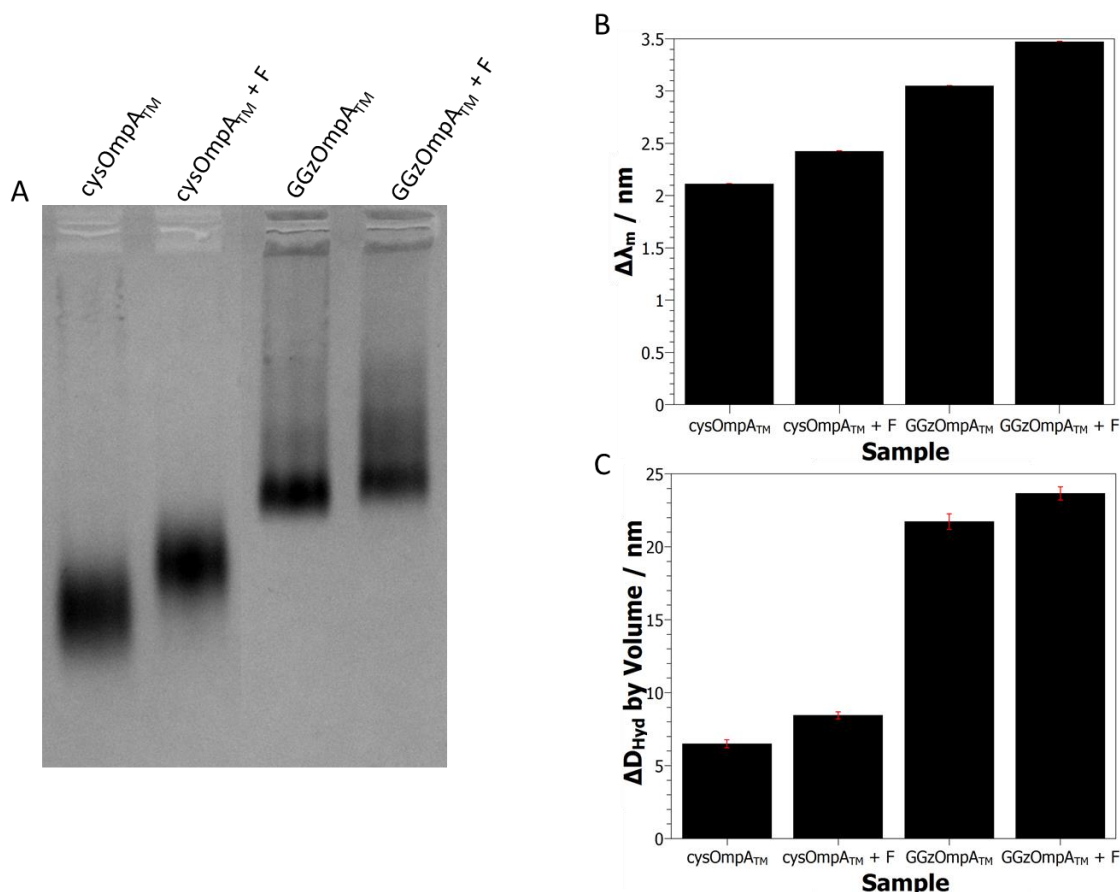


Figure 4.13. Agarose gel electrophoresis (A), UV-Vis spectroscopy (B) and DLS (C) results for GGz and cysOmpA_{TM} conjugated particles. 20 nm AuNP at 10 OD_{525nm} were incubated with 8 μM protein overnight before separating on a 1% agarose gel. “F” designates 8 μM filler addition after 30 minutes of protein incubation. UV-Vis spectroscopy and DLS samples were split into three aliquots, centrifuged and resuspended at 1 OD_{525nm} to remove any residual protein or filler before measuring. Error bars represent the standard error of the mean based upon duplicate measurements.

Transmission Electron Microscopy

GGzOmpA_{TM} conjugated nanoparticles were excised from an agarose gel, extracted with water and visualised using negative stain TEM. The isolated particles showed a halo of protein structures extending outwards from the surface for several nanometers (B Figure 4.14). The number of protein structures visible was variable between particles.

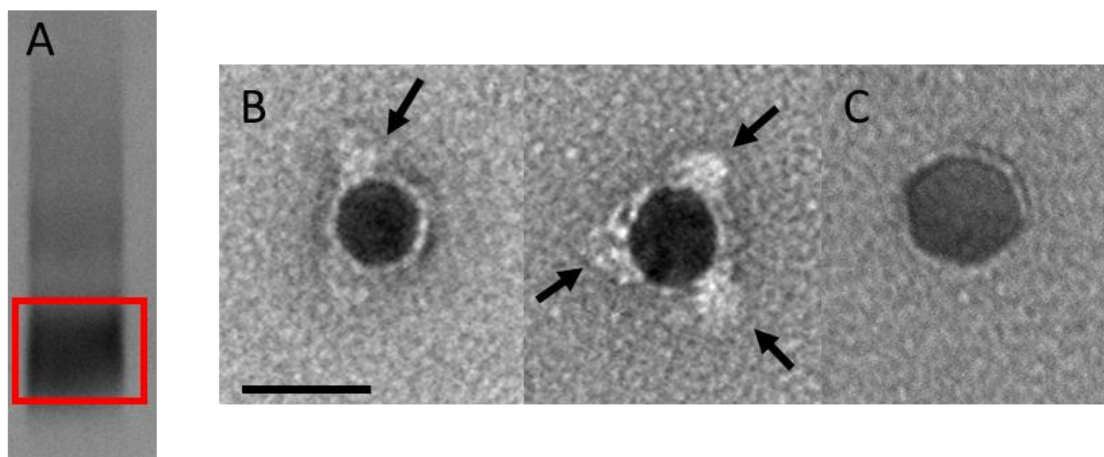


Figure 4.14 Transmission electron microscopy of GGzOmpATM conjugated nanoparticles.

(A) Excised agarose gel band, indicated by the red box, and representative negative stain micrographs of the conjugated particles (B) and a bare AuNP control (C). Arrows indicate the protein objects on the surface. Scale bar = 25 nm.

Stability

The stability of GGzOmpATM particles was investigated by UV-Vis spectroscopy and DLS. Conjugated particles, with and without filler, were challenged with increasing concentrations of NaBH₄ and the D_{hyd} measured by DLS. An increase in the D_{hyd} was seen with the addition of 1 mM NaBH₄, in agreement with cys and wtOmpATM experiments. Above 1 mM the size of the particles decreased when only protein was present on the surface. Particles with filler, however, were stable up to 20 mM NaBH₄ (A Figure 4.15). The effect of increasing ionic strength on GGzOmpATM conjugated particles with filler was analysed by UV-Vis spectroscopy. Only minor changes in the spectrum were observed up to 1 M NaCl concentrations (B Figure 4.15). The shift in the λ_{m} correlated with the changing refractive index of the buffer, suggesting that the sensitivity of the surface plasmon to the bulk refractive index was a factor in the spectral changes (C Figure 4.15).

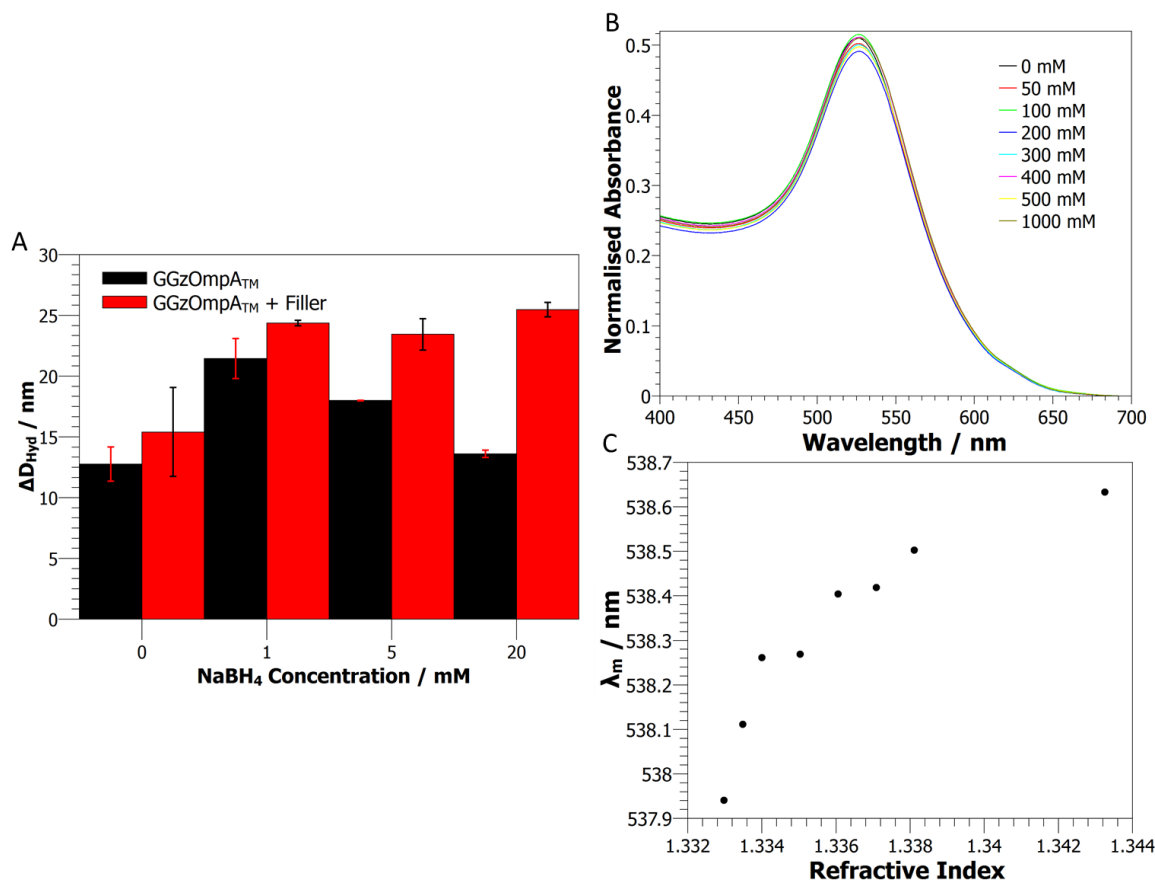


Figure 4.15. Stability data for GGzOmpA_{TM} conjugated AuNPs with and without filler. (A) DLS data showing the change in the D_{hyd} with increasing $NaBH_4$ concentration for GGzOmpA_{TM} particles, with and without filler. (B) UV-Vis spectra of GGzOmpA_{TM} particles with filler after incubation with increasing $NaCl$ concentration. (C) The λ_m for each of the spectra was calculated and plotted against the refractive index of the salt solution.

Small Angle Neutron Scattering

Small angle neutron scattering was carried out on 20 nm gold nanoparticles at different stages of GGzOmpA_{TM} assembly. Data was collected on bare particles, GGzOmpA_{TM} and GGzOmpA_{TM} + ThioAlkylPEG coated particles. The coated particles were prepared by overnight incubation with their respective molecules after which the AuNPs were pelleted by centrifugation and resuspended in D₂O. The resuspended samples were dialysed for 72 hours, with two solvent changes, against D₂O to ensure complete removal of any remaining H₂O and unbound residual protein or filler molecules. H₂O was not used as the solvent in these experiments due to its high incoherent scattering which would significantly reduce the coherent scattering signal from the particles. Initially, it was decided to measure the protein coated AuNPs in two different contrasts, D₂O and gold matched water (AuMW, 73% D₂O, 27% H₂O). This would have allowed

the protein component of the particles to be measured independently of the AuNP, thus providing much greater information on the protein layer structure. Unfortunately, measurements of the AuMW samples provided almost no signal. This was most likely due to the very low concentration of bound protein, in the region of 0.2 mg/ml, with SANS experiments usually requiring a minimum of ~2 mg/ml protein to produce significant levels of scattering (Clifton et al., 2012). The AuNP samples were analysed by DLS before carrying out SANS experiments. This showed that the samples remained homogeneous after dialysis into D₂O (Figure 4.16).

To see if the GGzOmpA_{TM} protein was still biologically active after assembly, the protein + filler coated particle sample was incubated with 1 µM of an alkaline phosphatase conjugated IgG (EMD Millipore, UK, used due to availability) for one hour before carrying out a further SANS measurement.

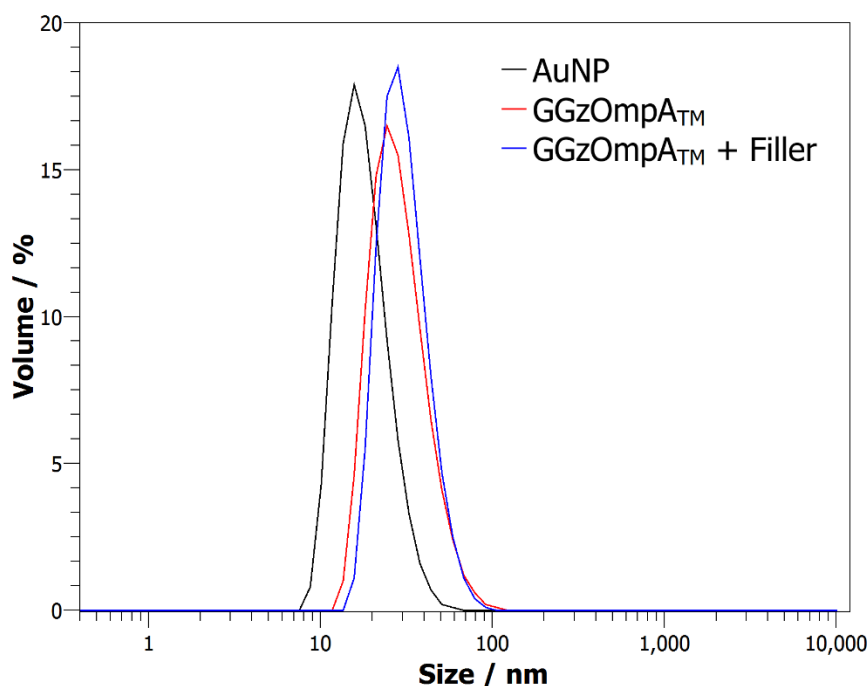


Figure 4.16 Particle size distributions, by DLS, of the nanoparticle samples used for SANS after 48 hours dialysis in D₂O. A 5 µl aliquot of each sample, at 10 OD_{525nm}, was taken and diluted in to 45 µl of D₂O before analysis using the Malvern Zetasizer Nano S. The viscosity of D₂O at 25°C was used for analysis.

Scattering Data

The radial scattering data from the detector was reduced to a one-dimensional scattering profile and the scattering of a buffer sample subtracted. Examination of the scattering profiles shows that the samples are weakly scattering, especially at high Q (blue box Figure 4.17). This was particularly problematic for the AuNP and the GGzOmpA_{TM}

samples where subtraction of the buffer blank resulted in negative intensity values at high Q. There were enough remaining points to carry out analysis of the AuNP data, however, this was not the case for GGzOmpA_{TM}. To correct for over-subtraction the data set was shifted upwards by adding a constant 1.5×10^{-3} . A comparison of the low Q region of the samples, also known as the Guinier region, (red box Figure 4.17) provides information on how the size of the particles changes with protein addition. There is a significant shift in this region after GGzOmpA_{TM} addition (red squares) on the AuNP surface (black circles), however, addition of the filler and antibody appeared to have a much smaller effect.

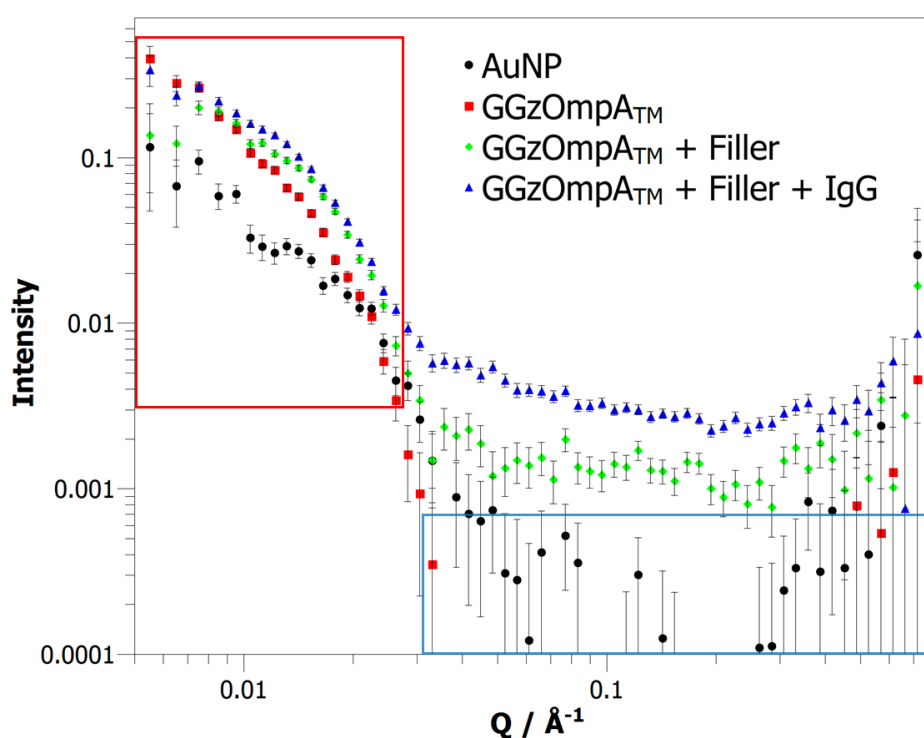


Figure 4.17 Raw SANS scattering data for the 20 nm AuNPs and GGzOmpA_{TM} coated particles. The red box indicates the Guinier region of the scattering profile, which contains the majority of the particle size information. A large shift in the AuNP scattering can be seen on addition of the protein on the surface, indicating an increase in the particle size. The blue box indicates the high Q region where the AuNP and GGzOmpA_{TM} data sets have been over-subtracted by the buffer blank, therefore removing some of the data points.

More detailed analysis of the particle size was carried out by performing an indirect Fourier transform of the one-dimensional scattering profile using the BayesApp web server (Hansen, 2012). This converts the data from reciprocal space, momentum transfer in \AA^{-1} , to real space, in \AA , to give the pair distance distribution function or $p(r)$. The $p(r)$ plot describes the probability of finding a point of distance r away from any given point

from within the particle. From this information, the radius of gyration, R_g , can be calculated, the maximum distance between points in the particle, D_{max} , obtained and information on the shape of the particles deduced. Analysis of the AuNP scattering data resulted in an $p(r)$ plot with two peaks centred at ~ 150 and 320 \AA (B

Figure 4.18). The location of the second peak and the increased error of the points would suggest that it is due to transient interparticle interactions. Examination of the low Q region of the scattering profile, where information on larger scale structures is contained, shows that the first five points appear separate from the rest of the data. Carrying out the data analysis without these points resulted in a $p(r)$ plot with a single peak, D_{max} of 207.25 \AA and R_g of 87.30 \AA (D

Figure 4.18). A hump remained at around 180 \AA which suggests that some contribution from the interparticle interactions remained.

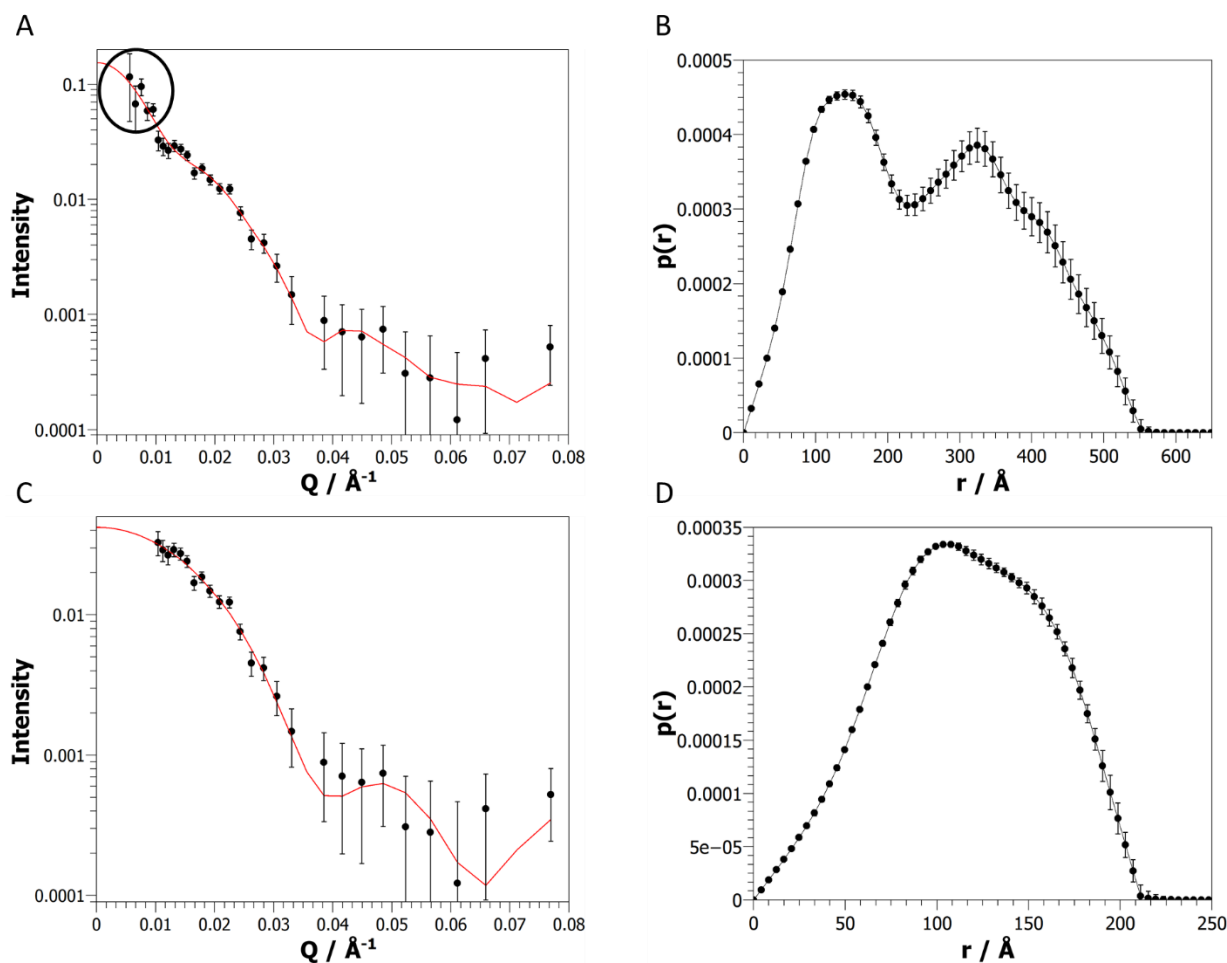


Figure 4.18 Fitting of the 20 nm AuNP SANS scattering profile by the BayesApp program is shown before (A) and after (C) truncation of the data at low Q . The pair distance distribution functions generated by the program are shown on the right of the corresponding data set (B and D). The red lines are the BayesApp fits of the data and the truncated data points are indicated by the black circle. Removal of the first five data points resulted in a significant change in the $p(r)$, with a large reduction in the D_{\max} and removal of the second peak.

The $p(r)$ plots generated from analysis of the protein coated AuNPs revealed that the particle sizes were similar with D_{\max} values of 382.98, 367.26 and 359.86 Å for the GGzOmpA_{TM}, GGzOmpA_{TM} + Filler and after IgG addition respectively (B Figure 4.20). The reducing size of the particles shows the opposite trend to the DLS results in Section 4.2.2. For the GGzOmpA_{TM} and GGzOmpA_{TM} + Filler coated particles this could be due to the differences in the way the two techniques “see” the particles. In a SANS experiment the scattering contributions from both the AuNP and protein

components of the system are measured and any scattering contributions from the solvent are subtracted. As the volume fraction of the protein layer is much lower than the nanoparticle, the scattering of the AuNP will dominate the scattering profile. This was shown by the lack of scattering when measuring the protein coated particles in gold matched water. In contrast, DLS measures the dynamics of the particles in solution and calculates their size from the diffusion coefficient, that is obtained from the correlation curve. Therefore, the DLS data describes solvated particles that are tumbling through the solution. The shape of the $p(r)$ plot generated for the GGzOmpA_{TM} coated particles shows that there is heterogeneity in the particle size when coated with protein alone (black circles Figure 4.20). This was reduced but not completely removed by the addition of the filler molecule (red circles Figure 4.20). While the maximum size of the particles is smaller than the DLS experiments, the D_{\max} of 367.26 Å for the GGzOmpA_{TM} + filler particles was still larger than expected for a single protein standing on the particle surface (Figure 4.19). This would be ~342.35 Å using the published height of GGzOmpA_{TM} in a planar array (135 Å) (Brun et al., 2015).

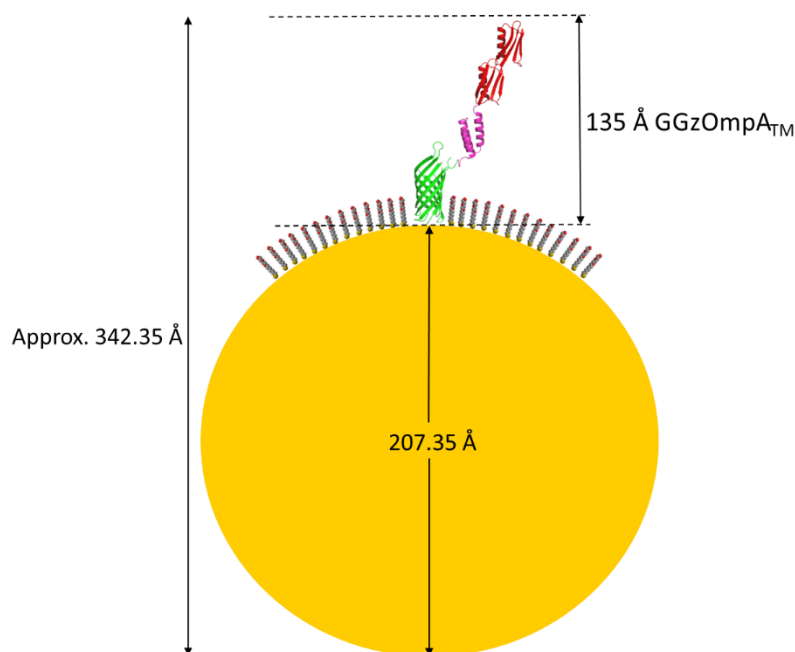


Figure 4.19 Schematic diagram of an AuNP with a single GGzOmpA_{TM} protein standing on the surface. The particle size was taken from the SANS data of the bare gold nanoparticles and the protein height was taken from (Brun et al., 2015).

No antibody binding was observed in this experiment, however the generated $p(r)$ plot did show a small change in the size distribution. The R_g and D_{\max} values obtained from the BayesApp analysis are summarised in Table 4.2. The anomalous results from the

SANS experiments could have been due to poor samples, poor data quality from the weak scattering intensity or very possibly from a combination of these two factors.

Table 4.2 Summary of the particle size parameters calculated from the SANS data.

<i>Sample</i>	<i>Radius of Gyration</i> $(R_g) / \text{Å}$	<i>Maximum Distance</i> $(D_{max}) / \text{Å}$
<i>AuNP</i>	87.30 ± 0.59	207.35 ± 4.56
<i>GGzOmpA_{TM}</i>	140.78 ± 1.43	382.98 ± 6.10
<i>GGzOmpA_{TM} + Filler</i>	127.24 ± 1.10	367.26 ± 6.20
<i>GGzOmpA_{TM} + Filler</i> <i>+ IgG</i>	130.67 ± 0.53	359.86 ± 3.06

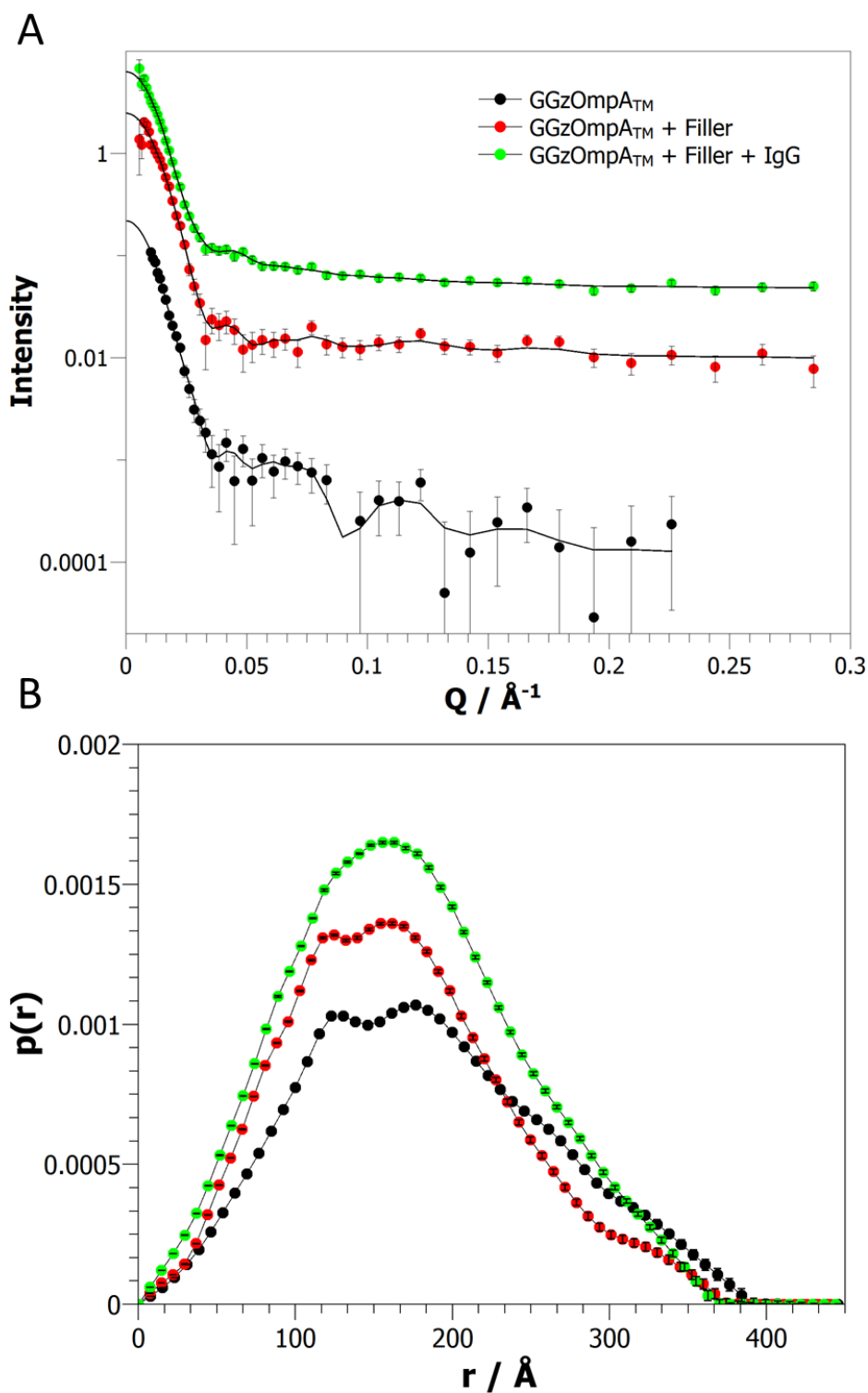


Figure 4.20 (A) Protein coated AuNP neutron scattering data with the BayesApp fits represented by the solid lines. (B) The $p(r)$ plots generated from the indirect Fourier transform of the data. The lower scattering intensity of the GGzOmpA_{TM} coated particles at high Q (black circles) resulted in much greater error and fewer data points being used for analysis. The data has been offset for clarity. The resulting $p(r)$ plots did not show a significant change in the size of the particles.

Analytical Ultracentrifugation

Further analysis of GGzOmpA_{TM} conjugated nanoparticles was carried out by analytical ultracentrifugation. AuNPs conjugated with GGzOmpA_{TM}, both with and without filler, were measured in comparison to citrate coated AuNPs. All the particles displayed a single sedimentation distribution peak indicating that a single species was present in each sample. Addition of GGzOmpA_{TM} decreases the sedimentation coefficient with a further decrease seen after the addition of the SH-C11-OEG6 filler molecule on to the surface (Figure 4.21). As discussed in Section 1.6.2 the sedimentation coefficient is proportional to the buoyant mass divided by the frictional coefficient of the particle. Addition of the protein on the surface will cause a greater increase in the frictional coefficient than the buoyant mass, leading to a lower sedimentation coefficient. This data agrees with the step wise increase in size seen by DLS. Interestingly addition of the protein and the filler on the surface appears to sharpen the peak suggesting that the functionalised AuNP samples have a lower polydispersity.

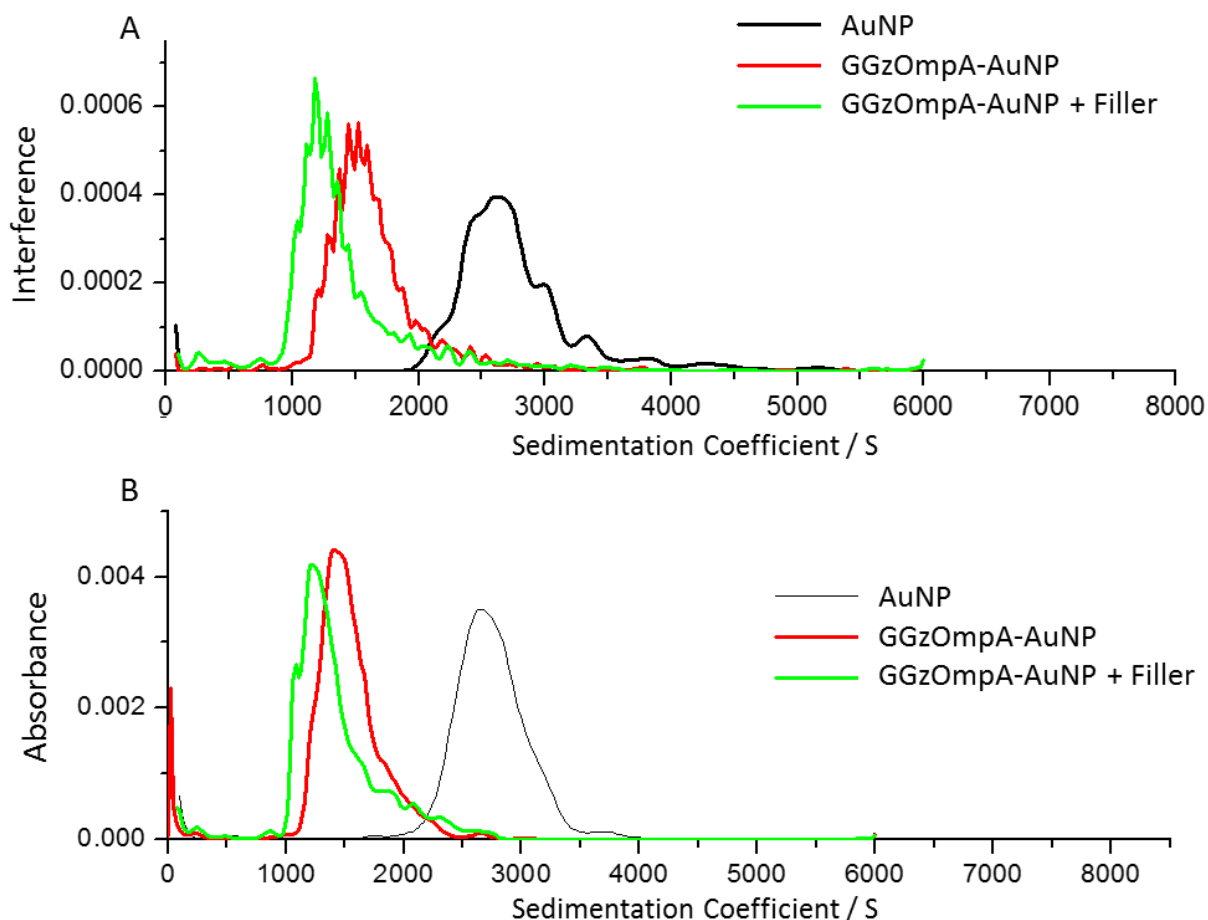


Figure 4.21 Sedimentation coefficient distributions of GGzOmpA_{TM} conjugated particles.

20 nm AuNPs at 1 OD_{525nm} were incubated with 0.8 μ M protein overnight, for samples with filler 0.8 μ M filler solution was added after 30 minutes. Before sedimentation velocity experiments were carried out, excess protein was removed by centrifugation of the particles and resuspension in protein free buffer. Data acquired using both interference (A) and absorbance (B) detectors was in good agreement. Absorbance was measured at 530 nm.

4.3 Discussion

Kinetic Analysis Indicates a Multi-Stage Binding Process

Both the pseudo-second order rate constants (k_2) and initial rates for wild type and cysOmpA_{TM} are quite similar, with the rates for cysOmpA_{TM} being 1.5 and 1.4 times larger respectively. This suggests that the addition of the cysteine has a minimal effect on protein binding in the early stages and up to tens of minutes. In contrast, proteins incubated with TCEP show more complex behaviour. The rate constants (k_2) for both proteins at 0.22 μ M TCEP are within error, however there is a much larger difference

between the initial rates, which are 19.73 and $95.24 \times 10^{-3} \text{ s}^{-1} \text{ nm}$ respectively for wild type and cysOmpA_{TM}. This would suggest that the kinetics are affected by multiple factors that differ between the proteins and change as binding progresses from the seconds to minutes timescales.

It was not expected that wtOmpA_{TM} kinetics would be affected by TCEP addition and whilst there are increases in the cysOmpA_{TM} binding rates this would suggest that the cysteine plays a more important role in the stabilisation of the protein layer (discussed later in further detail). The unexpected TCEP kinetics changes are possibly due to two secondary affects. Firstly, TCEP was purchased as a hydrochloride salt, so when dissolved the resulting solution has a pH of 2.5. Although buffers were used in the experiments a decrease of 1-2 pH units was observed using an indicator strip. Secondly, agarose gel electrophoresis carried out on citrate coated AuNPs incubated with TCEP showed an increase in mobility, indicative of surface charge modification (C Figure 4.3). It has been shown that changing the buffer pH affects protein binding to gold nanoparticles, with increased binding at lower pH (Kelly et al., 2015; Wang et al., 2016), binding can also be adjusted by changing the particle surface charge (Lundqvist et al., 2008).

Examination of the OmpA_{TM} structure provides evidence for possible electrostatic interactions. Although the overall charge is negative above pH 6.1 there are two basic residues, K73 and R102, that form a positively charged surface at the extracellular end of the barrel (A Figure 4.22). Analysis of the surface charge by APBS (Baker et al., 2001) shows an increase in the positive electrostatic potential of this surface when lowering the pH from 8 to 6 (B Figure 4.22), this is mirrored by a reduction in the net negative charge from -3.6 to +0.4 (C Figure 4.22). Lysine residues have been shown to mediate binding to negatively charged gold nanoparticles for the soluble proteins Ubiquitin and GB3 (Wang et al., 2016). Therefore, the rate increase is most likely due to higher electrostatic attraction between wtOmpA_{TM} and the AuNPs facilitated by a reduction in the overall net negative charge of the protein coupled with an increase in the nanoparticle surface charge.

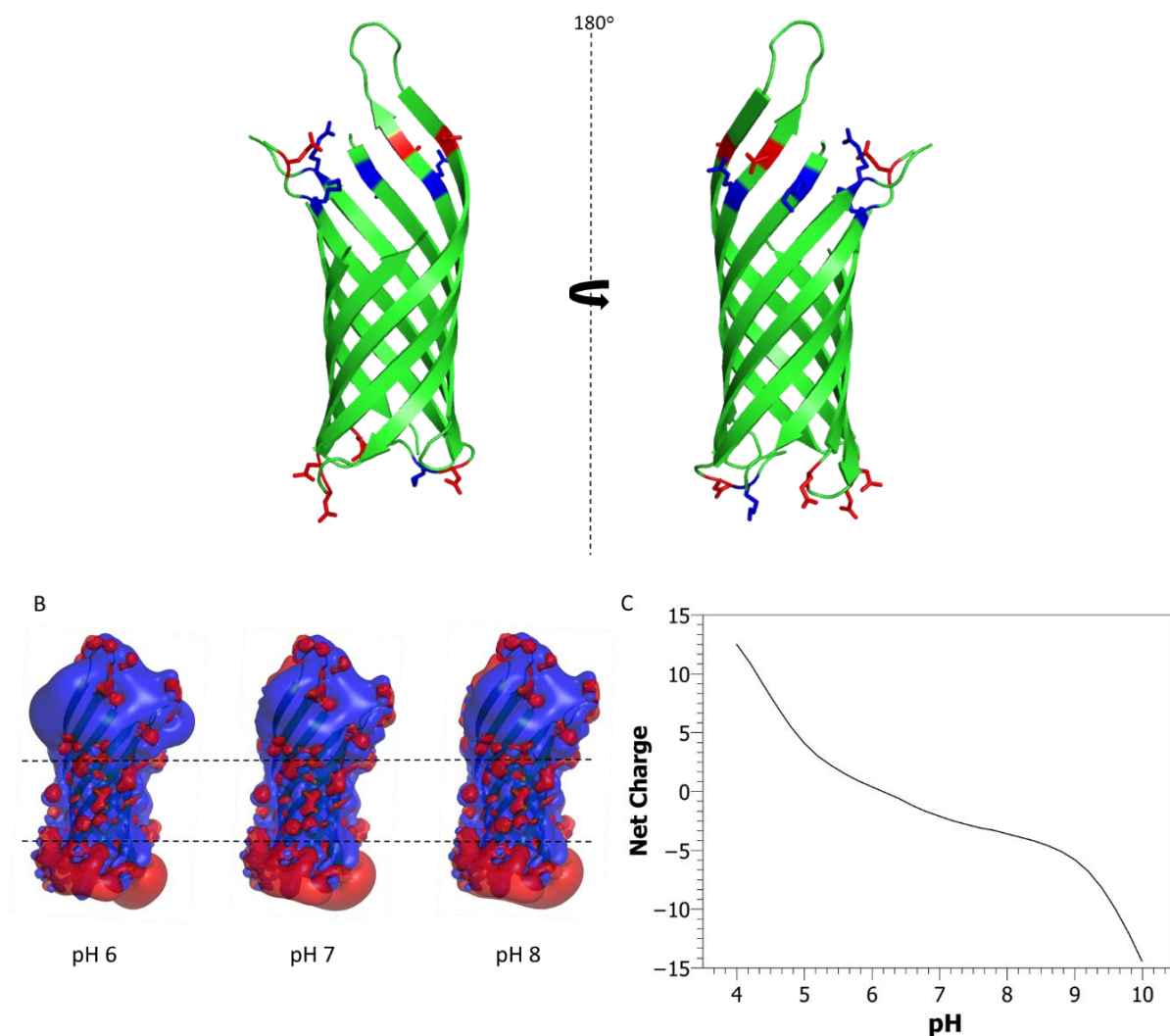


Figure 4.22 Examination of the solvent accessible surface charge and net charge of the OmpA_{TM} transmembrane domain. (A) Acidic residues, aspartate and glutamate, are coloured in red with basic residues, arginine and lysine, coloured in blue. (B) The electrostatic isosurface at different pHs was generated using APBS with contours shown between -1kT (red) and +1kT (blue), the dashed lines indicate the membrane region. (C) Net charge was estimated using the pKa values for each residue in isolation.

Although wtOmpA_{TM} kinetics are quite strongly affected by TCEP addition, the estimated steady state binding from the kinetics data are similar, with $\Delta\lambda_e$ values of 0.98 and 1.15 with and without TCEP respectively. This would suggest that TCEP has a smaller effect on the binding affinity of wtOmpA_{TM} and structure of the protein layers on the nanoparticle surface. cysOmpA_{TM} kinetics appear more complex, at 0.22 μ M TCEP there is a huge disparity between the initial rate and the pseudo-second order rate constant, much larger than seen with wtOmpA_{TM}. The second order rate constants for both proteins, however, are remarkably similar at 14.76 and $14.86 \times 10^{-3} \text{ s}^{-1} \text{ nm}^{-1}$ for wtOmpA_{TM} and cysOmpA_{TM} respectively. The much higher initial rate could be due to

an increase in the concentration of active cysOmpA_{TM}, after disulphide reduction and possibly a stronger interaction between the reduced protein and the citrate coated AuNPs. The variation in the initial rate and rate constants for both proteins indicates that after initial binding, > 10 seconds, the binding rate becomes progressively limited by protein reorganisation and Vroman type protein displacement on the surface (Vroman, 1962). Vroman effects take place when poorly bound proteins are displaced from the surface. This was first observed with blood serum proteins, small, highly-mobile proteins initially bound to the surface and were slowly replaced with larger proteins that had a higher surface affinity.

Cysteine Addition Stabilises Protein-NP Conjugates

The higher stability exhibited by cysOmpA_{TM}-AuNP conjugates is indicative of binding through the cysteine residue. However, the reduction in $\Delta\lambda_m$ when challenged with NaBH₄ (A Figure 4.7), would suggest that there are also non-specifically bound proteins on the surface. The increase in D_{hyd} after 1 mM NaBH₄ addition, observed for cysOmpA_{TM} and GGzOmpA_{TM}, could be due to protein reorganisation after poorly bound protein is removed from the surface, which would be consistent with the protein loss seen by UV-Vis spectroscopy. The addition of the thioAlkylPEG filler blocks NaBH₄ competition up to 20 mM, with no change in the D_{hyd} observed for Cys and GGzOmpA_{TM} (C Figure 4.7 and Figure 4.15). AuNPs conjugated with GGzOmpA_{TM} + filler also exhibit high stability in salt solutions, being resistant to aggregation up to 1 M NaCl. The SANS data for GGzOmpA_{TM} + filler particles also showed the fewest observed aggregates. The increase in stability after both protein and filler addition provides evidence for an organised monolayer where oriented OmpA_{TM} domains interact cooperatively with the surrounding filler molecules.

Cysteine Addition Increases Equilibrium Binding

The addition of a cysteine residue into the base of the OmpA_{TM} structure increased steady state binding of the protein to the nanoparticle surface. This could be due to two cysteine driven effects, firstly, the formation of an energetically favourable gold-thiol bond between the protein and nanoparticle causing irreversible binding to the surface. As the system is in a dynamic equilibrium of bound and unbound protein this would shift the equilibrium toward more bound protein on the surface. Secondly, a standing protein orientation, driven by the cysteine's location in one of the periplasmic loops, would reduce the footprint on the surface, increasing the number of proteins needed to

reach surface saturation. Furthermore, proteins in a standing orientation would maximise favourable interactions with neighbouring proteins in the hydrophobic core of the barrel, decreasing enthalpy, and reduce the number of hydrophobic residues exposed to the surrounding water, increasing entropy.

The equilibrium binding of wild type and cysOmpA_{TM} after incubation with TCEP gives further evidence of a cysteine related effect. TCEP is a strong reducing agent used to selectively break disulphide bonds, resulting in proteins with a reactive cysteine residue so should increase the active concentration of cysOmpA_{TM} while having no effect on the active wtOmpA_{TM} concentration (Begg and Speicher, 1999; Burns et al., 1991). The shift in the λ_m at equilibrium with 0.8 μ M protein was 34.7% larger for cysOmpA_{TM} after TCEP incubation compared with 14.8% for wtOmpA_{TM}. While this provides evidence of cysteine binding to the nanoparticle, the increase in apparent wtOmpA_{TM} binding suggests that TCEP also causes changes to the surface structure of the nanoparticle.

When analysing adsorption equilibrium data, adsorption isotherm models are traditionally used to extract thermodynamic and mechanistic information about the system. The most commonly used isotherm models are Langmuir, Freundlich and Brunauer-Emmett-Teller (Brunauer et al., 1938; Freundlich, 1906; Langmuir, 1916). Each model carries a set of assumptions which must be met for the results to be valid. For the Langmuir isotherm there are four assumptions, firstly, all of the adsorption sites on the surface are equivalent, secondly, each site only binds a single molecule, thirdly, dynamic reversible equilibrium is established and finally there are no interactions between the bound molecules. Protein adsorption data has previously been fitted to Langmuir isotherms, however, most do not satisfy the requirements needed for the model to be valid (Latour, 2015). This is particularly evident in the protein-nanoparticle system studied here. If you consider the typical gold nanoparticles used in these experiments, the surface is covered in a stabilising citrate coating. Park *et al* have shown that the citrate molecules form a hydrogen bonded network across the surface, which also bind preferentially to the (111) crystal faces (Park and Shumaker-Parry, 2014). Therefore, the binding energy required for protein adsorption will vary, depending on the geometry of the crystal face and the level of disruption to the H-bond network through citrate displacement. It is also possible for multiple protein orientations and transitions to occur between different states on the surface. Finally, it is not possible to

discount protein-protein interactions between closely localised proteins and in the case of the cysteine modified protein they may be irreversibly bound to the nanoparticle.

Great effort has been spent on developing more appropriate models for use with protein systems, taking in to account surface crowding, protein-protein interactions, multiple state transitions and multilayer formation among other factors. A review by Rabe *et al* discusses at length many of the models in use (Rabe *et al.*, 2011). For an equilibrium model to be suitable it must have a representative expression of the free energy of the system, taking into account enthalpic contributions from inter-protein and protein-surface interactions and also entropic contributions from the protein conformation and its interaction with external solvent. This is a particularly difficult and complex problem, especially as the number of states and the different interactions present in the OmpA_{TM}-nanoparticle system are not defined. It is possible to develop a model for a specific adsorption mechanism by using arbitrary parameters for the internal states and carrying out Monte Carlo simulations to model the system, as shown by Szöllösi *et al* (Szöllösi *et al.*, 2004), however, this is beyond the scope of this study.

Using prior knowledge of OmpA_{TM} assembly on planar gold surfaces from SPR and neutron reflectometry (Brun *et al.*, 2008; Shah *et al.*, 2007; Terrettaz *et al.*, 2002) a possible mechanistic explanation of the differences in cysOmpA and wtOmpA equilibrium binding can be proposed (Figure 4.23). At low protein concentrations both proteins exhibit poorly ordered sub-monolayer coverages, as the protein concentration increases wtOmpA_{TM} quickly forms a complete monolayer of proteins with several different conformations on the surface. In contrast cysOmpA_{TM} proteins, when in close proximity, assemble into more ordered domains, mediated by cysteine binding, thus reducing the protein footprint and allowing a more dense protein layer on the nanoparticle surface.

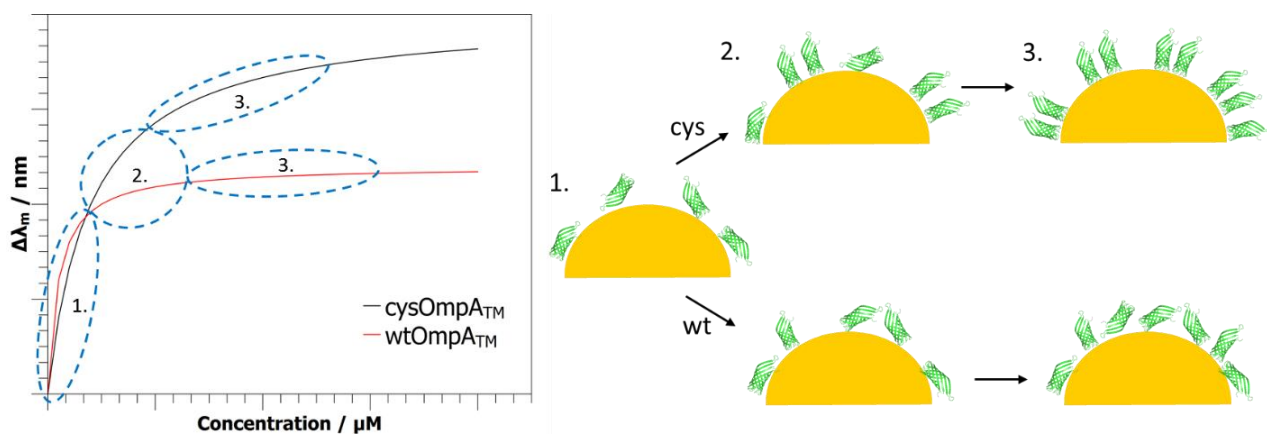


Figure 4.23 The three proposed binding regimes of wtOmpA_{TM} and cysOmpA_{TM} on gold nanoparticles. At low concentrations both proteins form sub-monolayers (1), as the protein concentration increases some orientational order forms for the cysOmpA_{TM} layer allowing for more protein to bind (2). The disordered wtOmpA_{TM} monolayer saturates quickly whereas cysOmpA_{TM} continues to slowly pack more protein on the surface (3).

Cysteine OmpA_{TM} Fusion Proteins Assemble in an Oriented Fashion

The thickness of the GGzOmpA_{TM} protein layer on gold nanoparticles, measured by DLS, was in good agreement with published neutron reflectometry data showing GGzOmpA_{TM} standing on a planar surface, embedded in a monolayer of filler molecules (Table 4.3) (Brun et al., 2015). The increase in layer thickness with the addition of the filler molecule is consistent with the filler assisting in protein orientation. Filler addition covering the particle surface was supported by overnight kinetics data of cysOmpA_{TM} addition. Without filler, the protein surface continues to evolve slowly, even after 15 hours, conversely if filler has been added it quickly blocks the remaining surface and stabilises the particle with no further increase in the λ_m (Figure 4.1). The same trend of increasing particle size as GGzOmpA_{TM} and filler are assembled on the surface was also observed by AUC.

Table 4.3 Comparison of protein layer thicknesses for GGzOmpA on planar and nanoparticle surfaces. †data from (Brun et al., 2015) ‡data from this study

<i>Sample</i>	<i>Protein Layer Thickness / nm</i>
<i>GGzOmpA_{TM} – DLS[‡]</i>	10.1 ± 0.53
<i>GGzOmpA_{TM} + Filler – NR[†]</i>	13.5 ± 0.16
<i>GGzOmpA_{TM} + Filler – DLS[‡]</i>	12.13 ± 0.68
<i>GGzOmpA_{TM} + mAb – NR[†]</i>	17.5 ± 0.11
<i>GGzOmpA_{TM} + mAb – DLS[‡]</i>	19.26 ± 2.04

Further evidence of orientated assembly is provided by retention of the antibody binding functionality of GGzOmpA_{TM}, shown by DLS. Binding was specific to the tandem B domains with very little binding observed for the cysOmpA_{TM} scaffold (Figure 4.12). Once again the thickness of the GGzOmpA_{TM}-mAb layer agreed with NR data on planar surfaces (Table 4.3).

The reproducibility of the DLS results and the tight width of the AUC peaks is a good indicator of uniform GGzOmpA_{TM} coverage on the nanoparticles. It is interesting to note that the width of the AUC peaks appears to reduce on protein and then filler addition. This could be due to selection of only the protein-nanoparticle conjugates when centrifuging the samples to remove excess protein. Alternatively, the sedimentation of the AuNPs could be more sensitive to variation in the citrate coating than the protein coating.

Multi-Domain Fusion Proteins Cause Aggregation at High Protein:NP Ratios

Protein induced particle aggregation was observed with GGzOmpA_{TM} suggesting that the formation of multi-layer structures is possible at high protein:nanoparticle ratios, i.e. above 638:1 (Figure 4.9). Aggregation was not observed with wild type and cysOmpA_{TM} at ratios above 638:1 (data not shown) indicating that this was due to the GGz domains of the fusion protein. Analysis of the overnight kinetics of GGzOmpA_{TM} at a ratio of 1276:1 provides some insight into the aggregation mechanism. Initial binding is rapid, <20 minutes, then slowing between 20-100 minutes, after which there is an inflection point, indicative of a secondary binding event, coupled with an exponential loss of the nanoparticles from free solution (B in Figure 4.10). This would suggest that initially GGzOmpA_{TM} binds quickly to the nanoparticle surface, forming a

sub monolayer. The binding rate then slows as proteins reorganise on the surface, however, due to the high protein concentration a number of non-specific binding events occur, probably between the GGz domains and proteins on the surface, forming multi-layer structures. The uncontrolled formation of multiple protein layers could then result in the precipitation of AuNP-Protein conjugates from the solution.

4.4 Conclusions

In this chapter it has been shown that incorporation of a single cysteine residue into a periplasmic loop of OmpA_{TM} results in increased steady state binding to AuNPs. This is most likely due to the formation of an energetically favourable cysteine-gold bond and a more organised protein layer on the surface. Effects on the binding kinetics were much less prevalent, suggesting that the cysteine addition plays a more minor role in initial protein binding. Electrostatic interactions were shown to be important, with significant effects on both the kinetics and equilibrium binding observed when changing the surface charge of both proteins and nanoparticles.

The correct orientation of the GGzOmpA_{TM} fusion protein on the nanoparticle surface was shown by DLS and SANS. Protein layer thicknesses indicative of a fully organised GGzOmpA_{TM} monolayer were only achieved after addition of the thioAlkylPEG filler molecule, which is consistent with previously published NR data (Brun et al., 2008; Le Brun et al., 2011). Surface display of the antibody binding domains was confirmed by specific binding to a monoclonal IgG.

Exchange experiments with NaBH₄ showed that addition of a cysteine in the OmpA_{TM} domain increased the stability of the protein:nanoparticle complexes. Increased stability was also observed after addition of the thioAlkylPEG filler for both the cysOmpA_{TM} and GGzOmpA_{TM} proteins, providing further evidence of an ordered protein layer that is stabilised through multiple cooperative filler-protein and protein-protein interactions.

5 USING PROTEIN- NANOPARTICLE ASSEMBLIES FOR BIOSENSING

5.1 Introduction

Gold coated glass surfaces have been extensively used for the detection of analytes and other biomolecular interactions, particularly in surface plasmon resonance biosensors (Homola, 2003). Although SPR has become routinely used for measuring binding affinities and kinetics, with several companies offering SPR machines, the equipment remains prohibitively expensive for many laboratories.

Gold nanoparticle assemblies on glass surfaces have been explored as a more cost effective substrate for sensing applications, using UV-Vis spectroscopy (Kumari and Moirangthem, 2016; Nath and Chilkoti, 2004) and surface enhanced raman spectroscopy (SERS) (Freeman et al., 1995; Kaminska et al., 2008; Seitz et al., 2003). Binding of biomolecules, such as streptavidin and antibodies, has been observed by spectroscopy, both from shifts in the LSPR peak λ_{\max} and increases the absorbance (Fujiwara et al., 2006; Mayer and Hafner, 2011; Nath and Chilkoti, 2002). The sensitivity of gold nanoparticle arrays, when using both LSPR and SERS, is affected by several factors including the particle shape, size and density on the surface (Masson and Yockell-Lelièvre, 2014; Nath and Chilkoti, 2004). These parameters can be adjusted to optimise the sensor surface for the analyte in question.

More highly ordered nanostructured surfaces have also been investigated for use in biosensing applications, for example, nanohole and nanoprism arrays (Dahlin, 2015; Huang et al., 2005). As discussed in Section 1.4, periodic arrays are usually generated by lithographic methods. Nanohole and nanoprism sensors have been fabricated using nanosphere lithography, where the assembly of colloidal particles on a surface is used as the mask in the lithographic process (Hulteen and Van Duyne, 1995; Malekian et al., 2017). The size of the colloids and their orientation on the surface can be used to adjust both the feature size and the order of the resulting arrays. Once again, the optical properties of these surfaces, such as LSPR and SERS, have been exploited for sensing (Cui et al., 2008; Sannomiya et al., 2011).

Gold nanoparticles in solution are commonly used for biosensing and have been utilised in several formats, including lateral flow and colorimetric assays. The lateral flow assay (LFA) is one of the most established and widely used rapid diagnostic tests in the world with a huge variety of detectable analytes. The majority of lateral flow based tests use antibody conjugated AuNPs as the detection molecule (Koczula and Gallotta, 2016; Sajid et al., 2015). Briefly, a typical lateral flow assay consists of a porous membrane

strip, normally nitrocellulose, with two antibody lines deposited at one end. One line containing a control antibody, the second a capture antibody. Antibody conjugated gold nanoparticles are mixed with the sample and added to the opposite end of the membrane strip. The mixture is transported down the membrane by capillary action and the AuNP conjugates, with associated antigen, will bind to the capture antibody in a sandwich configuration, resulting in the build-up of a characteristic red line (Figure 5.1).

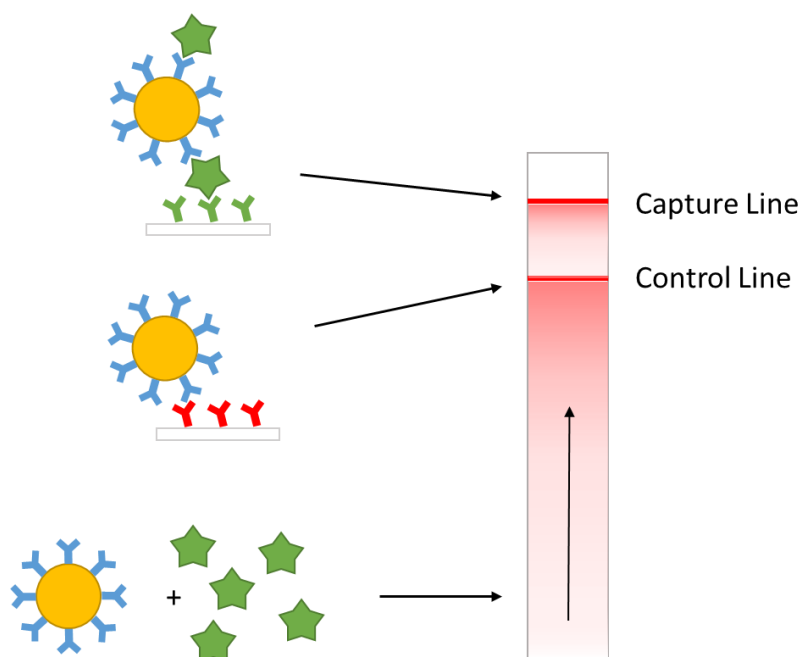


Figure 5.1 Schematic of a lateral flow assay. The nanoparticle conjugate and antigen are mixed together and added at the bottom of the strip. When the particles reach the antibody lines some will bind to the control antibody and those with a bound antigen will be bound by the capture antibody.

More recently, changes in the LSPR have been used for the detection of biomolecular interactions by colorimetric methods. Many of these assays observe AuNP aggregation caused by interparticle crosslinking; where protein-protein interactions link the particles through multivalent interactions (Figure 5.2), or destabilisation induced aggregation, where binding of the analyte causes a loss of particle stability (Sato et al., 2003; Thanh and Rosenzweig, 2002; Tsai et al., 2005; Zhao et al., 2008). Particle aggregation causes a large shift in the LSPR, with a visible colour change from red to purple, or a complete loss of the particles from solution which can be easily detected with simple instrumentation.

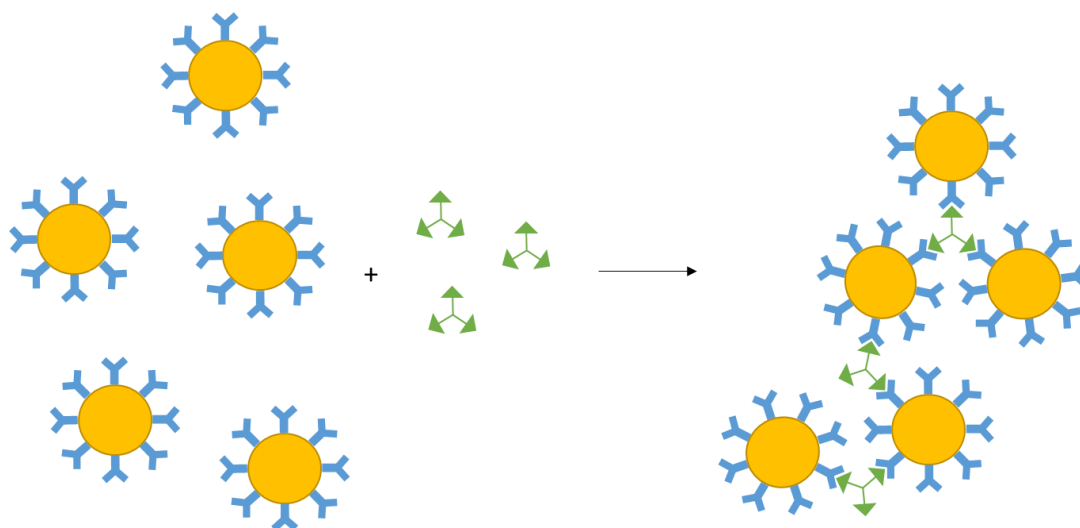


Figure 5.2 Gold nanoparticle aggregation induced by crosslinking with a multivalent analyte.

In this study the binding of antigens and antibodies to engineered OmpA_{TM} assemblies on gold nanoparticles was investigated. Detection was carried out using several methods, both with the AuNPs in solution and deposited on a glass surface. Antibody binding to gold nanoparticle-glass surfaces with assembled GGzOmpA_{TM} monolayers was assessed by fluorescence microscopy. The assembled protein surface was imaged after the addition of an Alexafluor 488 labelled IgG and the fluorescence intensity compared with a cysOmpA_{TM} control surface. GGzOmpA_{TM} mediates antibody binding through tandem B1 domains from Streptococcal protein G (GG), which were inserted at the N-terminus of circularly permuted OmpA_{TM}. The B domains of Streptococcal protein G are repeated small antibody binding domains consisting of an alpha helix packed against a four stranded beta sheet (Figure 5.3) (Derrick and Wigley, 1994; Gronenborn et al., 1991). Binding to the Fc region of IgG occurs between the alpha helix and third beta strand (Gronenborn and Clore, 1993). The alpha helical Z domain linker, which is a modified B domain from Staphylococcal protein A (Nilsson et al., 1987), separates the two regions of the fusion protein to aid folding (Brun et al., 2015). In Chapter 4 GGzOmpA_{TM} conjugated AuNPs were shown to bind IgG in solution by DLS, suggesting their potential application in the aforementioned diagnostic technologies.

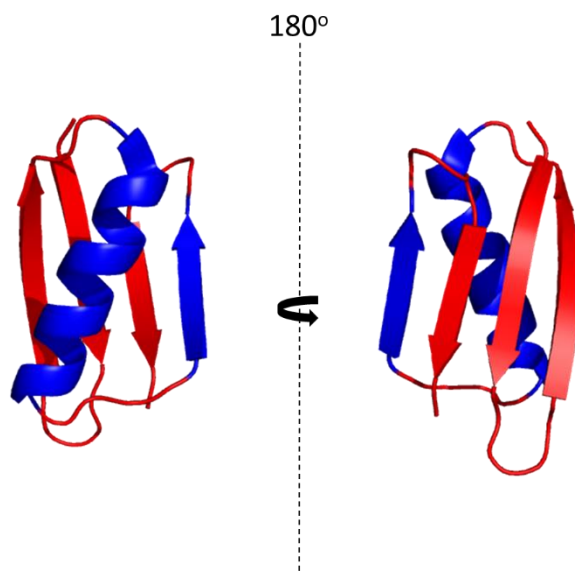


Figure 5.3 B1 domain from group G *Streptococci* with the helix and beta strand involved in antibody binding indicated in blue. (PDB ID:3GB1)

Diagnosis of influenza is of high importance with seasonal infections leading to the deaths of 250,000 to 500,000 people per year (WHO, n.d.). Pandemic strains of influenza type A have the potential to endanger large populations as seen during the Spanish flu of 1918 and the Asian flu of 1957 (Potter, 2001). Influenza nucleoprotein is the preferred target for detection over the variable surface glycoproteins, as it is both highly conserved between strains and type specific for influenza A and B (Brun et al., 2015; Farris et al., 2010).

Therefore, binding of an antigen, Influenza A nucleoprotein, to engineered OmpA_{TM} assemblies on AuNPs was investigated both in solution and on glass surfaces. The functional domain used to detect FluA NP was a single chain variable fragment, scFv, inserted at the N-terminus of a circularly permuted OmpA_{TM} scaffold. The scFv domain was connected to OmpA_{TM} by an alpha helical linker domain (unpublished, kindly shared by Professor J. Sayers, Sheffield University). An scFv is the smallest domain of an antibody that displays functional antigen binding. Selection of a functional scFv against a desired antigen is carried out *in vitro* through phage display of an scFv library and affinity selection techniques (Ahmad et al., 2012). The chosen antibody fragment can then be produced recombinantly in *E. coli*. Gold nanoparticles functionalised with a cysteine mutant scFv have previously been shown to bind rabbit IgG in an aggregation assay by Liu *et al* (Liu et al., 2009). To observe FluA NP binding to scFvOmpA_{TM} conjugated AuNPs, UV-Vis spectroscopy, DLS and transmission electron microscopy

were carried out. Following the analysis of FluA NP binding in solution two different biosensing approaches were used as a proof of concept for using scFvOmpA_{TM} conjugated AuNPs in a clinically relevant assay. The first assay utilised gold nanoparticle functionalised glass capillaries as a simple LSPR biosensor for detecting FluA NP binding to scFvOmpA_{TM} via the shift in the barycentric mean wavelength (λ_m) (Figure 5.4). Capillary based AuNP biosensors have been proposed as an inexpensive alternative to conventional SPR machines (Kumari and Moirangthem, 2016). The second assay developed was a lateral flow assay, which was chosen as it is an industry standard diagnostic test. The LFA, which is described in more detail in section 5.2, consisted of α -FluA NP and α -human IgG antibodies, as the capture and control lines respectively (Figure 5.9).

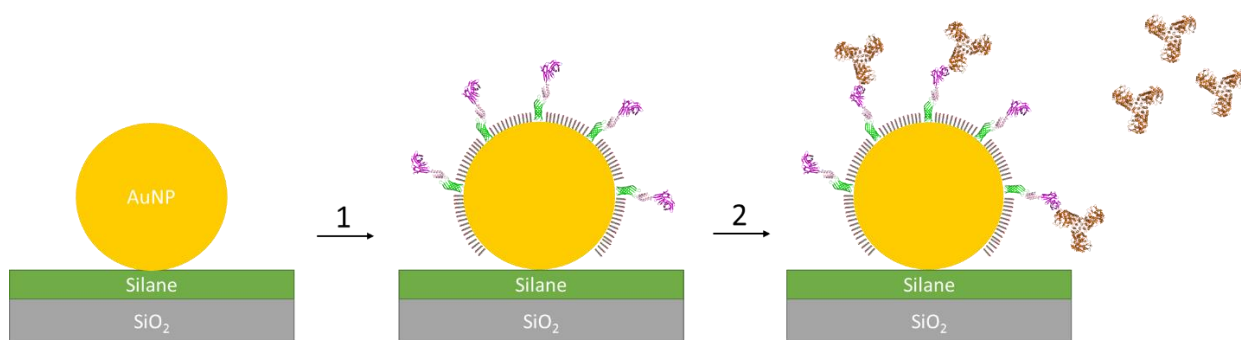


Figure 5.4 Schematic of LSPR biosensor assay for FluA NP detection. 1. After gold nanoparticle deposition on the glass capillary scFvOmpA_{TM} was co-assembled on the surface with a thioalkylPEG filler molecule. 2. The functional scFv domain can then bind free FluA NP in solution which can be observed as a shift in the λ_m .

5.2 Results

5.2.1 Antibody Binding to Engineered OmpA Monolayers

Binding of an Alexafluor 488 conjugated IgG to GGzOmpA_{TM} and cysOmpA_{TM} monolayers assembled on gold nanoparticle-glass surfaces was assessed by fluorescence microscopy. The experiment was carried out on a 20 nm gold nanoparticle functionalised glass coverslip (see Section 2.18 for method) which was placed in a four-well holder to allow different proteins to be assembled on separate areas of the same coverslip. One well was left blank to measure the background fluorescence of the surface. The GGzOmpA_{TM} surface exhibited strong fluorescence after incubation with the Alexafluor 488 conjugated IgG in comparison to the cysOmpA_{TM} surface (Figure 5.5). Very little background fluorescence was observed for the bare gold-glass surface.

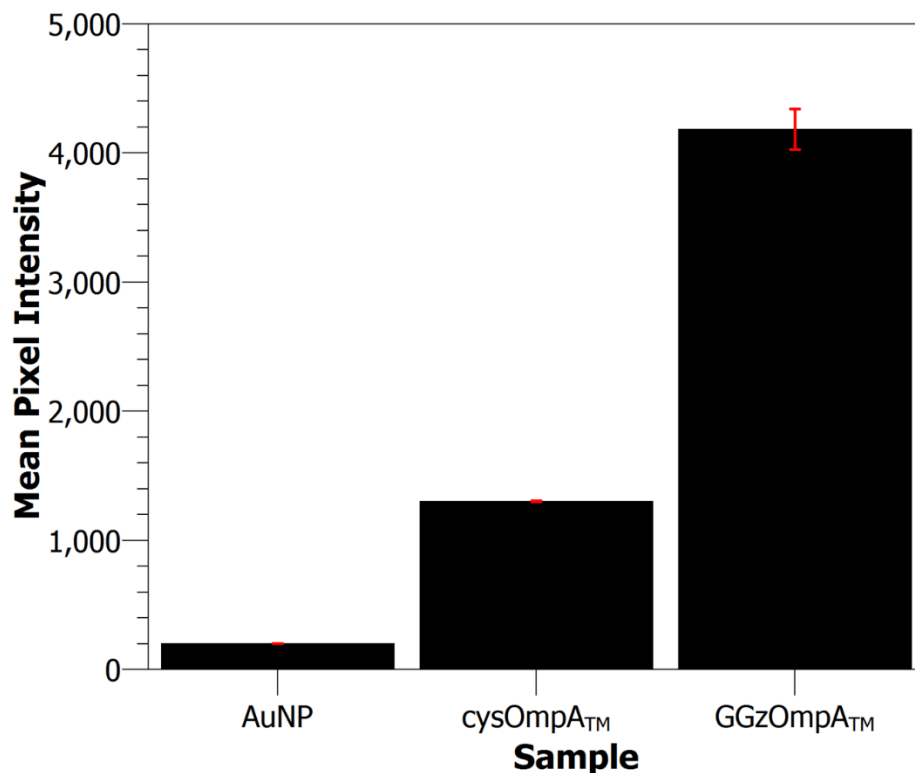


Figure 5.5. Fluorescence intensity of cysOmpA_{TM} and GGzOmpA_{TM} surfaces after incubation with Alexafluor 488 conjugated rabbit IgG. The protein surfaces were incubated with 100 µg/ml Alexafluor 488 conjugated IgG for 10 minutes before washing twice with TBS-Tween-20 and imaging. The AuNP surface showed almost no background fluorescence without antibody addition. Some non-specific binding was observed on the cysOmpA_{TM} control surface. Mean pixel intensity calculated from 3 random fields of view using ImageJ.

5.2.2 Antigen Binding to Single Chain Variable Fragment Fusion Proteins

In Solution

The binding of recombinant Influenza A nucleoprotein (FluA NP) to a single chain variable fragment-OmpA_{TM} fusion protein (scFvOmpA_{TM}) was investigated by UV-Vis spectroscopy, DLS and TEM. The scFvOmpA_{TM} protein and thioAlkylPEG filler were assembled on 20 nm AuNPs using the same method as GGzOmpA_{TM}. A significant shift in the LSPR peak of the nanoparticles was observed after incubation with FluA NP and a corresponding shift in the size of the particles was also seen by DLS (C and D Figure 5.6). An IgAPOmpA_{TM} control protein, without the scFv domain, was also assembled on 20 nm AuNPs with no significant change observed in either the LSPR spectra or particle size distribution after incubation with FluA NP (A and B Figure 5.6). Negative stain TEM images revealed large protein objects bound to the scFvOmpA_{TM} particles that were not present before addition of FluA NP (E and F Figure 5.6)

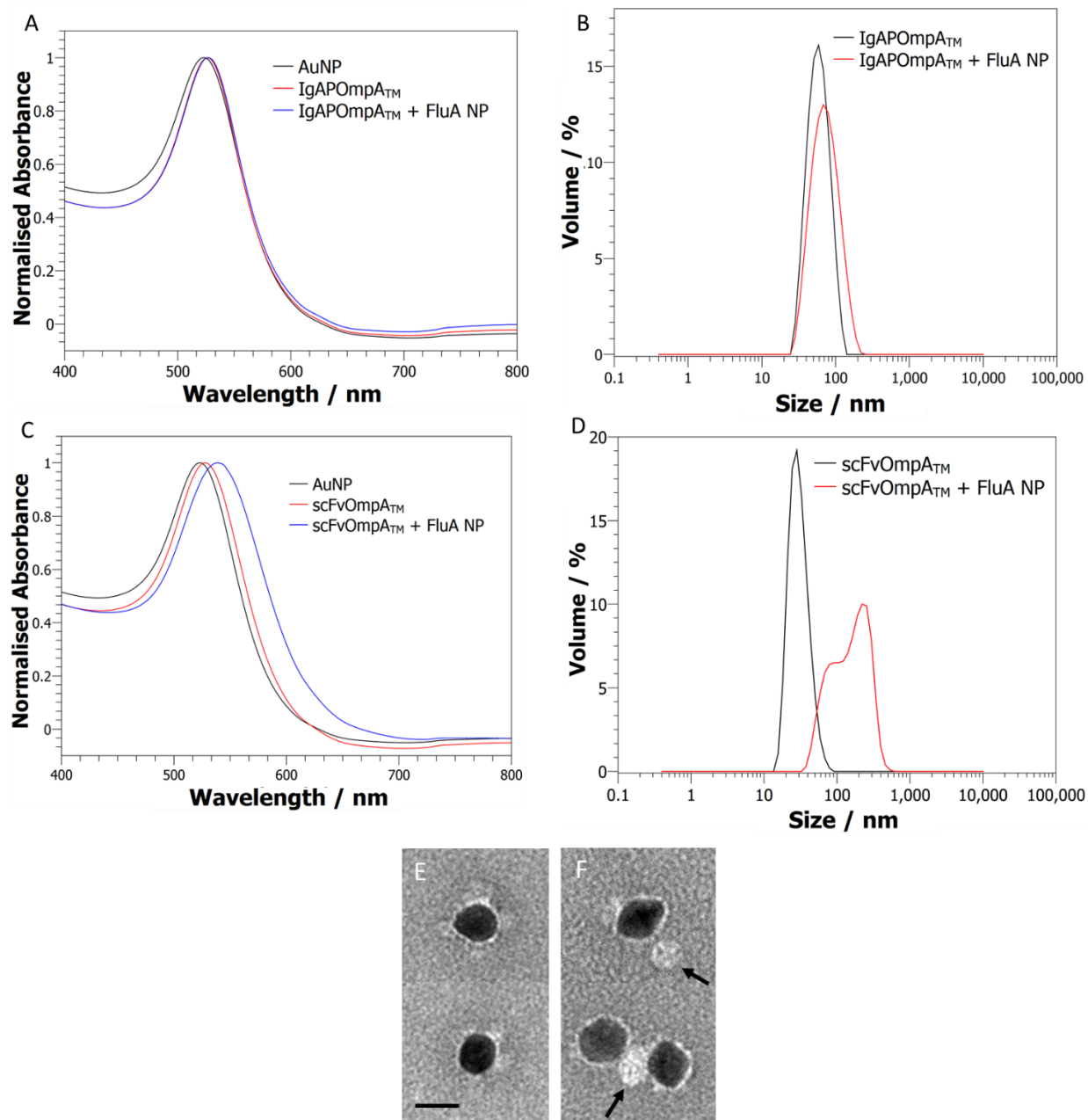


Figure 5.6. Influenza A nucleoprotein binding to scFvOmpA_{TM} and IgAPOmpA_{TM} conjugated AuNPs. The assembly of IgAPOmpA_{TM} (A) and scFvOmpA_{TM} (C) on AuNPs, and subsequent incubation with FluA NP was followed by UV-vis spectroscopy. (B) and (D) show the corresponding particle size distributions, measured by DLS, for IgAPOmpA_{TM} and scFvOmpA_{TM} particles, before and after incubation with FluA NP. Negative stain TEM of scFvOmpA_{TM} particles (E) revealed large protein objects (indicated by arrows) bound to the AuNP conjugates after incubation with FluA NP (F). The IgAPOmpA_{TM} control protein does not contain the scFv domain. 25 nm scale bar.

AuNP Coated Borosilicate Glass Capillaries

Simple LSPR biosensors were made by depositing 20 nm gold nanoparticles on AAPTMS functionalised borosilicate glass capillaries (see Section 2.19 for the method). Nanoparticle deposition was visible on the capillary surface as a uniform, transparent red colouring. UV-Vis spectroscopy of the functionalised capillaries, filled with water, revealed major and minor peaks in the absorbance spectrum at 530 and 628 nm respectively (A Figure 5.7). The sensitivity of the main LSPR peak (530 nm) to changes in the refractive index of the solvent was assessed by measuring the absorbance spectrum, between 400-800 nm, with glycerol:water solutions of increasing glycerol concentration. The barycentric mean (λ_m), calculated between 500-600 nm, increased linearly with the refractive index of the solution in the capillary and had a sensitivity of 39.95 ± 0.02 nm/RI unit, given by the slope of the linear regression.

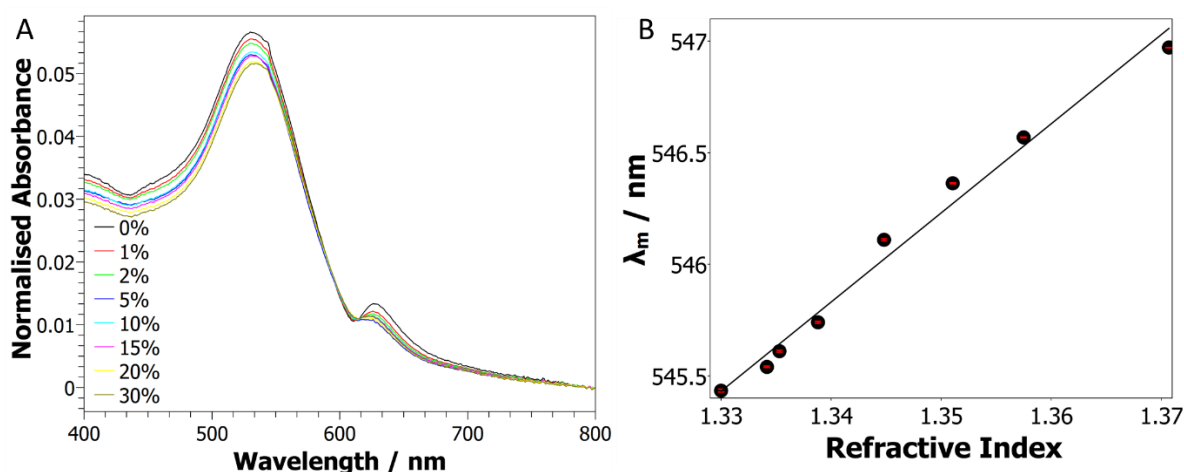


Figure 5.7 Bulk refractive index sensitivity of AuNP functionalised borosilicate glass capillaries. (A) UV-Vis spectra with increasing glycerol stock concentration (% w/w in H₂O). (B) Linear regression analysis of the calculated λ_m versus the refractive index of the glycerol stock. Measurements were carried out in triplicate.

Influenza A Nucleoprotein Binding

FluA NP binding to cysOmpA_{TM} and scFvOmpA_{TM} proteins assembled on AuNP functionalised glass capillaries was investigated by UV-Vis spectroscopy. A syringe was connected to the functionalised capillary via a length of rubber tubing to form a rudimentary flow cell. Injections were carried out *in situ* in the sample environment of the Cary 4E spectrometer prior to taking measurements. Assembly of both proteins on the capillary surface was observed by a shift in the λ_m ($\Delta\lambda_m$). A much greater increase in

$\Delta\lambda_m$ was observed for the scFvOmpA_{TM} surface after incubation with FluA NP than the cysOmpA_{TM} control surface (Figure 5.8).

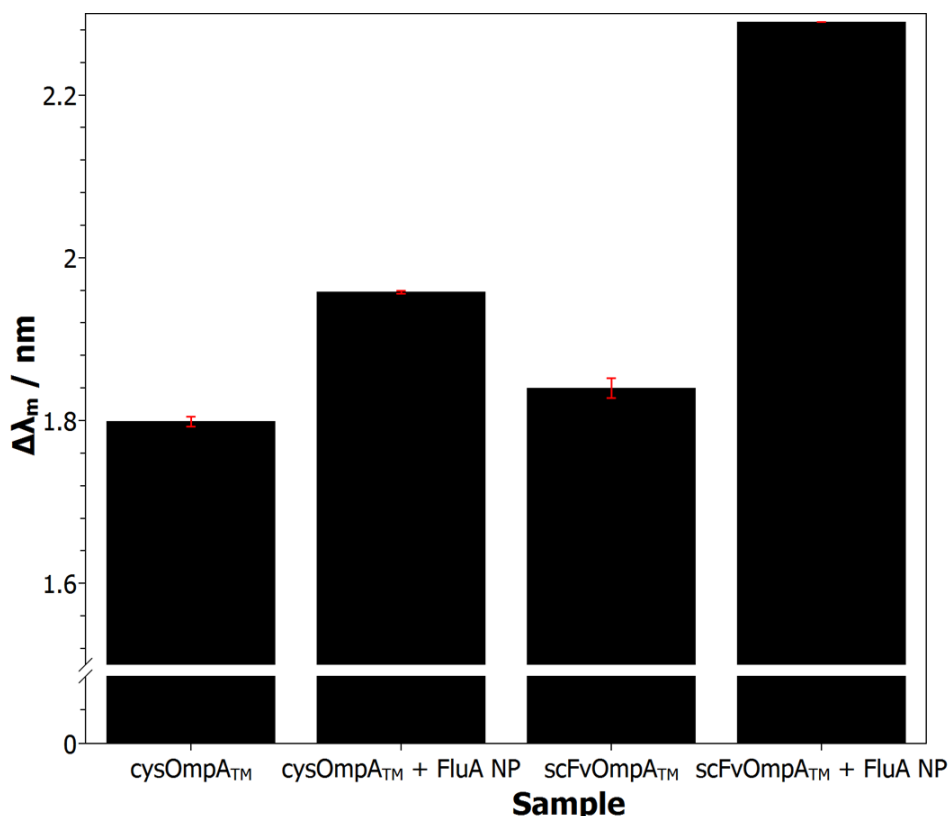


Figure 5.8. The shift in λ_m after assembly of cysOmpA_{TM} and scFvOmpA_{TM} on AuNP functionalised glass capillaries and subsequent incubation with FluA NP. The $\Delta\lambda_m$ was calculated in comparison to a AuNP functionalised capillary filled with water. Proteins were assembled on 20 nm AuNP surfaces with subsequent filler addition. 60 $\mu\text{g} / \text{ml}$ FluA NP was injected in to the capillary and incubated for 5 minutes before taking a measurement. Duplicate spectra were acquired for each sample.

Lateral Flow Assay

A lateral flow assay was developed to detect influenza A nucleoprotein using scFvOmpA_{TM} conjugated nanoparticles. Two antibody lines were bound to nitrocellulose strips, a capture line using a monoclonal α -FluA NP antibody (Hytest) and a second, control line, using a polyclonal α -Human IgG (Abcam). scFvOmpA_{TM} conjugated particles were mixed with FluA NP and transported down the porous nitrocellulose membrane towards the control and capture lines (Figure 5.9).

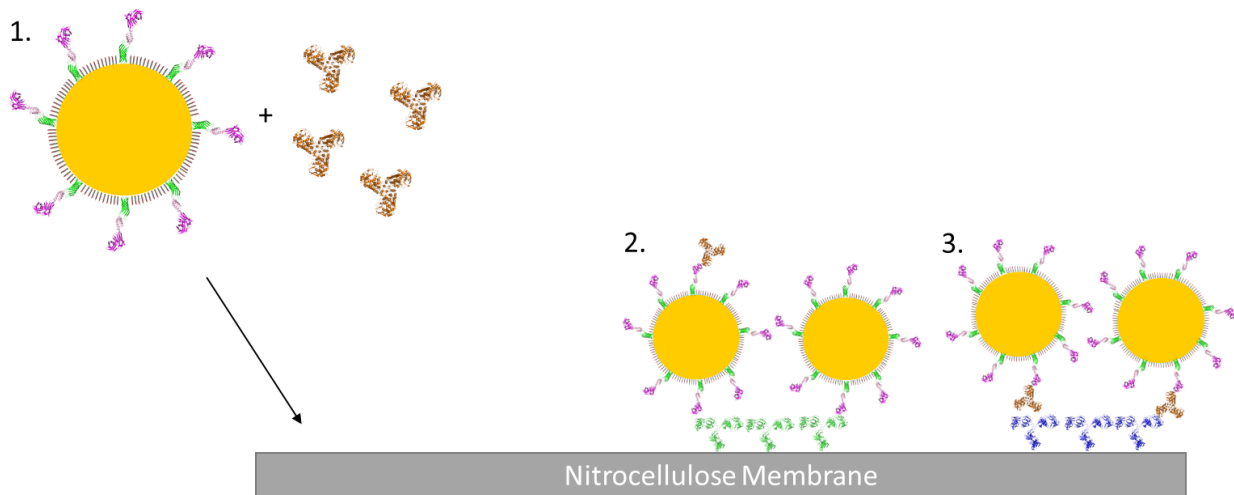


Figure 5.9 Schematic diagram of the influenza A nucleoprotein lateral flow assay. 1. scFvOmpA_{TM} conjugated particles are mixed with recombinant FluA NP and added to the porous nitrocellulose membrane. 2. As the particles move up the strip by capillary action, particles bind to the **control antibody line** via the scFv. 3. Particles with associated FluA NP bind to the **capture antibody line** through the FluA NP. Binding is detected by the formation of a characteristic red line on the strip.

Detection of recombinant FluA NP was achieved with a minimum observable concentration of 500 ng/ml (strips 1-4 Figure 5.10). scFvOmpA_{TM} conjugated particles did not show any non-specific binding when incubated with respiratory syncytial virus nucleoprotein, producing only a control line on the lateral flow strip (strip 6 Figure 5.10). Neither capture or control lines were observed when negative control particles conjugated with IgAPOmpA_{TM} were incubated with nucleoprotein and run on a lateral flow strip (strip 7 Figure 5.10).

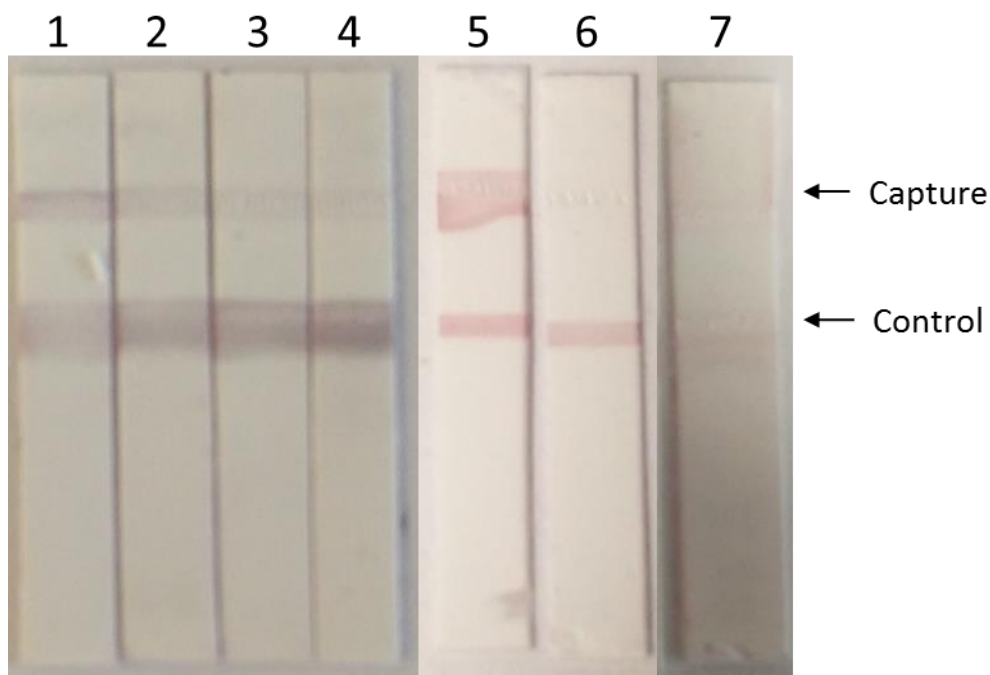


Figure 5.10 Lateral flow strips showing influenza nucleoprotein binding to scFvOmpATM conjugated particles and binding specificity. (1-4) Binding sensitivity was assessed by incubating scFvOmpATM particles with 5000, 2500, 1000 and 500 ng/ml of FluA NP. (5-6) Binding specificity was tested by incubating with 5000 ng/ml of FluA NP and respiratory syncytial virus nucleoprotein respectively. (7) Non-specific binding was tested with IgAPOmpATM conjugated control particles incubated with 5000 ng/ml FluA NP. All capture lines were monoclonal α -FluA NP antibody (Hyttest) and the control lines were polyclonal α -Human IgG (Abcam).

5.3 Discussion

Engineered OmpA-AuNP Conjugates Provide a Flexible Platform for Biosensing

The work presented in this chapter, and the previous, show that the assembly of functional engineered OmpA_{TM} proteins on AuNPs can be utilised in biosensing applications. Several different assays were developed with the same protein molecule applicable to both sensor chips, on solid substrates, and liquid format tests. The use of AuNPs in solution for biosensing assays is already well established, particularly in lateral flow tests. Glass surfaces decorated with gold nanoparticles have shown promise as inexpensive sensor substrates (Kumari and Moirangthem, 2016; Nath and Chilkoti, 2002). Glass is an attractive base material for biosensors; it is readily available in a variety of shapes and sizes that can be easily integrated into the optical systems needed for detection, thus, allowing for the design of simple detection equipment (Kumari and Moirangthem, 2016), or the use of existing instrumentation, as shown in this work. An advantage of using nanoparticle LSPR over planar gold surfaces for biomolecule sensing is the reduced distance that the plasmon field extends away from the surface, ~10 times lower, this means that any binding events are completely within the localised plasmon field which should enhance sensitivity (Richens and O'Shea, 2014).

Monitoring changes in the LSPR spectra provided robust information on protein binding on the nanoparticle surface. Analysing spectra using the barycentric mean method was sensitive and precise when used for both nanoparticles in solution (Section 4.2.2) and on a glass surface. One disadvantage of using a standard UV-Vis spectrometer for data collection is the volume needed to fill a sample cuvette, > 500 µl, which may not be possible if protein stocks are limited. A possible solution for this is to use a low volume spectrometer, such as a NanoDropTM system, which only requires 2 µl of sample. This could be used for rapid analysis of a panel of samples or for difficult to express proteins with limited supply. Results acquired for cysOmpA_{TM} binding using a NanoDropTM ND1000 spectrometer were comparable to those acquired using a Cary 4E (Figure 4.8). This result indicates that such instrumentation could, in principle, be used for studying biomolecular interactions.

While the AuNPs facilitated the use of several detection methods and multiple assay formats the OmpA_{TM} scaffold provides a robust and versatile platform for the generation of a wide variety of functional proteins. The bacterial domain and antibody fragment fusions documented in this work are only a small percentage of the protein

engineering possible. The variety of protein-protein interactions that can be studied with this system should only increase as new protein binding domains are discovered and their structures and sequences are analysed. scFv based fusions are limited by the phage display libraries that are available and the costs involved in screening and selection, although these should decrease as the technology continues to mature. By using a protein scaffold that mediates binding to the AuNP a standard conjugation procedure can be used for all the protein fusions, unlike traditional protein conjugation where optimisation steps are required for each new protein.

scFvOmpA_{TM} Conjugated Particles Specifically Bind a Target Antigen

AuNPs were successfully conjugated with an scFvOmpA_{TM} protein targeted to influenza A nucleoprotein. The scFv domain was required for detection, no FluA NP binding was observed for control particles made with either IgAPOmpA_{TM} or cysOmpA_{TM}, as shown by DLS, UV-Vis spectroscopy and lateral flow assays (Figure 5.6, Figure 5.8 and Figure 5.10). Binding was specific to influenza A nucleoprotein, with no binding of respiratory syncytial virus nucleoprotein observed using a lateral flow assay (6 in Figure 5.10). This work shows that OmpA_{TM} can be used as a robust scaffold for engineering targeted AuNP conjugates that are amenable to several detection methods. Both the scFv domain and OmpA_{TM} scaffold provide advantages for using this approach. In contrast to traditional mAb production scFvs are selected using a phage display library (Li et al., 2015), which is both more rapid than traditional methods and removes the need for an organism to immunize. The resulting novel antibody molecules are usually humanized, which is advantageous for therapeutic applications and other regulated uses, and readily expressed in *E. coli*, which provides a mature, well characterised expression platform. Although scFvs can be used as independent molecules it is often required for them to be expressed as fusion proteins to improve stability (Gil and Schrum, 2013; R. Wang et al., 2013), the OmpA_{TM} scaffold can help provide this stability while facilitating directed attachment to the nanoparticle surface.

Functionalised Glass Capillaries as Simple Biosensors

As predicted by Mie theory, borosilicate glass capillaries functionalised with 20 nm gold nanoparticles were shown to be sensitive to changes in the refractive index of the bulk solvent (Willems and Duyne, 2007). The LSPR spectrum, with its two peaks, was somewhat unusual (Figure 5.7). The capillaries were a uniform red colour with no obvious aggregation present, usually seen as purple patches on the glass. As the

refractive index of the solution was increased the λ_{\max} of both peaks red shifted. However, the absorbance of the major peak decreased while the minor increased. The smaller peak could be due to small aggregates on the surface, as its position in the spectrum would suggest, which are more sensitive to the changing bulk refractive index than the individual particles. Chemical bond coupled plasmon resonance splitting has been observed for self-assembled AuNP surfaces, resulting from sulphur-gold bonding which could theoretically occur for other conjugated bonding systems (Su et al., 2009). It is also possible that this second peak is an optical effect due to aberrant light scattering from the curved edges of the capillary, which could explain the opposing shifts in the absorbance of the two peaks. LSPR measurements of the main peak (500-600 nm) gave a sensitivity of 39.95 ± 0.02 nm/RI unit, using glycerol solution standards. Analysis of the full spectrum (400-800 nm) showed an increased sensitivity of 289.46 ± 18.03 nm/RI unit. These results are comparable with those seen for planar surfaces and capillaries (Kedem et al., 2011; Kumari and Moirangthem, 2016; Nath and Chilkoti, 2002).

The capillary format provided a convenient flow cell for protein binding experiments and demonstrated that the nanoparticle deposition method, described in Chapter 3, could be successfully applied to more complex glass shapes. The functionalised capillaries were easily integrated in to the Cary 4E sample environment with minor modifications, and could be fed *in situ* by a syringe or peristaltic pump. Alternatively, spectra could be acquired using a simple spectrometer assembled with a CCD sensor and white LED light source, as shown by Kumari *et al.* The quality of the spectra acquired for the functionalised capillaries with the Cary 4E spectrometer were comparable to previous studies using planar glass (Nath and Chilkoti, 2004) and capillaries (Kumari and Moirangthem, 2016). However, both of these studies required the use of high temperature annealing of either the silane layer or deposited nanoparticles to produce good quality spectra.

5.4 Conclusions

Building upon the work from the previous chapter it has been shown that multi-domain fusion proteins, made using the OmpA_{TM} scaffold, can be used in biomolecule detection assays after assembly on the surface of gold nanoparticles. The AuNPs provided a flexible platform that could be used in both, solution and surface based formats while

remaining amenable to several detection methods including fluorescence, UV-Vis spectroscopy and light scattering.

Detection of influenza A nucleoprotein was achieved using a single chain antibody fusion protein (scFvOmpA_{TM}) with binding observed using DLS, UV-Vis spectroscopy and TEM, when the particles were in solution, and by a novel spectroscopic assay when deposited on a glass capillary.

The AuNP functionalised glass capillary results built upon the work of Kumari *et al* and showed that assembly of engineered proteins on the gold nanoparticle surface can be used for specific detection of a protein antigen. The low cost of the glass substrates and the associated instrumentation needed to make these capillary based biosensors a good candidate for applications in developing countries.

A prototype lateral flow test for FluA NP was developed using scFvOmpA_{TM} conjugated 20 nm gold particles with a minimum concentration of 500 ng/ml detected. This provided a proof of concept for using self-assembling recombinant fusion proteins as the detection molecule in a lateral flow assay.

6 CONCLUSIONS AND FUTURE WORK

Nanoscale Topology of Deposited Gold Nanoparticles on Aminosilane Surfaces

The complex silane molecule, AAPTMS, was shown by atomic force microscopy to form smooth monolayers on SiO₂ surfaces when deposited from an aqueous ethanol solvent. The assembled monolayers were stable without a high temperature curing step and displayed a high density of primary amine groups for binding gold nanoparticles, ~4 NH₃⁺ per nm². The more commonly used silane molecule, APS, formed poorly stable multilayers under the same deposition conditions with large aggregate structures observed by AFM. Scanning electron microscopy revealed strikingly different surface topologies for the two different silane surfaces after gold nanoparticle deposition. AAPTMS facilitated evenly distributed sub-monolayer AuNP surfaces with a maximum observed area coverage of ~35%. Conversely, APS showed large islands of highly concentrated particle deposition with areas of bare surface.

Assembly of Engineered Protein on Gold Nanoparticles

The addition of a cysteine residue into a periplasmic loop of OmpA_{TM} was shown by UV-Vis spectroscopy to increase equilibrium binding to gold nanoparticles in solution. The resulting OmpA_{TM}-AuNP complexes also displayed higher stability in solution due to the formation of a gold-thiol bond. Structural studies of the multi-domain fusion protein, GGzOmpA_{TM}, by DLS and neutron reflectometry, provided evidence of oriented assembly on the surface of gold nanoparticles, both in solution and when deposited on a solid substrate. The assembled protein array could be modelled, using the neutron reflectometry data, as a dual layer where the 21.93 Å thick inner layer consisted of the OmpA_{TM} domain embedded in a dense thioAlkylPEG filler monolayer and the GGz domains extended away from the surface as a diffuse 75.09 Å thick outer layer. The outer domains retained their functionality, with antibody binding observed by DLS and fluorescence microscopy. The protein layer thicknesses obtained from the DLS data, 12.13 and 19.26 nm before and after antibody binding respectively, were in good agreement with the previously published GGzOmpA_{TM} structure on planar gold surfaces (Brun et al., 2015).

Biosensing using Engineered OmpA_{TM} Proteins on AuNPs

While engineered OmpA_{TM} proteins have previously been shown to bind protein antigens using SPR and neutron reflectometry (Brun et al., 2008, 2015), the time

consuming and expensive nature of these techniques make them unsuitable for most commercial applications. In this work, it has been shown that biomolecule binding to assembled engineered OmpA_{TM} proteins could be detected using more routine methods; such as fluorescence microscopy, dynamic light scattering, lateral flow and UV-Vis spectroscopy. The gold nanoparticles provided a flexible assembly platform that could be used in liquid suspension and bound to glass substrates, while their intrinsic optical properties facilitated simple, label free detection of bound antigens by UV-Vis spectroscopy. Analysis of the spectroscopic data using the barycentric mean provided a robust and sensitive measure of protein binding.

Detection of the antigen, influenza A nucleoprotein, was achieved using a single chain antibody fusion protein (scFvOmpA_{TM}) conjugated to 20 nm gold nanoparticles, both in solution and with the nanoparticles bound to the surface of glass capillaries. A prototype lateral flow assay was developed which could detect a minimum concentration of 500 ng/ml recombinant influenza A nucleoprotein. This work represents one of the first examples of using a self-assembled recombinant fusion protein array on gold nanoparticles to detect a clinically relevant antigen.

Future Work

Due to the time-limited nature of neutron reflection experiments and the need to prepare samples on site using specialist equipment, it was not possible to fully optimise the gold nanoparticle deposition procedure on the silicon blocks. Detailed analysis of neutron data works best when measurements are carried out after each component of the system is added to the surface, with each measurement taking 1-2 hours. However, this method was not optimal for sample preparation with the best quality AuNP surfaces generated by immediate deposition after the silanisation step, therefore reducing the chance of silane layer degradation. Alternatively, a quartz crystal microbalance with dissipation (QCM-D) could be used to gather real time information on the silane and gold deposition steps to complement the reflectometry data of the deposited nanoparticles and assembled proteins. A QCM is essentially a highly sensitive mass balance that measures the change in the resonant frequency of a single crystal quartz plate. Quartz is a piezoelectric material, therefore applying an alternating current causes the crystal to resonate. The deposition of material on the surface can be observed as a lowering of the resonant frequency. A QCM-D also measures the energy dissipation of the system which gives information on the viscoelastic properties of the deposited layer.

The quality of the neutron data could be improved by using polarised neutrons for the reflectivity experiments. Neutrons have a small magnetic moment, so can be separated depending on their spin property, i.e. up or down spin. The resulting polarised neutrons are reflected differently from magnetic materials, therefore, the addition of a magnetic reference layer introduces magnetic contrast to the system. Analysis of reflectometry data collected with up and down spin polarised neutrons generates two independent reflectivity profiles that only differ in the magnetic region. This approach reduces the ambiguity in the model when fitting to the reflectometry data and has previously been used to help analyse the complex layer structure of engineered OmpA_{TM} arrays on planar gold surfaces (Brun et al., 2008).

The poor quality of the SANS data for the protein coated gold nanoparticles could be improved by carrying out future experiments at the ILL neutron source in Grenoble. The ILL is a reactor source with a much higher flux than ISIS, therefore the scattering signal should be much higher. Carrying out a combined SAXS and SANS experiment could also provide more information on the protein layer. X-rays are not very sensitive to light atoms so the protein layer would be almost invisible when compared with the highly scattering AuNPs. Simultaneously fitting the X-ray data with the neutron data would effectively add a second contrast in which only the gold nanoparticles are observed. This method has been used to investigate the structural and thermodynamic properties of AuNP-HSA complexes (Spinozzi et al., 2017).

Analysis of the OmpA_{TM} surface charge (Figure 4.22) identified residues that could be modified in the future to improve nanoparticle binding and possibly direct protein orientation on the surface. Lysine residues have been shown to mediate protein binding to citrate coated AuNPs (Wang et al., 2016), presumably through electrostatic interactions between the positively charged residue and the negatively charged citrate coating. Therefore, the surface charge of OmpA_{TM} could be modified using a rational design approach to encourage binding to the nanoparticle through the base of the protein, where the cysteine residue is located in the cysOmpA_{TM} mutant. This could be achieved by replacing the lysine and arginine residues at positions 73 and 103 with aspartic acids and also replacing the aspartic acids at positions 4, 89 and 90 with lysine residues. These changes should generate a molecule with oppositely charged poles, resulting in a mostly positively charged periplasmic end and mostly negatively charged extracellular end. To test this hypothesis, modification of the OmpA_{TM} PDB file to

mutate the lysine, arginine and aspartic acid residues was carried out using Pymol and the surface charge analysed using APBS (Figure 6.1). This analysis indicated that the desired modification of the surface charge would be possible through these mutations, presenting a possible starting point for optimisation of the OmpA_{TM} structure for binding to gold nanoparticles.

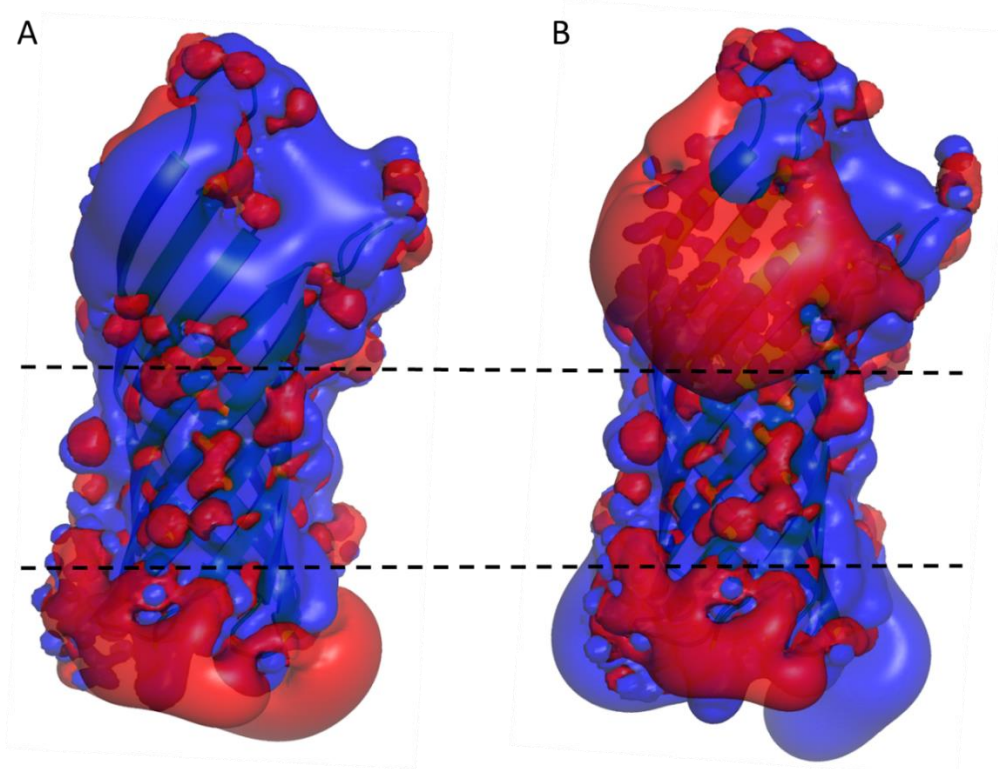


Figure 6.1 OmpA_{TM} surface charge before (A) and after (B) mutation of the charged residues. Five mutations were carried out to make (B); K73D, R103D, D4K, D89K and D90K. The electrostatic isosurface was generated using APBS at pH 7 with contours shown between -1kT (red) and +1kT (blue), the dashed lines indicate the membrane region. PDB ID:1QJP

The biosensing assays used in this study were developed as a proof of concept for using engineered OmpA_{TM} proteins as the biologically active molecule on gold nanoparticles. Further studies are required to compare the sensitivity and robustness of these assays with commercially available antibody-gold nanoparticle conjugates and other biosensing techniques, such as SPR.

7 APPENDICES

APPENDIX 1: NEUTRON REFLECTOMETRY DATA ANALYSIS 156

APPENDIX 1: NEUTRON REFLECTOMETRY DATA ANALYSIS

Bootstrap Error Analysis

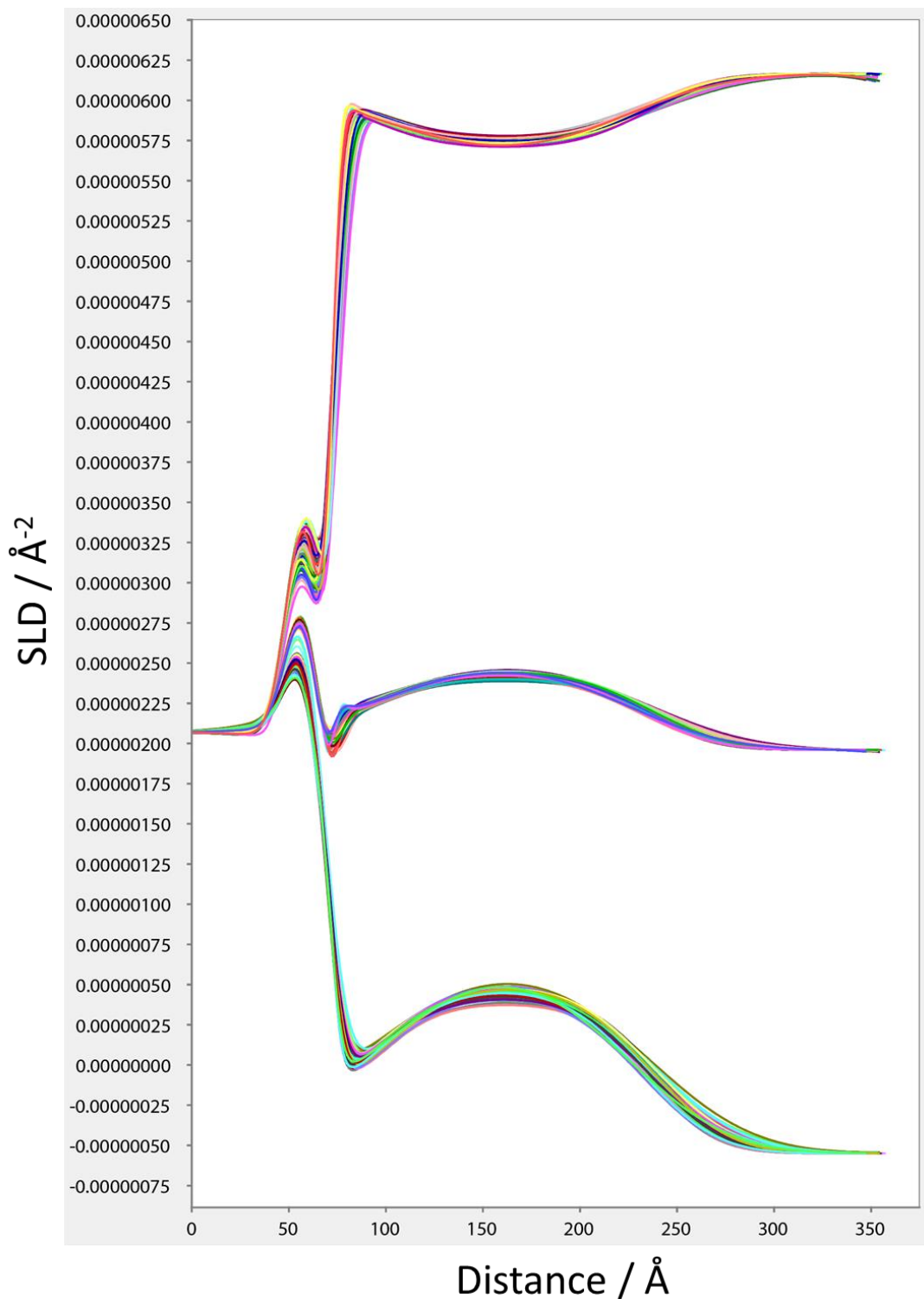


Figure 7.1 Graphical representation of the bootstrap error analysis for the AuNP surface using the slab model. Each line represents a single bootstrap run.

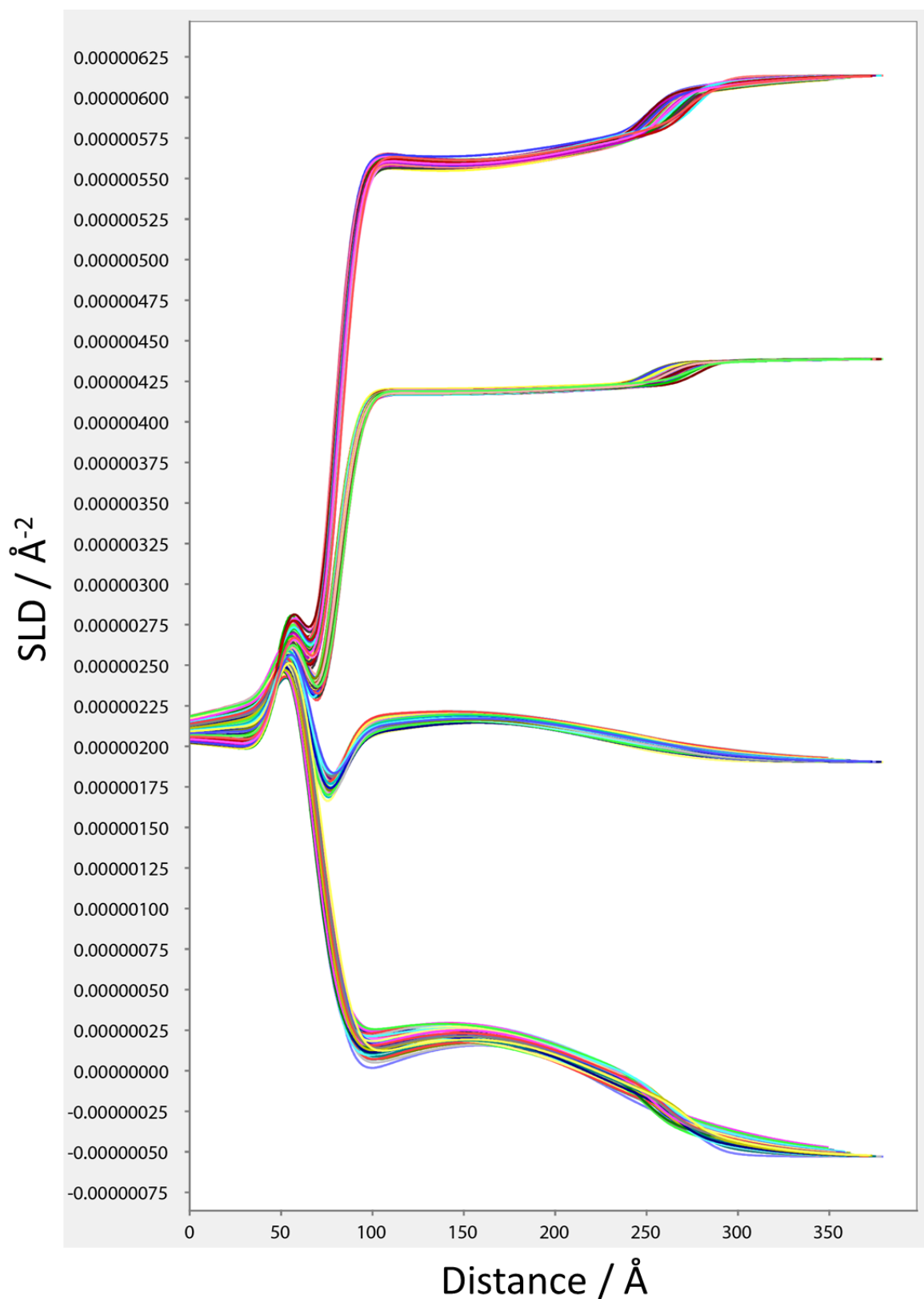


Figure 7.2 Graphical representation of the bootstrap error analysis for the AuNP + GGzOmpA_{TM} surface using the slab model. Each line represents a single bootstrap run.

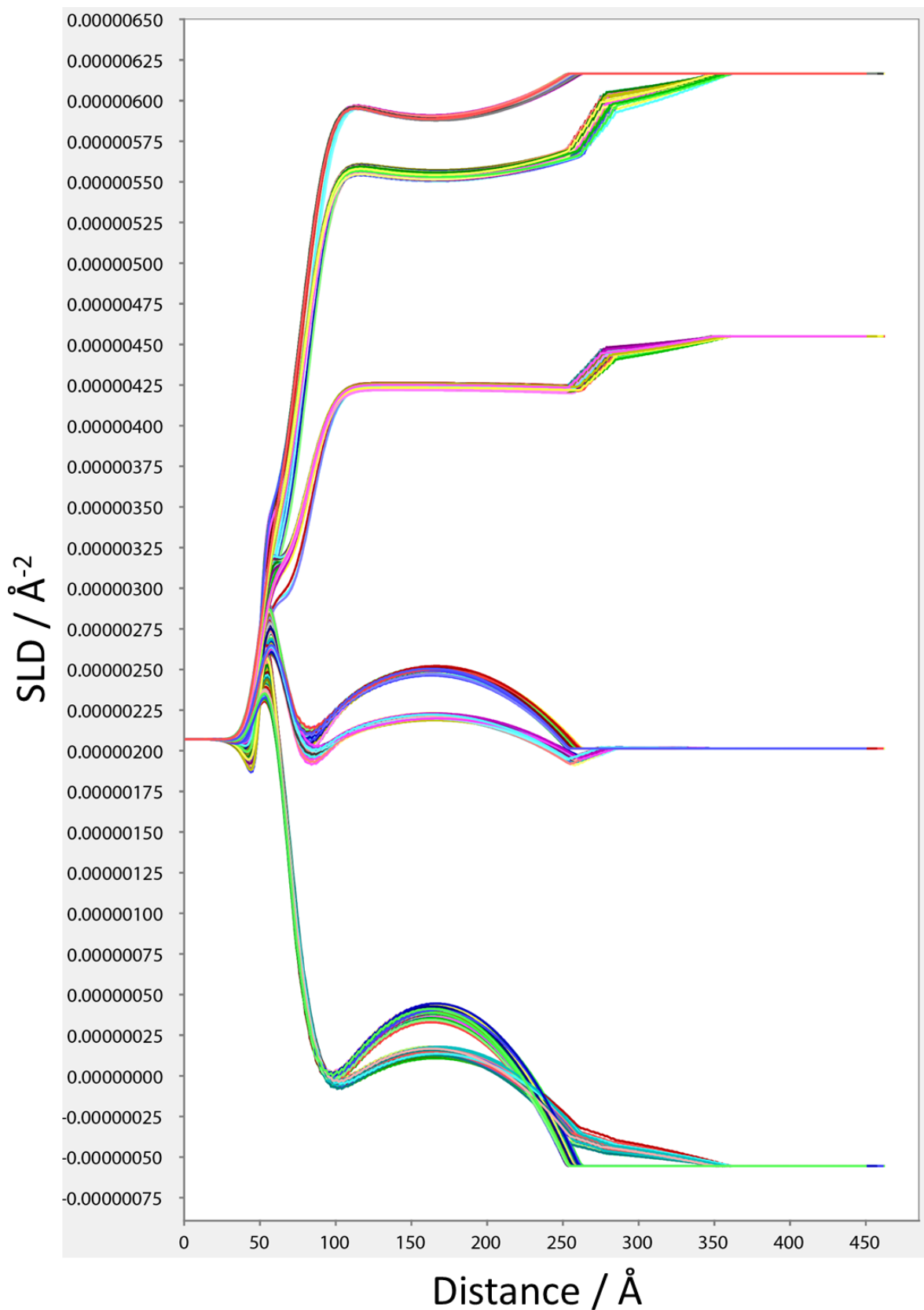


Figure 7.3 Graphical representation of the bootstrap error analysis for the AuNP and AuNP + GGzOmpA_{TM} surfaces using the sphere model. Each line represents a single bootstrap run.

Table 7.1 Model parameters fitted for the AuNP surface using the slab model.

<i>Parameter</i>	<i>Fitted Value</i>
<i>Substrate Roughness / Å</i>	7.32 ± 1.35
<i>SiO₂ Thickness / Å</i>	15.04 ± 0.13
<i>SiO₂ Roughness / Å</i>	7.98 ± 0.15
<i>SiO₂ Hydration / %</i>	17.47 ± 4.29
<i>SiO₂ SLD / Å² × 10⁻⁶</i>	3.49 ± 0.06
<i>Silane Thickness / Å</i>	8.57 ± 2.00
<i>Silane Roughness / Å</i>	5.85 ± 2.05
<i>Silane Hydration / %</i>	11.04 ± 22.01
<i>Silane SLD / Å² × 10⁻⁶</i>	1.00 ± 0.00
<i>Gold Layer Thickness / Å</i>	179.17 ± 5.65
<i>Gold Roughness / Å</i>	35.48 ± 10.62
<i>Gold Coverage / %</i>	23.01 ± 6.18
<i>Gold SLD / Å² × 10⁻⁶</i>	4.18 ± 0.09

Table 7.2 Model parameters fitted for the GGzOmpA_{TM} coated surface using the slab model.

<i>Parameter</i>	<i>Fitted Value</i>
<i>Substrate Roughness / Å</i>	7.93 ± 0.14
<i>SiO₂ Thickness / Å</i>	14.32 ± 1.27
<i>SiO₂ Roughness / Å</i>	10.50 ± 2.52
<i>SiO₂ Hydration / %</i>	12.59 ± 9.42
<i>SiO₂ SLD / Å⁻² × 10⁻⁶</i>	3.48 ± 0.05
<i>Silane Thickness / Å</i>	11.92 ± 4.73
<i>Silane Roughness / Å</i>	10.00 ± 0.1
<i>Silane Hydration / %</i>	0.09 ± 18.55
<i>Silane SLD / Å⁻² × 10⁻⁶</i>	0.57 ± 0.18
<i>Gold Layer Thickness / Å</i>	153.70 ± 14.25
<i>Gold Roughness / Å</i>	65.51 ± 15.76
<i>Gold Coverage / %</i>	23.71 ± 11.71
<i>Gold SLD / Å⁻² × 10⁻⁶</i>	4.10 ± 0.00
<i>Protein Thickness / Å</i>	30.33 ± 9.55
<i>Protein Roughness / Å</i>	9.98 ± 0.05
<i>Protein SLD / Å⁻² × 10⁻⁶</i>	1.49 ± 0.15
<i>Protein Hydration / %</i>	90.10 ± 0.27

Table 7.3 Model parameters fitted for the AuNP and GGzOmpA™ coated surfaces using the sphere model.

<i>Parameter</i>	<i>Fitted Value</i>
<i>Substrate Roughness / Å</i>	7.69 ± 4.29
<i>SiO₂ Thickness / Å</i>	15.07 ± 0.15
<i>SiO₂ Roughness / Å</i>	14.44 ± 0.73
<i>SiO₂ Hydration / %</i>	45.90 ± 7.03
<i>Silane Thickness / Å</i>	8.00 ± 1.00
<i>Silane Roughness / Å</i>	14.99 ± 0.01
<i>Silane Hydration / %</i>	99.80 ± 74.36
<i>Silane SLD / Å⁻² × 10⁻⁶</i>	0.97 ± 0.15
<i>Gold Layer Thickness / Å</i>	183.68 ± 4.82
<i>AuNP Coverage (without protein) / %</i>	38.90 ± 0.78
<i>AuNP Coverage (with protein) / %</i>	21.44 ± 1.78
<i>Inner Coating Thickness / Å</i>	22.93 ± 2.93
<i>Inner Coating Hydration / %</i>	0.05 ± 1.19
<i>Inner Coating SLD / Å⁻² × 10⁻⁶</i>	0.68 ± 0.19
<i>Outer Coating Thickness / Å</i>	75.09 ± 0.17
<i>Outer Coating Hydration / %</i>	84.40 ± 6.24

Data Fitting

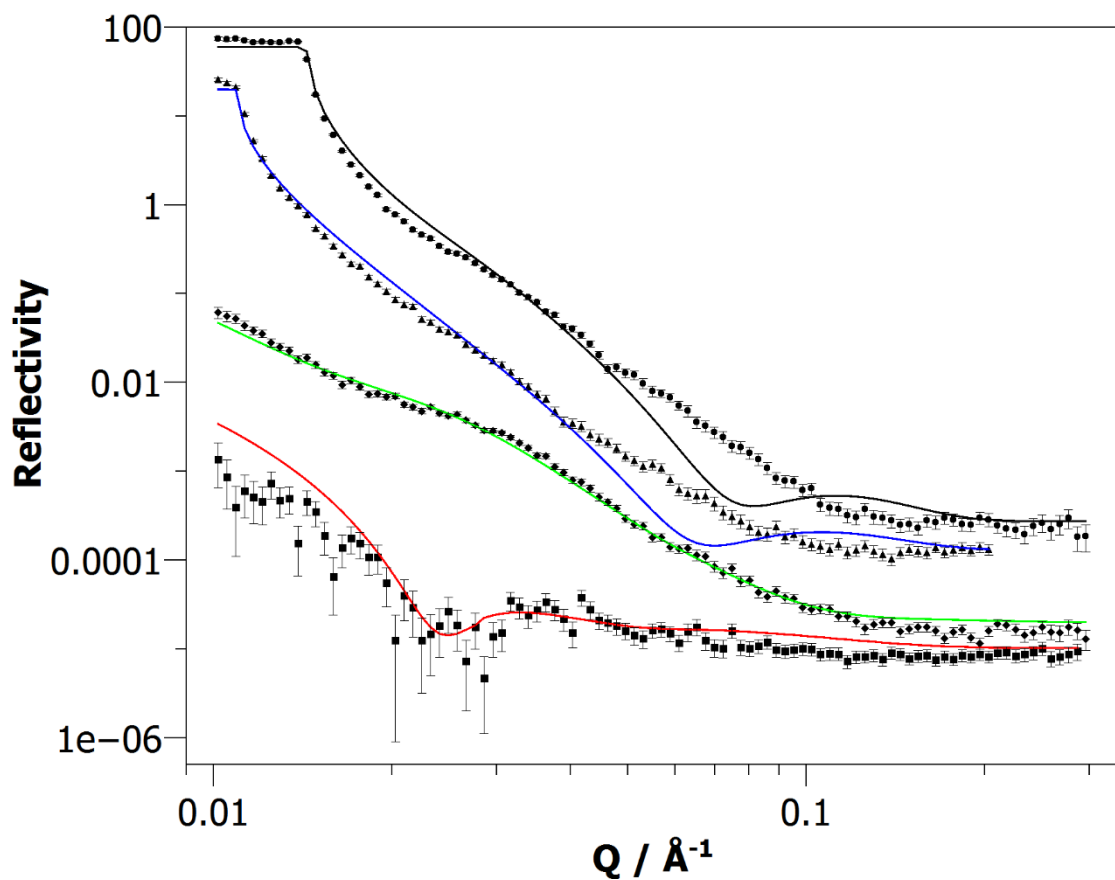


Figure 7.4 Fitting of the GGzOmpATM surface using the slab model of a bare AuNP surface. The solid lines correspond to the fits of the data sets, which are offset for clarity. The colours indicate the solvent contrast, D2O, SMW, GMW and H2O. The fit lines deviate significantly from the reflectivity profiles, showing that this model does not describe the data sets very well.

8 REFERENCES

- Ahmad, Z.A., Yeap, S.K., Ali, A.M., Ho, W.Y., Alitheen, N.B.M., Hamid, M., 2012. scFv Antibody: Principles and Clinical Application. *J. Immunol. Res.* 2012, e980250. <https://doi.org/10.1155/2012/980250>
- Ameer, F.S., Ansar, S.M., Hu, W., Zou, S., Zhang, D., 2012. Inner Filter Effect on Surface Enhanced Raman Spectroscopic Measurement. *Anal. Chem.* 84, 8437–8441. <https://doi.org/10.1021/ac302073f>
- Andersen, K.K., Vad, B., Omer, S., Otzen, D.E., 2016. Concatemers of Outer Membrane Protein A Take Detours in the Folding Landscape. *Biochemistry (Mosc.)* 55, 7123–7140. <https://doi.org/10.1021/acs.biochem.6b01153>
- Anker, J.N., Hall, W.P., Lyandres, O., Shah, N.C., Zhao, J., Van Duyne, R.P., 2008. Biosensing with plasmonic nanosensors. *Nat. Mater.* 7, 442–453. <https://doi.org/10.1038/nmat2162>
- Ansar, S.M., Ameer, F.S., Hu, W., Zou, S., Pittman, C.U., Zhang, D., 2013. Removal of Molecular Adsorbates on Gold Nanoparticles Using Sodium Borohydride in Water. *Nano Lett.* 13, 1226–1229. <https://doi.org/10.1021/nl304703w>
- Argekar, S.U., Kirley, T.L., Schaefer, D.W., 2013. Determination of structure-property relationships for 3-aminopropyltriethoxysilane films using x-ray reflectivity. *J. Mater. Res.* 28, 1118–1128. <https://doi.org/10.1557/jmr.2013.54>
- Armas, L.E.G., Menezes, J.W., Huila, M.G., Araki, K., Toma, H.E., 2016. Gold Nanohole Arrays Fabricated by Interference Lithography Technique as SERS Probes for Chemical Species Such As Rhodamine 6G and 4,4'-Bipyridine. *Plasmonics* 1–6. <https://doi.org/10.1007/s11468-016-0353-8>
- Arnold, O., Bilheux, J.C., Borreguero, J.M., Buts, A., Campbell, S.I., Chapon, L., Doucet, M., Draper, N., Ferraz Leal, R., Gigg, M.A., Lynch, V.E., Markvardsen, A., Mikkelsen, D.J., Mikkelsen, R.L., Miller, R., Palmen, K., Parker, P., Passos, G., Perring, T.G., Peterson, P.F., Ren, S., Reuter, M.A., Savici, A.T., Taylor, J.W., Taylor, R.J., Tolchenov, R., Zhou, W., Zikovsky, J., 2014. Mantid—Data analysis and visualization package for neutron scattering and μ SR experiments. *Nucl. Instrum. Methods Phys. Res. Sect. Accel. Spectrometers Detect. Assoc. Equip.* 764, 156–166. <https://doi.org/10.1016/j.nima.2014.07.029>

- Arora, A., Rinehart, D., Szabo, G., Tamm, L.K., 2000. Refolded Outer Membrane Protein A of Escherichia coli Forms Ion Channels with Two Conductance States in Planar Lipid Bilayers. *J. Biol. Chem.* 275, 1594–1600. <https://doi.org/10.1074/jbc.275.3.1594>
- Arunmanee, W., Pathania, M., Solovyova, A.S., Brun, A.P.L., Ridley, H., Baslé, A., Berg, B. van den, Lakey, J.H., 2016. Gram-negative trimeric porins have specific LPS binding sites that are essential for porin biogenesis. *Proc. Natl. Acad. Sci.* 113, E5034–E5043. <https://doi.org/10.1073/pnas.1602382113>
- Ayub, M., Bayley, H., 2016. Engineered transmembrane pores. *Curr. Opin. Chem. Biol., Synthetic Biology * Synthetic Biomolecules* 34, 117–126. <https://doi.org/10.1016/j.cbpa.2016.08.005>
- Bailey, R.C., Stevenson, K.J., Hupp, J.T., 2000. Assembly of Micropatterned Colloidal Gold Thin Films via Microtransfer Molding and Electrophoretic Deposition. *Adv. Mater.* 12, 1930–1934. [https://doi.org/10.1002/1521-4095\(200012\)12:24<1930::AID-ADMA1930>3.0.CO;2-F](https://doi.org/10.1002/1521-4095(200012)12:24<1930::AID-ADMA1930>3.0.CO;2-F)
- Bain, C.D., Troughton, E.B., Tao, Y.T., Evall, J., Whitesides, G.M., Nuzzo, R.G., 1989. Formation of monolayer films by the spontaneous assembly of organic thiols from solution onto gold. *J. Am. Chem. Soc.* 111, 321–335. <https://doi.org/10.1021/ja00183a049>
- Baker, N.A., Sept, D., Joseph, S., Holst, M.J., McCammon, J.A., 2001. Electrostatics of nanosystems: Application to microtubules and the ribosome. *Proc. Natl. Acad. Sci.* 98, 10037–10041. <https://doi.org/10.1073/pnas.181342398>
- Ballauff, M., 2001. SAXS and SANS studies of polymer colloids. *Curr. Opin. Colloid Interface Sci.* 6, 132–139. [https://doi.org/10.1016/S1359-0294\(01\)00072-3](https://doi.org/10.1016/S1359-0294(01)00072-3)
- Bartczak, D., Kanaras, A.G., 2011. Preparation of Peptide-Functionalized Gold Nanoparticles Using One Pot EDC/Sulfo-NHS Coupling. *Langmuir* 27, 10119–10123. <https://doi.org/10.1021/la2022177>
- Begg, G., Speicher, D., 1999. Mass spectrometry detection and reduction of disulfide adducts between reducing agents and recombinant proteins with highly reactive cysteines. *J. Biomol. Tech. JBT* 10, 17–20.
- Behlke, J., Ristau, O., 1997. Molecular mass determination by sedimentation velocity experiments and direct fitting of the concentration profiles. *Biophys. J.* 72, 428–434.
- Berkowitz, S.A., 2006. Role of analytical ultracentrifugation in assessing the aggregation of protein biopharmaceuticals. *AAPS J.* 8, E590–E605. <https://doi.org/10.1208/aapsj080368>
- Berne, B.J., Pecora, R., 2000. *Dynamic Light Scattering: With Applications to Chemistry, Biology, and Physics.* Courier Corporation.
- Biggs, S., Chow, M.K., Zukoski, C.F., Grieser, F., 1993. The Role of Colloidal Stability in the Formation of Gold Sols. *J. Colloid Interface Sci.* 160, 511–513. <https://doi.org/10.1006/jcis.1993.1430>
- Bond, P.J., Faraldo-Gómez, J.D., Sansom, M.S.P., 2002. OmpA: A Pore or Not a Pore? Simulation and Modeling Studies. *Biophys. J.* 83, 763–775. [https://doi.org/10.1016/S0006-3495\(02\)75207-7](https://doi.org/10.1016/S0006-3495(02)75207-7)
- Born, M., Wolf, E., 1970. *Principles of Optics*, 4th ed. Pergamon Press.

- Bosshart, P.D., Iordanov, I., Garzon-Coral, C., Demange, P., Engel, A., Milon, A., Müller, D.J., 2012. The Transmembrane Protein KpOmpA Anchoring the Outer Membrane of *Klebsiella pneumoniae* Unfolds and Refolds in Response to Tensile Load. *Structure* 20, 121–127. <https://doi.org/10.1016/j.str.2011.11.002>
- Boulos, S.P., Davis, T.A., Yang, J.A., Lohse, S.E., Alkilany, A.M., Holland, L.A., Murphy, C.J., 2013. Nanoparticle–Protein Interactions: A Thermodynamic and Kinetic Study of the Adsorption of Bovine Serum Albumin to Gold Nanoparticle Surfaces. *Langmuir* 29, 14984–14996. <https://doi.org/10.1021/la402920f>
- Brandow, S.L., Chen, M.-S., Dulcey, C.S., Dressick, W.J., 2008. Formation of Aromatic Siloxane Self-Assembled Monolayers. *Langmuir* 24, 3888–3896. <https://doi.org/10.1021/la703326m>
- Brewer, S.H., Glomm, W.R., Johnson, M.C., Knag, M.K., Franzen, S., 2005. Probing BSA Binding to Citrate-Coated Gold Nanoparticles and Surfaces. *Langmuir* 21, 9303–9307. <https://doi.org/10.1021/la050588t>
- Brown, T.S.D., Johnson, B.F.G., 1997. Nucleation and growth of nano-gold colloidal lattices. *Chem. Commun.* 1007–1008. <https://doi.org/10.1039/A701627A>
- Brun, A.P.L., Holt, S.A., Shah, D.S., Majkrzak, C.F., Lakey, J.H., 2008. Monitoring the assembly of antibody-binding membrane protein arrays using polarised neutron reflection. *Eur. Biophys. J.* 37, 639–645. <https://doi.org/10.1007/s00249-008-0291-2>
- Brun, A.P.L., Soliakov, A., Shah, D.S.H., Holt, S.A., McGill, A., Lakey, J.H., 2015. Engineered self-assembling monolayers for label free detection of influenza nucleoprotein. *Biomed. Microdevices* 17, 1–10. <https://doi.org/10.1007/s10544-015-9951-z>
- Brunauer, S., Emmett, P.H., Teller, E., 1938. Adsorption of Gases in Multimolecular Layers. *J. Am. Chem. Soc.* 60, 309–319. <https://doi.org/10.1021/ja01269a023>
- Brust, M., Walker, M., Bethell, D., Schiffrin, D.J., Whyman, R., 1994. Synthesis of thiol-derivatised gold nanoparticles in a two-phase Liquid–Liquid system. *J. Chem. Soc. Chem. Commun.* 801–802. <https://doi.org/10.1039/C39940000801>
- Burgess, N.K., Dao, T.P., Stanley, A.M., Fleming, K.G., 2008. β -Barrel Proteins That Reside in the *Escherichia coli* Outer Membrane in Vivo Demonstrate Varied Folding Behavior in Vitro. *J. Biol. Chem.* 283, 26748–26758. <https://doi.org/10.1074/jbc.M802754200>
- Burns, J.A., Butler, J.C., Moran, J., Whitesides, G.M., 1991. Selective reduction of disulfides by tris(2-carboxyethyl)phosphine. *J. Org. Chem.* 56, 2648–2650. <https://doi.org/10.1021/jo00008a014>
- Buscher, C.T., McBranch, D., Li, D., 1996. Understanding the Relationship between Surface Coverage and Molecular Orientation in Polar Self-Assembled Monolayers. *J. Am. Chem. Soc.* 118, 2950–2953. <https://doi.org/10.1021/ja9528590>
- Carney, R.P., Kim, J.Y., Qian, H., Jin, R., Mehenni, H., Stellacci, F., Bakr, O.M., 2011. Determination of nanoparticle size distribution together with density or molecular weight by 2D analytical ultracentrifugation. *Nat. Commun.* 2, 335. <https://doi.org/10.1038/ncomms1338>
- Carter, P., 1986. Site-directed mutagenesis. *Biochem. J.* 237, 1–7.

- Casals, E., Pfaller, T., Duschl, A., Oostingh, G.J., Puntès, V., 2010. Time Evolution of the Nanoparticle Protein Corona. *ACS Nano* 4, 3623–3632. <https://doi.org/10.1021/nn901372t>
- Casuso, I., Rico, F., Scheuring, S., 2011. Biological AFM: where we come from – where we are – where we may go. *J. Mol. Recognit.* 24, 406–413. <https://doi.org/10.1002/jmr.1081>
- Ceccon, A., Tugarinov, V., Bax, A., Clore, G.M., 2016. Global Dynamics and Exchange Kinetics of a Protein on the Surface of Nanoparticles Revealed by Relaxation-Based Solution NMR Spectroscopy. *J. Am. Chem. Soc.* 138, 5789–5792. <https://doi.org/10.1021/jacs.6b02654>
- Cedervall, T., Lynch, I., Lindman, S., Berggård, T., Thulin, E., Nilsson, H., Dawson, K.A., Linse, S., 2007. Understanding the nanoparticle–protein corona using methods to quantify exchange rates and affinities of proteins for nanoparticles. *Proc. Natl. Acad. Sci. U. S. A.* 104, 2050–2055. <https://doi.org/10.1073/pnas.0608582104>
- Chalton, D.A., Lakey, J.H., 2010. Simple Detection of Protein Soft Structure Changes. *Anal. Chem.* 82, 3073–3076. <https://doi.org/10.1021/ac902932c>
- Chandrasekharan, N., Kamat, P.V., 2001. Assembling Gold Nanoparticles as Nanostructured Films Using an Electrophoretic Approach. *Nano Lett.* 1, 67–70. <https://doi.org/10.1021/nl000184f>
- Chen, C.-L., Zhang, P., Rosi, N.L., 2008. A New Peptide-Based Method for the Design and Synthesis of Nanoparticle Superstructures: Construction of Highly Ordered Gold Nanoparticle Double Helices. *J. Am. Chem. Soc.* 130, 13555–13557. <https://doi.org/10.1021/ja805683r>
- Chen, J., Shi, J., Decanini, D., Cambril, E., Chen, Y., Haghiri-Gosnet, A.-M., 2009. Gold nanohole arrays for biochemical sensing fabricated by soft UV nanoimprint lithography. *Microelectron. Eng., MNE '08* 86, 632–635. <https://doi.org/10.1016/j.mee.2008.12.093>
- Chen, M.-S., Dulcey, C.S., Chrisey, L.A., Dressick, W.J., 2006. Deep-UV Photochemistry and Patterning of (Aminoethylaminomethyl)phenethylsiloxane Self-Assembled Monolayers. *Adv. Funct. Mater.* 16, 774–783. <https://doi.org/10.1002/adfm.200500744>
- Chiang, C.-H., Liu, N.-I., Koenig, J.L., 1982. Magic-angle cross-polarization carbon 13 NMR study of aminosilane coupling agents on silica surfaces. *J. Colloid Interface Sci.* 86, 26–34. [https://doi.org/10.1016/0021-9797\(82\)90037-6](https://doi.org/10.1016/0021-9797(82)90037-6)
- Choi, D.H., Lee, S.K., Oh, Y.K., Bae, B.W., Lee, S.D., Kim, S., Shin, Y.-B., Kim, M.-G., 2010. A dual gold nanoparticle conjugate-based lateral flow assay (LFA) method for the analysis of troponin I. *Biosens. Bioelectron.* 25, 1999–2002. <https://doi.org/10.1016/j.bios.2010.01.019>
- Chou, S.Y., Krauss, P.R., Renstrom, P.J., 1996. Nanoimprint lithography. *J. Vac. Sci. Technol. B Microelectron. Nanometer Struct. Process. Meas. Phenom.* 14, 4129–4133. <https://doi.org/10.1116/1.588605>
- Chusuei, C.C., Goodman, D.W., 2003. X-Ray Photoelectron Spectroscopy, in: Meyers, R.A. (Ed.), *Encyclopedia of Physical Science and Technology (Third Edition)*.

- Academic Press, New York, pp. 921–938. <https://doi.org/10.1016/B0-12-227410-5/00830-9>
- Cisneros, D.A., Muller, D.J., Daud, S.M., Lakey, J.H., 2006. An Approach To Prepare Membrane Proteins for Single-Molecule Imaging. *Angew. Chem. Int. Ed.* 45, 3252–3256. <https://doi.org/10.1002/anie.200504506>
- Claridge, S.A., Liang, H.W., Basu, S.R., Fréchet, J.M.J., Alivisatos, A.P., 2008. Isolation of Discrete Nanoparticle–DNA Conjugates for Plasmonic Applications. *Nano Lett.* 8, 1202–1206. <https://doi.org/10.1021/nl0802032>
- Clifton, L.A., Holt, S.A., Hughes, A.V., Daulton, E.L., Arunmanee, W., Heinrich, F., Khalid, S., Jefferies, D., Charlton, T.R., Webster, J.R.P., Kinane, C.J., Lakey, J.H., 2015. An Accurate In Vitro Model of the E. coli Envelope. *Angew. Chem. Int. Ed.* 54, 11952–11955. <https://doi.org/10.1002/anie.201504287>
- Clifton, L.A., Johnson, C.L., Solovyova, A.S., Callow, P., Weiss, K.L., Ridley, H., Brun, A.P.L., Kinane, C.J., Webster, J.R.P., Holt, S.A., Lakey, J.H., 2012. Low Resolution Structure and Dynamics of a Colicin-Receptor Complex Determined by Neutron Scattering. *J. Biol. Chem.* 287, 337–346. <https://doi.org/10.1074/jbc.M111.302901>
- Clifton, L.A., Sanders, M.R., Hughes, A.V., Neylon, C., Frazier, R.A., Green, R.J., 2011. Lipid binding interactions of antimicrobial plant seed defence proteins: puroidoline-a and β -purothionin. *Phys. Chem. Chem. Phys.* 13, 17153–17162. <https://doi.org/10.1039/C1CP21799B>
- Cloekaert, A., Wergifosse, P. de, Dubray, G., Limet, J.N., 1990. Identification of seven surface-exposed Brucella outer membrane proteins by use of monoclonal antibodies: immunogold labeling for electron microscopy and enzyme-linked immunosorbent assay. *Infect. Immun.* 58, 3980–3987.
- Cole, J.L., Lary, J.W., Moody, T., Laue, T.M., 2008. Analytical Ultracentrifugation: Sedimentation Velocity and Sedimentation Equilibrium. *Methods Cell Biol.* 84, 143–179. [https://doi.org/10.1016/S0091-679X\(07\)84006-4](https://doi.org/10.1016/S0091-679X(07)84006-4)
- Costello, S.M., Plummer, A.M., Fleming, P.J., Fleming, K.G., 2016. Dynamic periplasmic chaperone reservoir facilitates biogenesis of outer membrane proteins. *Proc. Natl. Acad. Sci.* 113, E4794–E4800. <https://doi.org/10.1073/pnas.1601002113>
- Coussot, G., Perrin, C., Moreau, T., Dobrijevic, M., Postollec, A.L., Vandenabeele-Trambouze, O., 2010. A rapid and reversible colorimetric assay for the characterization of aminated solid surfaces. *Anal. Bioanal. Chem.* 399, 1061–1069. <https://doi.org/10.1007/s00216-010-4363-7>
- Cui, B., Clime, L., Li, K., Veres, T., 2008. Fabrication of large area nanoprism arrays and their application for surface enhanced Raman spectroscopy. *Nanotechnology* 19, 145302. <https://doi.org/10.1088/0957-4484/19/14/145302>
- Cui, N.-Y., Liu, C., Yang, W., 2011. XPS and AFM characterization of the self-assembled molecular monolayers of a 3-aminopropyltrimethoxysilane on silicon surface, and effects of substrate pretreatment by UV-irradiation. *Surf. Interface Anal.* 43, 1082–1088. <https://doi.org/10.1002/sia.3698>
- Dahlin, A.B., 2015. Sensing applications based on plasmonic nanopores: The hole story. *Analyst* 140, 4748–4759. <https://doi.org/10.1039/C4AN02258K>

- Dahlin, A.B., Tegenfeldt, J.O., Höök, F., 2006. Improving the Instrumental Resolution of Sensors Based on Localized Surface Plasmon Resonance. *Anal. Chem.* 78, 4416–4423. <https://doi.org/10.1021/ac0601967>
- Danoff, E.J., Fleming, K.G., 2011. The soluble, periplasmic domain of OmpA folds as an independent unit and displays chaperone activity by reducing the self-association propensity of the unfolded OmpA transmembrane β -barrel. *Biophys. Chem.*, Special Issue: 25th Anniversary of the Gibbs Conference on Biothermodynamics 159, 194–204. <https://doi.org/10.1016/j.bpc.2011.06.013>
- Derrick, J.P., Wigley, D.B., 1994. The Third IgG-Binding Domain from Streptococcal Protein G. *J. Mol. Biol.* 243, 906–918. <https://doi.org/10.1006/jmbi.1994.1691>
- Døvling Kaspersen, J., Moestrup Jessen, C., Stougaard Vad, B., Skipper Sørensen, E., Kleiner Andersen, K., Glasius, M., Pinto Oliveira, C.L., Otzen, D.E., Pedersen, J.S., 2014. Low-Resolution Structures of OmpA·DDM Protein–Detergent Complexes. *ChemBioChem* 15, 2113–2124. <https://doi.org/10.1002/cbic.201402162>
- Drake, B., Prater, C.B., Weisenhorn, A.L., Gould, S.A., Albrecht, T.R., Quate, C.F., Cannell, D.S., Hansma, H.G., Hansma, P.K., 1989. Imaging crystals, polymers, and processes in water with the atomic force microscope. *Science* 243, 1586–1589. <https://doi.org/10.1126/science.2928794>
- Dreaden, E.C., Austin, L.A., Mackey, M.A., El-Sayed, M.A., 2012. Size matters: gold nanoparticles in targeted cancer drug delivery. *Ther. Deliv.* 3, 457–478.
- Dressick, W.J., Chen, M.-S., Brandow, S.L., 2000. Patterned Noncovalent Binding and Metallization of Adsorbates in Thin Film Nanocavities. *J. Am. Chem. Soc.* 122, 982–983. <https://doi.org/10.1021/ja992285p>
- Dressick, W.J., Dulcey, C.S., Chen, M.-S., Calvert, J.M., 1996. Photochemical studies of (aminoethylaminomethyl) phenethyltrimethoxysilane self-assembled monolayer films. *Thin Solid Films, Seventh International Conference on Organized Molecular Films* 284, 568–572. [https://doi.org/10.1016/S0040-6090\(95\)08424-X](https://doi.org/10.1016/S0040-6090(95)08424-X)
- Dykman, L., Khlebtsov, N., 2012. Gold nanoparticles in biomedical applications: recent advances and perspectives. *Chem. Soc. Rev.* 41, 2256–2282. <https://doi.org/10.1039/C1CS15166E>
- Einstein, A., 1905. Über einen die Erzeugung und Verwandlung des Lichtes betreffenden heuristischen Gesichtspunkt. *Ann. Phys.* 322, 132–148. <https://doi.org/10.1002/andp.19053220607>
- Emilsson, G., Schoch, R.L., Oertle, P., Xiong, K., Lim, R.Y.H., Dahlin, A.B., 2017. Surface plasmon resonance methodology for monitoring polymerization kinetics and morphology changes of brushes—evaluated with poly(N-isopropylacrylamide). *Appl. Surf. Sci.* 396, 384–392. <https://doi.org/10.1016/j.apsusc.2016.10.165>
- Engelhardt, H., Orth, P., 1987. Alkoxy Silanes for the Preparation of Silica Based Stationary Phases with Bonded Polar Functional Groups. *J. Liq. Chromatogr.* 10, 1999–2022. <https://doi.org/10.1080/01483918708066809>
- Fairman, J.W., Noinaj, N., Buchanan, S.K., 2011. The structural biology of β -barrel membrane proteins: a summary of recent reports. *Curr. Opin. Struct. Biol.*

- Engineering and design / Membranes 21, 523–531.
<https://doi.org/10.1016/j.sbi.2011.05.005>
- Falabella, J.B., Cho, T.J., Ripple, D.C., Hackley, V.A., Tarlov, M.J., 2010. Characterization of Gold Nanoparticles Modified with Single-Stranded DNA Using Analytical Ultracentrifugation and Dynamic Light Scattering. *Langmuir* 26, 12740–12747. <https://doi.org/10.1021/la100761f>
- Farris, L.R., Wu, N., Wang, W., Clarizia, L.-J.A., Wang, X., McDonald, M.J., 2010. Immuno-interferometric sensor for the detection of influenza A nucleoprotein. *Anal. Bioanal. Chem.* 396, 667–674. <https://doi.org/10.1007/s00216-009-3235-5>
- Faulk, W., Taylor, G., 1971. Communication to the editors. *Immunochemistry* 8, 1081–1083. [https://doi.org/10.1016/0019-2791\(71\)90496-4](https://doi.org/10.1016/0019-2791(71)90496-4)
- Fleetwood, F., Andersson, K.G., Ståhl, S., Löfblom, J., 2014. An engineered autotransporter-based surface expression vector enables efficient display of Affibody molecules on OmpT-negative *E. coli* as well as protease-mediated secretion in OmpT-positive strains. *Microb. Cell Factories* 13, 179. <https://doi.org/10.1186/s12934-014-0179-z>
- Förster, S., Neubert, I., Schlüter, A.D., Lindner, P., 1999. How Dendrons Stiffen Polymer Chains: A SANS Study. *Macromolecules* 32, 4043–4049. <https://doi.org/10.1021/ma9817929>
- Freeman, R., Grabar, K., Allison, K., Bright, R., Davis, J., Guthrie, A., Hommer, M., Jackson, M., Smith, P., Walter, D., Natan, M., 1995. Self-Assembled Metal Colloid Monolayers - an Approach to Sers Substrates. *Science* 267, 1629–1632. <https://doi.org/10.1126/science.267.5204.1629>
- Frens, G., 1973. Controlled Nucleation for the Regulation of the Particle Size in Monodisperse Gold Suspensions. *Nature* 241, 20–22. <https://doi.org/10.1038/10.1038/physci241020a0>
- Freundlich, H.M.F., 1906. Over the adsorption in solution. *J. Phys. Chem.* 57.
- Fujiwara, K., Watarai, H., Itoh, H., Nakahama, E., Ogawa, N., 2006. Measurement of antibody binding to protein immobilized on gold nanoparticles by localized surface plasmon spectroscopy. *Anal. Bioanal. Chem.* 386, 639–644. <https://doi.org/10.1007/s00216-006-0559-2>
- Ganguli, M., Babu, J.V., Maiti, S., 2004. Complex Formation between Cationically Modified Gold Nanoparticles and DNA: An Atomic Force Microscopic Study. *Langmuir* 20, 5165–5170. <https://doi.org/10.1021/la036049a>
- Gao, H., Henzie, J., Odom, T.W., 2006. Direct Evidence for Surface Plasmon-Mediated Enhanced Light Transmission through Metallic Nanohole Arrays. *Nano Lett.* 6, 2104–2108. <https://doi.org/10.1021/nl061670r>
- Geer, R.E., Stenger, D.A., Chen, M.S., Calvert, J.M., Shashidhar, R., Jeong, Y.H., Pershan, P.S., 1994. X-ray and Ellipsometric Studies of Self-Assembled Monolayers of Fluorinated Chlorosilanes. *Langmuir* 10, 1171–1176. <https://doi.org/10.1021/la00016a034>
- George, C., Ricci, D., Di Zitti, E., 2008. Gold nanoparticles self-assembled onto passivated glass substrates: Tuning the transition from 2D to 1D structures. *Superlattices Microstruct., E-MRS 2007 Symposium K Nanoscale Self-Assembly and Patterning* 44, 608–616. <https://doi.org/10.1016/j.spmi.2008.02.003>

- Gil, D., Schrum, A.G., 2013. Strategies to stabilize compact folding and minimize aggregation of antibody-based fragments. *Adv. Biosci. Biotechnol. Print* 4, 73–84. <https://doi.org/10.4236/abb.2013.44A011>
- Goldstein, J., Newbury, D.E., Echlin, P., Joy, D.C., Jr, A.D.R., Lyman, C.E., Fiori, C., Lifshin, E., 2012. *Scanning Electron Microscopy and X-Ray Microanalysis: A Text for Biologists, Materials Scientists, and Geologists*. Springer Science & Business Media.
- Goy-López, S., Juárez, J., Alatorre-Meda, M., Casals, E., Puentes, V.F., Taboada, P., Mosquera, V., 2012. Physicochemical Characteristics of Protein–NP Bioconjugates: The Role of Particle Curvature and Solution Conditions on Human Serum Albumin Conformation and Fibrillogenesis Inhibition. *Langmuir* 28, 9113–9126. <https://doi.org/10.1021/la300402w>
- Grabar, K.C., Allison, K.J., Baker, B.E., Bright, R.M., Brown, K.R., Freeman, R.G., Fox, A.P., Keating, C.D., Musick, M.D., Natan, M.J., 1996a. Two-Dimensional Arrays of Colloidal Gold Particles: A Flexible Approach to Macroscopic Metal Surfaces. *Langmuir* 12, 2353–2361. <https://doi.org/10.1021/la950561h>
- Grabar, K.C., Brown, K.R., Keating, C.D., Stranick, S.J., Tang, S.-L., Natan, M.J., 1997. Nanoscale Characterization of Gold Colloid Monolayers: A Comparison of Four Techniques. *Anal. Chem.* 69, 471–477. <https://doi.org/10.1021/ac9605962>
- Grabar, K.C., Freeman, R.G., Hommer, M.B., Natan, M.J., 1995. Preparation and Characterization of Au Colloid Monolayers. *Anal. Chem.* 67, 735–743. <https://doi.org/10.1021/ac00100a008>
- Grabar, K.C., Smith, P.C., Musick, M.D., Davis, J.A., Walter, D.G., Jackson, M.A., Guthrie, A.P., Natan, M.J., 1996b. Kinetic Control of Interparticle Spacing in Au Colloid-Based Surfaces: Rational Nanometer-Scale Architecture. *J. Am. Chem. Soc.* 118, 1148–1153. <https://doi.org/10.1021/ja952233+>
- Green, R.J., Davies, M.C., Roberts, C.J., Tendler, S.J.B., 1999. Competitive protein adsorption as observed by surface plasmon resonance. *Biomaterials* 20, 385–391. [https://doi.org/10.1016/S0142-9612\(98\)00201-4](https://doi.org/10.1016/S0142-9612(98)00201-4)
- Gronenborn, A.M., Clore, G.M., 1993. Identification of the Contact Surface of a Streptococcal Protein G Domain Complexed with a Human Fc Fragment. *J. Mol. Biol.* 233, 331–335. <https://doi.org/10.1006/jmbi.1993.1514>
- Gronenborn, A.M., Filpula, D.R., Essig, N.Z., Achari, A., Whitlow, M., Wingfield, P.T., Clore, G.M., 1991. A novel, highly stable fold of the immunoglobulin binding domain of streptococcal protein G. *Science* 253, 657–661. <https://doi.org/10.1126/science.1871600>
- Grossman, P.D., Colburn, J.C., 2012. *Capillary Electrophoresis: Theory and Practice*. Academic Press.
- Gu, Y., Li, H., Dong, H., Zeng, Y., Zhang, Z., Paterson, N.G., Stansfeld, P.J., Wang, Z., Zhang, Y., Wang, W., Dong, C., 2016. Structural basis of outer membrane protein insertion by the BAM complex. *Nature* 531, 64–69. <https://doi.org/10.1038/nature17199>

- Guinier, A., 1939. La diffraction des rayons X aux très petits angles : application à l'étude de phénomènes ultramicroscopiques. *Ann. Phys.* 11, 161–237. <https://doi.org/10.1051/anphys/193911120161>
- Guo, X.H., Zhao, N.M., Chen, S.H., Teixeira, J., 1990. Small-angle neutron scattering study of the structure of protein / detergent complexes. *Biopolymers* 29, 335–346. <https://doi.org/10.1002/bip.360290206>
- Haddada, M., Huebner, M., Casale, S., Knopp, D., Niessner, R., Salmain, M., Boujday, S., 2016. Gold Nanoparticles Assembly on Silicon and Gold Surfaces: Mechanism, Stability, and Efficiency in Diclofenac Biosensing. *J. Phys. Chem. C* 120, 29302–29311. <https://doi.org/10.1021/acs.jpcc.6b10322>
- Haes, A.J., Zou, S., Schatz, G.C., Van Duyne, R.P., 2004. A Nanoscale Optical Biosensor: The Long Range Distance Dependence of the Localized Surface Plasmon Resonance of Noble Metal Nanoparticles. *J. Phys. Chem. B* 108, 109–116. <https://doi.org/10.1021/jp0361327>
- Hames, B.D. (Ed.), 1998. *Gel Electrophoresis of Proteins: A Practical Approach*, Third Edition. ed, Practical Approach Series. Oxford University Press, Oxford, New York.
- Han, L., Zheng, J., Wang, Y., Yang, X., Liu, Y., Sun, C., Cao, B., Zhou, H., Ni, D., Lou, J., Zhao, Y., Huang, Y., 2016. Structure of the BAM complex and its implications for biogenesis of outer-membrane proteins. *Nat. Struct. Mol. Biol.* 23, 192–196. <https://doi.org/10.1038/nsmb.3181>
- Hanauer, M., Pierrat, S., Zins, I., Lotz, A., Sönnichsen, C., 2007. Separation of Nanoparticles by Gel Electrophoresis According to Size and Shape. *Nano Lett.* 7, 2881–2885. <https://doi.org/10.1021/nl071615y>
- Hansen, S., 2012. BayesApp: a web site for indirect transformation of small-angle scattering data. *J. Appl. Crystallogr.* 45, 566–567. <https://doi.org/10.1107/S0021889812014318>
- Harris, R., 1997. *Negative Staining and Cryoelectron Microscopy*, 2nd ed. Bios Scientific.
- Ho, Y.-S., 2006. Review of second-order models for adsorption systems. *J. Hazard. Mater.* 136, 681–689. <https://doi.org/10.1016/j.jhazmat.2005.12.043>
- Holt, S.A., Brun, A.P.L., Majkrzak, C.F., McGillivray, D.J., Heinrich, F., Lösche, M., Lakey, J.H., 2009. An ion-channel-containing model membrane: structural determination by magnetic contrast neutron reflectometry. *Soft Matter* 5, 2576–2586. <https://doi.org/10.1039/B822411K>
- Homola, J., 2003. Present and future of surface plasmon resonance biosensors. *Anal. Bioanal. Chem.* 377, 528–539. <https://doi.org/10.1007/s00216-003-2101-0>
- Hong, H., Szabo, G., Tamm, L.K., 2006. Electrostatic couplings in OmpA ion-channel gating suggest a mechanism for pore opening. *Nat. Chem. Biol.* 2, 627–635. <https://doi.org/10.1038/nchembio827>
- Howlett, G.J., Minton, A.P., Rivas, G., 2006. Analytical ultracentrifugation for the study of protein association and assembly. *Curr. Opin. Chem. Biol., Analytical techniques / Mechanisms* 10, 430–436. <https://doi.org/10.1016/j.cbpa.2006.08.017>

- Huang, P.-S., Boyken, S.E., Baker, D., 2016. The coming of age of de novo protein design. *Nature* 537, 320–327. <https://doi.org/10.1038/nature19946>
- Huang, W., Qian, W., El-Sayed, M.A., 2005. The Optically Detected Coherent Lattice Oscillations in Silver and Gold Monolayer Periodic Nanoprism Arrays: The Effect of Interparticle Coupling. *J. Phys. Chem. B* 109, 18881–18888. <https://doi.org/10.1021/jp0526647>
- Huang, X., El-Sayed, M.A., 2010. Gold nanoparticles: Optical properties and implementations in cancer diagnosis and photothermal therapy. *J. Adv. Res.* 1, 13–28. <https://doi.org/10.1016/j.jare.2010.02.002>
- Hughes, A.V., Howse, J.R., Dabkowska, A., Jones, R.A.L., Lawrence, M.J., Roser, S.J., 2008. Floating Lipid Bilayers Deposited on Chemically Grafted Phosphatidylcholine Surfaces. *Langmuir* 24, 1989–1999. <https://doi.org/10.1021/la702050b>
- Hughes, R.A., Miklos, A.E., Ellington, A.D., 2011. Gene Synthesis. *Methods Enzymol., Synthetic Biology, Part B* 498, 277–309. <https://doi.org/10.1016/B978-0-12-385120-8.00012-7>
- Hulteen, J.C., Van Duyne, R.P., 1995. Nanosphere lithography: A materials general fabrication process for periodic particle array surfaces. *J. Vac. Sci. Technol. Vac. Surf. Films* 13, 1553–1558. <https://doi.org/10.1116/1.579726>
- Iadanza, M.G., Higgins, A.J., Schiffrin, B., Calabrese, A.N., Brockwell, D.J., Ashcroft, A.E., Radford, S.E., Ranson, N.A., 2016. Lateral opening in the intact β -barrel assembly machinery captured by cryo-EM. *Nat. Commun.* 7, ncomms12865. <https://doi.org/10.1038/ncomms12865>
- Ishida, H., Garcia-Herrero, A., Vogel, H.J., 2014. The periplasmic domain of Escherichia coli outer membrane protein A can undergo a localized temperature dependent structural transition. *Biochim. Biophys. Acta BBA - Biomembr.* 1838, 3014–3024. <https://doi.org/10.1016/j.bbamem.2014.08.008>
- Jang, L.-S., Liu, H.-J., 2009. Fabrication of protein chips based on 3-aminopropyltriethoxysilane as a monolayer. *Biomed. Microdevices* 11, 331–338. <https://doi.org/10.1007/s10544-008-9239-7>
- Jans, H., Liu, X., Austin, L., Maes, G., Huo, Q., 2009. Dynamic Light Scattering as a Powerful Tool for Gold Nanoparticle Bioconjugation and Biomolecular Binding Studies. *Anal. Chem.* 81, 9425–9432. <https://doi.org/10.1021/ac901822w>
- Jazayeri, M.H., Amani, H., Pourfatollah, A.A., Pazoki-Toroudi, H., Sedighimoghaddam, B., 2016. Various methods of gold nanoparticles (GNPs) conjugation to antibodies. *Sens. Bio-Sens. Res.* 9, 17–22. <https://doi.org/10.1016/j.sbsr.2016.04.002>
- Ji, X., Song, X., Li, J., Bai, Y., Yang, W., Peng, X., 2007. Size Control of Gold Nanocrystals in Citrate Reduction: The Third Role of Citrate. *J. Am. Chem. Soc.* 129, 13939–13948. <https://doi.org/10.1021/ja074447k>
- Johnson, A., Song, Q., Ko Ferrigno, P., Bueno, P.R., Davis, J.J., 2012. Sensitive Affimer and Antibody Based Impedimetric Label-Free Assays for C-Reactive Protein. *Anal. Chem.* 84, 6553–6560. <https://doi.org/10.1021/ac300835b>

- Jonkheijm, P., Weinrich, D., Schröder, H., Niemeyer, C.M., Waldmann, H., 2008. Chemical Strategies for Generating Protein Biochips. *Angew. Chem. Int. Ed.* 47, 9618–9647. <https://doi.org/10.1002/anie.200801711>
- Jönsson, U., Fägerstam, L., Ivarsson, B., Johnsson, B., Karlsson, R., Lundh, K., Löfås, S., Persson, B., Roos, H., Rönnerberg, I., 1991. Real-time biospecific interaction analysis using surface plasmon resonance and a sensor chip technology. *BioTechniques* 11, 620–627.
- Kaminska, A., Inya-Agha, O., Forster, R.J., Keyes, T.E., 2008. Chemically bound gold nanoparticle arrays on silicon: assembly, properties and SERS study of protein interactions. *Phys. Chem. Chem. Phys.* 10, 4172–4180. <https://doi.org/10.1039/B803007C>
- Kausaite-Minkstimiene, A., Ramanaviciene, A., Kirlyte, J., Ramanavicius, A., 2010. Comparative Study of Random and Oriented Antibody Immobilization Techniques on the Binding Capacity of Immunosensor. *Anal. Chem.* 82, 6401–6408. <https://doi.org/10.1021/ac100468k>
- Ke, H., Wang, J., Dai, Z., Jin, Y., Qu, E., Xing, Z., Guo, C., Yue, X., Liu, J., 2011. Gold-Nanoshelled Microcapsules: A Theranostic Agent for Ultrasound Contrast Imaging and Photothermal Therapy. *Angew. Chem. Int. Ed.* 50, 3017–3021. <https://doi.org/10.1002/anie.201008286>
- Kedem, O., Vaskevich, A., Rubinstein, I., 2011. Improved Sensitivity of Localized Surface Plasmon Resonance Transducers Using Reflection Measurements. *J. Phys. Chem. Lett.* 2, 1223–1226. <https://doi.org/10.1021/jz200482f>
- Kelly, P.J., Arnell, R.D., 2000. Magnetron sputtering: a review of recent developments and applications. *Vacuum* 56, 159–172. [https://doi.org/10.1016/S0042-207X\(99\)00189-X](https://doi.org/10.1016/S0042-207X(99)00189-X)
- Kelly, P.M., Åberg, C., Polo, E., O’Connell, A., Cookman, J., Fallon, J., Krpetić, Ž., Dawson, K.A., 2015. Mapping protein binding sites on the biomolecular corona of nanoparticles. *Nat. Nanotechnol.* 10, 472–479. <https://doi.org/10.1038/nnano.2015.47>
- Khlebtsov, B.N., Khlebtsov, N.G., 2011. On the measurement of gold nanoparticle sizes by the dynamic light scattering method. *Colloid J.* 73, 118–127. <https://doi.org/10.1134/S1061933X11010078>
- Kim, B., Tripp, S.L., Wei, A., 2001. Self-Organization of Large Gold Nanoparticle Arrays. *J. Am. Chem. Soc.* 123, 7955–7956. <https://doi.org/10.1021/ja0160344>
- Klein, A.G., Werner, S.A., 1983. Neutron optics. *Rep. Prog. Phys.* 46, 259. <https://doi.org/10.1088/0034-4885/46/3/001>
- Koczula, K.M., Gallotta, A., 2016. Lateral flow assays. *Essays Biochem.* 60, 111–120. <https://doi.org/10.1042/EBC20150012>
- Koebnik, R., 1996. In vivo membrane assembly of split variants of the E.coli outer membrane protein OmpA. *EMBO J.* 15, 3529–3537.
- Krueger, S., Meuse, C.W., Majkrzak, C.F., Dura, J.A., Berk, N.F., Tarek, M., Plant, A.L., 2001. Investigation of Hybrid Bilayer Membranes with Neutron Reflectometry: Probing the Interactions of Melittin. *Langmuir* 17, 511–521. <https://doi.org/10.1021/la001134t>

- Kuhl, T.L., Majewski, J., Wong, J.Y., Steinberg, S., Leckband, D.E., Israelachvili, J.N., Smith, G.S., 1998. A Neutron Reflectivity Study of Polymer-Modified Phospholipid Monolayers at the Solid-Solution Interface: Polyethylene Glycol-Lipids on Silane-Modified Substrates. *Biophys. J.* 75, 2352–2362. [https://doi.org/10.1016/S0006-3495\(98\)77679-9](https://doi.org/10.1016/S0006-3495(98)77679-9)
- Kuhn, S.J., Finch, S.K., Hallahan, D.E., Giorgio, T.D., 2007. Facile production of multivalent enzyme-nanoparticle conjugates. *J. Magn. Magn. Mater., Proceedings of the Sixth International Conference on the Scientific and Clinical Applications of Magnetic Carriers* 311, 68–72. <https://doi.org/10.1016/j.jmmm.2006.10.1165>
- Kumar, S., Aaron, J., Sokolov, K., 2008. Directional conjugation of antibodies to nanoparticles for synthesis of multiplexed optical contrast agents with both delivery and targeting moieties. *Nat. Protoc.* 3, 314–320. <https://doi.org/10.1038/nprot.2008.1>
- Kumar, S., Aswal, V.K., Kohlbrecher, J., 2011. SANS and UV–vis Spectroscopy Studies of Resultant Structure from Lysozyme Adsorption on Silica Nanoparticles. *Langmuir* 27, 10167–10173. <https://doi.org/10.1021/la201291k>
- Kumari, S., Moirangthem, R.S., 2016. Portable and economical plasmonic capillary sensor for biomolecular detection. *Sens. Actuators B Chem.* 231, 203–210. <https://doi.org/10.1016/j.snb.2016.03.011>
- Kwak, E.-S., Henzie, J., Chang, S.-H., Gray, S.K., Schatz, G.C., Odom, T.W., 2005. Surface Plasmon Standing Waves in Large-Area Subwavelength Hole Arrays. *Nano Lett.* 5, 1963–1967. <https://doi.org/10.1021/nl051339s>
- Lacerda, S.H.D.P., Park, J.J., Meuse, C., Pristinski, D., Becker, M.L., Karim, A., Douglas, J.F., 2010. Interaction of Gold Nanoparticles with Common Human Blood Proteins. *ACS Nano* 4, 365–379. <https://doi.org/10.1021/nn9011187>
- Laemmli, U.K., 1970. Cleavage of Structural Proteins during the Assembly of the Head of Bacteriophage T4. *Nature* 227, 680–685. <https://doi.org/10.1038/227680a0>
- Lakey, J.H., 2009. Neutrons for biologists: a beginner's guide, or why you should consider using neutrons. *J. R. Soc. Interface* 6, S567–S573. <https://doi.org/10.1098/rsif.2009.0156.focus>
- Langmuir, I., 1916. THE CONSTITUTION AND FUNDAMENTAL PROPERTIES OF SOLIDS AND LIQUIDS. PART I. SOLIDS. *J. Am. Chem. Soc.* 38, 2221–2295. <https://doi.org/10.1021/ja02268a002>
- Larson, T.A., Bankson, J., Aaron, J., Sokolov, K., 2007. Hybrid plasmonic magnetic nanoparticles as molecular specific agents for MRI/optical imaging and photothermal therapy of cancer cells. *Nanotechnology* 18, 325101. <https://doi.org/10.1088/0957-4484/18/32/325101>
- Latour, R.A., 2015. The langmuir isotherm: A commonly applied but misleading approach for the analysis of protein adsorption behavior. *J. Biomed. Mater. Res. A* 103, 949–958. <https://doi.org/10.1002/jbm.a.35235>
- Le Brun, A.P., Holt, S.A., Shah, D.S.H., Majkrzak, C.F., Lakey, J.H., 2011. The structural orientation of antibody layers bound to engineered biosensor surfaces. *Biomaterials* 32, 3303–3311. <https://doi.org/10.1016/j.biomaterials.2011.01.026>

- Leatherbarrow, R.J., Fersht, A.R., 1986. Protein engineering. *Protein Eng. Des. Sel.* 1, 7–16. <https://doi.org/10.1093/protein/1.1.7>
- Lee, J.M., Park, H.K., Jung, Y., Kim, J.K., Jung, S.O., Chung, B.H., 2007. Direct Immobilization of Protein G Variants with Various Numbers of Cysteine Residues on a Gold Surface. *Anal. Chem.* 79, 2680–2687. <https://doi.org/10.1021/ac0619231>
- Lewis, M., 2006. Biomolecule retaining material and methods for attaching biomolecules to a surface. US20060257920 A1.
- Li, K., Zettlitz, K.A., Lipianskaya, J., Zhou, Y., Marks, J.D., Mallick, P., Reiter, R.E., Wu, A.M., 2015. A fully human scFv phage display library for rapid antibody fragment reformatting. *Protein Eng. Des. Sel.* 28, 307–316. <https://doi.org/10.1093/protein/gzv024>
- Li, Y., Lee, J., Lal, J., An, L., Huang, Q., 2008. Effects of pH on the Interactions and Conformation of Bovine Serum Albumin: Comparison between Chemical Force Microscopy and Small-Angle Neutron Scattering. *J. Phys. Chem. B* 112, 3797–3806. <https://doi.org/10.1021/jp077392h>
- Liang, X., Wei, H., Cui, Z., Deng, J., Zhang, Z., You, X., Zhang, X.-E., 2011. Colorimetric detection of melamine in complex matrices based on cysteamine-modified gold nanoparticles. *Analyst* 136, 179–183. <https://doi.org/10.1039/C0AN00432D>
- Liljeström, V., Mikkilä, J., Kostianen, M.A., 2014. Self-assembly and modular functionalization of three-dimensional crystals from oppositely charged proteins. *Nat. Commun.* 5, ncomms5445. <https://doi.org/10.1038/ncomms5445>
- Lin, W., Insley, T., Tuttle, M.D., Zhu, L., Berthold, D.A., Král, P., Rienstra, C.M., Murphy, C.J., 2015. Control of Protein Orientation on Gold Nanoparticles. *J. Phys. Chem. C* 119, 21035–21043. <https://doi.org/10.1021/acs.jpcc.5b07701>
- Liu, H., Shen, X., Wang, Z.-G., Kuzyk, A., Ding, B., 2014. Helical nanostructures based on DNA self-assembly. *Nanoscale* 6, 9331–9338. <https://doi.org/10.1039/C3NR06913C>
- Liu, S., Zhu, T., Hu, R., Liu, Z., 2002. Evaporation-induced self-assembly of gold nanoparticles into a highly organized two-dimensional array. *Phys. Chem. Chem. Phys.* 4, 6059–6062. <https://doi.org/10.1039/B208520H>
- Liu, X., Huo, Q., 2009. A washing-free and amplification-free one-step homogeneous assay for protein detection using gold nanoparticle probes and dynamic light scattering. *J. Immunol. Methods* 349, 38–44. <https://doi.org/10.1016/j.jim.2009.07.015>
- Liu, Yang, Liu, Yi, Mernaugh, R.L., Zeng, X., 2009. Single chain fragment variable recombinant antibody functionalized gold nanoparticles for a highly sensitive colorimetric immunoassay. *Biosens. Bioelectron.* 24, 2853–2857. <https://doi.org/10.1016/j.bios.2009.02.016>
- Löfblom, J., Frejd, F.Y., Ståhl, S., 2011. Non-immunoglobulin based protein scaffolds. *Curr. Opin. Biotechnol.*, 22/6 Chemical biotechnology and Pharmaceutical biotechnology 22, 843–848. <https://doi.org/10.1016/j.copbio.2011.06.002>
- Love, J.C., Estroff, L.A., Kriebel, J.K., Nuzzo, R.G., Whitesides, G.M., 2005. Self-Assembled Monolayers of Thiolates on Metals as a Form of Nanotechnology. *Chem. Rev.* 105, 1103–1170. <https://doi.org/10.1021/cr0300789>

- Lundqvist, M., Stigler, J., Elia, G., Lynch, I., Cedervall, T., Dawson, K.A., 2008. Nanoparticle size and surface properties determine the protein corona with possible implications for biological impacts. *Proc. Natl. Acad. Sci.* 105, 14265–14270. <https://doi.org/10.1073/pnas.0805135105>
- Lyu, Z.X., Zhao, X.S., 2015. Periplasmic quality control in biogenesis of outer membrane proteins. *Biochem. Soc. Trans.* 43, 133–138. <https://doi.org/10.1042/BST20140217>
- Ma, L., Li, F., Fang, T., Zhang, J., Wang, Q., 2015. Controlled Self-Assembly of Proteins into Discrete Nanoarchitectures Templated by Gold Nanoparticles via Monovalent Interfacial Engineering. *ACS Appl. Mater. Interfaces* 7, 11024–11031. <https://doi.org/10.1021/acsami.5b02823>
- Malekian, B., Xiong, K., Emilsson, G., Andersson, J., Fager, C., Olsson, E., Larsson-Langhammer, E.M., Dahlin, A.B., 2017. Fabrication and Characterization of Plasmonic Nanopores with Cavities in the Solid Support. *Sensors* 17, 1444. <https://doi.org/10.3390/s17061444>
- Malmström, J., Agheli, H., Kingshott, P., Sutherland, D.S., 2007. Viscoelastic Modeling of Highly Hydrated Laminin Layers at Homogeneous and Nanostructured Surfaces: Quantification of Protein Layer Properties Using QCM-D and SPR. *Langmuir* 23, 9760–9768. <https://doi.org/10.1021/la701233y>
- Maniatis, T., Fritsch, E.F., Sambrook, J., 1982. *Molecular cloning: A laboratory manual*. Cold Spring Harbor Laboratory, Cold Spring Harbor, N.Y.
- Mano, J.F., Silva, G.A., Azevedo, H.S., Malafaya, P.B., Sousa, R.A., Silva, S.S., Boesel, L.F., Oliveira, J.M., Santos, T.C., Marques, A.P., Neves, N.M., Reis, R.L., 2007. Natural origin biodegradable systems in tissue engineering and regenerative medicine: present status and some moving trends. *J. R. Soc. Interface* 4, 999–1030. <https://doi.org/10.1098/rsif.2007.0220>
- Manson, J., Kumar, D., Meenan, B.J., Dixon, D., 2011. Polyethylene glycol functionalized gold nanoparticles: the influence of capping density on stability in various media. *Gold Bull.* 44, 99–105. <https://doi.org/10.1007/s13404-011-0015-8>
- Marcoux, J., Politis, A., Rinehart, D., Marshall, D.P., Wallace, M.I., Tamm, L.K., Robinson, C.V., 2014. Mass Spectrometry Defines the C-Terminal Dimerization Domain and Enables Modeling of the Structure of Full-Length OmpA. *Structure* 22, 781–790. <https://doi.org/10.1016/j.str.2014.03.004>
- Martinez-Perdiguero, J., Retolaza, A., Juarros, A., Otaduy, D., Merinoa, S., 2012. Enhanced Transmission through Gold Nanohole Arrays Fabricated by Thermal Nanoimprint Lithography for Surface Plasmon Based Biosensors. *Procedia Eng.*, 26th European Conference on Solid-State Transducers, EUROSENSOR 2012 47, 805–808. <https://doi.org/10.1016/j.proeng.2012.09.269>
- Martinez-Perdiguero, J., Retolaza, A., Otaduy, D., Juarros, A., Merino, S., 2013. Real-Time Label-Free Surface Plasmon Resonance Biosensing with Gold Nanohole Arrays Fabricated by Nanoimprint Lithography. *Sensors* 13, 13960–13968. <https://doi.org/10.3390/s131013960>
- Masson, J.-F., Yockell-Lelièvre, H., 2014. Spectroscopic and Physical Characterization of Functionalized Au Nanoparticles: A Multiweek Experimental Project. *J. Chem. Educ.* 91, 1557–1562. <https://doi.org/10.1021/ed500067u>

- Materne, T., de Buyl, F., Witucki, G., n.d. *Organosilane Technology in Coating Applications: Review and Perspectives*. Dow Corning.
- Mayer, K.M., Hafner, J.H., 2011. Localized Surface Plasmon Resonance Sensors. *Chem. Rev.* 111, 3828–3857. <https://doi.org/10.1021/cr100313v>
- Mazzer, A.R., Clifton, L.A., Perevozchikova, T., Butler, P.D., Roberts, C.J., Bracewell, D.G., 2017. Neutron reflectivity measurement of protein A–antibody complex at the solid-liquid interface. *J. Chromatogr. A* 1499, 118–131. <https://doi.org/10.1016/j.chroma.2017.03.084>
- McMillan, R.A., Paavola, C.D., Howard, J., Chan, S.L., Zaluzec, N.J., Trent, J.D., 2002. Ordered nanoparticle arrays formed on engineered chaperonin protein templates. *Nat. Mater.* 1, 247–252. <https://doi.org/10.1038/nmat775>
- McMorran, L.M., Brockwell, D.J., Radford, S.E., 2014. Mechanistic studies of the biogenesis and folding of outer membrane proteins in vitro and in vivo: What have we learned to date? *Arch. Biochem. Biophys.* 564, 265–280. <https://doi.org/10.1016/j.abb.2014.02.011>
- Medintz, I., 2006. Universal tools for biomolecular attachment to surfaces. *Nat. Mater.* 5, 842–842. <https://doi.org/10.1038/nmat1776>
- Muller, D.J., 2008. AFM: A Nanotool in Membrane Biology. *Biochemistry (Mosc.)* 47, 7986–7998. <https://doi.org/10.1021/bi800753x>
- NanoDrop: How it works [WWW Document], n.d. URL <https://www.thermofisher.com/uk/en/home/industrial/spectroscopy-elemental-isotope-analysis/molecular-spectroscopy/ultraviolet-visible-visible-spectrophotometry-uv-vis-vis/uv-vis-vis-instruments/nanodrop-microvolume-spectrophotometers/nanodrop-products-guide/nanodrop-how-it-works.html> (accessed 5.28.17).
- Nath, N., Chilkoti, A., 2004. Label-Free Biosensing by Surface Plasmon Resonance of Nanoparticles on Glass: Optimization of Nanoparticle Size. *Anal. Chem.* 76, 5370–5378. <https://doi.org/10.1021/ac049741z>
- Nath, N., Chilkoti, A., 2002. A Colorimetric Gold Nanoparticle Sensor To Interrogate Biomolecular Interactions in Real Time on a Surface. *Anal. Chem.* 74, 504–509. <https://doi.org/10.1021/ac015657x>
- Niemeyer, C.M., 2001. Nanoparticles, Proteins, and Nucleic Acids: Biotechnology Meets Materials Science. *Angew. Chem. Int. Ed.* 40, 4128–4158. [https://doi.org/10.1002/1521-3773\(20011119\)40:22<4128::AID-ANIE4128>3.0.CO;2-S](https://doi.org/10.1002/1521-3773(20011119)40:22<4128::AID-ANIE4128>3.0.CO;2-S)
- Nikaido, H., 2003. Molecular Basis of Bacterial Outer Membrane Permeability Revisited. *Microbiol. Mol. Biol. Rev.* 67, 593–656. <https://doi.org/10.1128/MMBR.67.4.593-656.2003>
- Nilsson, B., Moks, T., Jansson, B., Abrahmsén, L., Elmlblad, A., Holmgren, E., Henrichson, C., Jones, T.A., Uhlén, M., 1987. A synthetic IgG-binding domain based on staphylococcal protein A. *Protein Eng.* 1, 107–113.
- Noinaj, N., Kuszak, A.J., Balusek, C., Gumbart, J.C., Buchanan, S.K., 2014. Lateral Opening and Exit Pore Formation Are Required for BamA Function. *Structure* 22, 1055–1062. <https://doi.org/10.1016/j.str.2014.05.008>

- Nuttall, S.D., Walsh, R.B., 2008. Display scaffolds: protein engineering for novel therapeutics. *Curr. Opin. Pharmacol., Anti-infectives/New technologies* 8, 609–615. <https://doi.org/10.1016/j.coph.2008.06.007>
- Ochiai, T., Isozaki, K., Nishiyama, S., Miki, K., 2014. Enhancement of self-assembly of large (>10 nm) gold nanoparticles on an ITO substrate. *Appl. Phys. Express* 7, 065001. <https://doi.org/10.7567/APEX.7.065001>
- Ofir, Y., Samanta, B., M. Rotello, V., 2008. Polymer and biopolymer mediated self-assembly of gold nanoparticles. *Chem. Soc. Rev.* 37, 1814–1825. <https://doi.org/10.1039/B712689C>
- Okamoto, T., Yamaguchi, I., 2003. Optical Absorption Study of the Surface Plasmon Resonance in Gold Nanoparticles Immobilized onto a Gold Substrate by Self-Assembly Technique. *J. Phys. Chem. B* 107, 10321–10324. <https://doi.org/10.1021/jp034537l>
- Osterloh, F., Hiramatsu, H., Porter, R., Guo, T., 2004. Alkanethiol-Induced Structural Rearrangements in Silica–Gold Core–Shell-type Nanoparticle Clusters: An Opportunity for Chemical Sensor Engineering. *Langmuir* 20, 5553–5558. <https://doi.org/10.1021/la0348719>
- Paciotti, G.F., Myer, L., Weinreich, D., Goia, D., Pavel, N., McLaughlin, R.E., Tamarkin, L., 2004. Colloidal Gold: A Novel Nanoparticle Vector for Tumor Directed Drug Delivery. *Drug Deliv.* 11, 169–183. <https://doi.org/10.1080/10717540490433895>
- Parak, W.J., Pellegrino, T., Micheel, C.M., Gerion, D., Williams, S.C., Alivisatos, A.P., 2003. Conformation of Oligonucleotides Attached to Gold Nanocrystals Probed by Gel Electrophoresis. *Nano Lett.* 3, 33–36. <https://doi.org/10.1021/nl025888z>
- Park, J.-W., Shumaker-Parry, J.S., 2014. Structural Study of Citrate Layers on Gold Nanoparticles: Role of Intermolecular Interactions in Stabilizing Nanoparticles. *J. Am. Chem. Soc.* 136, 1907–1921. <https://doi.org/10.1021/ja4097384>
- Parratt, L.G., 1954. Surface Studies of Solids by Total Reflection of X-Rays. *Phys. Rev.* 95, 359–369. <https://doi.org/10.1103/PhysRev.95.359>
- Pautsch, A., Schulz, G.E., 2000. High-resolution structure of the OmpA membrane domain1. *J. Mol. Biol.* 298, 273–282. <https://doi.org/10.1006/jmbi.2000.3671>
- Penfold, J., Thomas, R.K., 1990. The application of the specular reflection of neutrons to the study of surfaces and interfaces. *J. Phys. Condens. Matter* 2, 1369. <https://doi.org/10.1088/0953-8984/2/6/001>
- Politou, A.S., Gautel, M., Pfuhl, M., Labeit, S., Pastore, A., 1994. Immunoglobulin-type domains of titin: same fold, different stability? *Biochemistry (Mosc.)* 33, 4730–4737. <https://doi.org/10.1021/bi00181a604>
- Potter, C. w., 2001. A history of influenza. *J. Appl. Microbiol.* 91, 572–579. <https://doi.org/10.1046/j.1365-2672.2001.01492.x>
- Puchner, E.M., Gaub, H.E., 2009. Force and function: probing proteins with AFM-based force spectroscopy. *Curr. Opin. Struct. Biol., Carbohydrates and glycoconjugates / Biophysical methods* 19, 605–614. <https://doi.org/10.1016/j.sbi.2009.09.005>
- Puertas, S., Moros, M., Fernández-Pacheco, R., Ibarra, M.R., Grazú, V., Fuente, J.M. de la, 2010. Designing novel nano-immunoassays: antibody orientation versus

- sensitivity. *J. Phys. Appl. Phys.* 43, 474012. <https://doi.org/10.1088/0022-3727/43/47/474012>
- Pyrz, W.D., Buttrey, D.J., 2008. Particle Size Determination Using TEM: A Discussion of Image Acquisition and Analysis for the Novice Microscopist. *Langmuir* 24, 11350–11360. <https://doi.org/10.1021/la801367j>
- Rabe, M., Verdes, D., Seeger, S., 2011. Understanding protein adsorption phenomena at solid surfaces. *Adv. Colloid Interface Sci.* 162, 87–106. <https://doi.org/10.1016/j.cis.2010.12.007>
- Raider, S.I., Flitsch, R., Palmer, M.J., 1975. Oxide Growth on Etched Silicon in Air at Room Temperature. *J. Electrochem. Soc.* 122, 413–418. <https://doi.org/10.1149/1.2134225>
- Rash, J.E., Yasumura, T., Hudson, C.S., Agre, P., Nielsen, S., 1998. Direct immunogold labeling of aquaporin-4 in square arrays of astrocyte and ependymocyte plasma membranes in rat brain and spinal cord. *Proc. Natl. Acad. Sci.* 95, 11981–11986. <https://doi.org/10.1073/pnas.95.20.11981>
- Rice, J.J., Schohn, A., Bessette, P.H., Boulware, K.T., Daugherty, P.S., 2006. Bacterial display using circularly permuted outer membrane protein OmpX yields high affinity peptide ligands. *Protein Sci.* 15, 825–836. <https://doi.org/10.1110/ps.051897806>
- Richens, J.L., O'Shea, P., 2014. 3 - Next generation techniques for biomedical imaging, in: Morris, P. (Ed.), *Biomedical Imaging*. Woodhead Publishing, pp. 65–92. <https://doi.org/10.1533/9780857097477.1.65>
- Rief, M., Gautel, M., Oesterhelt, F., Fernandez, J.M., Gaub, H.E., 1997. Reversible Unfolding of Individual Titin Immunoglobulin Domains by AFM. *Science* 276, 1109–1112. <https://doi.org/10.1126/science.276.5315.1109>
- Robinson, I., Tung, L.D., Maenosono, S., Wälti, C., Thanh, N.T.K., 2010. Synthesis of core-shell gold coated magnetic nanoparticles and their interaction with thiolated DNA. *Nanoscale* 2, 2624–2630. <https://doi.org/10.1039/C0NR00621A>
- Roque, A.I., Soliakov, A., Birch, M.A., Philips, S.R., Shah, D.S.H., Lakey, J.H., 2014. Reversible Non-Stick Behaviour of a Bacterial Protein Polymer Provides a Tuneable Molecular Mimic for Cell and Tissue Engineering. *Adv. Mater. Deerfield Beach Fla* 26, 2704–2709. <https://doi.org/10.1002/adma.201304645>
- Rugar, D., Hansma, P., 2008. Atomic Force Microscopy. *Phys. Today*. <https://doi.org/10.1063/1.881238>
- Sajid, M., Kawde, A.-N., Daud, M., 2015. Designs, formats and applications of lateral flow assay: A literature review. *J. Saudi Chem. Soc.* 19, 689–705. <https://doi.org/10.1016/j.jscs.2014.09.001>
- Sannomiya, T., Scholder, O., Jefimovs, K., Hafner, C., Dahlin, A.B., 2011. Investigation of Plasmon Resonances in Metal Films with Nanohole Arrays for Biosensing Applications. *Small* 7, 1653–1663. <https://doi.org/10.1002/sml.201002228>
- Santhanam, V., Liu, J., Agarwal, R., Andres, R.P., 2003. Self-Assembly of Uniform Monolayer Arrays of Nanoparticles. *Langmuir* 19, 7881–7887. <https://doi.org/10.1021/la0341761>

- Sapsford, K.E., Algar, W.R., Berti, L., Gemmill, K.B., Casey, B.J., Oh, E., Stewart, M.H., Medintz, I.L., 2013. Functionalizing Nanoparticles with Biological Molecules: Developing Chemistries that Facilitate Nanotechnology. *Chem. Rev.* 113, 1904–2074. <https://doi.org/10.1021/cr300143v>
- Sato, K., Hosokawa, K., Maeda, M., 2003. Rapid Aggregation of Gold Nanoparticles Induced by Non-Cross-Linking DNA Hybridization. *J. Am. Chem. Soc.* 125, 8102–8103. <https://doi.org/10.1021/ja034876s>
- Schabert, F.A., Henn, C., Engel, A., 1995. Native Escherichia coli OmpF porin surfaces probed by atomic force microscopy. *Science* 268, 92–94. <https://doi.org/10.1126/science.7701347>
- Schacht, K., Vogt, J., Scheibel, T., 2016. Foams Made of Engineered Recombinant Spider Silk Proteins as 3D Scaffolds for Cell Growth. *ACS Biomater. Sci. Eng.* 2, 517–525. <https://doi.org/10.1021/acsbomaterials.5b00483>
- Schagger, H., 2006. Tricine-SDS-PAGE : Article : Nature Protocols. *Nat Protoc.* 1, 16–22. <https://doi.org/10.1038/nprot.2006.4>
- Schiffrin, B., Calabrese, A.N., Devine, P.W.A., Harris, S.A., Ashcroft, A.E., Brockwell, D.J., Radford, S.E., 2016. Skp is a multivalent chaperone of outer-membrane proteins. *Nat. Struct. Mol. Biol.* 23, 786–793. <https://doi.org/10.1038/nsmb.3266>
- Seeman, N.C., Belcher, A.M., 2002. Emulating biology: Building nanostructures from the bottom up. *Proc. Natl. Acad. Sci.* 99, 6451–6455. <https://doi.org/10.1073/pnas.221458298>
- Sehgal, D., Vijay, I.K., 1994. A Method for the High Efficiency of Water-Soluble Carbodiimide-Mediated Amidation. *Anal. Biochem.* 218, 87–91. <https://doi.org/10.1006/abio.1994.1144>
- Seitz, O., Chehimi, M.M., Cabet-Deliry, E., Truong, S., Felidj, N., Perruchot, C., Greaves, S.J., Watts, J.F., 2003. Preparation and characterisation of gold nanoparticle assemblies on silanised glass plates. *Colloids Surf. Physicochem. Eng. Asp.* 218, 225–239. [https://doi.org/10.1016/S0927-7757\(02\)00594-0](https://doi.org/10.1016/S0927-7757(02)00594-0)
- Shah, D.S., Thomas, M.B., Phillips, S., Cisneros, D.A., Le Brun, A.P., Holt, S.A., Lakey, J.H., 2007. Self-assembling layers created by membrane proteins on gold. *Biochem. Soc. Trans.* 35, 522. <https://doi.org/10.1042/BST0350522>
- Sharpe, J.C., Mitchell, J.S., Lin, L., Sedoglavich, N., Blaikie, R.J., 2008. Gold Nanohole Array Substrates as Immunobiosensors. *Anal. Chem.* 80, 2244–2249. <https://doi.org/10.1021/ac702555r>
- Shenhar, R., Jeoung, E., Srivastava, S., Norsten, T.B., Rotello, V.M., 2005. Crosslinked Nanoparticle Stripes and Hexagonal Networks Obtained via Selective Patterning of Block Copolymer Thin Films. *Adv. Mater.* 17, 2206–2210. <https://doi.org/10.1002/adma.200500624>
- Shukla, R., Bansal, V., Chaudhary, M., Basu, A., Bhonde, R.R., Sastry, M., 2005. Biocompatibility of Gold Nanoparticles and Their Endocytotic Fate Inside the Cellular Compartment: A Microscopic Overview. *Langmuir* 21, 10644–10654. <https://doi.org/10.1021/la0513712>
- Siriwardana, K., Wang, A., Vangala, K., Fitzkee, N., Zhang, D., 2013. Probing the Effects of Cysteine Residues on Protein Adsorption onto Gold Nanoparticles

- Using Wild-Type and Mutated GB3 Proteins. *Langmuir* 29, 10990–10996. <https://doi.org/10.1021/la402239h>
- Slabaugh, W.H., 1962. A short textbook of colloid chemistry (Jirgensons, B.; Straumanis, M. E.). *J. Chem. Educ.* 39, 656. <https://doi.org/10.1021/ed039p656.2>
- Smith, D., 1996. Agarose Gel Electrophoresis, in: Harwood, A. (Ed.), *Basic DNA and RNA Protocols, Methods in Molecular Biology™*. Humana Press, pp. 17–21. <https://doi.org/10.1385/0-89603-402-X:17>
- Smith, S.G.J., Mahon, V., Lambert, M.A., Fagan, R.P., 2007. A molecular Swiss army knife: OmpA structure, function and expression. *FEMS Microbiol. Lett.* 273, 1–11. <https://doi.org/10.1111/j.1574-6968.2007.00778.x>
- Spinozzi, F., Ceccone, G., Moretti, P., Campanella, G., Ferrero, C., Combet, S., Ojea-Jimenez, I., Ghigna, P., 2017. Structural and Thermodynamic Properties of Nanoparticle–Protein Complexes: A Combined SAXS and SANS Study. *Langmuir* 33, 2248–2256. <https://doi.org/10.1021/acs.langmuir.6b04072>
- SPR Instruments [WWW Document], n.d. URL <https://www.sprpages.nl/instruments> (accessed 6.17.17).
- Stathopoulos, C., 1996. An alternative topological model for Escherichia coli OmpA. *Protein Sci.* 5, 170–173. <https://doi.org/10.1002/pro.5560050122>
- Su, Y.H., Chang, S.-H., Teoh, L.G., Chu, W.-H., Tu, S.-L., 2009. Plasmons: Chemical Bonding Coupling Induced Surface Plasmon Resonance Splitting in Self-Assembled Gold Nanoparticles. *J. Phys. Chem. C* 113, 3923–3928. <https://doi.org/10.1021/jp807584h>
- Sugawara, E., Nikaido, H., 1994. OmpA protein of Escherichia coli outer membrane occurs in open and closed channel forms. *J. Biol. Chem.* 269, 17981–17987.
- Sugawara, E., Nikaido, H., 1992. Pore-forming activity of OmpA protein of Escherichia coli. *J. Biol. Chem.* 267, 2507–2511.
- Sugawara, E., Steiert, M., Rouhani, S., Nikaido, H., 1996. Secondary structure of the outer membrane proteins OmpA of Escherichia coli and OprF of Pseudomonas aeruginosa. *J. Bacteriol.* 178, 6067–6069.
- Svergun, D.I., Richard, S., Koch, M.H.J., Sayers, Z., Kuprin, S., Zaccai, G., 1998. Protein hydration in solution: Experimental observation by x-ray and neutron scattering. *Proc. Natl. Acad. Sci.* 95, 2267–2272.
- Szöllősi, G.J., Derényi, I., Vörös, J., 2004. Reversible mesoscopic model of protein adsorption: From equilibrium to dynamics. *Phys. Stat. Mech. Its Appl.* 343, 359–375. <https://doi.org/10.1016/j.physa.2004.06.062>
- Tamm, L.K., Hong, H., Liang, B., 2004. Folding and assembly of β -barrel membrane proteins. *Biochim. Biophys. Acta BBA - Biomembr., Lipid-Protein Interactions* 1666, 250–263. <https://doi.org/10.1016/j.bbamem.2004.06.011>
- Tan, S.J., Campolongo, M.J., Luo, D., Cheng, W., 2011. Building plasmonic nanostructures with DNA. *Nat. Nanotechnol.* 6, 268–276. <https://doi.org/10.1038/nnano.2011.49>
- Terrettaz, S., Ulrich, W.-P., Vogel, H., Hong, Q., Dover, L.G., Lakey, J.H., 2002. Stable self-assembly of a protein engineering scaffold on gold surfaces. *Protein Sci. Publ. Protein Soc.* 11, 1917–1925.

- Thakurta, S.G., Subramanian, A., 2012. Fabrication of dense, uniform aminosilane monolayers: A platform for protein or ligand immobilization. *Colloids Surf. Physicochem. Eng. Asp.* 414, 384–392. <https://doi.org/10.1016/j.colsurfa.2012.08.049>
- Thanh, N.T.K., Rosenzweig, Z., 2002. Development of an Aggregation-Based Immunoassay for Anti-Protein A Using Gold Nanoparticles. *Anal. Chem.* 74, 1624–1628. <https://doi.org/10.1021/ac011127p>
- Thoma, J., Burmann, B.M., Hiller, S., Müller, D.J., 2015. Impact of holdase chaperones Skp and SurA on the folding of β -barrel outer-membrane proteins. *Nat. Struct. Mol. Biol.* 22, 795–802. <https://doi.org/10.1038/nsmb.3087>
- Thompson, S.E., Parthasarathy, S., 2006. Moore's law: the future of Si microelectronics. *Mater. Today* 9, 20–25. [https://doi.org/10.1016/S1369-7021\(06\)71539-5](https://doi.org/10.1016/S1369-7021(06)71539-5)
- Tsai, C.-S., Yu, T.-B., Chen, C.-T., 2005. Gold nanoparticle-based competitive colorimetric assay for detection of protein–protein interactions. *Chem. Commun.* 4273–4275. <https://doi.org/10.1039/B507237A>
- Tsai, D.-H., DelRio, F.W., Keene, A.M., Tyner, K.M., MacCuspie, R.I., Cho, T.J., Zachariah, M.R., Hackley, V.A., 2011. Adsorption and Conformation of Serum Albumin Protein on Gold Nanoparticles Investigated Using Dimensional Measurements and in Situ Spectroscopic Methods. *Langmuir* 27, 2464–2477. <https://doi.org/10.1021/la104124d>
- Tsirigotaki, A., De Geyter, J., Šoštarić, N., Economou, A., Karamanou, S., 2017. Protein export through the bacterial Sec pathway. *Nat. Rev. Microbiol.* 15, 21–36. <https://doi.org/10.1038/nrmicro.2016.161>
- Turkevich, J., Cooper Stevenson, P., Hillier, J., 1951. A study of the nucleation and growth processes in the synthesis of colloidal gold. *Discuss. Faraday Soc.* 11, 55–75. <https://doi.org/10.1039/DF9511100055>
- van der Heide, S., Russell, D.A., 2016. Optimisation of immuno-gold nanoparticle complexes for antigen detection. *J. Colloid Interface Sci.* 471, 127–135. <https://doi.org/10.1016/j.jcis.2016.03.001>
- Vandenberg, E.T., Bertilsson, L., Liedberg, B., Uvdal, K., Erlandsson, R., Elwing, H., Lundström, I., 1991. Structure of 3-aminopropyl triethoxy silane on silicon oxide. *J. Colloid Interface Sci.* 147, 103–118. [https://doi.org/10.1016/0021-9797\(91\)90139-Y](https://doi.org/10.1016/0021-9797(91)90139-Y)
- Vroman, L., 1962. Effect of Adsorbed Proteins on the Wettability of Hydrophilic and Hydrophobic Solids. *Nature* 196, 476–477. <https://doi.org/10.1038/196476a0>
- Wang, A., Perera, Y.R., Davidson, M.B., Fitzkee, N.C., 2016. Electrostatic Interactions and Protein Competition Reveal a Dynamic Surface in Gold Nanoparticle–Protein Adsorption. *J. Phys. Chem. C* 120, 24231–24239. <https://doi.org/10.1021/acs.jpcc.6b08469>
- Wang, A., Vangala, K., Vo, T., Zhang, D., Fitzkee, N.C., 2014. A Three-Step Model for Protein–Gold Nanoparticle Adsorption. *J. Phys. Chem. C* 118, 8134–8142. <https://doi.org/10.1021/jp411543y>

- Wang, G., Lu, Y., Hou, H., Liu, Y., 2017. Probing the binding behavior and kinetics of silver nanoparticles with bovine serum albumin. *RSC Adv.* 7, 9393–9401. <https://doi.org/10.1039/C6RA26089F>
- Wang, H., Andersen, K.K., Vad, B.S., Otzen, D.E., 2013. OmpA can form folded and unfolded oligomers. *Biochim. Biophys. Acta BBA - Proteins Proteomics, Special Section: Chemistry and mechanism of phosphatases, diesterases and triesterases* 1834, 127–136. <https://doi.org/10.1016/j.bbapap.2012.09.002>
- Wang, M., Liechti, K.M., Wang, Q., White, J.M., 2005. Self-Assembled Silane Monolayers: Fabrication with Nanoscale Uniformity. *Langmuir* 21, 1848–1857. <https://doi.org/10.1021/la048483y>
- Wang, R., Xiang, S., Feng, Y., Srinivas, S., Zhang, Y., Lin, M., Wang, S., 2013. Engineering production of functional scFv antibody in *E. coli* by co-expressing the molecule chaperone Skp. *Front. Cell. Infect. Microbiol.* 3. <https://doi.org/10.3389/fcimb.2013.00072>
- Wang, X., Mei, Z., Wang, Y., Tang, L., 2017. Comparison of four methods for the biofunctionalization of gold nanorods by the introduction of sulfhydryl groups to antibodies. *Beilstein J. Nanotechnol.* 8, 372–380. <https://doi.org/10.3762/bjnano.8.39>
- Wangoo, N., Suri, C.R., Shekhawat, G., 2008. Interaction of gold nanoparticles with protein: A spectroscopic study to monitor protein conformational changes. *Appl. Phys. Lett.* 92, 133104. <https://doi.org/10.1063/1.2902302>
- Welbourn, R., 2016. Adsorbed layers under challenging conditions at the solid-liquid interface.
- Whitney, A.V., Elam, J.W., Zou, S., Zinovev, A.V., Stair, P.C., Schatz, G.C., Van Duyne, R.P., 2005. Localized Surface Plasmon Resonance Nanosensor: A High-Resolution Distance-Dependence Study Using Atomic Layer Deposition. *J. Phys. Chem. B* 109, 20522–20528. <https://doi.org/10.1021/jp0540656>
- WHO, n.d. WHO [WWW Document]. WHO. URL <http://www.who.int/mediacentre/factsheets/fs211/en/> (accessed 5.31.17).
- Wijaya, E., Lenaerts, C., Maricot, S., Hastanin, J., Habraken, S., Vilcot, J.-P., Boukherroub, R., Szunerits, S., 2011. Surface plasmon resonance-based biosensors: From the development of different SPR structures to novel surface functionalization strategies. *Curr. Opin. Solid State Mater. Sci.* 15, 208–224. <https://doi.org/10.1016/j.cossms.2011.05.001>
- Willets, K.A., Duyne, R.P.V., 2007. Localized Surface Plasmon Resonance Spectroscopy and Sensing. *Annu. Rev. Phys. Chem.* 58, 267–297. <https://doi.org/10.1146/annurev.physchem.58.032806.104607>
- Williams, D.B., Carter, C.B., 2009. The Transmission Electron Microscope, in: *Transmission Electron Microscopy*. Springer US, pp. 3–22. https://doi.org/10.1007/978-0-387-76501-3_1
- Williams, H.B., Chang, L.T., 1951. Gold Number Studies, with Some Observations on Sensitization and Protection. *J. Phys. Chem.* 55, 719–725. <https://doi.org/10.1021/j150488a011>
- Wuithschick, M., Birnbaum, A., Witte, S., Sztucki, M., Vainio, U., Pinna, N., Rademann, K., Emmerling, F., Kraehnert, R., Polte, J., 2015. Turkevich in New

- Robes: Key Questions Answered for the Most Common Gold Nanoparticle Synthesis. *ACS Nano* 9, 7052–7071. <https://doi.org/10.1021/acsnano.5b01579>
- Yang, H., Liu, L., Li, J., Chen, J., Du, G., 2015. Rational Design to Improve Protein Thermostability: Recent Advances and Prospects. *ChemBioEng Rev.* 2, 87–94. <https://doi.org/10.1002/cben.201400032>
- Yi, Y.W., Robinson, H.G., Knappe, S., MacLennan, J.E., Jones, C.D., Zhu, C., Clark, N.A., Kitching, J., 2008. Method for characterizing self-assembled monolayers as antirelaxation wall coatings for alkali vapor cells. *J. Appl. Phys.* 104, 023534. <https://doi.org/10.1063/1.2958329>
- Yong, W., Lomakin, A., Kirkitadze, M.D., Teplow, D.B., Chen, S.-H., Benedek, G.B., 2002. Structure determination of micelle-like intermediates in amyloid β -protein fibril assembly by using small angle neutron scattering. *Proc. Natl. Acad. Sci.* 99, 150–154. <https://doi.org/10.1073/pnas.012584899>
- Yu, Q., Golden, G., 2007. Probing the Protein Orientation on Charged Self-Assembled Monolayers on Gold Nanohole Arrays by SERS. *Langmuir* 23, 8659–8662. <https://doi.org/10.1021/la7007073>
- Yuan, M., Zhan, S., Zhou, X., Liu, Y., Feng, L., Lin, Y., Zhang, Z., Hu, J., 2008. A Method for Removing Self-Assembled Monolayers on Gold. *Langmuir* 24, 8707–8710. <https://doi.org/10.1021/la800287e>
- Zakharian, E., Reusch, R.N., 2005. Kinetics of Folding of Escherichia coli OmpA from Narrow to Large Pore Conformation in a Planar Bilayer†. *Biochemistry (Mosc.)* 44, 6701–6707. <https://doi.org/10.1021/bi047278e>
- Zanchet, D., Micheel, C.M., Parak, W.J., Gerion, D., Williams, S.C., Alivisatos, A.P., 2002. Electrophoretic and Structural Studies of DNA-Directed Au Nanoparticle Groupings. *J. Phys. Chem. B* 106, 11758–11763. <https://doi.org/10.1021/jp026144c>
- Zanzoni, S., Pedroni, M., D’Onofrio, M., Speghini, A., Assfalg, M., 2016. Paramagnetic Nanoparticles Leave Their Mark on Nuclear Spins of Transiently Adsorbed Proteins. *J. Am. Chem. Soc.* 138, 72–75. <https://doi.org/10.1021/jacs.5b11582>
- Zehner, R.W., Lopes, W.A., Morkved, T.L., Jaeger, H., Sita, L.R., 1998. Selective Decoration of a Phase-Separated Diblock Copolymer with Thiol-Passivated Gold Nanocrystals. *Langmuir* 14, 241–244. <https://doi.org/10.1021/la971086l>
- Zhao, L., Jiang, D., Cai, Y., Ji, X., Xie, R., Yang, W., 2012. Tuning the size of gold nanoparticles in the citrate reduction by chloride ions. *Nanoscale* 4, 5071–5076. <https://doi.org/10.1039/C2NR30957B>
- Zhao, W., Brook, M.A., Li, Y., 2008. Design of Gold Nanoparticle-Based Colorimetric Biosensing Assays. *ChemBioChem* 9, 2363–2371. <https://doi.org/10.1002/cbic.200800282>
- Zheng, C., Yang, L., Hoopmann, M.R., Eng, J.K., Tang, X., Weisbrod, C.R., Bruce, J.E., 2011. Cross-linking Measurements of In Vivo Protein Complex Topologies. *Mol. Cell. Proteomics* 10, M110.006841. <https://doi.org/10.1074/mcp.M110.006841>
- Zhu, S.-Q., Zhang, T., Guo, X.-L., Wang, Q.-L., Liu, X., Zhang, X.-Y., 2012. Gold nanoparticle thin films fabricated by electrophoretic deposition method for

highly sensitive SERS application. *Nanoscale Res. Lett.* 7, 613.
<https://doi.org/10.1186/1556-276X-7-613>

Zook, J.M., Rastogi, V., MacCuspie, R.I., Keene, A.M., Fagan, J., 2011. Measuring Agglomerate Size Distribution and Dependence of Localized Surface Plasmon Resonance Absorbance on Gold Nanoparticle Agglomerate Size Using Analytical Ultracentrifugation. *ACS Nano* 5, 8070–8079.
<https://doi.org/10.1021/nn202645b>